A study of the mechanisms of damage and recovery of the central nervous system in demyelinating diseases using diffusion tensor imaging and functional magnetic resonance imaging

Olga Ciccarelli

A thesis submitted to the University College London for the degree of

Doctor of Philosophy

May 2004

NMR Research Unit

Department of Headache, Brain Injury and Rehabilitation

Institute of Neurology, University College London

Queen Square

London WC1N 3BG

United Kingdom

ProQuest LLC
789 East Eisenhower Parkway
P.O. Box 1346
Ann Arbor, MI 48106-1346

Abstract

The aim of this thesis was to develop and apply Diffusion Tensor Imaging (DTI) and functional Magnetic Resonance Imaging (fMRI) in patients with demyelinating diseases in order to provide further insights into the mechanisms of damage and recovery.

We used DTI to investigate pathological changes in the normal-appearing (NA) brain of patients with multiple sclerosis (MS), using regions of interest. Our results showed that diffusion changes were associated with disability and progression in MS, and that the NA white matter damage related to focal lesions.

We then extended the investigation to the whole white matter tracts, using the novel technique of diffusion-based tractography, in three separate studies. In the first study, we assessed the reproducibility of fast marching tractography in quantifying the major white-matter pathways. In the second, we created probabilistic group maps of these tracts in healthy volunteers, in order to estimate their normal inter-subjects variability. In the third study, we employed these group mapping techniques to investigate pathologic changes in the optic radiations of patients affected by optic neuritis, and found that patients had a lower voxel-scale connectivity in the optic radiations when compared with controls.

To complement these studies, we developed a motor paradigm that allows investigation of the brain functional response to active and passive movements of the foot. We then used this paradigm to determine the role of cortical reorganisation in patients with primary progressive MS, and concluded that brain functional changes, in our cohort of patients, represented both adaptive and non-adaptive responses to central nervous system damage.

Finally, we combined the data obtained from tractography with those obtained by fMRI, in patients with optic neuritis, and demonstrated the potential of this methodology to understand the relationship between structural and functional mechanisms.

Acknowledgements

I would like to thank the following, without whom this thesis may never have been possible. The NMR Research Unit that provided me with all the necessary facilities to carry out this research, thanks to a generous grant from the MS Society of Great Britain and Northern Ireland. Teva Pharmaceuticals Ltd. and the Department of Headache, Brain Injury and Neurorehabilation, which funded me throughout the project and allow me to attend international conferences.

A special thanks to my principal supervisor, Professor Alan Thompson, for his invaluable advice and assistance, and for never giving up in his attempts to teach me the use of the tricky word "the" in the English language.

A warm "grazie" to my second supervisor, Dr Claudia Wheeler-Kingshott, for shedding light on the dark and murky world of physics, for helping me with the methodology of this research, and for being such a good friend.

I would like to thank Professor David Miller, who five years ago, allowed me to come here from Rome for six months, and whose support and advice has contributed to the completion of this thesis. I would also like to thank Professor Paul M. Matthews, at the fMRIb Centre in Oxford, for his suggestion about the fMRI paradigm and analysis.

I warmly thank Dr Ahmed Toosy, for his tireless assistance in analysing and writing up the papers and seemingly endless knowledge of SPM, statistics and cricket, although I do not think that I will ever really understand the latter.

Many thanks to Dr Geoff Parker for his collaboration in the development of the tractography algorithm used in this thesis, Professor Gareth Barker for his assistance with implementing DTI and fMRI analysis, and Dr Daniel Altmann for his statistical advice.

Thanks to David MacManus, Chris Benton and Ros Gordon, for their assistance with the MRI scanner. I would also like to thank Dr Jaume Sastre-Garriga, Dr Gordon Ingle and all the other fellows for their kind support.

I am very grateful to the SPM meetings at the Functional Imaging Laboratory, led by Professor Karl Friston, Wellcome Department of Cognitive Neurology, London, for guidance and advice on the SPM analysis, and to Dr Catherine Miszkiel for reviewing all the conventional brain and spinal cord scans.

Thanks to all those who "volunteered", after my considerable persuasion, to be scanned as normal controls, and to all those patients who agreed to take part in the studies described in this thesis, and thereby played a vital role in increasing our knowledge of neurological diseases.

I would like to thank Toby Vanhegan, who I met at the time I was carrying out the work described in chapter 1, and who asked me to marry him during the writing up of chapter 5, for proof reading this thesis and forcing me to go to Rome for holidays. A special thanks to my mother and father for their unconditional support when I wanted to be a lawyer, a doctor in Rome, and now a Neuroscientist in England.

Publications associated with this thesis

Ciccarelli O, Werring DJ, Wheeler-Kingshott CAM, Barker GJ, Parker GJM, Thompson AJ, Miller DH. Investigation of MS normal-appearing brain using diffusion tensor MRI with clinical correlations. *Neurology* 56: 926-933, 2001.

Ciccarelli O, Werring DJ, Barker GJ, Griffin CM, Wheeler-Kingshott CAM, Miller DH, Thompson AJ. A study of the mechanisms of normal-appearing white matter damage in multiple sclerosis using diffusion tensor imaging: evidence of Wallerian degeneration. *Journal of Neurology* 250:287-292, 2003.

Ciccarelli O, Parker GJM, Toosy AT, Wheeler-Kingshoot CAM, Barker GJ, Boulby PA, Miller DH, Thompson AJ. From diffusion tractography to quantitative white-matter tract measures: a reproducibility study. *NeuroImage* 18:348-359, 2003.

Ciccarelli O, Toosy AT, Parker GJM, Wheeler-Kingshoot CAM, Barker GJ, Miller DH, Thompson AJ. Diffusion tractography based group mapping of major white-matter pathways in the human brain. *NeuroImage* 19:1545-1555, 2003.

Toosy AT, **Ciccarelli O**, Parker GJM, Wheeler-Kingshott CAM, Barker GJ, Miller DH, Thompson AJ. Characterising function-structure relationships in the human visual system with functional MRI and diffusion tensor imaging. *NeuroImage* 21: 1452-1463, 2004.

Ciccarelli O, Toosy AT, Hickman SJ, Parker GJM, Wheeler-Kingshoot CAM, Miller DH, Thompson AJ. Optic radiation changes after optic neuritis detected by tractography based group mapping. *Human Brain Mapping* (In Press), 2004.

Ciccarelli O, Toosy AT, Marsden JF, Wheeler-Kingshott CM, Sahyoun C, Matthews PM, Miller DH, Thompson AJ. Identifying brain regions for integrative sensorimotor processing with foot movement. *Experimental Brain Research* (In Press), 2004.

Ciccarelli O, Toosy AT, Marsden JF, Wheleer-Kingshott CM, Miller DH, Matthews PM, Thompson AJ. Functional mechanisms diminish with increasing disability in patients with primary-progressive multiple sclerosis. *Human Brain Mapping* (Submitted), 2004.

Table of Contents

List of Figures

Chapter 4

Chapter 5

Chapter 6

List of Tables

Chapter 5

Chapter 6

Abbreviations

B_0	magnetic field strenght
ω_0	frequency of precession
ADC	apparent diffusion coefficient
BBB	blood brain barrier
BOLD	blood oxygen level dependent
CC	corpus callosum
CNS	central nervous system
CV	coefficient of variation
CSE	conventional spin echo
CSF	cerebrospinal fluid
DTI	diffusion tensor imaging
DW	diffusion weighting
EDSS	expanded disability status scale
EPI	echo planar imaging
FID	free induction decay
FMT	fast marching tractography
fMRI	functional magnetic resonance imaging
FA	fractional anisotropy
FSE	fast spin echo
Gd	gadolinium (contrast agent)
MD	mean diffusivity
MNI	Montreal Neurological Institute
MRS	MR spectroscopy
MS	multiple sclerosis
MTI	magnetisation transfer imaging
MTR	magnetisation transfer ratio
NAA	N-acetyl-aspartate
NABT	normal appearing white matter
NAGM	normal appearing grey matter
NAWM	normal appearing brain tissue

NV	normalised volume
PD	proton density
PD-WI	proton density weighted imaging
PICo	probabilistic index of connectivity
PP	primary progressive
RR	relapsing remitting
ROI	region of interest
SNR	signal-to-noise ratio
SP	secondary progressive
T1	longitudinal relaxation time
T1-WI	T1 weighted imaging
T2	transversal relaxation time
T2*	loss of phase due to inhomogeneities within the magnetic field
T2-WI	T2 weighted imaging
TE	echo time
TR	repetition time
VEP	visual evoked potential
VSC	voxel scale connectivity

Chapter 1

An introduction to demyelinating diseases and the clinical application of Magnetic Resonance Imaging

The first application of Magnetic Resonance Imaging (MRI) in multiple sclerosis (MS) was described in 1981 (Young et al. 1981). Since then, the use of MRI in MS has evolved rapidly and has become the primary technique with which neurologists support the diagnosis of MS, and with which researchers monitor disease evolution in both natural history studies and treatment trials. New MRI techniques have been developed to provide additional information on the pathology of MS. They have offered insights into the pathophysiology of the disease, and have confirmed that MS is not only a disease of the white matter in the central nervous system (CNS), but also of the grey matter, and that pathologic abnormalities can affect the brain tissue beyond the demyelinating lesions.

This thesis is concerned with investigating the mechanisms of damage and recovery of the CNS in demyelinating diseases. Two clinical models are considered: 1) the visual pathway; 2) the motor system. In the first model we investigate optic neuritis, which is a common symptom of MS, characterised by the development of an acute inflammatory, demyelinating lesion within the optic nerve. In the second model, primary progressive MS, which is a model of chronic spinal cord syndrome, is considered. The methods used diffusion tensor imaging (DTI), which investigates pathologic damage, and functional MRI (fMRI), which examines cortical reorganisation following tissue damage and its role in clinical recovery.

This chapter describes the main clinical and radiological characteristics of the demyelinating diseases which are studied in this work and is organised in two parts. The first part gives a brief introduction to MS, particularly primary progressive MS, and optic neuritis. The second part deals with the applications of both conventional and new MRI techniques to MS and other demyelinating diseases.

1.1. Demyelinating diseases

1.1.1. Multiple Sclerosis

Multiple sclerosis (MS) is a chronic disease of the CNS that begins most commonly in young adults, and is pathologically characterised by multiple areas of white matter inflammation, demyelination, and gliosis. The white matter lesions are, therefore, multiple *in space*. The clinical course of MS varies from a benign course to a rapidly progressive and disabling disorder. Most patients, however, begin with a relapsing-remitting illness, which is caused by the occurrence of multiple lesions that are disseminated *in time* as well as *in space*. The cause remains elusive, although autoimmune mechanisms, possibly triggered by environmental factors in genetically susceptible individuals, are thought to be important. This section deals generally with the clinical characteristics and pathologic data of MS and, in particular, of primary progressive MS and optic neuritis.

1.1.1.1. Clinical features

Age at onset follows a unimodal distribution with a peak between the ages of 20 and 30. MS is more common amongst women than men (women-to-men ratio from 1.4 to 3.1:1). In patients with later onset the sex ratio tends to be equal. The geographic distribution is uneven (Kurtzke 1993): the disease increases in frequency with latitude in both the northern and southern hemispheres, although the rates tend to decrease above 65° north or south. Most of northern Europe, the United States, southern Canada, southern Australia and New Zealand are areas of prevalence equal to or higher than 30/100,000, whilst Japan, China, Latin and South America are regions of low prevalence (5/100,000) (Sawcer et al. 1997). Although there is no doubt that latitude affects its prevalence, racial differences may help to explain the geographic distribution of the disease. Indeed, although Britain and Japan are at the same

latitude, they have very different prevalence rates (Britain: 85/100,000, Japan: 8.5/100,000). Studies of migrant populations (Gale and Martyn 1995) have provided evidence of a pathogenetic role in environmental factors. Other studies conducted on people migrating from the Indian subcontinent or the West Indies to Great Britain, suggested that age at the time of immigration played an important role (Dean et al. 1976); individuals migrating before the age of 15 have the same risk of developing MS as that of the country to which they move, while after the age of 15 they have the risk of the country of origin. Reports of epidemics of MS further support the importance of an environmental factor in the pathogenesis of the disease. The most impressive epidemic occurred in the Faroe Islands, where cases appeared shortly after the islands were occupied by British troops in World War II (Kurtzke 1993).

Besides environmental factors, genetics also play a role in the pathogenesis of MS (Willer and Ebers 2000). However, studies in twins have shown that the concordance of MS is 26% in monozygous twins and 2% in dizygous twins, suggesting that genetic factors are not sufficient for the disease expression (Ebers et al. 1986). Moreover, studies on familial MS in Northern Europe have reported a risk of the disease of around 15% in first degree relatives (Riise 1997).

The symptoms and signs of MS are several and can result from injury to any part of the CNS, from the spine to the brain. However, some areas and systems are more often affected than others: optic nerve, brain stem, cerebellum, lateral and posterior columns of the spinal cord are commonly involved. The most common visual symptom is optic neuritis (see below). The typical visual symptom is internuclear ophalmoplegia, which is caused by a lesion in the medial longitudinal fasciculus. Common brainstem symptoms include trigeminal neuralgia, due to the involvement of the V cranial nerve, weakness of the muscles of the lower half of one side of the face, due to VII nerve involvement, and bulbar signs, such as dysarthria and

dysphagia. Limb weakness is the most common sign, almost always present in advanced cases, and can affect from one to all limbs. Cerebellar signs include dysarthria, gait ataxia, tremor and lack of coordination of the trunk or limbs. Therefore, the gait can be impaired by a combination of weakness, spasticity, cerebellar and sensory ataxia. Urinary symptoms are also common and include incontinence, frequency, and urgency. Other symptoms of autonomic dysfunction include constipation, loss of libido and sexual dysfunction. Sensory symptoms, such as parasthesias, sensory loss, and Lhermitte's sign, are common. Mental symptoms are also frequent, and they include impaired memory, reduced concentration and attention. Fatigue is another common symptom that is not related to age or to the amount of physical disability. Mood disorders are also frequent.

The clinical course of MS has been observed to vary between subjects. Five patterns of the disease have been recognized. Most patients (about 85%) present with one or more neurological symptoms that recover fully; further episodes of neurological deterioration typically occur with a frequency of 1.5 a year (relapsing-remitting (RR) MS). In about 30-40% of these patients, after a period of about 10, the disease evolves into a secondary progressive (SP) course (Figure 1.1) (Weinshenker et al. 1989b). Relapses may occur or not during this progressive phase. The third clinical variant of MS is primary progressive (PP), which affects a minority of patients (10-15%) and is characterised by a progressive illness from onset (Figure 1.1) (Thompson et al. 1997). Another variant of MS is so-called benign MS and is present in about 20% of the cases with little or no disability after 15 years (Lublin and Reingold 1996). However, this is a somewhat artificial distinction because it is based on disease disability rather than course. Patients rarely present with a fatal form of demyelination, called Marburg form (Ozawa et al. 1994). Patients with this form die within one year from the onset, and post-mortem studies detected particularly destructive lesions in the brain (Lucchinetti et al. 1996).

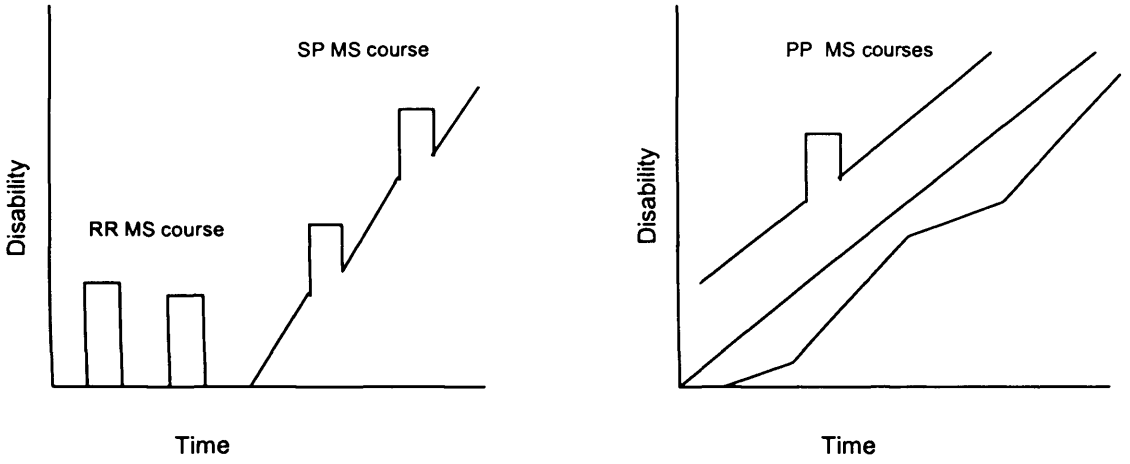

Figure 1.1. Different forms of MS. Relapsing-remitting (RR) and secondary progressive (SP) courses are displayed on the left side of the figure; primary progressive (PP) courses, with or without superimposed relapses, are displayed on the right side.

1.1.1.2. Diagnostic criteria

The diagnosis of MS rests upon the history and clinical examination findings, which often allow a diagnosis to be made with considerable confidence. However, in clinical trials and research studies, it is necessary to define precisely the population of patients studied. Therefore, a number of diagnostic classifications have been proposed over the years. The existing diagnostic criteria (Poser et al. 1983) were recently reassessed and modified by an international panel and new criteria were proposed (McDonald et al. 2001)(Table 1.1). Poser's diagnostic criteria required clinical evidence of dissemination *in time* and *space*, i.e. at least two relapses in separate locations. When the clinical evidence alone does not allow a diagnosis to be made, the new criteria allow the use of radiological and laboratory findings, including MRI, and the analysis of cerebrospinal fluid (CSF) and visual evoked potential (VEP), to make the diagnosis. Among these paraclinical tests, MRI is the most sensitive and specific tool for demonstrating disease dissemination *in time* and *space*.

An MRI scan is considered to show dissemination *in space* when there is evidence of at least three of the following (Barkhof et al. 1997;Tintore et al. 2000):

- One gadolinium-enhancing lesion or nine T2 hyperintense lesions if a gadolinium enhancing lesion is not present (Note: one cord lesion can substitute for one brain lesion);
- At least one infratentorial lesion;
- At least one juxtacortical lesion;
- At least three periventricular lesions.

MRI can also provide evidence of dissemination *in time* when:

- A gadolinium-enhancing lesion is demonstrated on a scan taken at least three months following the onset of a single attack at a different site from the attack or
- In the absence of gadolinium-enhancing lesions on the three month scan, a subsequent follow-up scan after an additional three months shows a gadolinium-enhancing lesion or a new T2 lesion.

These new MRI criteria have been proved to be of value in predicting those patients who will develop clinically definite MS after an isolated neurological episode (Dalton et al. 2002). If the criteria indicated are fulfilled, the diagnosis is MS; if they are partially met, the diagnosis is "possible MS".

Table 1.1. McDonald's diagnostic criteria (from McDonald, Ann Neurol 2001).

CLINICAL PRESENTATION	ADDITIONAL DATA NEEDED FOR MS DIAGNOSIS
Two or more attacks; objective clinical evidence of 2 or more lesions	None
Two or more attacks; objective clinical evidence of 1 lesion	Dissemination **in space** demonstrated by MRI- *Or* Two or more MRI lesions consistent with MS plus positive CSF *Or* Await further clinical attack implicating a different site
One attack; objective clinical evidence of 2 or more lesions	Dissemination **in time** demonstrated by MRI *Or* Second clinical attack
One attack; objective clinical evidence of 1 lesion (Clinically Isolated Syndrome)	Dissemination **in space** demonstrated by MRI *Or* Two or more MRI lesions consistent with MS plus positive CSF *And* Dissemination **in time** demonstrated by MRI *Or* Second clinical attack
Insidious neurological progression suggestive of MS	Positive CSF *And* Dissemination **in space** demonstrated by MRI (see diagnosis in PP MS) *And* Dissemination **in time** demonstrated by MRI *Or* Continued progression for 1 year

1.1.1.3. Pathology

The pathological hallmarks of MS are the destruction of myelin, the death of oligodendrocytes, and the loss of axons (Lassmann 1998;Prineas 1975). These changes occur against an inflammatory background which consists of inflammatory infiltrates composed of macrophages, microglia, T and B cells. A diffuse inflammatory process occurs throughout the

brain, and is accentuated in actively demyelinating lesions (Lassmann et al. 1994). In the early or acute lesions there is a marked hypercellularity, with macrophage infiltration and astrocytosis, perivenous inflammation with lymphocytes and plasmacells, and breakdown of myelin. With time, the lesions become inactive and hypocellular, and show prominent demyelination, almost total loss of oligodendrocytes, and gliosis. It is thought that the remyelination in lesions may follow the early acute phase, and result from the differentiation of a precursor cell that is common to type II astocytes and oligodendrocytes. This remyelination, however, is usually aberrant and incomplete, and leads to the formation of "shadow" plaques.

A recent histopathological study in a large series of MS patients found two distinct patterns of myelin and oligodendrocyte pathology (Lucchinetti et al. 1999). The first showed a reduction of oligodendrocytes in lesions with ongoing demyelination and then reappearance of oligondendrocytes after resolution, leading to remyelination. The second pattern revealed severe destruction of oligodendrocytes without remyelination. This finding supports the hypothesis that the immunopathologic mechanisms, which lead to myelin and/or oligodendrocyte injury in MS, are variable.

A pathologic follow-up study of active demyelinating lesions investigated the presence of different mechanisms of damage (Lucchinetti et al. 2000). Four different immunopathogenetic subtypes or patterns were identified on the basis of their cellular infiltrates: 1) T cell/macrophage-mediated demyelination; 2) Antibody/complement-mediated demyelination; 3) Oligodendrocyte dystrophy with myelin protein dysregulation and oligodendrocyte apoptosis; 4) Primary oligodendrocyte degeneration with features similar to those of viral infection or toxic oligodendrocyte damage, but not to those of autoimmunity. The first four patterns were distributed homogenously among the different disease courses. In contrast, pattern 4 was exclusively observed in three cases of PP MS. An interesting finding was that

there was heterogeneity between patients, but that only one distinct pattern was observed in multiple lesions in any given patient at the time of the investigation.

Besides oligodendrocyte/myelin pathology, the pathology of axons has been shown to be a major factor in the development of clinical disability (Trapp et al. 1998). Axonal damage can occur in active lesions (Ferguson et al. 1997;Trapp et al. 1998), due to inflammatory substances that are produced by activated immune and glial cells, and in the white matter tissue that appears normal on the conventional MRI (called normal-appearing white matter (NAWM)), due to the degeneration of axons transected in focal lesions. Moreover, axonal loss may also occur independently of demyelination, perhaps due to antibodies anti-axonal proteins, such as the anti-ganglioside antibodies (Sadatipour et al. 1998), or to the synthesis of nitric oxide (Smith and Lassmann 2002), which can directly damage neurons and axons. A further form of degeneration of axons may occur in those that are chronically demyelinated due to the lack of trophic support from myelin or myelin-forming cells (Griffiths et al. 1998). It is thought that the transition from RR to SP MS and the subsequent development of irreversible disability could occur when a threshold of neuronal or axonal loss is reached, or when adaptive responses of the CNS are exhausted (Trapp et al. 1999).

1.1.1.4. Prognosis

Prognosis of MS is highly variable, and the time from disease onset to an EDSS score of 4 ranges from 1 year to 33 years (Confavreux et al. 2000). The progressive forms of MS have a worse prognosis compared with RR MS (Weinshenker et al. 1989a). Unfortunately, no reliable prognostic indicators are available. A benign course is associated with onset before the age of 40 years, onset with optic neuritis or sensory symptoms, complete remission of initial symptoms, minimal disability 5 years after the onset, and long intervals between the

onset and the first relapse, and between the onset to the assignment of an EDSS score of 4 (Confavreux et al. 2003;Kantarci et al. 1998;Kurtzke et al. 1977;Ramsaransing et al. 2001;Trojano et al. 1995;Weinshenker et al. 1989a). Poor prognostic indicators include: polysymptomatic onset, male gender, and older age at onset (Kantarci et al. 1998;Kurtzke et al. 1977;Noseworthy et al. 1983;Weinshenker et al. 1989a). Moreover, an EDSS of 4.5 is associated with higher risk of progression in the following 3 years (Weinshenker et al. 1996). A recent study showed that once a score of 4 has been reached, all these factors are no longer predictive of the subsequent disability progression (Confavreux et al. 2003), suggesting that MS is a two-stage disease, with an initial phase influenced by clinical variables, and a second phase which does not depend upon the baseline characteristics. It is possible that the first stage, which represents the RR course, is related to the occurrence of inflammatory lesions, whereas the second stage, which develops during the progressive phase of the disease, is due to pre-determined degeneration (Confavreux et al. 2003).

1.1.2. Primary Progressive MS

Nearly 150 years ago, Charcot (Charcot 1868) recognised that some forms of MS could be progressive from onset, failing to exhibit any of the acute episodes of neurological deterioration that characterises the more common clinical course of the disease. This form of progressive disease has been called primary progressive MS (PP MS). As mentioned earlier, PP MS is the least common clinical disease phenotype exhibited by MS patients, being present in about 15% of cases. Although 5% of these cases will eventually experience one or more relapses (Stevenson et al. 1999), only about 10% of all MS patients fall strictly in the category of PP MS. Little information has been available on the natural history and demographic

features of PP MS (Confavreux et al. 1980), but in the last few years the scientific interest in this form of MS has grown.

1.1.2.1. Clinical features and diagnosis

The onset of PP MS appears to occur almost a decade later than in other form of MS (Weinshenker et al. 1989b). In absolute terms, more women are still affected by this phenotype (male-to-female ratio 1:1.3) (Cottrell et al. 1999), although compared to other MS subtypes the proportion of affected men is relatively higher. The most common presenting symptom is motor deficit, present in 39% (Cottrell et al. 1999) to 83% of patients (Stevenson et al. 1999). In particular, the majority of PP MS patients present with progressive myelopathy, most often with a spastic paraparesis (Bashir and Whitaker 1999;Cottrell et al. 1999;Thompson et al. 1997) or, less commonly, with a progressive hemiparesis or ataxia. Less frequent presentations included cerebellar dysfunction (8%), hemiplegia (6%), visual loss (1%), brainstem symptoms (1%) or cognitive deficits (1%) (Stevenson et al. 1999).

The Poser criteria for the diagnosis of MS, which concentrated on relapses as a requirement for disease dissemination *in time* and *space* (Poser et al. 1983), have been shown to be inadequate to diagnose PP MS (McDonnell and Hawkins 1997;Thompson et al. 1997). Therefore, some European investigators have formulated diagnostic criteria specific for PP MS (Thompson et al. 2000)(Table 1.2). The main elements of the new diagnostic criteria are the following: at least one year's history of clinical progression, the exclusion of other conditions, a graded level of diagnostic certainty (definite, probable and possible MS), and a central role for the presence of intrathecal IgG synthesis for a definite diagnosis. Moreover, the new criteria incorporated specific findings on MRI, including the presence of at least nine hyperintense lesions on T2-W images, each having a diameter of at least 3 mm, or at least two

intrinsic spinal cord lesions. If brain imaging alone does not reach the level necessary for positive evidence, but between four and eight lesions are seen, the additional presence of one spinal cord lesion is considered as satisfying positive MRI criteria. In large part, these new diagnostic criteria were incorporated into the new international panel criteria for the diagnosis of all forms of MS, discussed above (McDonald et al. 2001).

Table 1.2. Diagram for the diagnosis of PP MS (adapted from Thompson et al., 2000).

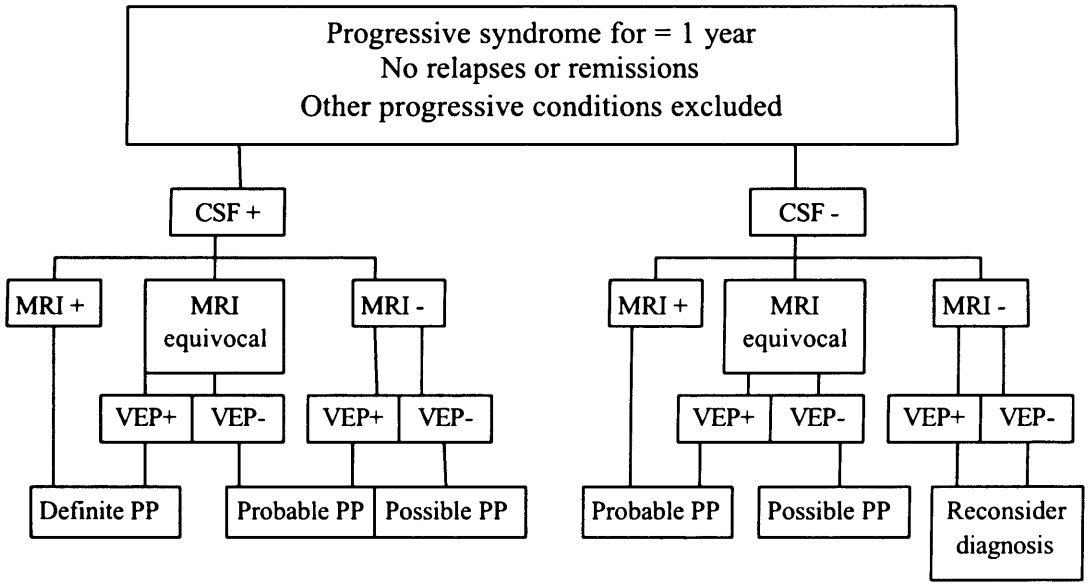

1.1.2.2. Pathology

Very few studies have focused on the question of whether the PP form is also characterised by a specific pathology. However, there is evidence that indicates that the differences between PP MS and the other MS categories are both quantitative and qualitative. The main quantitative difference is that a significantly lower amount of inflammation has been detected in PP MS compared with SP MS (Revesz et al. 1994). This difference was detected in lesions of the cerebral hemispheres, the brainstem, and the spinal cord. Although inflammation may be less severe, it seems to persist for longer than in RR and SP MS lesions (Zettl et al. 1998). Other quantitative differences include a more pronounced oligodendrocyte loss in lesions of PP MS (Lucchinetti et al. 1999) and a lower amount of acutely damaged axons than in SP MS (Bitsch

et al. 2000). Moreover, the anti-ganglioside antibodies, which seem to cause loss of axons independently from demyelination, were more numerous in PP MS than in SP and RR MS (Sadatipour et al. 1998). On the other hand, the main qualitative difference includes the occurrence of one immunopathological subtype of demyelination (Lassmann et al. 2001;Lucchinetti et al. 2000), i.e. the primary degeneration of oligodendrocytes in at least a subgroup of PP patients.

1.1.2.3. Prognosis

From the onset of MS, the prognosis has been shown to be worse for patients with PP MS, although there is little difference between the PP and SP patients after the onset of disease progression (Cottrell et al. 1999). Among the PP patients, those who present with multiple system involvement at the onset (Cottrell et al. 1999) and early accumulation of disability were found to show a worse prognosis (Weinshenker et al. 1989a). A recent study found that none of the clinical factors which predicted the clinical disability in patients with RR MS showed a significant influence on the progression of patients with PP MS (Confavreux et al. 2003). The only exception was a slower progression in females. Moreover, no difference in the clinical course was found between those patients which presented with clinical attacks and those without.

1.1.3. Optic neuritis

Optic neuritis is a term used to refer to inflammation of the optic nerve. When it is associated with a swollen optic nerve, it is called "papillitis" or "anterior optic neuritis". When the optic disc appears normal, the terms "retrobulbar optic neuritis" or "retrobulbar neuritis" are used.

In the absence of signs of MS or other systemic disease, optic neuritis is referred to as isolated, monosymptomatic, or idiopathic. The pathogenesis of isolated optic neuritis is presumed to be demyelination of the optic nerve, similar to that seen in MS lesions. About 69% of cases which present with an acute, isolated and unilateral optic neuritis will develop MS later in life (Brex et al. 2002). Optic neuritis is also a frequent manifestation of MS, and, indeed, in about 20% of the cases, is the presenting symptom (Perkin and Rose 1979). This section deals with acute demyelinating optic neuritis, occurring in isolation, or in association with MS.

1.1.3.1. Clinical features

The annual incidence of acute optic neuritis has been estimated in population-based studies to be between 1 and 5 per 100,000 (Rodriguez et al. 1995). The majority of patients are between the ages of 20 and 50 years, with a mean age of 30-35 years. Females are more commonly affected than males. There are two major symptoms in patients with acute optic neuritis. The first, which is present in more than 90% of patients, is loss of central visual acuity (Optic Neuritis Study Group 1991). This is usually acute, occurring over several hours to several days, and varies between complete blindness, with no perception of light, to a minimal reduction. The majority of patients describe diffuse blurred vision in one eye, although some may report a central blurring. A minority of patients present with a loss of peripheral vision, usually in the inferior or superior region of the visual field, and normal visual acuity (Kupersmith et al. 1983). The second major symptom is pain in or around the eye. It is usually mild, although it can be very severe, is exacerbated by eye movement and lasts no more than a few days. It may precede or occur concurrently with visual loss (Optic Neuritis Study Group 1991).

On examination there are signs of optic nerve dysfunction. Visual acuity is reduced in most cases and varies from a mild reduction to no light perception (Optic Neuritis Study Group 1991). Colour vision is impaired in almost all cases, and is often more severely affected than visual acuity itself (Menage et al. 1993). Visual field loss can vary from mild to severe. Any type of visual field defect can occur, including central scotoma (Beck 1998), arcuate defect, cecocentral scotoma, superior or inferior altitudinal defect and hemianopic defect (Keltner et al. 1993). A relative afferent pupillary defect is almost always present (Cox et al. 1981) and detectable with a swinging flashlight test in almost all unilateral cases. Patients with optic neuritis can also be shown to have a reduced sensation of brightness in the affected eye. The optic disc may appear normal (retrobulbar neuritis) or swollen (papillitis) (Optic Neuritis Study Group 1991), and if the patient has experienced a previous clinical or subclinical attack of optic neuritis, or has an ongoing chronic optic neuritis, the disc may appear pale. The optic disc pallor persists even when the visual acuity and other parameters of vision improve, and may be diffuse or more often located to the temporal region. However, neither the swelling nor the pallor are specific findings in demyelinating optic neuritis, and can be present in optic neuritis which accompanies other inflammatory or infectious disease. Other tests of optic nerve function, such as contrast sensitivity (Arden and Gucukoglu 1978) and VEP, are almost always abnormal (Keltner et al. 1993;Optic Neuritis Study Group 1991). Numerous studies have reported that asymptomatic visual dysfunction may be detected in the unaffected eyes of patients with acute unilateral optic neuritis (Keltner et al. 1993), and it usually resolves over several months, suggesting that it may be caused by subclinical acute demyelination in the fellow optic nerve.

1.1.3.2. Pathology

Little information about the pathological changes in the optic nerve of patients with acute optic neuritis is available and almost all the material available has been obtained by studies in patients with MS (McDonald 1974;Prineas 1975;Traugott et al. 1983). These studies detected active demyelinating plaques in the optic nerve, similar to those present in the brain. In such plaques, the inflammatory response is associated with optic nerve swelling, following which the myelin sheaths begin to break down into fat droplets. As degeneration proceeds, the nerve fibres are destroyed, with axonal destruction occurring in both the proximal and distal segments. As the inflammatory reaction subsides, fat-laden macrophages become numerous, and glial proliferation occurs.

Studies on experimental animal models of retrobulbar optic neuritis (Hayreh et al. 1981;Rao et al. 1977) detected inflammatory infiltrates, extensive demyelination, and axonal degeneration of the optic nerve. It is believed that demeyelination of the nerve fibres leads to complete conduction block, slowing conduction, or a failure to transmit a rapid train of impulses (McDonald 1974;McDonald 1976).

1.1.3.3. Visual prognosis

The natural history of acute demyelinating optic neuritis is that it worsens over several days to weeks, and then improves. For most patients, recovery begins within the first month (Beck et al. 1994), but a further improvement can occur up to one year after the onset (Beck and Cleary 1993). Most patients retain good to excellent vision more than 10 years after an attack of optic neuritis (Beck et al. 2004). Other parameters of visual function, including contrast sensitivity, colour perception, and visual field, improve in addition to visual acuity (Keltner et al. 1994).

Thus, the prognosis of optic neuritis is extremely good, and the visual recovery seems to be independent of the degree of visual loss, and others factors, such as age, gender, optic disc appearance, and visual field defects (Beck et al. 1994). However, disturbances in visual acuity, colour vision, visual field, and VEP may all persist after resolution of acute optic neuritis (Beck 1998).

Atrophy of the brain in MS correlates with clinical progression and may indicate axonal loss (Losseff et al. 1996a). Optic neuritis provides an excellent model for studies to investigate the mechanism of axonal damage, and development of MRI techniques for quantifying atrophy in the optic nerve after an episode of optic neuritis. It has been shown that a good recovery of visual acuity is possible despite a significant degree of optic atrophy (Hickman et al. 2001), suggesting either some redundancy in the anterior visual pathway, or a significant cortical reorganisation of visual function (Werring et al. 2000b). A study that assessed the degree of atrophy over a 1-year period and investigated the effect of atrophy on the visual acuity, reported that no patients had worsening visual acuity over the study, despite the progression in the optic nerve atrophy (Hickman et al. 2002).

1.2. Clinical applications of conventional and new MRI techniques

1.2.1. Conventional brain imaging

1.2.1.1. T2-weighted imaging

The conventional spin echo (CSE) T2 and PD-W sequences are widely applied in MS and are the most sensitive sequences for detecting lesions. Both acute and chronic lesions appear as areas of high signal intensity compared with the adjacent normal regions. Discrete MS lesions

appear to be well circumscribed, round or ovoid in shape, with the main axis perpendicular to the principal axis of the lateral ventricles and parallel to the white matter vessels (perivenular). They commonly range from a few millimetres to more than 1 cm in diameter. Some lesions are confluent and may have an irregular shape (McDonald 1998). MS lesions have a high propensity in certain regions of the brain. Commonly involved areas include the periventricular white matter (Ormerod et al. 1987) and the corpus callosum (Gean-Marton et al. 1991). Lesions are often localised in the brainstem, mainly in the floor of the IV ventricle, periacqueductal region and mesancephalon, pons and cerebellar peduncles. Lesions frequently appear at the interface between grey and white matter (i.e. juxtacortical lesions) and sometimes in the basal ganglia. Discrete hyperintensities adjacent to the body or temporal horn of the lateral ventricles are frequent in MS and rarely seen in other disorders. Lesions around the frontal or posterior horns are also often detected, but more difficult to distinguish from the periventricular caps that occur also in normal subjects. Although pathological examinations of MS brains have reported a high number of cortical lesions ((Kidd et al. 1999;Peterson et al. 2001), such lesions are rarely evident on MRI because of the small size of these abnormalities, less optimal contrast of MS lesions against adjacent grey matter, and partial volume effects from adjacent CSF.

Although the CSE T2-WI is the most sensitive paraclinical test in the diagnosis of MS, its specificity is limited. Any pathology from edema and mild demyelination through to completely necrotic plaques may appear bright, and there is evidence than even remyelinated lesions have an abnormal signal. This lack of histopathological specificity accounts, in part, for the modest correlation between clinical disability and MRI parameters, often referred to as the clinical radiological paradox (Barkhof and van Walderveen 1999).

1.2.1.2. Gadolinium enhanced imaging

Gadolinium-diethyl-enetriaminepentacetic acid (Gd-DTPA) is a paramagnetic contrast agent that is used to increase the diagnostic specificity of MRI in MS (Grossman et al. 1986). It reaches areas of the brain in which there is damage to the blood-brain barrier (BBB), which is thought to be the earliest pathological event in the development of MS lesions (Kermode et al. 1990). However, new MRI techniques have shown that changes in the brain tissue which appears normal on conventional images (NAWM) might precede the development of lesions (Goodkin et al. 1998). The paramagnetic effect induces shortening of the T1 relaxation time of nearby water protons, and thus these regions are visualised as areas of hyperintensities or enhancement on post-contrast T1-WI. Gd-enhancement is a regular finding in new MS lesions, but may also indicate the recurrence of inflammation within pre-existing lesions (Miller et al. 1993). The enhancement is a transient phenomenon, and in over 70% of new lesions it lasts one month or less (Miller et al. 1988b). Approximately 30% of lesions continue to enhance for more than one month and a smaller number (5%) persist for 3-4 months (Ciccarelli et al. 1999;Miller et al. 1998). The presence on the same images of acute enhancing lesions and old non-enhancing lesions is suggestive, but not conclusive, of dissemination of lesions *in time*. The detection of enhancement depends both on the concentration of the Gd and the timing of the scan. A dosage of 0.1 mmol/Kg body weight and a time interval of 5 minutes between the injection of Gd and the post-contrast T1-WI are sufficient for a diagnostic purpose. However, the use of a triple-dose of contrast (0,3 mmol/Kg) has been shown to increase the number of enhancing lesions detected, since it can identify also those with "low-grade" inflammation (Filippi et al. 1998).

1.2.1.3. Unenhanced T1-weighted imaging

On conventional T1-W sequences, around 10 to 20% of T2 hyperintensities appear as areas of low signal intensity compared with normal white matter, while the remaining lesions appear isointense (Fazekas et al. 1999). In the acute phase, i.e. when the lesion shows enhancement on post-contrast T1-WI, T1 hypointensity is probably consequent upon marked edema with or without matrix destruction. This acute T1 hypointensity can disappear after 1-6 months, probably because of the resorption of edema and inflammatory cells and possibly because of remyelination (Ciccarelli et al. 1999;van Waesberghe et al. 1998). In contrast, chronic foci of hypointensity, also known as persisting "black holes", indicate areas with most severe tissue damage. Several histopathological studies have found a correlation between the degree of T1 hypointensity of lesions and axonal loss (van Walderveen et al. 1998). These hypointense T1 lesions correlate better with disability than do lesions on T2 images, and therefore it has been suggested that the T1 lesion load may be more suitable for monitoring disease progression than the overall T2 lesion burden.

1.2.2. Spinal cord imaging

The spinal cord is a common site of involvement in MS. A post-mortem study in patients with MS revealed spinal cord involvement in 99% of cases (Ikuta and Zimmerman 1976). An MRI study using multiarray coils and FSE imaging showed that lesions in the spinal cord could be seen in 75% of cases (Kidd et al. 1993). Cord lesions are more difficult to detect than those in the brain because they are less conspicuous and spinal cord MRI is technically more challenging. Spinal cord lesions in MS have a similar signal pattern to cerebral lesions, except for the absence of "black holes" (Gass et al. 1998). On sagittal scans, they have a cigar shape and may be located centrally, anteriorly, or posteriorly. Axial scans show lesion extension toward the periphery with a propensity for the dorsal columns. Typically lesions are shorter

than two vertebral segments, tend to occupy only part of the cross-sectional area of the cord, and are not commonly associated with swelling of the cord (Tartaglino et al. 1995). The cervical spinal cord is twice as likely to be affected than the lower cord, and the midcervical region is most often involved (Kidd et al. 1993). Disease activity, including contrast enhancement and the development of new lesions, is much less frequent in the spine than in the brain (Thorpe et al. 1996a). However, spinal cord lesions are more likely to be symptomatic than brain lesions.

In the diagnostic setting, spinal cord imaging is valuable for two reasons: 1) Asymptomatic spinal lesions are very rare in disorders other than MS, 2) Asymptomatic spinal lesions may help to confirm a diagnosis of MS when few or no brain lesions are present (Lycklama et al. 2003).

The quality of the spinal cord imaging is important for diagnosis and research into MS. However, a recent study, which compared post-mortem sagittal cord MRI acquired at 1.5T with high resolution axial MRI at 4.7 T and histopathology, showed that cord abnormalities were underestimated by sagittal images at 1.5 T(Bergers et al. 2002), indicating that *in vivo* MRI lacks a sufficient signal-to-noise ratio as well as sufficient spatial or contrast resolution.

As with brain images, T1-WI of spinal cord may be used to measure the atrophy of the cord at cervical level, which correlates with clinical disability (Kidd et al. 1993;Losseff et al. 1996b).

1.2.3. Conventional MRI findings in different clinical types of MS

1.2.3.1. Conventional MRI in RR and SP MS

MRI studies have revealed differences between clinical subgroups of MS (Nijeholt et al. 1998) (Table 1.3). In this paragraph, we describe the typical MRI features of RR and SP MS, whilst in the following paragraph we will discuss the radiological characteristics of PP MS.

In RR MS, brain abnormalities consist mainly of focal lesions on T2-WI. In the SP phase, more and larger lesions are found, and a larger proportion of these lesions are hypointense on T1-WI, which is related to clinical disability (Nijeholt et al. 1998). Likewise, brain atrophy is more pronounced in SP disease. Patients with PP MS, as discussed below, often have few brain lesions compared with SP MS, even when groups are matched for disability (Thompson et al. 1997). Apart from differences in the number of focal lesions, abnormalities in the NAWM are more pronounced in SP and PP MS compared with RR MS, as suggested by magnetization transfer (MT) (Rovaris et al. 2001) and spectroscopy MR (Tourbah et al. 1999) studies. Besides differences in MRI findings in the brain, clear differences are found in the spinal cord between subgroups of MS (Nijeholt and Barkhof 2003). RR MS patients typically show focal spinal cord lesions, while in the SP phase a higher numbers of focal abnormalities and more cord atrophy are present.

Table 1.3. Conventional MRI features in the different types of MS (adapted from Nijeholt et al., 1998).

Measures	RR MS	SP MS	PP MS
BRAIN			
Focal T2 lesions	Many	Many	Moderate or few
Focal T1 lesions	Few	Many	Few
Enhancing lesions	Often	Often	Seldom
Diffuse abnormalities	Seldom	Variable	Frequent
Brain atrophy	Mild	Moderate or marked	Mild
SPINE			
Focal T2 lesions	Frequent	Frequent	Frequent
Focal T1 lesions	Never	Never	Never
Diffuse abnormalities	Seldom	Variable	Frequent
Spinal cord atrophy	Mild	Marked	Moderate

1.2.3.2. Conventional MRI in PP MS

Brain and spinal cord MRI in patients with PP MS revealed differences compared with other types of MS (Nijeholt and Barkhof 2003). Distinctive features of PP MS patients present on brain imaging include the following: i) A lower amount of focal lesions which appear hyperintense on T2 and hypointense on T1-WI (Filippi et al. 1999), but higher T1/T2 ratio (van Walderveen et al. 2001); ii) A lower number of Gd-enhancing lesions (Thompson et al. 1991); iii) A higher rate of abnormalities in the brain NAWM (Rovaris et al. 2001). However, recent evidence has shown that 42% of early PP MS patients show brain enhancing lesions, and those patients are characterised by higher disability and more MRI abnormalities (Ingle et al. 2003). Although a less pronounced brain atrophy has been reported in patients with PP MS (Nijeholt et al. 1998), the same extent of cortical grey matter atrophy is present in patients with RR and PP MS (De Stefano et al. 2003). Moreover, in patients with PP MS the cortical atrophy correlates with EDSS, but not with T2 lesion load (De Stefano et al. 2003), suggesting that, although a proportion of the grey matter changes may be secondary to white matter inflammation, an independent neurodegenerative process is also active in PP MS and contributes to neurological impairment.

Besides the differences between types of MS present in the MRI appearance of the brain, differences are also found in the spinal cord. Patients with PP MS have less atrophy (Nijeholt et al. 1998;Stevenson et al. 1999) and lower lesion load in the cord than patients with SP MS (Filippi et al. 2000a;Stevenson et al. 1999). However, for some PP MS patients, the MRI abnormalities can be entirely confined to the spinal cord (Thorpe et al. 1996b). PP MS patients often present with diffuse abnormalities throughout the spinal cord without focal lesions (Nijeholt et al. 1998). A previous MR-histopathology study found that the MRI finding of mild and diffuse signal hyperintensity in the cord of PP MS corresponded to a little involvement of the central grey matter and partial demyelination (Nijeholt et al. 2001).

1.2.4. Conventional MRI in optic neuritis

Optic nerve MRI can be used to confirm the diagnosis of demyelinating optic neuritis and exclude optic nerve compression in patients who present with an atypical course of the disease. MRI can show areas of inflammation within the optic nerve, most often evident in the intraorbital portion of the nerve (Guy et al. 1992). The intracanicular portion of the nerve is affected with moderate frequency, while lesions in the intracranial portion and chiasm are seen less often. MRI of the optic nerve is challenging, because of its tortuosity and mobility, its short length, and the presence of surrounding CSF and orbital fat. Optimum results are obtained with multiarray surface coils, high-resolution sequences, and coronal slices with fat suppression methods. Such an approach reveals the presence of lesions in the optic nerve in more than 90% of patients with optic neuritis (Gass et al. 1995). A new imaging technique, using a fat-saturated short-echo fast fluid-attenuated inversion recovery (sTE fFLAIR) sequence, which suppresses the high signal from fat and CSF, has allowed quantification of the optic nerve area following a single episode of isolated optic neuritis (Hickman et al. 2001). In particular, after a median time since onset of optic neuritis of 21 months, the mean area of the affected optic nerve was found to be significantly lower than that of the controls and of the contralateral nerve. There was a significant negative correlation between time since onset of optic neuritis and the size of the affected optic nerve (Hickman et al. 2001). This suggests two possible mechanisms, either an ongoing axonal loss in persistently demyelinated lesions, or Wallerian degeneration distal to axonal damage during the acute inflammatory phase.

Brain MRI in patients with optic neuritis may allow identification of white matter abnormalities, usually in the periventricular regions, consistent with demyelination. The percentage of patients with optic neuritis which presents with multiple lesions in the brain

varies from 49% to 64% (Miller et al. 1988a;Optic Neuritis Study Group 1991). The presence of one or more demyelinating lesions in the brain appears to be the most significant risk factor for developing MS (Beck et al. 2003). A recent study, which has been carried out in our Centre, followed patients for 14 years after the onset of clinically isolated syndromes, including optic neuritis, brainstem or spinal cord syndrome, and found that clinically definite MS developed in 88% of patients with an abnormal MRI scan at baseline and in 19% of patients with a normal scan (Brex et al. 2002). Moreover, patients with worse clinical outcomes had larger numbers and volumes of lesions on MRI at baseline and greater increases in lesion volume over the first 5 years, suggesting that development of lesions at baseline and in the early years of the disease has an influence on the long-term disability (Brex et al. 2002). Previous work has revealed asymptomatic lesions in the optic radiations in 71% of patients with optic neuritis (Hornabrook et al. 1992). The most common site of involvement was around the trigones. In contrast to the findings associated with symptomatic lesions, there was no relationship between the latency of the VEPs and the presence of asymptomatic posterior visual pathway lesions. A possible explanation for this result is the low sensitivity of VEPs to the detection of postchiasmal abnormalities (Plant et al. 1992). In contrast, VEPs are very sensitive to prechiasmal lesions: increased VEP latency and reduced VEP amplitude correlated with the optic nerve lesion length (Davies et al. 1998) and atrophy (Hickman et al. 2002).

1.2.5. New MRI techniques in MS

New MRI techniques have been developed to provide additional *in vivo* information on the pathological substrates of the disease. They showed that MS pathology is not restricted to plaques but also involves the NAWM, confirming post-mortem data.

Magnetisation transfer imaging (MTI). MTI provides quantitative information on the NABT with a high specificity to demyelination. A post-mortem study reported that the magnetisation transfer ratio (MTR) values derived from MS lesions and NAWM correlated with the percentage of residual axons and the degree of demyelination (van Waesberghe et al. 1999). The same study also confirmed that T2 hyperintense MS lesions may have a wide range of MTR values, confirming their pathological heterogeneity. All the MTR histograms-derived metrics of the NAWM and NA grey matter (NAGM) from patients with MS were lower than those obtained in controls, suggesting the presence of a diffuse tissue damage in NAWM and GM (Cercignani et al. 2001a). Interestingly, changes in MTR histograms-derived metrics from the whole brain of 73 patients with MS over a period of one year predicted disability progression during a median follow-up of 4.5 years (Rovaris et al. 2003). Comparisons of MTR histograms of the cervical spinal cord between different forms of MS suggested that the amount and severity of spinal cord damage were greater in the progressive forms and correlated with disability (Filippi et al. 2000a). Whole brain and NABT MTR histogram analysis in a cohort of 91 PP MS patients did not detect any differences between PP and SP patients with similar disability (Rovaris et al. 2001). Moreover, in the sample of PP, average brain MTR values correlated only in part to T2 and T1 lesion load, suggesting that the pathology of the NABT is, at least in part, independent of lesions. A recent paper in PP MS patients showed that the MTR histograms metrics in the NAWM and NAGM were significantly different from those in controls, and there was an association between EDSS and mean NAGM MTR (Dehmeshki et al. 2003).

MR Spectroscopy (MRS). Proton MRS is a valuable tool for studying *in vivo* the pathology of the brain in patients with MS because it can provide indices of several metabolities: (i) N-acetyl-aspartate (NAA), which is a marker of axonal integrity and metabolism; (ii) Creatine (Cr) plus phosphocreatine, which may reflect greater cellular metabolic activity and has been

found to be abnormal in demyelinating lesions and MS NAWM (Brex et al. 1999;Suhy et al. 2000); (iii) Choline containing compounds, which is a marker of increased cell turnover; (iv) Lipids, which are markers of ongoing myelin disruption; (v) Myo-inositol, which is a marker of glial proliferation; (vi) Glutamate plus its precursor glutamine (Glx), which offer less cell-specific information, being present in the neurons, oligodendrocytes and astrocytes.

Several MRS studies have contributed to understand the mechanism of axonal damage in MS, confirming that it is present both in lesions and NAWM, progresses over time, and correlates with clinical disability (De Stefano et al. 1998;Fu et al. 1998;Rovaris and Filippi 2000;Sarchielli et al. 1999). A recent MRS study has reported that metabolite changes that also occurred in the cortical GM were detected early in the clinical course of MS, and related to function (Chard et al. 2002a). Another work showed that, at initial clinical diagnosis, the global concentration of NAA in the whole brain in MS was reduced on average by 22% compared with normal controls, and did not correlate with lesion load (Filippi et al. 2003), suggesting that axonal injury occurs early in the course of MS and independently from inflammation. However, most of the NAA reduction seen at the early stages of MS could be due to impairment of mitochondrial function rather than to axonal loss, and, therefore, it may be partly reversible (Lassmann 2003).

Diffusion tensor imaging (DTI). In the second chapter the technique of DTI is described in detail. In the last few years, an increasing number of DT MRI studies have been conducted in MS, and they have consistently found a higher amount of water diffusion (diffusivity) and lower anisotropy in MS lesions and in the NAWM compared with controls (Bammer et al. 2000;Cercignani et al. 2001a;Filippi et al. 2000b;Henry et al. 2003;Werring et al. 1999). However, few studies have included PP MS patients (Cercignani et al. 2001b;Rocca et al. 2003b). Filippi et al. investigated 30 PP MS patients and found no significant correlation between EDSS and diffusion measures in lesions and NAWM, contrary to the findings in SP

MS (Filippi et al. 2001b). A further confirmation of these results came from a histogram study in PP MS patients (Cercignani et al. 2001b); the histogram derived quantities did not correlate with patients' disability. A recent study in 96 patients with PP MS found that the diffusivity values in lesions and in the NAWM and NAGM were higher in SP than in PP patients (Rovaris et al. 2002a), although they were abnormal in the PP group. These findings confirm the occurrence of subtle pathology in the brain of PP patients, not only in the NAWM, but also in the NAGM. Similarly to the MTR findings, no significant correlation was found between any of the diffusion parameters in the NABT and T2 lesion load in PP MS (Rocca et al. 2003b), supporting the hypothesis that the diffuse damage of the brain is at least in part independent of the focal pathology.

Functional MRI (fMRI). The second chapter describes in detail the technique of fMRI. In this paragraph, we briefly summarize the main findings reported in MS and, in particular, in PP MS.

In a case report on a RR MS patient, Reddy et al. monitored clinical evolution and cortical activation with a motor task during 6-month follow up after presentation of a clinical relapse (Reddy et al. 2000b). The activation in the contralateral and ipsilateral motor areas increased at 3 and 6 weeks, and returned to normal level at the final scan, in parallel with clinical recovery, suggesting that these dynamic functional changes contribute to clinical improvement. A follow-up study of a group of MS patients showed a positive correlation between T2 lesion load and the ipsilateral motor cortex activation, suggesting that the degree of compensation increases in proportion to the degree of injury (Lee et al. 2000). Moreover, the extent of T1 lesion load along the pyramidal tract correlated with the functional brain reorganisation in patients who recovered from a single attack of MS (Pantano et al. 2002a). Similarly, the decreased NAA along the descending corticospinal tract correlated with the increased activation in the ipsilateral motor cortex in patients with early RR MS and absent

clinical impairment (Reddy et al. 2000a). More recent work has shown that adaptive cortical functional changes occurred in the brain of patients with other forms of MS, such as SP (Rocca et al. 2003a), supporting the hypothesis that brain reorganisation occur in order to limit the impact of brain injury on clinical function.

Previous functional studies in PP MS are discussed in greater detail in chapter 5. Here we only mention two studies which have used a motor task in order to investigate the differences in the extent of cortical activation between PP patients and healthy subjects. The first study found significant cortical activation changes in PP MS patients during both the motor tasks involving the affected and the unaffected limb (Rocca et al. 2002b). Interestingly, activation of "non-motor" areas was detected in PP MS patients, suggesting that regions which represent areas of multimodal integration may be recruited to retain the function in response to tissue damage. In the second study, the authors used motor fMRI and MT and DT MRI and found significant correlations between activations in several areas and MRI measures of brain and spinal cord damage, suggesting that increase tissue pathology induces greater functional changes in the cortex (Filippi et al. 2002b).

1.3. Conclusion

In this chapter we have discussed the main applications of conventional and new MRI techniques to patients with PP MS and optic neuritis. Both conditions represent ideal models for studying the mechanisms of damage and recovery in the CNS. In optic neuritis, which is characterised by clinical recovery, the damage in the visual pathway can be monitored using MRI and tests for visual function, whilst PP MS allows investigation of the progression of disability due to spinal cord damage and lack of repair mechanisms. In the next chapter, the

principles of MRI, in particular DTI and fMRI, are detailed, in order to show the potential application of these new MRI techniques in demyelinating diseases.

Chapter 2

An introduction to the principles of MRI, diffusion tensor imaging and functional MRI

The history of MRI dates back to the 1940s when researchers at Harvard University, led by Purcell, and at Stanford University, led by Bloch, described the resonance phenomenon in samples placed in a magnetic field. Since then, many other researchers have contributed to developing the imaging sequences that started to be applied in radiology in about the 1970s. Although the unique potential of conventional MRI sequences to confirm the diagnosis of multiple sclerosis and follow up the evolution of a disease is well recognised, they have some limitations, including the long scanning time and the lack of pathological specificity. Over the last few years new MRI techniques, including MR spectroscopy, MTI, DTI and fMRI have been developed in order to provide further insights into the pathological changes that occur in the brain tissue.

This chapter is intended to provide an overview of MRI theory and the main DTI and fMRI features, in order to introduce the clinical applications that are reported in the subsequent chapters of this thesis.

2.1. Principles of MRI

2.1.1. Physics of MRI

Protons, which are contained in the nuclei of atoms, have a positive electrical charge, and constantly turn, or spin around their own axis. In other words, protons possess a spin, and a spinning nucleus produces a magnetic dipole moment, referred to as μ, which tends to align with an externally applied magnetic field. Quantum mechanics theory tells us that the alignment of protons occurs on two different energy levels: one at low energy level, which is aligned with the magnetic field, and one at high energy level, which is against the field (Figure 2.1).

Protons aligned in a magnetic field show a peculiar motion, called "precession", which is due to the circular movement of the spin axis forming a cone shape (Figure 2.1). The speed of the precession is called precession frequency, and this depends on the strength of the magnetic field, which is described by the following formula or Larmor equation:

$$\omega_0 = \gamma B_0 \qquad (2.1)$$

where ω_0 is the Larmor frequency given in Hz or rad s^{-1}, B_0 is the external magnetic field given in Tesla, and γ is the gyromagnetic ratio. The equation states that the precession frequency increases with the strength of the magnetic field, and this relationship is determined by the gyromagnetic ratio, which is different for different nuclei. The importance of the Larmor frequency relates to the fact that it determines the frequency required for the transition of protons from one energy level to the other. For the scanners commonly used in clinical practice, which have an external magnetic field of 1.5 Tesla, the Larmor frequency is $\approx$ 64 MHz.

When a tissue, which contains protons, is placed in a magnetic field B_0, it becomes magnetised, with the bulk magnetisation (M) initially aligned along B_0. M is the summation of the individual dipole moments of the sample, divided by the volume of the sample, and is proportional to the magnetic field. It is represented as a vector in the direction of the magnetic field and is called *equilibrium magnetisation*. It is not possible to measure this magnetic force because it is in the same direction as the magnetic field. In order to visualise the magnetisation we need to introduce a frame that rotates in the same direction as the magnetisation. In this case, M appears stationary and B_0 is equal to zero (Boulby 2003).

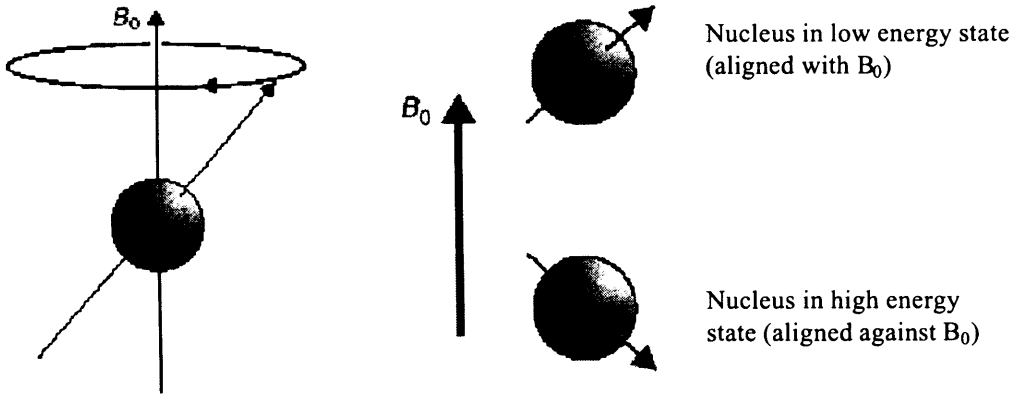

Figure 2.1. Precession of proton and its orientation in an external magnetic field. The left side of the figure shows that as well as spinning about its own axis, the proton also precesses about the direction of the field B_0. The angular rate of precession, ω_0, is proportional to the magnetic field B_0. The right side of the figure shows that when the proton is exposed to a magnetic field it can exist only in two orientations.

2.1.2. The spin echo phenomenon

In the basic Hahn spin echo sequence, the application of a radiofrequency 90° RF pulse along the y axis of the rotating frame (i.e. perpendicular to B_0) produces a *transverse magnetisation* along the x axis, because it causes protons to perform a transition to a higher level of energy and to precess in phase. After the RF pulse is switched off, protons lose phase coherence and the transverse magnetisation starts to disappear. This process is called *transverse relaxation* or *spin-spin relaxation* and is related to a spin-spin interaction. At the same time protons go back to the lower state of energy and the longitudinal magnetisation returns to its original size. This process is called *longitudinal relaxation* or *spin-lattice relaxation* and is due to the release of energy from the spins, which are returning to the lower level of energy of their surrounding lattice (Bloch 1946). Two time constants describe these processes: 1) T2, which is the time constant for decay of the transverse magnetisation in a homogeneous (i.e. uniform) static magnetic field; 2) T1, which is the time constant for recovery of the longitudinal magnetisation.

If a 180° pulse is applied along the y axis it flips the spins from close to the +x axis to close to the –x axis. This second pulse rephases the protons that are getting out of phase. In particular, since the spins continue to precess in the same direction and at the same speed as before the 180° pulse, they lead to rephasing of the transverse magnetisation along the -x axis, giving a spin echo signal (Hahn 1950). Successive 180° pulses can be used to generate a spin echo train (Carr and Purcell 1954).

2.1.3. T2* decay

The transverse and longitudinal magnetisation vectors add up to a sum vector, which represents the total magnetic moment of a tissue. This vector also performs a spiral motion. After a 90° pulse, the bulk magnetisation vector M is seen to tilt away from the direction of B_0 and spiral towards the transverse plane. As soon as the magnetisation has a component in the transverse plane, it will generate the MR signal or spin echo signal. When, after a 90° pulse is switched off, the net component of magnetisation lying in the transverse plane dephases, the detectable signal diminishes, and the sum vector tends to change direction from the transverse plane to the longitudinal plane. This type of signal is called a *Free Induction Decay (FID) signal* and is characterised by a reduction in intensity with time and by a constant frequency. The rate at which the signal dies away takes the form of an exponential decay (Figure 2.2), and in its simplest form it can be described by:

$$S(t) = S_0 \exp(t/T2) \qquad (2.2)$$

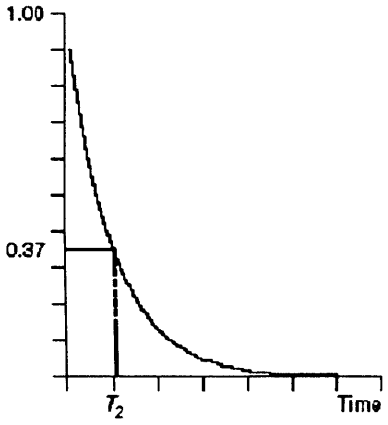

Figure 2.2. Free induction decay of T2 in the rotating frame. At a time equal to T2 after the occurrence of transverse magnetisation, the detectable signal has fallen to 37% of its value.

Although we should expect the decay of the MR signal to occur with a time T2, in practice it occurs with the shorter time T2*. This is due to the fact that the local magnetic field is always heterogeneous because of: 1) the non-uniformity of an applied field, due to imperfections in the windings of the coil itself and 2) the differences in magnetic susceptibility between adjacent regions. This means that the Larmor frequency and the phase of precession of the spins are both spatially dependent, and consequently different regions respond differently to the applied magnetic field. In a perfect magnetic field, the value of T2* can approach that of T2.

A major difference between T2 and T2* relaxation is that T2* processes can be refocused by applying a 180° pulse, whereas the T2 processes cannot, because they result from random fluctuations in the Larmor frequency at the molecular level.

The boundaries between tissue components with very different magnetic susceptibilities, such as the air/tissue interfaces near the sinuses, lead to very rapid local T2* relaxation. The variation in magnetic susceptibilities are also seen in blood vessels, where the level of deoxyhaemoglobin in the blood affects the T2* in tissue around the vessels. This effect is the basis of the BOLD contrast used in fMRI and is discussed in greater depth in the section dedicated to fMRI.

2.1.4. Spin echo imaging

To create a SE image it is necessary to apply RF pulses and gradients at very specific time points in order to select the slice to image and record the signal at each point in that slice. The spin echo diagram (Figure 2.3) gives the timing and the amplitude of RF pulses or gradients along a system of logical coordinates (z, x, and y). Creating an image requires (Kuperman 2000):

1) Slice selection (SS, G_{slice}, "z");
2) Frequency encoding (FE, G_{read}, "x");
3) Phase encoding (PE, G_{phase}, "y").

} Spatial Encoding

For a two-dimensional image, frequency encoding is applied in one direction and phase encoding in the other. For a three-dimensional image, the slice selection is not employed, frequency encoding is applied in one direction and phase encoding in the remaining two. The 3-dimensional approach allows higher spatial resolution and higher signal-to-noise compared with 2-dimensional multi-slice scanning, but is characterised by a relatively long scan time.

In the presence of a *slice select (Gz)* gradient, the magnetic field changes strength from point to point, and, consequently, the precession frequency of the protons changes with location. When a 90° RF pulse is applied, only those spins that have the precessing frequency equal to the frequency of the pulse, contribute to the formation of a transverse magnetisation. At time t=TE/2 a 180° pulse is applied which rephases the protons that are getting out of phase, and, at time TE, an echo is produced. After the slice select gradient, the *frequency encoding* or *readout (Gx)* gradient is applied in the direction of the x axis. This results in different precession frequencies along the x axis, and thus a different frequency of the corresponding signal. The *phase encoding (Gy)* gradient, which is perpendicular to the frequency encoding gradient, is applied after the 90° pulse in order to induce different phases to the echo signal. In

conclusion, the excited slice is imaged in the x and y directions using *frequency* and *phase encoding* gradients.

In order to obtain a SE image it is necessary to define the repetition time (TR) and the echo time (TE). TR is defined as the time between two pulse sequences, i.e. from one 90° to the next (Hahn 1950). The TE, as mentioned above, is defined as the time between the 90° and the echo. Since TR is often much longer than TE, the delay between the end of data acquisition and the next 90° pulse can be used to excite a second slice without affecting the first slice. The echo of the first phase encode step of a second slice can be acquired before returning to excite the first slice for its second phase encode step. In other words, the strength of the phase encoding gradient varies in a step-like fashion, while its duration remains constant. With a sufficiently long TR, several slices can be fitted into a single TR.

Different combinations of TR and TE produce different degrees of contrast (intensity differences) between tissues. Changing TR, changes the contrast between tissues with different T1 relaxation times. For example, in the case of a short TR, the longitudinal magnetisation of a specific tissue, which has to be flipped in turn by the second pulse, does not have time to recover totally after the first pulse, and it produces a smaller transverse magnetisation with consequent lower signal. On the other hand, in the case of a very long TR, all tissues will have recovered their longitudinal magnetisation. Changing TE, changes the contrast between tissues with different T2 relaxation times. In particular, the shorter the TE, the stronger the signal is from the tissue. However, with a short TE, the difference in signal intensity between two tissues with different T2 is very small, and both tissues can hardly be distinguished. Conversely, in the case of a long TE, the differences in signal intensity between tissues, which have different T2 times, become visible.

Thus, by changing the TE and TR we can obtain different types of sequences: 1) T1-WI, which is characterised by short TE and short TR, and is able to detect differences between

tissues due to their differences in T1 relaxation times; 2) Proton density (PD)-WI, which is characterised by short TE and long TR, and is sensitive to detect differences in signal related to different proton density (the signal is neither T1 nor T2-weighted); 3) T2-WI, which is characterised by long TE and long TR, and is able to detect differences between tissues due to their differences in T2 relaxation times.

Due to spin refocusing following a 180° pulse, spin echo imaging is not sensitive to the presence of magnetic field inhomogeneities. Therefore, the spin echo image intensity depends on T2 rather than on T2*. The use of a 180° pulse is usually associated with sequences that have longer TR and TE compared with those used in gradient echo imaging, which are discussed later.

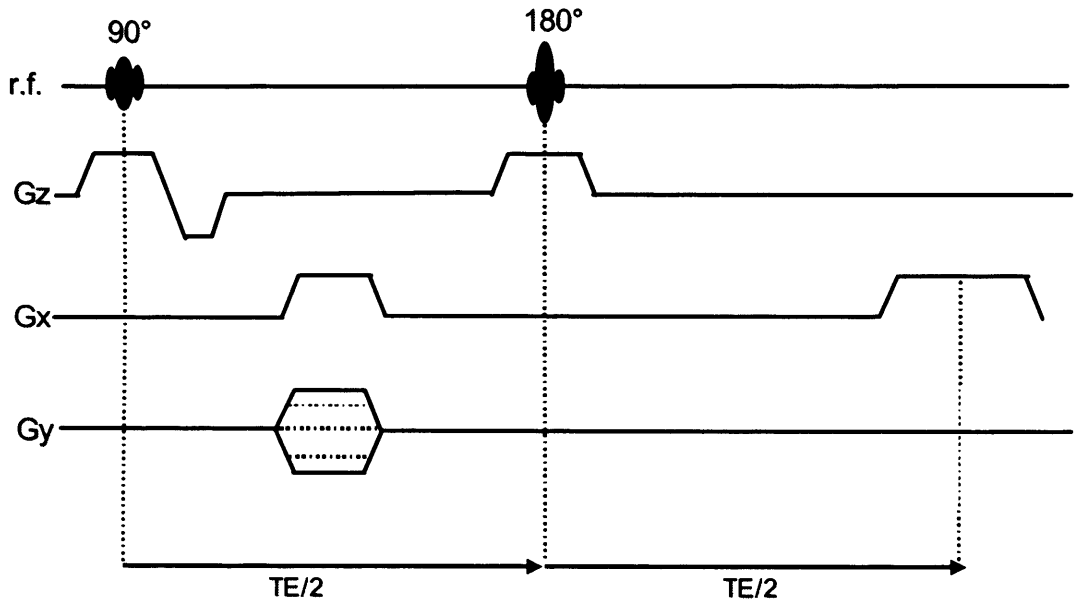

Figure 2.3. Spin echo sequence diagram.

2.1.5. Gradient echo imaging

The gradient echo sequence differs from spin echo by the addition of an initial "α" pulse, whose flip angle is typically less that 90°, and by the lack of a 180° pulse. A flip angle smaller than 90° allows for some residual longitudinal magnetisation, which is tilted by the next pulse. The gradient echo pulse sequence, which includes slice selective gradients, phase encoding and readout gradients, is repeated several times with different strengths of the phase encoding gradient.

Gradient echo imaging often suffers from signal loss caused by dephasing of spins in the presence of magnetic field inhomogeneities. Thus, the gradient echo image intensity depends on T2* rather than on T2. Since dephasing of spins increases with increasing TE, gradient-echo imaging is acquired with very short TE (a few milliseconds) in order to reduce signal loss. Gradient echo imaging with short TR is used for rapid *in vivo* MRI in order to reduce scan time and reduce motion artefacts (Haase et al. 1986;van Meulen et al. 1985).

2.1.6. From MR signal detection to image reconstruction

As mentioned above, the FID induces a current into the receiver coil at the Larmor frequency. The recorded signal can be digitised to a set of numbers representing its amplitude at specific time points. The *Fourier transformation* can convert these numbers into a set of amplitudes at specific frequencies, which provide the image intensity at particular positions. Thus, the Fourier formula translates the information regarding the frequencies and the phases of the signal, along with their relative proportions, to the amplitude of the signal at each time point (Kuperman 2000).

Tweig (Tweig 1983) and Ljunggren (Ljunggren 1983) suggested a very useful interpretation of the signal acquisition as sampling along trajectories in a spatial frequency space, or *k-space*. Measuring a signal at a specific time is equivalent to sampling a particular point in k-space, which is the space in which the raw data lives. The axes on a plot of k-space are k_x, k_y, and k_z. Arbitrary trajectories along k-space can be produced by time-varying gradients applied during signal acquisition. The time during which the signal can be acquired along k-space is limited by the T2* decay and, therefore, only a limited numbers of lines of k-space can be acquired. In general, few rules apply in order to move a trajectory along a k-space: 1) Soon after the slice selection $k_x = k_y = 0$; 2) The application of frequency encoding gradient moves the trajectory along k_x, whilst the application of phase encoding gradient moves the trajectory along k_y; 3) A 180° pulse reflects the k-space coordinate through the point $k_x = k_y = 0$.

The signal amplitude at low spatial frequencies in the central region of k-space is higher than the signal amplitude at high spatial frequencies on the periphery of the k-space. In particular, low spatial frequencies are required to reconstruct the overall form of the image, whilst high spatial frequencies are required to describe rapid spatial variations in the objects (e.g. sharp edges). Moreover, zero spatial frequency at the centre of the k-space is used to describe the overall intensity of the whole image. The range of spatial frequencies in k-space is inversely proportional to the spatial resolution of the image. The total area of k-space covered corresponds to the pixel size, and the spacing between k-space points represents the field of view (i.e. the total area of an image which has been covered).

Many different k-space sampling schemes can be used and each of them has practical or theoretical advantages. For example, a small number of k-space trajectories are used to allow rapid acquisition of MR images, such as the echo-planar images (see below).

2.1.7. Echo planar imaging

Echo-planar imaging (EPI), created by Mansfield in 1977 (Mansfield and Pykett 1978), is one of the fastest MRI techniques currently used. A basic EPI pulse sequence and the corresponding k-space are shown in Figure 2.4. EPI uses a very efficient k-space sampling scheme by acquiring a number of lines in k-space after each excitation pulse. As a result, EPI images can be produced with only a few excitation pulses. The fastest EPI scanning, known as *single-shot* EPI, is obtained when all required signals are collected after a single excitation pulse.

A particular EPI sequence, widely used, is *gradient-echo EPI* (Figure 2.4). It is obtained by applying a 90° pulse and then repetitively reversing the sign of the frequency encoding or readout gradient (Gx) at the end of data acquisition in order to rephase the signal. This allows the acquisition of a high number of gradient echoes (echo train) in a short time. The peak of each gradient echo occurs when the spins are all in phase. The application of "blips" of the phase encoding gradient (Gy) between reversals of the frequency encoding gradient moves the k-space trajectory to the beginning of a new line in k-space. Since the successive frequency encoding gradients are positive and negative, the lines in the EPI k-space are sampled in opposite directions.

The major disadvantage of EPI sequences is their sensitivity to image artefacts, such as geometric distortions, which occur in regions where the magnetic field homogeneity is poor (frontal and temporal regions) and relate to the long readout time required to generate the echo train. However, since the gradient echo EPI allows shorter scan time (100ms per image) and a higher signal-to-noise ratio compared with other rapid pulse sequences, it is often used for fMRI.

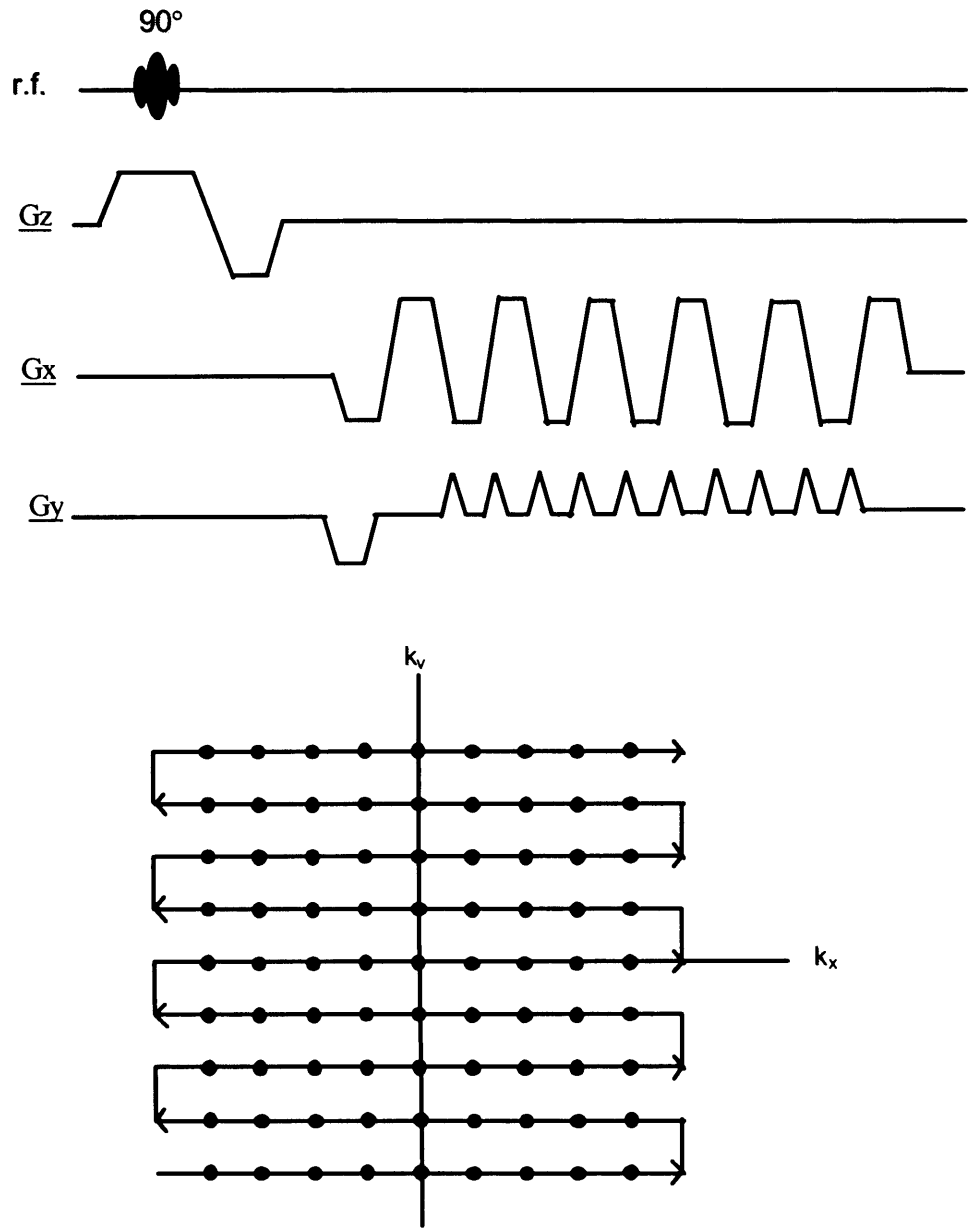

Figure 2.4. Gradient echo EPI pulse sequence and EPI k-space sampling.

2.2. Diffusion tensor imaging

Diffusion tensor imaging (DTI) can provide a unique insight into tissue structure and organisation *in vivo*, because it is able to measure the displacement of water molecules occurring between 10^{-8} and 10^{-4}m in a timescale from a few milliseconds to a few seconds. Since the diffusion of water *in vivo* is restricted by the presence of membranes and

organelles, the measurement of the diffusion properties of a specific tissue reflects the integrity of its microstructure. For example, the white matter and grey matter of a normal brain are characterised by different diffusion measurements, which reflect their structural complexity and integrity. When the tissue structure is affected by pathology, the measures of water diffusion change and, therefore, DTI has been shown to be useful in studying *in vivo* brain pathological damage. This section deals with the principles of DTI and introduces its future developments, such as diffusion based tractography.

2.2.1. Physics principles of the phenomenon of diffusion

Diffusion phenomena are the consequence of a microscopic random motion, known as Brownian motion. As an effect of molecular thermal energy, every particle in a fluid is moving and is struck by other molecules. With every hit, a particle changes direction randomly, so that, over time, its path can be described as a random walk. In non-uniform system (where there is a gradient in the concentration (C) of a diffusing fluid), diffusion results in a macroscopic flux of the fluid, which can be measured and is described by the *Fick's first law of diffusion*. In particular, this law states that that the diffusion process moves substances from areas of high concentration to areas of lower concentration (Wheeler-Kingshott and Barker 2003):

$$F = -D\frac{\partial C}{\partial x} \tag{2.3}$$

The negative sign takes account of the fact that the flux is in the opposite direction to that of increasing concentration, and D is referred to as the "diffusion coefficient".

Conversely, when the concentration is stable, diffusion can only be described statistically, i.e. by measuring the probability that a molecule travels a given distance in a given time. In isotropic medium, like simple liquid, such probability has a Gaussian distribution and the

molecules are free to diffuse in any direction without restriction (Wheeler-Kingshott and Barker 2003). In biological tissues this characterisation is no longer valid because diffusing molecules may be reflected, or have their mobility interrupted, by the interactions with the cell membranes and other intracellular and extracellular structures. Therefore, water diffusion becomes *anisotropic*, that means that it is restricted or hindered by cellular structures. In this situation, different directional components of diffusion must be analysed separately and the diffusion process can be described by a 3 x 3 tensor matrix. The diffusion tensor (DT) is characterised by 9 elements (Basser et al. 1994). Dxx, Dyy and Dzz are the diagonal elements and define the diffusion constants along the main axes (x,y,z). The remaining elements (Dxy, Dxz, and Dyz) are off-diagonal and indicate how strongly random displacements are correlated in the x, y and z directions.

$$D = \begin{pmatrix} Dxx & Dxy & Dxz \\ Dyx & Dyy & Dyz \\ Dzx & Dzy & Dzz \end{pmatrix} \qquad (2.4)$$

Note that the matrix is symmetric about the diagonal, meaning that only six elements must be measured to estimate the full DT.

2.2.2. Effects of diffusion on the MRI signal

The signal on MRI depends on the behaviour of proton spins in a magnetic field. As previously discussed, in the case of the spin echo (SE) sequence, the first 90° pulse excites the sample, whilst the second 180° pulse reverses the phase of the spins and refocuses the magnetisation. In the absence of motion or diffusion of the water molecules, the dephasing that occurs after the first pulse is exactly rephased after the 180° pulse. If, instead, there is a random motion of the spins between dephasing and rephasing, then the refocusing of the spins is incomplete and there is a loss in the transverse magnetisation and a reduction in the

signal amplitude. The extent of this signal attenuation depends on: 1) The diffusion properties of the tissue, which are, in turn, related to its structure; 2) The magnetic field gradients and the time during which the diffusion process takes place.

2.2.3. The pulsed field gradient sequence

In 1965 Stejskal and Tanner (Stejskal and Tanner 1965) proposed a practical scheme to introduce diffusion weighting in an MRI acquisition, adding a pair of pulsed magnetic field gradients (g) into a SE sequence and positioning them around a 180° refocusing pulse (Westin et al. 2002) (Figure 2.5). This is the pulsed field gradient (PFG) method. The first gradient pulse induces a phase shift for all spins; the second reverses this phase shift, thus cancelling the phase shift for static spins. The spins which have changed location due to the diffusion of molecules during the time period between the two gradients (Δ in figure) are not completely refocused by the second gradient pulse, and cause a signal attenuation.

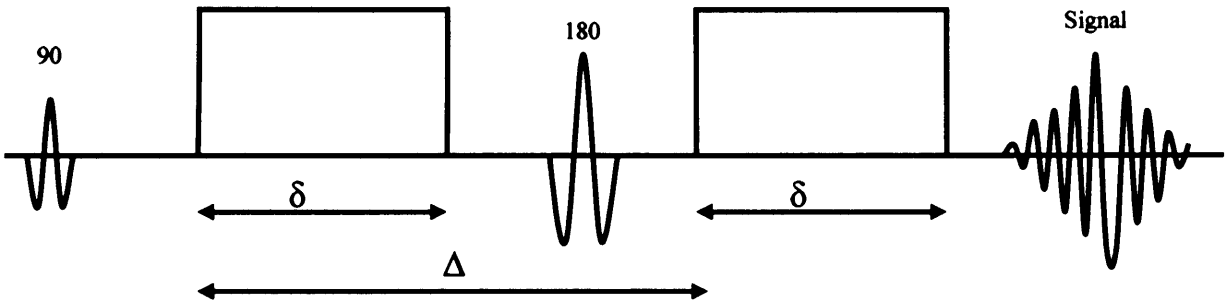

Figure 2.5. The Stejskal-Tanner Pulse Field Gradient (PFG) sequence (adapted from Westin et al., 2002).

If two acquisitions are performed, one without superimposed diffusion gradient (i.e. b value = 0), and one with diffusion gradient (i.e. $b \neq 0$), diffusion can be calculated using the equation of Stejskal and Tanner:

$$S = S_0 e^{-bD} \qquad (2.5)$$

where S is the NMR signal in the presence of diffusion gradients, S_0 is the signal in the absence of diffusion gradients, and *b* is the diffusion weighting factor, introduced by LeBihan et al (Le Bihan et al. 1986):

$$b = \gamma^2 \delta^2 \left(\Delta - \frac{\delta}{3} \right) G^2 \qquad (2.6)$$

where γ is the proton gyromagnetic ratio (267×10^6 rad s^{-1} T^{-1}), and G is the strength of the diffusion sensitising gradient pulses. Therefore, the *b* factor depends on the amplitude of the diffusion gradient and on the diffusion times (Δ and δ). If the diffusion gradient is small (i.e. the *b* factor is small), there will be a small signal attenuation due to diffusion. On the other hand, if the diffusion gradient is very big (i.e. the *b* factor is big), there will be a much higher loss of signal (Figure 2.6).

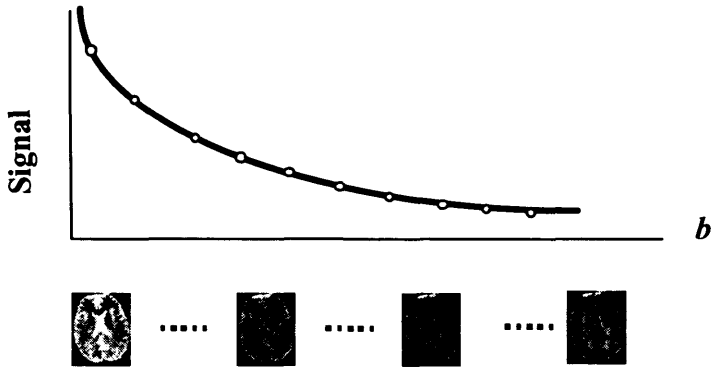

Figure 2.6. Diffusion signal decay curve showing a relationship between the *b* factor and signal.

2.2.4. Diffusion-weighted images

The Pulse Field Gradient (PFG) method can be included in most MRI sequences to introduce diffusion weighting (DW) along multiple directions. The highest reduction in signal is observed in areas where the diffusion coefficient in that direction is the highest. In fact, in the anisotropic areas, where the diffusion is preferential along one direction, which is generally the main axis of axons, the signal attenuation is most evident when the diffusion

gradients are applied along that direction. On the other hand, the signal attenuation in the isotropic areas is independent from the directions of the application of the diffusion gradients. For example, the genu of the corpus callosum appears dark only when the diffusion gradients are applied along x, whilst the lateral ventricles appear dark independent of the gradient diffusion directions (Figure 2.7).

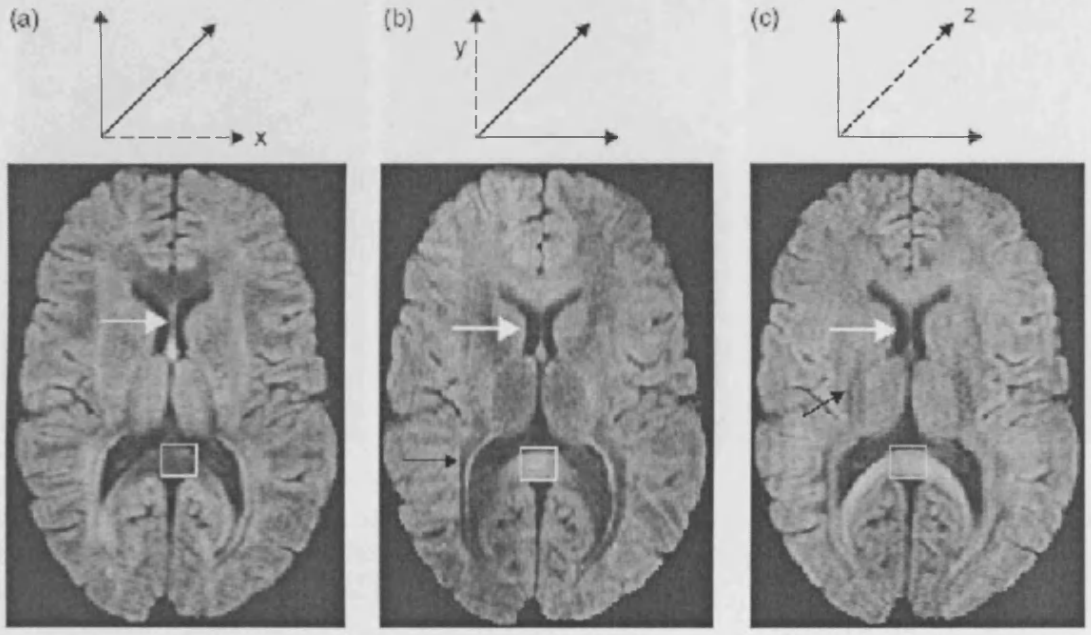

Figure 2.7. Axial slices obtained after application of diffusion gradients along three orthogonal directions (x, y and z), which are indicated above each image as dotted lines. The white arrows indicate isotropic areas. The white box indicates the corpus callosum, which shows a signal loss when the diffusion gradients are applied along x, and appears bright when the diffusion directions are applied in the directions orthogonal to the main callosal fibers (y or z). The black arrows in (b) and (c) indicate areas of fiber alignement along y and z, respectively.

From the formula 2.5, the diffusion coefficient or D can be computed at each voxel. This diffusion coefficient measured in vivo by MRI is always lower then that of free water. Therefore, the term *apparent diffusion coefficient* (ADC) is used to indicate that it is understood that the diffusion process is the same; however, the diffusion distance is lessened by the interaction of water molecules with cellular structures, not by a reduction in the diffusion coefficient (Cercignani and Horsfield 2001). Thus, a voxel-by-voxel calculation of

the ADC produces a *diffusion map*, which has an intensity scale that is inverted compared to the DWI used to calculate it (Figure 2.8).

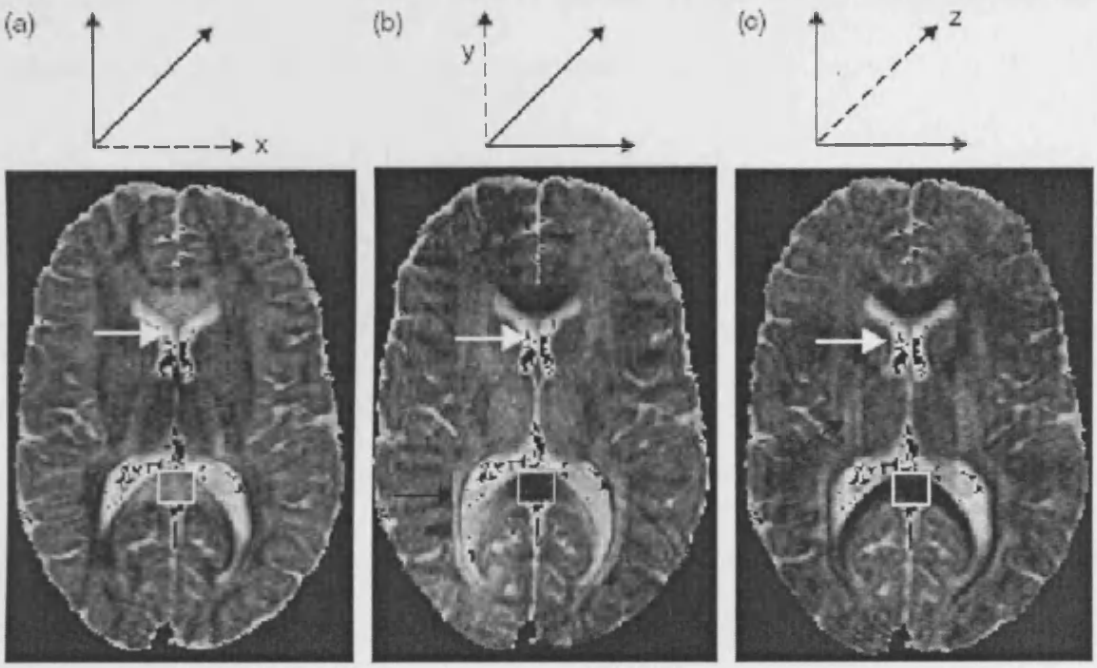

Figure 2.8. ADC maps of the axial slices shown in Figure 2.7. Note that the isotropic areas dark on the DWI are bright here. The black pixels correspond to areas where the ADC calculation produced unacceptable number.

2.2.5. Diffusion tensor and its scalar invariants

As mentioned above, in anisotropic tissue, the diffusion properties of a substance are best described by the DT (**D**) rather than a single diffusion coefficient. The main advantage of using the DT is that rotationally invariant indices can be derived. These indices are independent of the position of the subject inside the scanner and can be used to compare different groups of subjects and to perform longitudinal studies.

Basser et al. described the use of multivariate linear regression to calculate **D** from a non-diffusion-weighted images plus six or more diffusion–weighted measurements along non-collinear directions (Basser et al. 1994). The diffusion weighting is obtaining by simultaneously applying diffusion gradients along combinations of the three physical axes.

Given the six different components of the DT, it is possible to transform (or perform a matrix diagonalisation) the DT into another tensor D', with off-diagonal elements equal to zero and diagonal elements reflecting the intrinsic properties of the tissue, independently of the coordinate system in which they have been measured:

$$D' = \begin{pmatrix} \lambda 1 & 0 & 0 \\ 0 & \lambda 2 & 0 \\ 0 & 0 & \lambda 3 \end{pmatrix} \qquad (2.7)$$

$\lambda 1$, $\lambda 2$, $\lambda 3$ are the *eigenvalues* of **D** and represent the ADC values associated with the prinicipal *eigenvectors,* $\varepsilon 1$, $\varepsilon 2$, $\varepsilon 3$, which are orthogonal in the scanner reference frame and represent the directions along which molecular displacement are not correlated. For each DT, the combination of eigenvectors and eigenvalues is unique and reflects the diffusion properties of the tissue. The eigenvectors are ordered according to the decreasing value of their eigenvalues, so that $\varepsilon 1$ represents the principal direction of diffusivity characterised by $\lambda 1 > \lambda 2$ and $\lambda 2 > \lambda 3$. In conclusion, the acquisition and the diagonalisation of the DT allows $\varepsilon 1$ to be obtained, and $\varepsilon 1$ is always aligned with the main diffusion direction within each voxel, with $\lambda 1$ corresponding to the maximum diffusivity in each voxel, regardless of the position of the head. Several parameters, which are rotationally invariant, can be defined from the DT and describe the behaviour of diffusion within each voxel. The most commonly used are mean diffusivity and fractional anisotropy. The mean diffusivity (MD) is the average of the eigenvalues of the DT in a voxel:

$$MD = \frac{\lambda 1 + \lambda 2 + \lambda 3}{3} \qquad (2.8)$$

Fractional anisotropy (FA) (Basser and Pierpaoli 1996) is equal to the ratio between the square root of the variance of the eigenvalues and the square root of the sum of the squares of the eigenvalues. Therefore FA estimates what proportion of D is due to anisotropic diffusion.

$$FA = \frac{\sqrt{(\lambda 1 - \langle D \rangle)^2 + (\lambda 2 - \langle D \rangle)^2 + (\lambda 3 - \langle D \rangle)^2}}{\sqrt{\lambda 1^2 + \lambda 2^2 + \lambda 3^2}} \qquad (2.9)$$

While MD is relatively uniform throughout the brain, FA is different between the grey and white matter, being low in the former and high in the latter (Pierpaoli et al. 1996;Pierpaoli and Basser 1996).

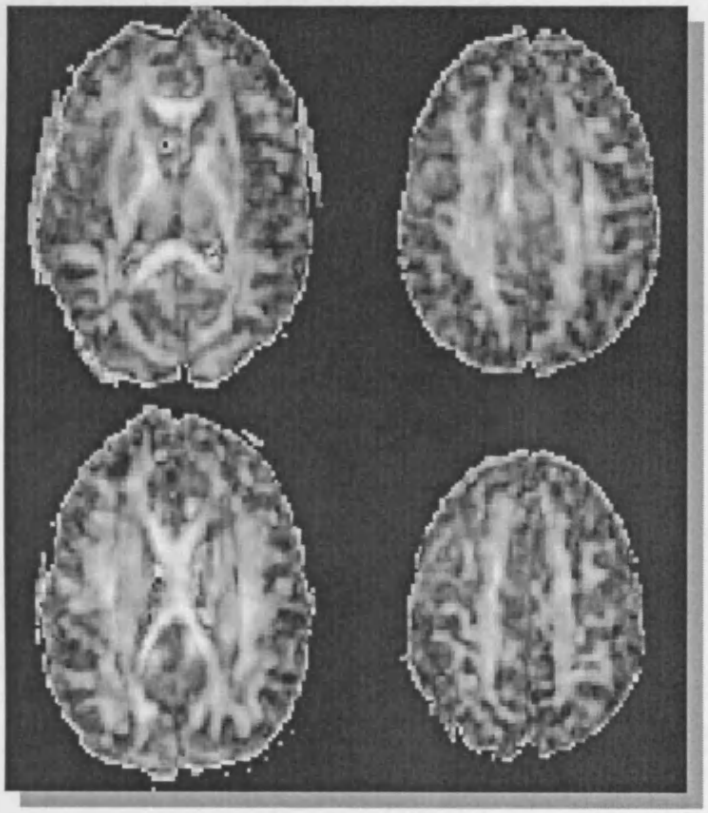

Figure 2.9. Fractional anisotropy maps. The brightest areas indicate regions with high anisotropy, in which the fibre are higly aligned. Regions of low anisotropy appear dark.

2.2.6. Clinical protocols

The PFG method has been incorporated into a number of pulse sequences to collect DW MRI data and thus calculate the DT. Since large diffusion gradients are used, all DW techniques are sensitive to motion artefacts, caused by movements of the head or pulsation of the brain because of blood and CSF motion. One possible solution is to use fast image

acquisitions, such as a single-shot DW-EPI. However, even using the EPI sequence, which offers the highest SNR per unit time, considerable signal averaging is required. Consequently, in order to obtain good resolution, the scanning time becomes relatively long. A final consideration relates to the sampling of the signal decay curve. Although it was thought that the best fit would have been obtained by sampling the signal corresponding to different *b* factors, it has become evident that a two-point fit is preferable in term of SNR per unit time (Jones et al. 1999a). However, this estimation does not allow for a distinction to be made between different diffusion compartments, such as the intra and extracellular water, which requires many points along the curve and very high *b* values. For a two-point acquisition it is possible to optimise the *b* factor used. Since, at low *b* factor, the process of perfusion, which involves the microcirculation of blood in the capillary system, contributes to the loss of signal (Le Bihan et al. 1986), a minimum *b* (bmin) different from zero can be used in order to reduce the effect of perfusion (Henkelman et al. 1994). For the scanner used in the works included in this thesis, the optimum difference in b values between the b=0 or bmin≠0 and the maximum b factor (bmax) seems to be of the order of 1035 x smm^{-2} (Jones et al. 1999a).

2.2.7. Diffusion based tractography

As mentioned earlier, DTI gives two types of information about the property of water diffusion in white matter: 1) the extent of diffusion anisotropy; 2) the orientation of anisotropy. The main assumption is that the principal axis of the diffusion tensor aligns with the predominant fibre orientation within a voxel. However, DTI provides no explicit information about the connection of fibres between neighbouring voxels. The 3-dimensional reconstruction of tract trajectories, or *tractography*, is a method of inferring *in vivo*

continuity of fibres from voxel to voxel (Mori and van Zijl 2002). Several tractography techniques have been developed (Basser et al. 2000;Behrens et al. 2003b;Conturo et al. 1999;Jones et al. 1999c;Koch et al. 2002;Lazar et al. 2003;Mori et al. 1999;Poupon et al. 2000) and they can be roughly divided in two types: 1) Line propagation techniques, which use the local tensor information; 2) Energy minimisation techniques, which determine the energetically most favourable path between two pixels.

The line propagation techniques include: i) Linear approaches, which simply propagate "a line" following the main direction of vectors through a continuos vector field (Mori et al. 1999); ii) Interpolation techniques, which utilise interpolation of the tensor or eigenvector field to draw a line between adjacent voxels (Basser et al. 2000;Conturo et al. 1999); iii) Tract editing or white matter parcellation techniques, which identify all tracts that pass through two regions of interest (ROIs) (Conturo et al. 1999;Stieltjes et al. 2001). For example, the corticospinal tract can be traced by locating one ROI at the level of the cerebral peduncle and one ROI on the lower pons and medulla (Stieltjes et al. 2001).

The energy minimisation techniques include: i) Fast marching techniques, which are discussed in the following paragraph; and ii) The simulated annealing approach, which generates a line or "path" between two points based on the alignment of the line to the vector field (i.e. energy minimisation process) (Tuch et al. 2001).

Before describing the tractography algorithms that have been developed and applied in this thesis, it is important to discuss some limitations of tractography techniques, which are related to the low resolution of DTI and the inhomogeneity of white matter structures. In typical DTI acquisitions, the voxel dimensions vary from 1 to 5 mm, whilst the diameter of axons is less than 10 μm (Beaulieu 2002). The diffusion of water molecules that is hindered or restricted by the presence of axons is averaged and measured within a much bigger voxel. Therefore, DTI cannot adequately reflect the case of a voxel containing more than one

population of axonal bundles with different orientations. This will occur when a voxel includes "crossing" or "kissing" fibres. Moreover, curvature of axonal tracts within a voxel violates the assumption described above that the diffusion process along any arbitrary axis is Gaussian, thereby invalidating the routine tensor calculation. This will occur when, for example, the sub-cortical U-fibres, which are highly convoluted, are contained within a voxel. Finally, DTI acquisitions contain noise, and, consequently, the calculated vector direction may deviate from the real fibre orientation. In conclusion, all these limitations may induce not only tracking errors, which become larger as the propagation becomes longer (Basser and Pajevic 2000;Lori et al. 2002), but also reconstruction of adjacent and unrelated white matter tracts (Lazar and Alexander 2003).

In the next paragraph, we will introduce two tractography methods that have been developed in this work, Fast Marching Tractography (FMT) and Probabilistic Index of Connectivity (PICo). The developments and the applications of FMT are presented in chapter 4, while the PICo algorithm, which presents some advantages compared with FMT, is discussed in the final chapter of this thesis.

2.2.7.1. Fast Marching Tractography

FMT allows the estimation of connectivity of any brain region to a starting voxel, and generates connection pathways with their branching fibres (Parker et al. 2002c). FMT includes three steps, each of which requires the information obtained by the previous one.

The first step involves the growth of a front from a starting point, and is called the *front evolution* step. The rate at which the front propagates is linked to the information contained in the eigenvector map, and therefore it will be faster if the eigenvectors of two adjacent voxels are in line, or pointing towards each other, which implies continuity of fibres, and

slower if there is no coherence of eigenvectors of neighbouring voxels. The former case occurs in the white matter tracts, whilst the latter is seen in grey matter regions. The evolution of a front can be visualised as a drop of ink which spreads on a cloth, and the eigenvector map indicates which way the ink is spreading.

The second step of FMT produces *a time of arrival map*. It is based on the theory that the time at which the front reaches each point in the image is determined by the front evolution, and it will be lower when the principal eigenvectors are aligned. This second step allows calculation of the shape of the stain from the vector field, which is equivalent to a contour line showing the distance from the origin travelled by the ink within the same amount of time. Multiple contour lines can be calculated, each representing the stain shape at a different time point. These multiple contours represent a likelihood-of-connection map. The most likely path between an aribitrary point and the seed voxel (origin of the stain) can be found by following the gradient steepest path, similar to water flowing to a sink hole from arbitrary points in the sink. Therefore, each voxel in a brain may be connected to a starting point.

The third step allows the creation of a connectivity metric, or *voxel-scale connectivity (VSC) map*, which ranks, at each voxel, the strength of connection to a starting point (see Figure 4.3. and 4.4). In particular, the value of the VSC map at each voxel is obtained by the relationship between the most likely path and the underlying eigenvector field. Therefore, in the context of the FMT method, the term "connectivity" indicates bulk inter-regional anatomical connectivity.

The main limitation of FMT is that this VSC map indicates the degree of connection to the starting point in an arbitrary way and does not compute a probabilistic map that truly reflects the underlying fibre structure. A step toward the generation of an accurate map of probability of connection has been obtained by the development of a novel tractography algorithm, called Probabilistic Index of Connectivity (PICo), which is discussed in the next paragraph.

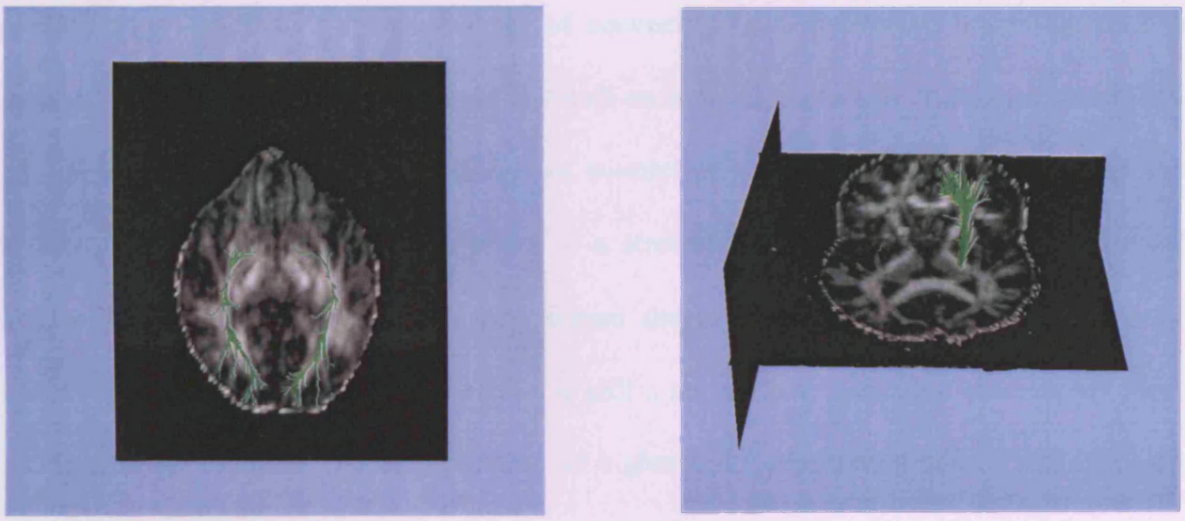

Figure 2.10. Optic radiations and cortico-spinal tract reconstructed using FMT and representing the most likely paths between the starting points and any other voxel within the pathways under investigation.

2.2.7.2. Streamline-based Probabilistic Index of Connectivity

Probabilistic Index of Connectivity (PICo) (Parker et al. 2003) is a novel tractography method also included in the line propagation techniques. It has been developed in this work after FMT and has been applied in one study presented in the last chapter of this thesis. As mentioned earlier, the main advantage of PICo compared with FMT is that it generates *probabilistic maps* of fibre connectivity between voxels. Two orders of uncertainty, based on $\varepsilon 1$ orientation, are introduced: a 0^{th} order, assigning uncertainty using the anisotropy of the tensor; and a 1^{st} order, assigning uncertainty using the relative magnitudes of λ_2 and λ_3 and the orientations of their associated eigenvectors. When the second and third eigenvalues are high compared with that of the principal eigenvalue, the uncertainty is large, suggesting the presence of crossing or branching fibres. This uncertainty is also combined with an estimate of data noise. Based on this information, PICo generates a probability distribution function (PDF), which reflects the best estimate of the tissue microstructure responsible for a given DT, within each voxel. Then, a line propagation is repeated N times in a Monte Carlo

process, thus establishing the confidence of connection to a distributed brain region. The number of occasions over *N* repetitions at which each voxel is crossed or hit by a streamline is used to define a map of the probability of connection to the starting point. Although the idea to incorporate the uncertainty of ε1 in a streamline analysis allows computation of probability maps, and represents a step toward the assessment of crossing white matter fibres, the form of the PDF used by PICo is still a not perfect estimation of complex fibre architecture in a voxel. The incorporation of higher order representations of the diffusion profile than the DT in the PDF calculation, such as those obtained by spherical harmonic descriptions (Alexander et al. 2002), may lead to more accuracy in the connectivity estimation.

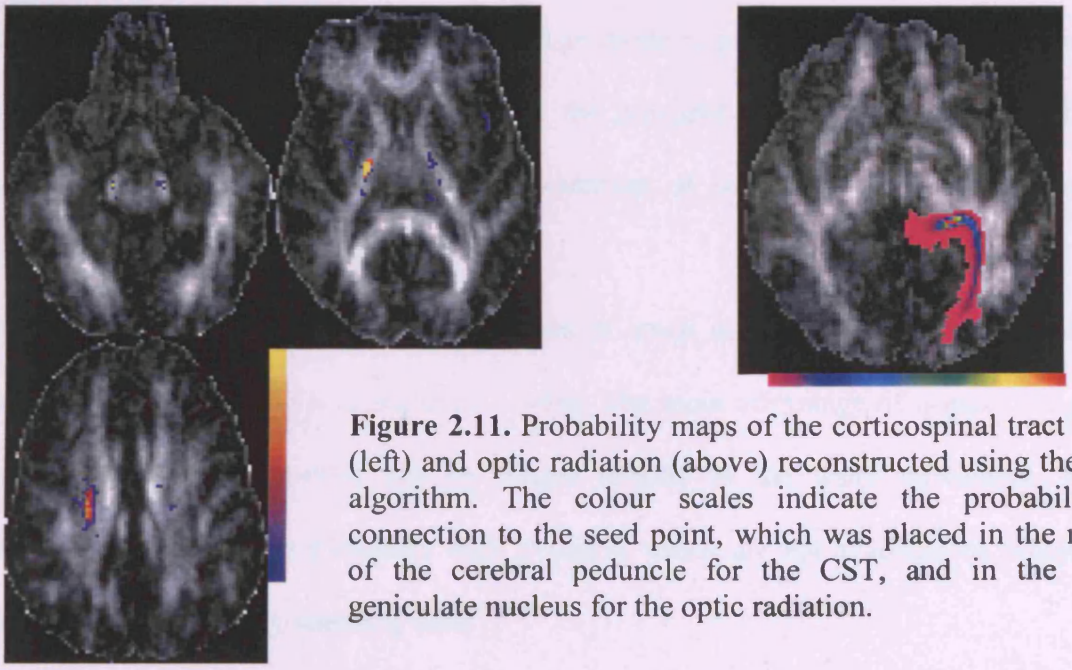

Figure 2.11. Probability maps of the corticospinal tract (CST) (left) and optic radiation (above) reconstructed using the PICo algorithm. The colour scales indicate the probability of connection to the seed point, which was placed in the middle of the cerebral peduncle for the CST, and in the lateral geniculate nucleus for the optic radiation.

2.3. Beyond the single diffusion tensor

Although the DT has provided a major contribution to understanding the pathologic mechanisms underlying neurological diseases, several groups have been focusing their latest

research on developing models that can explain the complex behaviour of water *in vivo* and properly track crossing, branching or "kissing" fibres, which cannot be distinguished when diffusion is modelled as a single tensor. We are going to discuss the main areas of interest.

As mentioned earlier, within a single voxel, the behaviour of diffusion might be not correctly described by a Gaussian probability density function, because different fibre directions are present. In these cases, the ADC profile can be modelled as a set of spherical harmonics (Alexander et al. 2002;Frank 2002). Alexander et al. (2002) confirmed that non-Gaussian profiles of the diffusion process occur in the brain regions where crossing fibres are known to be present (e.g. pons). Frank et al. (2002) showed that isotropic diffusion, anisotropic diffusion from a single fibre, and anisotropic diffusion from multiple fibre directions can be detected by a spherical harmonic transform. Thus, the use of spherical harmonics might be used to identify voxels in which the single tensor model is poor. In these voxels, a mixture of two Gaussian densities might be fitted, and the principal directions of the two diffusion tensors might provide estimates of the orientation of the crossing fibres and improve tractography results (Parker et al. 2004).

The q-space approach allows the measurement of small displacements of water molecules using high gradient strength (King et al. 1994). The main advantage of q-space imaging is that the displacement profiles can be related directly to the water movement, without Gaussian fitting, although it requires high gradients which are not available on whole-body clinical scanner, and long scanning time.

Diffusion spectrum imaging (DSI) is a compromise between the Gaussian behaviour of water molecules displacement of DTI and the use of infinitely small d for q-space-like imaging (Tseng et al. 2002;Wedeen et al. 2000). Lin et al. recently demonstrated that this technique is able to resolve the fibre structure in the grey matter of rat brains, and validated the DSI technique by using manganese-enhanced MRI. However, the scanning time was of about 35

hours (Lin et al. 2003). A recent study showed that DSI is sensitive to the pathological changes occurring in the NAWM and lesions of patients with MS, confirming the potential diagnostic capacity of this technique (Assaf et al. 2002).

Finally, a recent model describes a "compartmentation" of water diffusion (Clark and Le Bihan 2000). This model assumes that intra-cellular water is characterised by a slow diffusion tensor, whilst the extra-cellular water is described by a fast diffusion tensor. The latter can be measured by b-factor of 1000 smm^{-2}, whilst the former only with b-factor of about 4000 smm^{-2}. The possibility of being able to estimate the two compartments *in vivo* has potential application for studying the complex pathologic changes affecting the brain tissue.

2.4. Functional Magnetic Resonance Imaging

When a population of neurons is functionally "activated", they undergo local metabolic changes, which are related to the synthesis and release of neurotransmitters at the synapses (Duncan et al. 1987). Further metabolic changes also occur in the glia cells, which are responsible for the re-uptake of neurotransmitters (Magistretti and Pellerin 1996). These metabolic changes require energy, and, since the brain energy production depends on oxidative metabolism, there is a greater demand for delivery of oxygen. To meet the increased metabolic demand, neuronal activation is accompanied by increased local blood flow. The increase in blood flow is accompanied, in turn, by a small increase in local blood volume. The increment of blood flow changes leads to a greater availability of oxygenated haemoglobin. All these haemodynamic changes provide the basis for a number of functional MRI (fMRI) methods. This paragraph includes only one fMRI method that is sensitive to the detection of changes in blood oxygenation. Although the mechanisms of coupling the haemodynamic response to neuronal activity are still incompletely understood, fMRI has the

potential to provide important information about brain function in both normal and pathological conditions. In the next paragraph the basis of the *blood oxygen level dependent* (BOLD) response and fMRI is presented and the principles of fMRI analysis are discussed.

2.4.1. Oxygen utilisation by the brain

Before examining the BOLD signal, it is useful to review briefly the Fick's law that describes changes occurring in blood flow or blood oxygenation during brain activity (Jezzard and Ramsey 2003). The rate of oxygen consumption in a tissue is related to the flow and venous oxygenation level of the blood following Fick's principle, which states that:

$$CMRO_2 = CBF \times 4[Hb^{TOT}](Y_a - Y_v) \qquad (2.10)$$

In this formula, $CMRO_2$ is the metabolic rate of oxygen consumption (expressed in units of moles of oxygen consumed per gram of tissue per second). CBF is the cerebral blood flow, which is interpreted as the blood that is delivered to the tissue, (expressed in millilitres of blood perfusing each gram of tissue per second). Hb^{TOT} is the total concentration of haemoglobin (oxygenated and deoxygenated) (in units of moles per millilitre of blood), and the factor 4 accounts for the fact that 4 molecules of oxygen bind a haemoglobin molecule. Ya and Yv are the oxygen saturation values (i.e. the fraction of haemoglobin which is oxygenated) for arterial and venous blood. Therefore, (Ya – Yv) is the oxygen extraction fraction (OEF, value between 0 and 1) and is a measure of the arterio-venous difference in haemoglobin oxygen saturation.

In the case where Ya and total haemoglobin concentration are at fixed levels, Fick's principle can be revised as follows:

$$\frac{\Delta CMRO_2}{CMRO_2} = \frac{\Delta CBF}{CBF} + \frac{\Delta OEF}{OEF} \qquad (2.11)$$

During brain activation there is an increase in $CMRO_2$, accompanied by an increase in CBF and, somewhat counter-intuitively, a decrease in OEF (i.e. the oxygen saturation value in the veins (Yv) is increased). Thus, during local brain activation the oxygenation level of the venous blood actually rises. This is the effect that is used in BOLD fMRI experiments (Jezzard and Ramsey 2003).

2.4.2. Uncoupling of blood flow and oxygen metabolism

In the mid 1980s studies performed with positron emission tomography (PET) found that during a somatosensory stimulation task there were increases in CBF and glucose consumption (of about 30%), but only a very small increase in $CMRO_2$ (of about 5%) (Fox and Raichle 1986). This finding was in conflict with the well established assumption that during brain activity, which leads to increased cellular metabolism, there would be an increased consumption of oxygen and a proportional increase in regional CBF. Therefore, it is possible that the increased metabolism occurring in neurons is anaerobic rather than aerobic (Gjedde 2001). Although an uncoupling of blood flow and oxygen metabolism definitely occurs, it has been reported that there is, after all, a linear relationship between the small increase in oxygen consumption and the much bigger increase in CBF (Hoge et al. 1999).

A possible explanation of this uncoupling is that a large increase in CBF is required in order to provide a relatively small increase in the oxygen concentration gradient between capillaries and mitochondria, which, in turn, causes the oxygen to diffuse from the blood to the neurons.

2.4.3. The BOLD effect

The image contrast in fMRI was named *'blood oxygenation level dependent'* or BOLD, because it is dependent on the presence of oxygenated haemoglobin in the blood vessels. Pauling and Coryell (1936) found that deoxy-haemoglobin was slightly paramagnetic relative to tissue, whereas oxy-haemoglobin was diamagnetic relative to tissue (Pauling and Coryell 1936). Later, Thulborn et al. reported that the oxy-haemoglobin had a small magnetic susceptibility effect, did not significantly alter the regional magnetic field, and did not greatly affect tissue T2*, while the deoxygenated haemoglobin led to a large magnetic susceptibility effect shortening tissue T2* (Thulborn et al. 1982). Thus, it is this local distortion of the magnetic field homogeneity, occurring on a microscopic scale, that provides the contrast mechanism in the fMRI experiment and enables changes in blood oxygenation level to be detected.

In 1990 Ogawa et al. described the first BOLD contrast imaging experiment reporting a loss of signal around blood vessels in a cat that was made hypoxic (Ogawa et al. 1990). The authors interpreted the cause to be the creation of local magnetic field inhomogeneities from deoxy-haemoglobin, and termed it the BOLD method. They also suggested that the effect could be used to image the smaller change in the relative blood oxygenation that accompanies neuronal activation in the brain. A similar effect was demonstrated with ultra-fast EPI in animals breathing an oxygen-deprived atmosphere (Turner et al. 1991). Shortly afterwards, a similar effect was confirmed in humans during breath holding (Kwong et al. 1992).

Although the mechanisms underlying BOLD contrast are still unclear, a widely accepted model is as follows. Increased neuronal activity induces local vasodilatation, and consequently, increased cerebral blood flow and cerebral blood volume. Cerebral blood flow increases more than blood volume, and oxygen delivery quickly exceeds the local demands

of the activated tissue. Increase in local blood flow in the arterioles and small arteries is therefore uncoupled from local metabolism. The net effect is a larger ratio of oxygenated to deoxygenated haemoglobin in the capillary and venous vascular beds, which, in turn, leads to a longer regional T2* compared with the surrounding tissue and increases the signal intensity on the T2*-weighted images. For typical cortical activation tasks, the image signal intensity varies from 1 to 15%, depending on field strength.

2.4.3.1. Origin of the BOLD signal

As discussed above, the relationship between the haemodynamic changes and neuronal activity is still unclear. A study recently published in *Nature* has provided further insights into the mechanisms underlying the haemodynamic changes (Logothetis et al. 2001). The authors studied 10 healthy monkeys who underwent a visual fMRI experiment during which a checkerboard pattern was presented. At the same time, electrophysiological recordings were performed by implanting specially constructed microelectrodes in the occipital pole. Results demonstrated that a spatially localised increase in neural activity is directly correlated with signals detected by BOLD fMRI. This finding supports the assumptions made from all fMRI studies that the haemodynamic response mirrors neural activity. The neural signal increased immediately on presentation of the visual stimulus and decreased as soon as the stimulus was terminated. Moreover, the neural signal had a higher signal-to-noise ratio than the haemodynamic response, suggesting that the extent of activation in human fMRI experiment is often underestimated due to the variation in the vascular response. Consequently, caution was recommended when mapping studies try to precisely localise neural activity. The authors also reported that the local field potentials (LFPs), which reflect the neural activity related to signal input and local information processing, allow a better

estimate of BOLD responses than the multi-unit activity, i.e. the firing rates of a group of neurons, which reflects the output of a neural population. However, this conclusion is in disagreement with previous models that suggested a quantitative relationship between the spike rate of neurons, which controls the release of neurotransmitters, and the haemodynamic response (Rees et al. 2000).

2.4.3.2. Temporal and spatial resolution of the BOLD response

The theoretical limit of the *temporal resolution* of fMRI depends mainly on the temporal characteristics of the haemodynamic response. The BOLD response varies within and between subjects, and has typical features (Figure 2.7). There is an initial small decrease in BOLD signal intensity (the early "dip") that evolves over the first second following a stimulus (Ernst and Hennig 1994) and is often seen only at high field strength. After 2-4 seconds, there is a progressive increase in BOLD signal. The time to peak varies depending on the anatomical region (Bandettini et al. 1997) and on the duration and other parameters of the stimulus. For example, it varies from 1 second for a very short stimulus, such as a flash of light, to 8 seconds for a robust stimulus, such as a flickering checkerboard. For a simple stimulus, the signal change is maintained at a relatively constant level for the period of stimulation (Bandettini et al. 1997). Interestingly, for stimulus longer than 4 seconds the BOLD response "saturates", and increases in stimulus duration cause only a change in the peak width. After the stimulus stops, the curve takes only a few seconds to return to zero, and decreases to a level below the initial baseline (the post-stimulus "undershoot"), from which it recovers slowly over a further few seconds. The duration of this recovery phase places limits on how fast the stimulus can be repeated. Overall, the time from onset to final return to baseline is about 12-18 seconds. Figure 2.7b shows an "overshoot" period during

the early positive BOLD response, which is another common feature observed in fMRI experiments.

A specific physiological interpretation of the time course of the BOLD response has been provided by studies in cat brains with optical imaging methods (Malonek et al. 1997). The initial dip is hypothesised to arise from the rapid deoxygenation of capillary blood accompanying the increased oxygen utilisation. Then there is an increase in blood flow (typically of 50-70%), which increases the ratio of oxygenated haemoglobin to de oxygenated haemoglobin causing increased signal intensity. The overshoot observed at the beginning of the positive BOLD response may be a result of the slower blood volume response, which allows the BOLD response to briefly reach a higher value than its steady-state response until the slower increase of blood volume occurs. After the stimulus stops, the ratio decays back to baseline. However, the blood volume decreases more slowly, creating a brief undershoot of the BOLD response (Buxton et al. 1998).

Although venules and capillaries contribute similar volume of blood per voxel, the venules make a greater contribution to the BOLD signal because they carry less oxygenated blood. Consequently, larger signal changes can be detected in voxels localised over draining veins.

The *spatial resolution* of the BOLD response depends on the intrinsic resolution of the imaging experiment. In order to localise activation at the level of the cortical colums, a voxel size of 100 microns will be required. This hypothetical resolution is not desired because it will reduce the signal-to-noise ratio. However, activation in two very closely adjacent cortical columns has been resolved using a subtraction procedure (Menon and Goodyear 1999). Other limitations to the spatial resolution of fMRI are related to the facts that the haemodynamic response is not spatially very specific to areas of activation (Logothetis et al. 2001) and that signal changes from draining veins can displace the activation response.

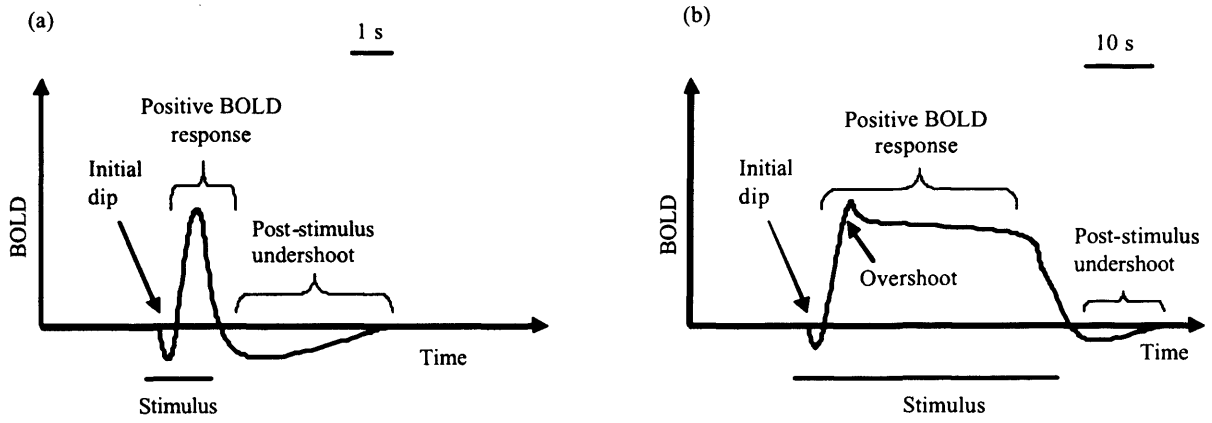

Figure 2.12. Diagram showing the BOLD response to a brief period of neuronal stimulation (a) and more sustained period of neuronal stimulation (b) [Adapted from Jezzard and Ramsey, 2003].

2.4.4. Typical scan protocols

Most fMRI experiments use gradient echo EPI sequences because they are naturally sensitive to T2* contrast. They allow coverage of the whole brain in 2 to 3 seconds. In an fMRI experiment, a large number of brain volumes are acquired as time series (e.g. 100-500 multislice volumes). The TR varies between 3 and 5 seconds and the TE is generally close to the T2* of the tissue, of about 40-50 ms, to optimise the ability to detect BOLD contrast. The in plane resolution is between 2 and 4 mm (field of view 24 cm^2 and matrix size 64^2 to 128^2), and slice thickness varies between 3 and 5 mm. However, gradient echo EPI has some disadvantages: i) Its effective minimum spatial resolution is around 3 mm (Engel et al. 1997) regardless of imaging resolution; ii) It is usually not useful to go much faster than an on-off cycle of 8 s on and 8 s off (Jezzard and Ramsey 2003); iii) Signal loss occurs at the interface between air and bone, for example in the region of the petrous temporal bone or the frontal air sinuses; iv) Geometric distortions are common; v) Head motion is a major source of artefact, and is often unavoidable, depending on the task.

2.4.5. Experimental designs

An experimental design requires formulating a hypothesis about the brain activity that occurs during the performance of a specific task. The task consists of "triggering" the brain function under investigation in a specific and temporally defined fashion, which is called experimental design. The task has to be repeated more than once throughout the experiment, because the signal change due to brain activation is of a small magnitude compared to the baseline signal and there is also noise. Thus, the type of experimental design varies with the aim of the study (Jezzard and Ramsey 2003).

The simplest fMRI experiment includes alternating periods (epochs) of two different experimental conditions. The two conditions, which alternate in an *"on-off"* design, are task performance (or sensory stimulation) and rest. Sometimes the off period consists of those functions that are not relevant to the brain function under investigation and need to be eliminated. The block designs are very effective in detecting the brain response to a stimulus, although they have a limited temporal resolution (epochs are usually between 20 and 40s in duration) and are unable to detect unpredictable or aperiodic types of brain activity.

A second type of experimental design is a *parametric* study, usually used in cognitive studies (Braver et al. 1997), in which the same task is performed, but with different levels of difficulty. All the functions that are necessary to perform the task are involved at all levels, but only the processing load changes from one level to the others. Therefore, the parametric design allows detecting brain regions where activity increases with the level of the task.

A third type of fMRI experiment is an *event-related* design. In event-related designs a short stimulus is presented either at long (Bandettini and Cox 2000) or short intervals (Buckner 1998). The reason why the stimulus is presented at high frequency is that the brain response under investigation is extremely short, and can last only a few milliseconds.

Other important factors which have to be considered in designing an fMRI experiment are: 1) habituation or fatigue, which may result from prolonged task performance; 2) learning effects, which may occur when experiments are repeated at short intervals.

2.4.6. fMRI analysis

The aim of fMRI data analysis is to detect areas of significant brain activation in response to specific stimuli. Analysis of fMRI data has developed extensively over the last decade, resulting in the availability of several sophisticated software packages from major fMRI centres [e.g. from University College London, from NIH and from Oxford]. The following section describes the basic principles of one of these statistical tools, called Statistical Parametric Mapping (SPM; Wellcome Department of Imaging Neuroscience, London, UK) (Friston et al. 1995;Worsley and Friston 1995), which is used for the analysis of the fMRI experiments reported in chapter 5.

The first SPM was used to establish functional specialisation for colour processing in 1989 (Lueck et al. 1989). The methodology and the principles of SPM were described in two papers in 1990 (Friston et al. 1990) and in 1991 (Friston et al. 1991). Since then there have been many mathematical developments and even different versions of SPM. The name SPM was chosen for several reasons: 1) To acknowledge significant probability mapping developed in the field of EEG; 2) For consistency with the nomenclature of parametric maps of physiological parameters, such as regional CBF maps obtained from PET studies; 3) In reference to the *parametric* statistic that assumes the errors are additive and Gaussian (see below). This is in opposition to non-parametric approaches, which are generally less sensitive and more computationally intensive, but do not make any assumption about the distribution of the error terms.

The analysis of neuroimaging data with SPM involves several steps (Figure 2.7). These are as follows: 1) spatial processing; 2) estimating the parameters of a statistical model; 3) making inferences about those parameter estimates with appropriate statistics. We will now discuss these three steps with particular regard to a block design study, in which a series of images (usually from multiple brain slices) are acquired sequentially with a constant TR throughout the experiment.

2.4.6.1. Spatial processing

The aim of spatial processing is to combine scans from the same subject and to make comparisons between scans from different subjects. In particular, spatial processing reduces the variance components in the voxel time-series that are induced by movement or shape differences among a series of scans. It is a necessary step because SPM assumes that the data from a particular voxel all derive from the same part of the brain. If this assumption is violated, because, for example, there is a slight movement of the head over the course of the fMRI study, it is possible to obtain large signal changes in the image time series that obscure the subtle signal changes under investigation.

The first step in spatial processing is to "realign", or spatially register, the data to cancel the effect of movement during the scanning session (Figure 2.7). The effect of the realignment or "motion correction" is that any particular voxel's time series does (over time) refer to the same point in the brain. *Realignment* consists of two steps: (i) Registration, that consists of an estimation of the 6 parameters (3 rotations, 3 translations) of an affine "rigid-body" transformation (Woods et al. 1992) that minimises the differences between each successive scan and a reference or "target" scan (usually the first or the average of all scans in the time series); and (ii) Application of the transformation parameters by re-sampling the data.

However, even after a perfect realignment, movement-related signal changes can still persist. This is because there are some movement effects that cannot be modelled using a linear affine model, such as the spin-excitation history effects (Friston et al. 1996b). A method to correct for this phenomenon has been proposed by Friston et al. (Friston et al. 1996). It states that the estimated movement parameters obtained from the realignment procedure can be used to calculate movement-related signal that is, in turn, subtracted from the original data. This adjustment can be performed by including the movement parameters in the model estimation, as shown in chapter 5.

After realigning the data, spatial *normalisation* of the data into a standard anatomical space (e.g. MNI (Tzourio-Mazoyer et al. 2002)) is performed (Figure 2.7). The effect of the spatial normalisation is that regions derived from different subjects are as close as possible. In particular, a mean image of the series is used to estimate some warping parameters that map it onto a template, which conforms to a standard anatomical space. These parameters are then applied back to all the images in an fMRI experiment.

The last step in spatial processing consists of spatially *smoothing* the data (Figure 2.7). It consists of a convolution of each volume with a Gaussian profile filter. There are two main reasons for smoothing: (1) It can increase signal-to-noise ratio in the data; (2) The statistical theory which might be used in later processing requires the data to be spatially smoothed for the assumptions underlying the statistical theory to be valid. The Gaussian random field theory (see below) assumes that the error terms are a reasonable lattice representation of an underling and smooth Gaussian field. This requires that the smoothness has to be twice or three times greater than the voxel size. However, smoothing may result in loss or in enlargement of active regions that are of the size of the voxel (Rutten et al. 1999).

2.4.6.2. The general linear model

The general linear model (GLM) is used to estimate some parameters that explain the data at each voxel in the brain (Friston et al 1995) (Figure 2.7). It is also known as "analysis of covariance" or "multiple regression analysis" and is summarised by the following equation:

$$Y = X\beta + \varepsilon$$

This equation states that the observed response variable Y is produced by a linear combination of explanatory variable X and the error term ε. In particular, X represents the *design matrix*, in which each column corresponds to the effect that has been built into the experiment (e.g. experiment condition) or may confound the results (e.g. movement parameters). These are referred to as explanatory variables, covariates or regressors. The last column is a constant. The purpose of considering several covariates in the design matrix is to reduce the variation in signal which is not related to the brain response. Each column of X has an associated unknown parameter. Some of these parameters (β) are of interest (e.g. the effect of a particular motor task), whilst others are not, and are considered as confounding effects. Inferences about the parameter estimates are made by using their standard error (i.e. square root of the estimated variance). This allows us to test the *null hypothesis* that all the estimates are zero using the F statistic, or that a particular combination of the estimates is zero using the T statistic. Thus, the null distribution at each voxel in the brain is modelled and then compared with the observed data in order to give either a F map (SPM[F]) or a T map (SPM[T]). In particular, a T statistic is obtained by dividing a contrast of the parameter estimates, which is obtained by a linear combination of the same estimates, by the estimated standard error of that contrast.

2.4.6.3. Statistical inference and the theory of random fields

Since the creation of a T statistical map requires the performance of many separate statistical comparisons, a correction for multiple comparisons has to be performed. The Gaussian random field (GRF) theory provides a method for correcting p values, taking into account that the neighbouring voxels in an image are not independent. The threshold that is used in the GRF depends on the study. If the goal is to search for a regional response, then a high threshold has to be applied in order to minimise false positive (or type I error) activations. However, if the brain activity is known and the aim is to localise it within a small region, then a small search volume (Worsley et al. 1996) and, consequently, a lower threshold may be used. As result of applying a threshold, an "activation" map that shows the significantly activated voxels is generated (Figure 2.7).

Thus, activation is ultimately considered as an expression of how much the design matrix explains the variation of the signal over time. It depends not only on the magnitude of signal changes due to the BOLD response, but also on the signal changes related to noise, due for example to pulsatile motion of the brain caused by cardiac cycles. These noise contributors can be reduced by filtering the data or can be measured and then modelled.

Although an important advantage of fMRI is that it can localise brain regions activated by an experimental task in a single individual, often the aim is to combine data from a group of subjects in order to generalise the results to the general population. SPM allows us to distinguish between the analysis of the activation within one subject, called *fixed-effect* analysis or first level analysis, and between subjects, called *random-effect* analysis or second level analysis. In the first level analysis, the error variance is estimated on *a scan to scan* basis in the same subject, whilst in the second level analysis, it is based on activation from *subject to subject*. The random-effect analysis is usually more conservative than the fixed-effect, but allows the inferences to be generalised to the population from which the subjects are selected. In order to perform a second level analysis, the contrasts of parameters

estimated from a fixed-effect analysis have to be entered into a design matrix at the second level analysis. This ensures that there is only one contrast per subject, respecting the assumption underlying the use of GRF correction that the errors are independently distributed. The second level design matrix simply tests the null hypothesis that the contrast are zero and usually contains only one column.

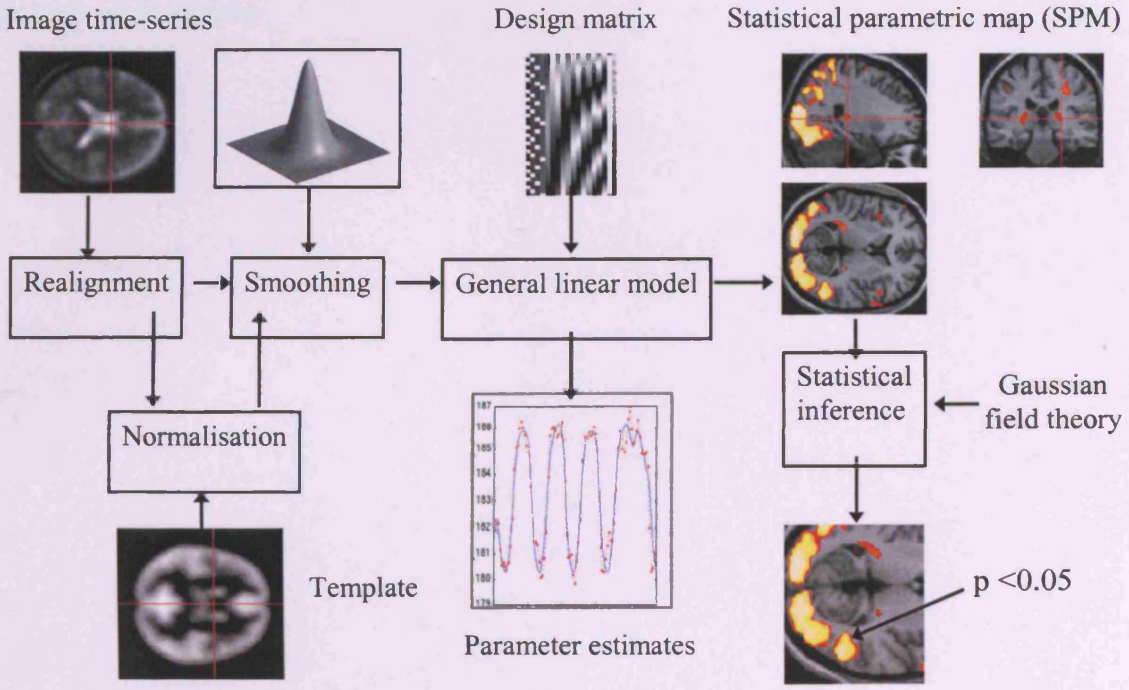

Figure 2.13. This diagram summaries all the steps involved in the analysis of fMRI data using SPM. Realignment of the images and normalization procedure ensure that the data are in the same anatomical space. After smoothing, the GLM is employed (i) to estimate the parameters of the model and (ii) to derive the appropriate univariate test statistic at every voxel. The T or F statistics constitute the statistical parametric maps. The final step is to make statistical inferences on the basis of the statistical parametric maps and GRF theory.

2.5. Conclusion

In this chapter we have discussed the lack of pathological specificity of conventional MRI, which explains, at least in part, the clinical-radiological paradox in MS, and described the principles of DTI and fMRI. We have used these new MRI techniques to improve detection or differentiation of the pathological processes in MS. In particular, we have used: (i) DTI to investigated pathological changes in NAWM of patients with MS (see chapter 3), (ii)

Diffusion based tractography to examine pathological changes in the visual pathways of patients with optic neuritis (see chapter 4), and (iii) Motor fMRI to assess whether functional reorganisation has an adaptive role in maintaining clinical function in patients with primary progressive MS (see chapter 5). The last chapter of this thesis shows the results obtained when we combined structural information, provided by DTI, with functional data, given by fMRI, in patients with optic neuritis.

Chapter 3

Investigations of the mechanisms of brain damage in MS using diffusion tensor imaging

This chapter presents two studies aim at investigating the mechanisms of damage in the normal-appearing brain of 39 patients with MS using DTI. The first study measures changes in diffusion indices in the normal-appearing basal ganglia and cerebellar grey matter, and supratentorial and infratentorial NAWM, using a region of interest approach. Correlations between DTI-derived indices and clinical measures were performed to investigate whether the structural damage in the normal-appearing brain is associated with disability. The second study investigates the relationship between the diffusion indices in the normal-appearing corpus callosum (CC) and the lesion loads in connected cerebral regions in the same group of patients, to test the hypothesis that NAWM damage relates to focal pathology.

3.1. Investigation of normal-appearing brain damage with clinical correlations

3.1.1. Introduction

DTI is able to distinguish between white-matter, which has an oriented microstructure, due to similarly aligned fibre tracts, and high anisotropy, and grey matter, which is characterised by less ordered tissue and relatively low anisotropy. Changes in DTI-derived indices are related to the pathological processes that modify cellular structures, thus providing a mechanism whereby DTI can investigate the structural damage in the MS brain, both in lesions and NAWM (Filippi et al. 2000b;Horsfield et al. 1996;Rocca et al. 2000;Rovaris et al. 2002b). These pathological insights have important clinical relevance because of the potential of pathology in NAWM to contribute to disability in patients with MS, as confirmed by spectroscopy studies (Chard et al. 2002a;De Stefano et al. 2000;De Stefano et al. 2001;Fu et al. 1998;Sarchielli et al. 1999). Previous DTI studies have demonstrated abnormally low FA and high MD in MS lesions and NAWM (Bammer et al. 2000;Cercignani et al. 2001a;Filippi

et al. 2000b;Werring et al. 1999), and have found that diffusion indices in the NAWM moderately correlated with clinical disability (Filippi et al. 2001b).

Although MS predominantly affects white matter regions, lesions occur also in deep and cortical grey matter (Bo et al. 2003;Brownell and Hughes 1962;Kidd et al. 1999;Peterson et al. 2001). The functional significance of deep grey matter abnormalities is not well established. Studies using PET (Bakshi et al. 1998;Blinkenberg et al. 2000) and conventional MRI (Bakshi et al. 2002;Grimaud et al. 1995;Russo et al. 1997) have demonstrated functional and structural abnormalities in normal-appearing basal ganglia beyond the focal inflammatory lesions. In particular, deep grey matter T2 hypointensity, due to iron deposition, has been recently reported to be a strong predictor of disability (Bakshi et al. 2002). Recent studies using MR spectroscopy and atrophy measures (Cifelli et al. 2002;Wylezinska et al. 2003) have reported neuronal loss and reduced volume in the thalamus of patients with RR and SP MS. Moreover, decreased perfusion in the basal ganglia of PP and SP MS patients has been seen with perfusion imaging (Rashid et al. 2004). Diffusion studies using histogram analysis have demonstrated structural damage in NAGM, including cortical and deep regions, in patients with MS (Bozzali et al. 2002;Cercignani et al. 2001a). Furthermore, there is evidence that the diffuse damage in the NAGM contributes to clinical disability. Diffusion histograms metrics derived from NAGM have been shown to correlate with the severity of language, attention and memory deficits in patients with RR MS (Rovaris et al. 2002c). Metabolite concentrations in the cortical NAGM also correlated with disability in the early phases of the disease (Chard et al. 2002a).

Therefore, the aims of this study were: (i) to investigate changes in MD and FA in the NAWM and in the normal-appearing deep grey matter, (ii) to determine the relationship between these indices and clinical disability and disease duration in 39 patients with MS.

3.1.2. Methods

3.1.2.1. Patients

Thirty-nine patients with clinically definite MS (Poser et al. 1983) attending the National Hospital for Neurology and Neurosurgery, London, were studied. The mean age was 45 ± 11.2 years; the median Kurtzke expanded disability status scale (EDSS) (Kurtzke 1983) was 4.0 (range 1.5-8.5); the median pyramidal score was 2 (range 0-5) and the median cerebellar score was 0 (range 0-3). The median disease duration was 13 years (range 3-33). There were 20 men and 19 women. The following MS subgroups were classified according to standard criteria (Lublin and Reingold 1996): 11 benign (median EDSS 2.0, range 1.5-3.0; median disease duration 20 years, range 13-31), 9 RR (median EDSS 2.5, range 1.5-5.0; median disease duration 7 years, range 3-24), 11 SP (median EDSS 6.0, range 3.5-8.0; median disease duration 14 years, range 7-33), 8 PP (median EDSS 6.0, range 5.0-8.5; median disease duration 12 years, range 4-18). Twenty-one healthy matched controls (mean age 40.3 ± 9.7 years, 14 men and 7 women) were included in the study. Informed consent was obtained from all subjects before entry into the study.

3.1.2.2. MRI protocol

All scans were performed on a 1.5 T Signa Echospeed MRI system (General Electric, Millwaukee, USA). All patients had conventional SE PD and T2-WI (TR 2000 ms, TE 30 ms, 120 ms; matrix size 256×256; FOV 240 mm; 28 contiguous axial slices of 5 mm thickness) acquired prior to DTI. The diffusion protocol consisted of three series of 7 interleaved slices, each acquired with a single-shot DW-EPI sequence. The total of 21

contiguous slices was compiled into a single file after reconstruction. The DW-EPI parameters were: TE 78 ms, matrix size 96×96, FOV 240 mm, and 4 *b* values, increasing linearly with G^2 (G= gradient amplitude) from 0 to 700 smm^{-2}, applied in each of seven non-collinear directions. In the presence of large diffusion gradients, on-line time domain averaging can cause disruption of the averaged signal due to large phase changes between successive shots. A minimum of four signal averages was collected for off-line averaging. The resultant magnitude images were averaged after reconstruction to improve the signal-to-noise ratio (SNR). Cardiac gating was also used to reduce motion artefacts due to pulsation of blood and cerebrospinal fluid. Correction of eddy-current distortions in DW-EPI was performed using a two-dimensional image registration technique (Symms et al. 1997), which also minimised the effect of any slight head motion during acquisition. The data were then processed to determine the diffusion tensor on a pixel-by-pixel basis for each of the 21 slices (Basser et al. 1994). FA and MD were calculated from the principal diffusivities of the diffusion tensor (Basser and Pierpaoli 1996;Pierpaoli and Basser 1996).

3.1.2.3. Region of interest analysis

All images were displayed on a Sun workstation (Sun Microsystems, Mountain View, CA using the DispImage software package (Plummer 1992). Thirtyone square regions of interest (ROIs) of uniform size (9 pixels; 31.72 mm^2) were placed bilaterally in 14 different anatomical regions, and in the middle of the genu, body and splenium of the CC, of each subject. Supratentorial and infratentorial regions were defined as the areas located above and below the tentorium of cerebellum respectively. The ROIs were outlined on the non-diffusion weighted b0 (b=0) images of the DW-EPI dataset, with guidance from corresponding slices of the T_2 WI and PD WI to ensure that lesions were avoided. The ROIs were automatically

transferred to the FA and MD maps and visually checked by the observer (O.C.) in order to confirm their location and to ensure that partial volume effects were minimised. The mean value, SD and range of diffusion parameters within each ROI were automatically recorded.

3.1.2.4. Noise evaluation

To ensure similar SNR in patients and controls, which would therefore allow a valid statistical comparison, the degree of noise contamination was determined by locating a ROI outside the brain (and away from any imaging artefacts) on the b0 images. For each ROI on the b0 images, the SNR was calculated as SNR= $S(b0)/\sigma$, where S(b0) is the mean of the signal intensity in each region and σ is the mean of the noise in the region outside the brain.

3.1.2.5. Statistical analysis

The average values of FA and MD within each subject for each anatomical region were calculated. For bilateral ROIs, e.g. the anterior limb of internal capsule, the values of each diffusion parameter from left and right ROIs were averaged to give a single figure per subject. The mean FA and MD for the whole CC were calculated from the three callosal regions, while the mean FA and MD for the basal ganglia were derived from the caudate, putamen and thalamus. The values of each diffusion parameter of all ROIs located in the supratentorial and infratentorial areas were averaged to provide one value for each subject.
To compare the diffusion parameters between patients and controls the Mann-Whitney U test was used. The relationship between diffusion parameters and EDSS, pyramidal and cerebellar functional scores, and disease duration, was assessed using Spearman's correlation coefficient. SNR for each anatomical region between controls and patients was compared

using the Mann-Whitney U test. Since this was an exploratory study, a multiple comparison adjustment was not performed; the p values indicate differences requiring further, definitive, investigation.

3.1.3. Results

3.1.3.1. Fractional anisotropy

An example of some of the ROIs located in the NAWM and in the NAGM on the FA map is shown in Figure 3.1(B,E). The median values of FA for each NAWM and GM region are summarised in Table 3.1. The ROIs of NAGM and NAWM that show a significant difference in FA between the two groups are illustrated in Figure 3.2.

FA was lower in patients with MS than controls in all the supratentorial NAWM ROIs combined ($p<0.0001$) and in the infratentorial NAWM ($p=0.01$). Interestingly, FA in the cerebral peduncles was lower in patients compared with controls ($p=0.02$). Patients showed lower FA in each callosal region considered separately compared with controls, although the statistical significance was reached only in the splenium ($p<0.01$). When the three callosal regions were combined, FA was significantly lower in patients than controls in the whole CC ($p=0.02$). Considering the GM regions, patients showed higher FA in the basal ganglia than controls ($p=0.002$); the most marked differences were in the putamen ($p=0.002$) and thalamus ($p=0.003$).

3.1.3.2. Correlations between fractional anisotropy and clinical indices

In all patients with MS, FA in the cerebral peduncles correlated with EDSS (r=-0.34, p=0.03) (Figure 3.3,a) and with the pyramidal functional score (r=-0.32, p=0.05). Other regions in the pyramidal tract, including the posterior limb of the internal capsule, did not show a significant correlation with the functional score. FA in the infratentorial NAWM showed an inverse correlation with disease duration (r=-0.39, p=0.01). In the whole MS group, FA in the NAGM did not correlate with cerebellar functional score.

When the MS subgroups were considered separately, patients with RR showed a strong correlation between EDSS and FA in the supratentorial NAWM (r=-0.68, p=0.04) (Figure 3.3,c) and in the infratentorial NAWM (r=-0.81, p=0.008) (Figure 3.3,d). Patients with SPMS showed a correlation between FA in the cerebral peduncles and disease duration (r=-0.75, p=0.008).

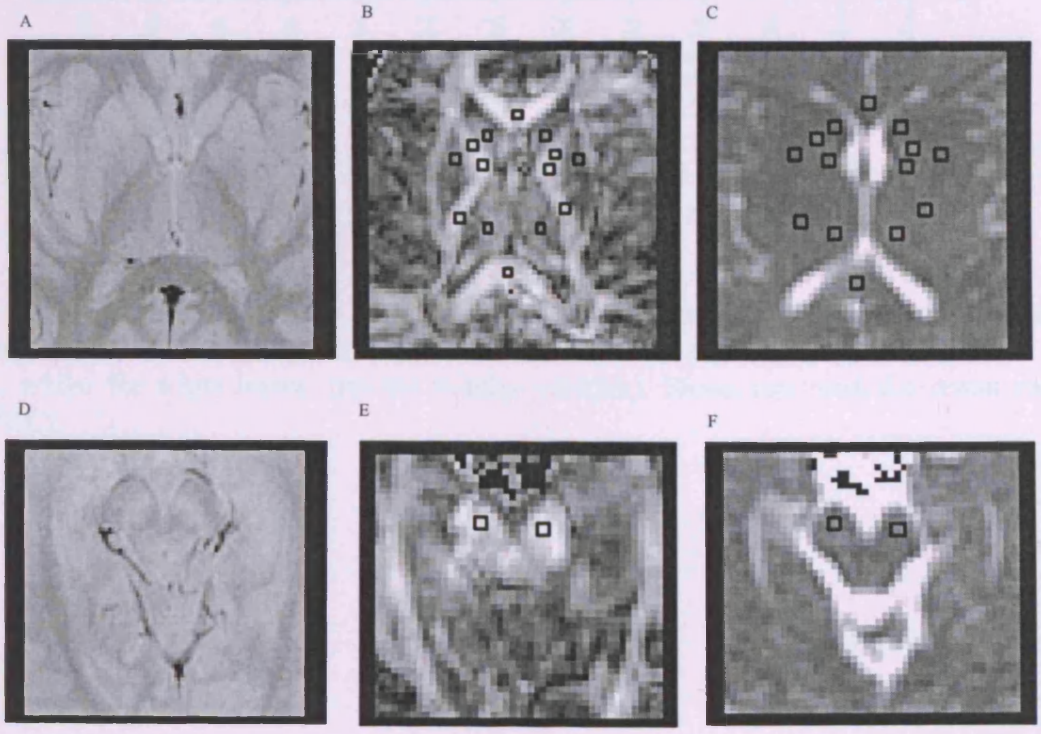

Figure 3.1. (A,D) Proton density-weighted images, (B,E) fractional anisotropy maps, and (C,F) mean diffusivity maps. Regions of interest are placed in the anterior limb, genu, and posterior limb of internal capsule, caudate nucleus, putamen, thalamus, genu and splenium of corpus callosum, and cerebral peduncles.

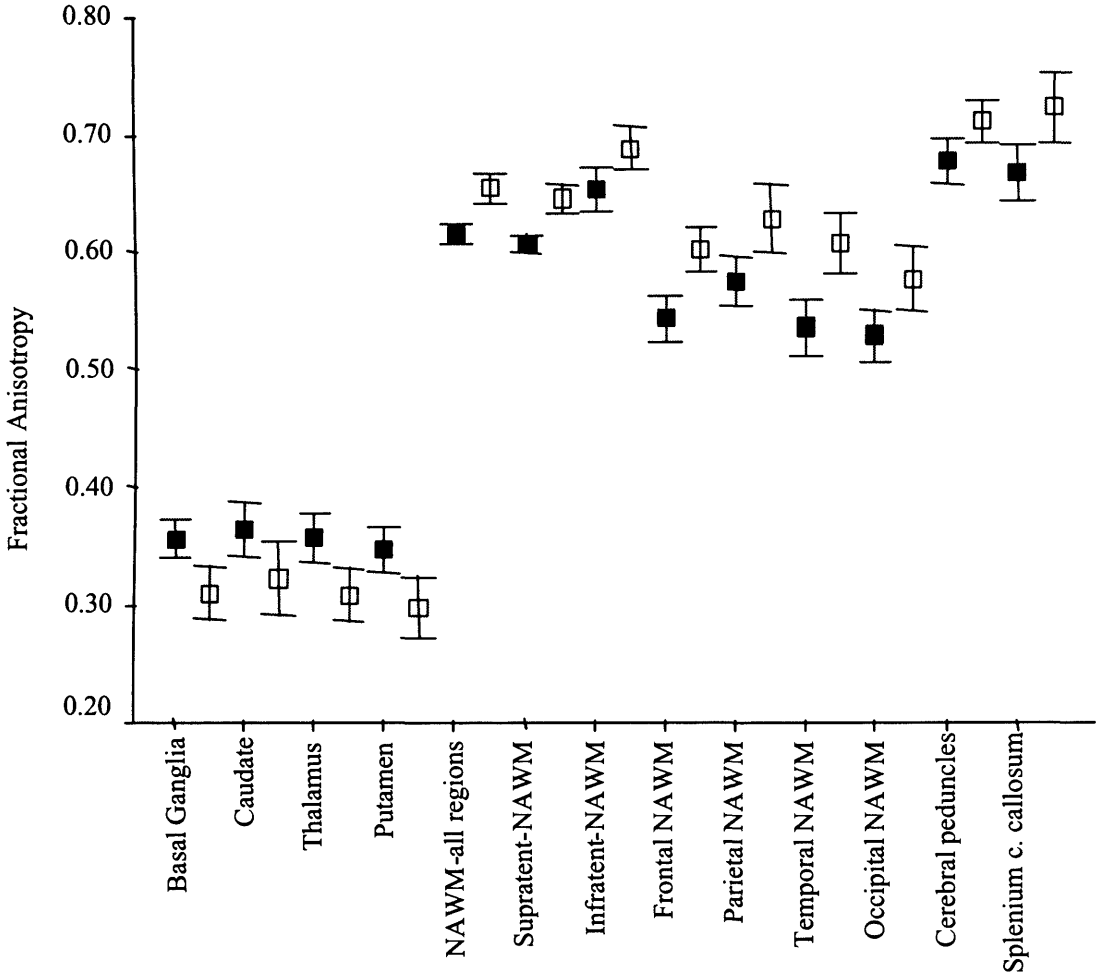

Figure 3.2. Fractional anisotropy in the NAWM regions and basal ganglia that show a significant difference between patients with MS and controls (the black boxes represent MS patients, whilst the white boxes indicate healthy controls). Boxes represent the mean value, bars 95% CI.

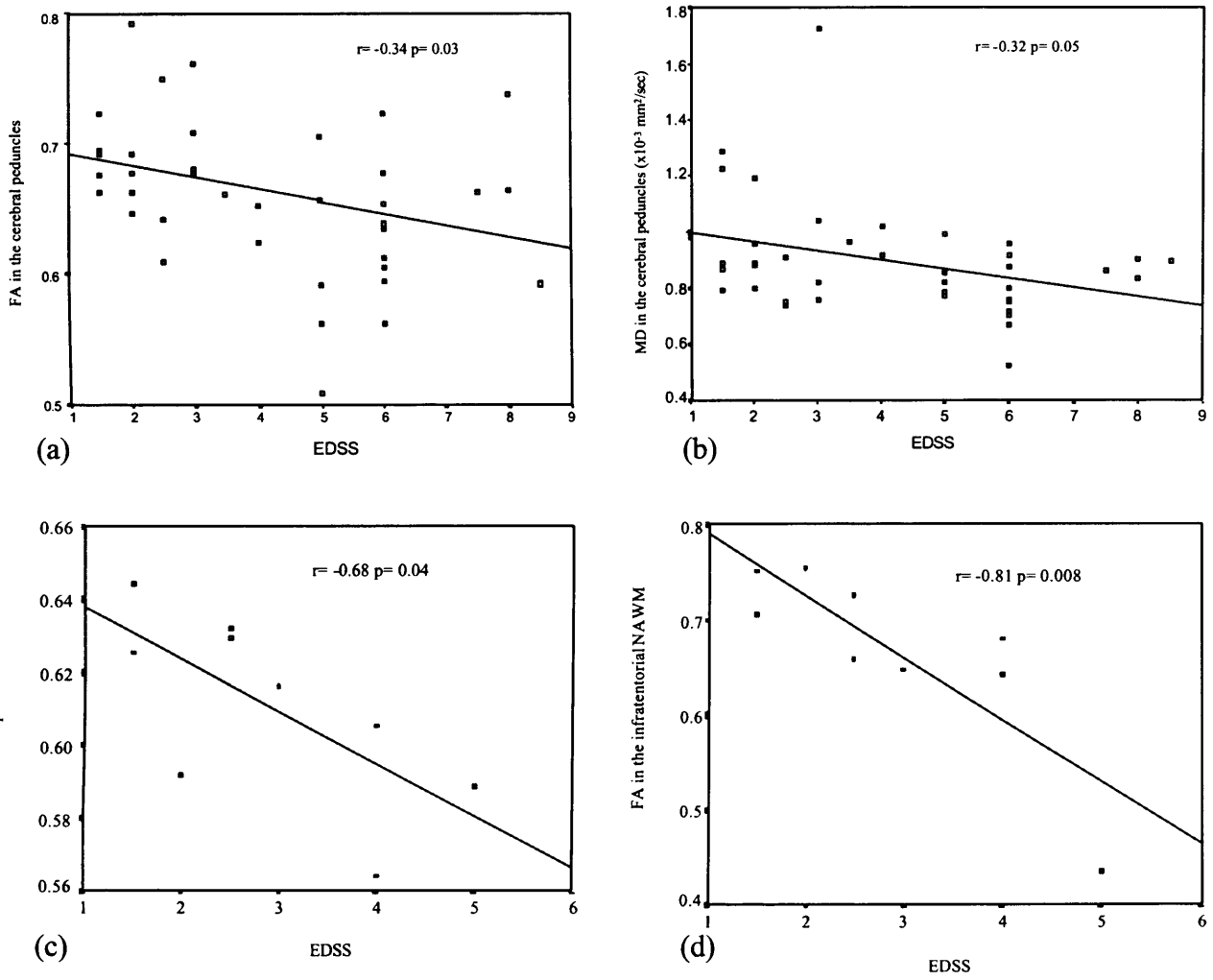

Figure 3.3. Plots of significant correlations between DTI-indices and EDSS. The lines represent the linear regression of the data. (a) FA in the cerebral peduncles versus EDSS in all patients with MS; (b) MD in the cerebral peduncles versus EDSS in all patients with MS; (c) FA in the supratentorial NAWM versus EDSS in patients with RR MS; (d) FA in the infratentorial NAWM versus EDSS in patients with RR MS.

3.1.3.3. Mean diffusivity

An example of some ROIs located in the NAWM and in the NAGM on the MD map is shown in Figure 3.1(C,F). The median values of the MD for each NAWM and GM region are summarised in Table 3.1.

MD in all the NAWM ROIs combined was slightly higher in patients with MS than controls ($p=0.09$) and only the frontal lobes ($p<0.01$) and the splenium of the CC ($p<0.001$) showed a significant difference between the two groups. When the three callosal regions were

combined, MD was significantly higher in patients than controls in the whole CC (p=0.03). Within the GM regions, MD in the putamen was lower in patients than controls (p=0.02).

3.1.3.4. Correlations between mean diffusivity and clinical indices

In all patients with MS, there were inverse correlations between MD in the cerebral peduncles and both EDSS (r=-0.32, p=0.05) (Figure 3.3,b) and pyramidal score (r=-0.36, p=0.02). MD in the other regions of NAWM and NAGM did not correlate with disease duration or cerebellar score. Patients with PPMS showed a strong correlation between disease duration and MD in the infratentorial NAWM (r=-0.86, p=0.006).

3.1.3.5. Correlations between diffusion indices

Although MD and FA in the supratentorial NAWM were correlated in both the control group (r=-0.50, p=0.02) and patient group (r=-0.38 p=0.02), no correlation was found between these two diffusion parameters in the basal ganglia and cerebral peduncles.

3.1.3.5. Clinical subgroups comparisons

No differences in diffusion indices were observed between the MS subgroups, including a comparison of patients with PPMS with all other relapse onset patients.

3.1.3.6. Noise evaluation

Mean SNRs calculated on the b0 images were not significantly different between patients and controls and were as follows: in patients, 39.3 ± 5.7 for all NAWM regions and 40 ± 6.4 in basal ganglia; in controls, 37.3 ± 3.9 for all NAWM regions and 40.7 ± 4.1 in basal ganglia. The SNR for the other anatomical regions studied showed no difference between MS patients and controls.

Table 3.1. Diffusion indices for different sets of ROIs in the NAWM and in the grey matter.

Anatomical regions	**FA controls Median (Range)**	**FA patients Median (Range)**	**MD ($x10^{-3}$ mm^2/sec) controls Median (Range)**	**MD ($x10^{-3}$ mm^2/sec) patients Median (Range)**
NAWM				
Anterior limb of internal capsule	0.64 (0.57-0.70)	0.61* (0.45-0.70)	0.82 (0.71-0.96)	0.79 (0.73-1)
Genu of internal capsule	0.68 (0.61-0.67)	0.67 (0.53-0.75)	0.79 (0.64-0.93)	0.79 (0.67-1)
Posterior limb of internal capsule	0.68 (0.57-0.8)	0.68 (0.57-0.83)	0.77 (0.54-0.9)	0.71 (0.6-0.9)
Frontal lobe	0.59 (0.51-0.66)	0.54**** (0.42-0.68)	0.84 (0.77-0.9)	0.90** (0.72-1.4)
Temporal lobe	0.60 (0.5-0.75)	0.54**** (0.37-0.67)	0.80 (0.71-0.9)	0.83 (0.7-0.99)
Occipital lobe	0.58 (0.46-0.71)	0.53** (0.37-0.72)	0.82 (0.7-0.93)	0.79 (0.62-0.95)
Parietal lobe	0.64 (0.53-0.72)	0.58** (0.41-0.7)	0.82 (0.72-0.97)	0.81 (0.67-0.99)
Genu of corpus callosum	0.77 (0.62-0.88)	0.76 (0.53-0.9)	0.82 (0.64-1)	0.84 (0.63-1.4)
Body of corpus callosum	0.66 (0.49-0.77)	0.63 (0.41-0.75)	0.86 (0.68-1.06)	0.91 (0.7-1.5)
Splenium of corpus callosum	0.73 (0.63-0.89)	0.66** (0.54-0.83)	0.96 (0.75-1.1)	1.1*** (0.76-1.6)
Cerebral peduncle	0.70 (0.64-0.8)	0.68* (0.52-0.81)	0.84 (0.67-0.97)	0.87 (0.53-1.7)

Middle cerebellar peduncle	0.68	0.64	0.87	0.88
	(0.57-0.73)	(0.34-0.76)	(0.6-1)	(0.74-1.2)
Supratentorial NAWM regions	0.65	0.60****	0.81	0.82
	(0.6-0.68)	(0.56-0.64)	(0.76-0.9)	(0.75-0.98)
Infratentorial NAWM regions	0.69	0.66*	0.86	0.88
	(0.62-0.76)	(0.43-0.75)	(0.71-0.97)	(0.75-1.3)
Whole corpus callosum	0.71	0.68*	0.88	0.92*
(genu, body and splenium)	(0.66-0.81)	(0.54-0.78)	(0.80-0.98)	(0.79-1.3)
All NAWM regions	0.65	0.62****	0.82	0.84
	(0.61-0.69)	(0.56-0.66)	(0.77-0.91)	(0.78-0.98)
Grey matter				
Caudate nucleus (head)	0.32	0.36*	0.83	0.83
	(0.20-0.44)	(0.23-0.53)	(0.83-1.1)	(0.65-0.98)
Putamen	0.29	0.35**	0.79	0.75*
	(0.21-0.43)	(0.18-0.51)	(0.65-1)	(0.66-0.88)
Thalamus (pulvinar)	0.29	0.36**	0.84	0.82
	(0.24-0.40)	(0.21-0.51)	(0.72-1)	(0.62-0.99)
Hippocampus	0.29	0.29	0.94	0.95
	(0.21-0.44)	(0.16-0.49)	(0.72-1.1)	(0.65-1.4)
Cerebellar grey matter	0.24	0.28	0.85	0.90
	(0.16-0.35)	(0.14-0.44)	(0.75-1.1)	(0.71-1.3)
All basal ganglia regions	0.31	0.35**	0.82	0.80
	(0.24-0.42)	(0.24-0.46)	(0.7-1)	(0.66-0.92)

*Significantly different from controls at Mann-Whitney U test ($p< 0.05$), ** Significantly different from controls at Mann-Whitney U test ($p<0.01$), *** Significantly different from controls at Mann-Whitney U test ($p<0.001$), **** Significantly different from controls at Mann-Whitney U test ($p<0.0001$)

3.1.4. Discussion

DTI provides information to quantify the magnitude and the anisotropy of the diffusion of water molecules *in vivo* (Basser and Pierpaoli 1996;Pierpaoli et al. 1996) and to investigate the pathological changes occurring in the brain of patients with MS (Bammer et al. 2000;Filippi et al. 2001b;Werring et al. 1999). In particular, the assessment of the anisotropy indices allows *in vivo* assessment of the structural integrity and directional

coherence of fibre tracts in the NAWM (Pierpaoli and Basser 1996). The present study indicates that the CC, cerebral peduncles and internal capsule are the regions with the highest degree of anisotropy, suggesting that they are characterised by an ordered and parallel arrangement of fibres (Peled et al. 1998;Virta et al. 1999). The cerebellar grey matter and the basal ganglia also appear to show some degree of anisotropy (Wiegell et al. 2003) that may in part be explained by the origin or termination of myelinated fibre tracts, or by intrinsic neuronal connections.

Firstly, we shall discuss the changes in diffusion parameters in NAWM and grey matter in patients with MS, and secondly, their relationships with clinical disability and disease duration.

3.1.4.1. Changes in diffusion indices in normal-appearing brain

We found that anisotropy was significantly lower in the NAWM of patients with MS compared to the white matter of controls, confirming other studies (Bammer et al. 2000;Cercignani et al. 2001b;Filippi et al. 2001b;Henry et al. 2003;Rashid W. et al. 2004;Werring et al. 1999). The reduction of anisotropy was apparent in almost all areas of NAWM studied, both supratentorially and infratentorially. These differences in FA between patients and controls appeared to be genuine and not affected by noise contamination, because the SNR of corresponding ROIs was not significantly different. In contrast to previous reports (Bammer et al. 2000;Cercignani et al. 2000;Filippi et al. 2000b;Filippi et al. 2001b;Rovaris et al. 2002b;Werring et al. 1999), however, MD was not significantly higher when all the NAWM regions in the MS group were combined, although it was significantly increased in the frontal lobes and in the splenium of the CC. The CC is known to be affected by pathological changes at the earliest stage of MS, as confirmed by a recent

work which reported increased MD, decreased MTR, and reduced NAA/Cho ratio in the CC of patients with a clinically isolated syndrome suggestive of MS (Ranjeva et al. 2003). The reason why the differences in FA and MD in the CC between patients and controls in our study reached statistical significance only in the splenium is not clear, but it could be related to the differences in fibre composition of the CC (Aboitiz et al. 1992). Indeed, thin fibres (smaller than 2 μm diameter) are most dense in the splenium, and smaller axons seem to be preferentially susceptible to injury in MS (Evangelou et al. 2001).

By considering the findings from previous pathological studies (Allen and McKeown 1979;Evangelou et al. 2000a;Kornek and Lassmann 2003;Kuhlmann et al. 2002;Peterson et al. 2001), an attempt can be made to interpret these changes in diffusion indices in the MS NAWM. The NAWM is affected by several pathological processes: 1) Oedema associated with inflammation, which could increase the diffusivity; 2) Axonal loss that may result in an expanded extracellular space which increases diffusivity, but which also reduces the directionality (anisotropy) of water molecules (Barnes et al. 1991;Bitsch et al. 2000); 3) Gliosis, a disorganized and dense pathological process, which could reduce both anisotropy and diffusivity (Petzold et al. 2002). The overall pattern of reduced FA and preserved MD could therefore represent a combination of axonal loss (which reduces FA and increases MD), and gliosis (which reduces both FA and MD). This pattern detected in the cerebral peduncles is similar to that reported in the cortico-spinal tract distal to cerebral infarction using DTI (Werring et al. 2000c), and may be due to Wallerian degeneration from lesions in connected brain regions (Simon et al. 2000;Werring et al. 2000a).

The lack of a significant overall increase in MD in all NAWM regions could also be explained by a population with less disease activity than those reported by others (Cercignani et al. 2001b;Filippi et al. 2001b;Rocca et al. 2003b;Rovaris et al. 2002b), and also with less lesion activity, the presence of which has been associated with increased diffusion in remote

NAWM (Werring et al. 2000a), possibly due to subtle oedema and inflammation (Moreau et al. 1996). Furthermore, the present cohort has a longer disease duration than that investigated previously, and thus may be associated with more gliosis in the NAWM per se. Alternatively, the approach used in the current study might underestimate subtle differences between the two groups, because, unlike previous studies (Bammer et al. 2000;Cercignani et al. 2000;Filippi et al. 2000b;Werring et al. 1999), the values of diffusion parameters obtained within individuals ROIs were not considered as independent observations. Rather, the data from all ROIs in the same subject were pooled into one mean observation.

Our analysis included also the basal ganglia and the cerebellar grey matter, but not the cerebral cortex, because the latter appeared significantly affected by the partial volume of CSF in the cortical sulci, which might easily contaminate diffusion measurements. There was a trend towards a lower MD in the basal ganglia of MS patients, which was statistically significant only in the putamen. The basal ganglia are important components of cortico-subcortical circuits, including the motor circuit that links the supplementary motor area, premotor and sensorimotor cortex to the putamen, which then projects to the thalamus and back to the cortex (Alexander et al. 1990). Previous PET studies (Bakshi et al. 1998;Blinkenberg et al. 2000;Paulesu et al. 1996;Roelcke et al. 1997) investigating regional glucose metabolism, have reported hypometabolism in the basal ganglia, suggesting that damage to the connection fibres can cause a remote functional metabolic effect on subcortical nuclei (diaschisis). This disturbance of metabolism may cause restricted diffusion, as has been reported in experimental studies status epilepticus (Fabene et al. 2003).These studies raised the possibility that damage of the neural connections in MS could induce a metabolic dysfunction in the basal ganglia that slightly decreases the MD.

More impressively, the FA in all the basal ganglia nuclei examined was significantly higher in MS patients than controls. The basal ganglia nuclei are connected to each other by intrinsic

connections (Alexander et al. 1990), which show anisotropy. If the white matter fibres that connect cortical areas with the basal ganglia are selectively affected by Wallerian degeneration or by neuronal dysfunction (diaschisis), the intact intrinsic connections could show an increase in their coherence. This underlying structure may in effect be "unmasked" by damage to cortico-subcortical projections. A recent spectroscopy study reported a trend toward a relationship between thalamic NAA/Cr ratio and NAA/Cr ratio in the frontal NAWM, suggesting that axonal loss in the distant white matter regions relates to thalamic neuronal injury (Wylezinska et al. 2003). T2 hypointensity in the basal ganglia (possibly due to local iron deposition) has been shown to be a stronger predictor of disability and clinical course of MS, and was associated with higher T2 lesion load (Bakshi et al. 2002). Although local iron deposition could in theory increase field disturbance and as a consequence affect the anisotropy values, we do not think this can explain the difference observed in anisotropy as no difference in SNR of basal ganglia ROIs was found between patients and controls. The observation that anisotropy and diffusivity did not correlate with one another in the basal ganglia suggests that in these regions they may be sensitive to different pathological aspects of the disease.

The findings of increased FA in the basal ganglia and a trend towards a reduced MD in the putamen are not in agreement with data published by other authors (Fabiano et al. 2003;Filippi et al. 2001a). However, any comparison between studies has to be treated cautiously, since the clinical characteristics of the cohorts are different. On the available evidence, changes in anisotropy in the thalamus and putamen may be more prominent than changes in diffusivity.

3.1.4.2. Clinical correlations

DTI detects clinically relevant changes in the normal appearing brain tissue, confirming findings of other MR techniques (Chard et al. 2002a;De Stefano et al. 1998;De Stefano et al. 2001;Filippi et al. 1995;Fu et al. 1998;Traboulsee et al. 2003). In the present study, when the MS subgroups were considered separately, three strong correlations were observed: 1) between EDSS and FA in both the supratentorial and infratentorial NAWM in patients with RRMS; 2) between disease duration and FA in the cerebral peduncles in patients with SPMS; 3) between disease duration and MD in the infratentorial NAWM in patients with PPMS. Moreover, if all patients were combined, both FA and MD in the cerebral peduncles inversely correlated with EDSS and pyramidal functional score, albeit modestly.

Overall, these clinical correlations suggest that the pathological damage detected on DTI in NAWM regions, including the pyramidal tract, is a significant factor contributing to disability and progression in MS.

3.2. Investigation of the mechanisms of NAWM damage: evidence of Wallerian degeneration

3.2.1. Introduction

In the previous study we reported decreased FA and a trend toward increased MD in the NAWM in patients with MS. These diffusion changes could reflect axonal loss with associated expanded extracellular space, which may result in a pattern of increased diffusivity and reduced anisotropy. As discussed earlier, this explanation is supported by post-mortem findings of a substantial loss of axons in the NAWM (Evangelou et al. 2000a).

Of the different pathogenetic mechanisms that could cause a decrease in axonal density in the NAWM, Wallerian degeneration of axons transected by MS lesions may play an important role (Ferguson et al. 1997;Trapp et al. 1998). To date, only limited *in vivo* evidence of this

potential mechanism has been reported (Bjartmar et al. 2001;De Stefano et al. 1999;Simon et al. 2000;Werring et al. 2000a).

Thus, a key question is the extent to which NAWM pathology depends on the severity of focal lesion damage in MS. DTI has the potential to answer this question by virtue of its sensitivity to fibre degeneration (Henry et al. 2003;Pierpaoli et al. 2001;Werring et al. 2000c). By examining DTI indices in the CC, in which there is a topographic and homologous arrangement of inter-hemispheric projections (Crosby E.C. et al. 1962), it is possible to test whether lesion extent in individual lobes correlates with diffusion indices in connected callosal regions.

We therefore used whole-brain DTI to investigate *in vivo* the relationship between changes in the MD and FA in the normal-appearing CC with the lesion loads in connected cerebral lobes in the same 39 patients with MS that we studied in the previous study.

3.2.2. Methods

3.2.2.1. Patients

The characteristics of these patients are described above (paragraph 3.2.1.1)

3.2.2.2. MRI protocol

The MRI protocol is described above (paragraph 3.2.1.2).

3.2.2.3. Lesion load calculation

Lesions were identified by a single observer (O.C.) blinded to the clinical details and classified according to their location. Lesions were then quantified on the axial b0 images (with reference to the conventional PD WI) using a semi-automated local thresholding technique (Plummer 1992). The intra-observer coefficient of variation was less than 5%. The lesion loads in each cerebral lobe and in the whole supratentorial brain were calculated on b0 images for each patient. Lesions of area <20 mm^2 or in proximity to CSF were excluded to eliminate partial volume artefact.

3.2.2.4. Statistical analysis

The relationship between diffusion parameters and lesion load was assessed using Spearman's correlation coefficient (one-tailed).

3.2.3. Results

The median lesion load in the whole supratentorial brain was 11.58 cm^3 (range: 1.04-52.63); the largest lesion load was detected in the parietal lobes (median: 3.19 cm^3; range: 0.16-17.82), followed by the frontal (median: 2.76 cm^3; range: 0.14-17.26) and occipital lobes (median: 1.14 cm^3; range: 0.0-19.92); the lowest lesion load was found in the temporal lobes (median: 0.69 cm^3; range: 0.0-10.77).

Correlations between the lesion load in each cerebral lobe and the callosal regions are reported in Table 3.2. The strongest correlations were found between FA and MD in the body of the CC and lesion loads in all cerebral regions, in particular the parietal lobes. As might be expected from the callosal anatomy, frontal lesion load correlated with FA and MD in the genu and occipital lesion load correlated with FA and showed a trend with MD in the

splenium. Frontal lesion load also correlated with MD in the splenium, whilst occipital lesion load correlated with MD in the genu. When the total brain lesion load and the whole CC were included in the analysis, there was a significant correlation between total lesion load and both FA (r= -0.56, p<0.0001) and MD (r= 0.54, p<0.0001) of the whole CC (Figure 3.4).

Table 3.2. Relationship between lesion load in each cerebral lobe and diffusion indices in the callosal regions.

	Frontal lesion load	Parietal lesion load	Occipital lesion load
FA genu	r= -0.31, =0.027	r=-0.38, p=0.009	r=-0.27, p=0.05
MD genu	r=0.39, p=0.007	r=0.42, p=0.004	r=0.32, p=0.02
FA body	r=-0.54, p<0.0001	r=-0.62, p<0.0001	r=-0.5, p<0.001
MD body	r=0.52, p<0.0001	r=0.56, p<0.0001	r=0.42, p=0.004
FA splenium	r=-0.19, p=0.13	r=-0.19, p=0.12	r=-0.28, p=0.04
MD splenium	r=0.28, p=0.04	r=0.18, p=0.14	r=0.25, p=0.06

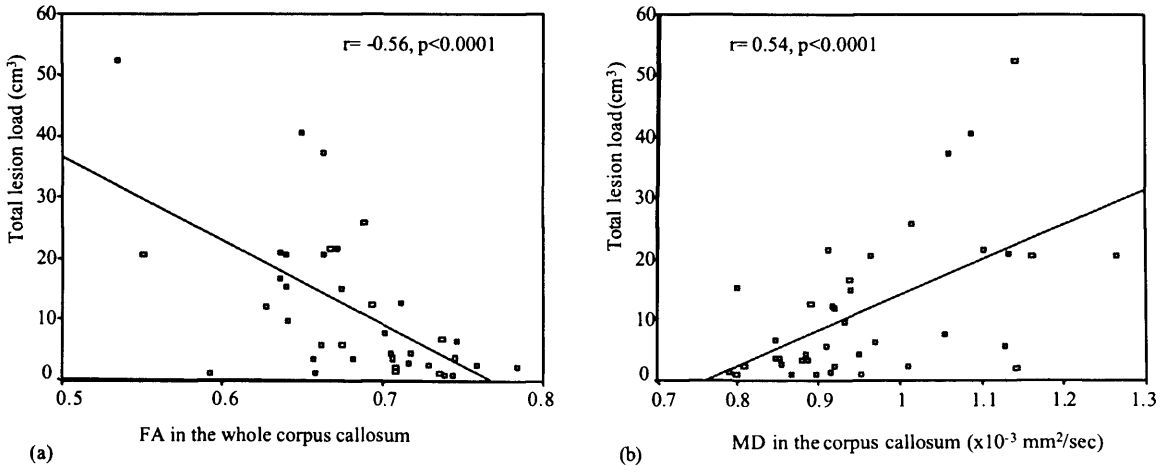

Figure 3.4. Plots of significant correlations between total lesion load and (a) fractional anisotropy and (b) mean diffusivity in the whole corpus callosum. The lines represent the linear regression of the data.

3.2.4. Discussion

3.2.4.1. Mechanisms of NAWM damage

We assessed to what extent NAWM pathology depends on focal lesions in MS, by investigating the relationship between the diffusion changes in the CC and lesion volume in connected cerebral areas. The reduced FA in the CC, which was discussed in the first study reported in this chapter, could reflect Wallerian degeneration of axons transected in remote MS lesions (Bitsch et al. 2000;Ferguson et al. 1997;Kornek et al. 2000;Trapp et al. 1998). Our findings of significant correlations between the damage in the CC and the lesion loads in connected regions support this hypothesis. Additionally, a post-mortem study has shown an inverse correlation between the regional lesion load and the total number of axons crossing the corresponding projection areas in the CC (Evangelou et al. 2000b). However, only limited data has been provided so far to confirm *in vivo* that the damage to axons traversing inflammatory lesions may be transmitted over long distances in the connected NAWM in patients with MS (Bjartmar et al. 2001;De Stefano et al. 1999;Narayana et al. 1998;Werring et al. 2000a).

The strong correlations found between the diffusion changes in the genu, body and splenium of CC with the lesion load in the cerebral lobes most strongly connected to those regions (frontal, parietal and occipital lobes respectively) might therefore be explained by considering the anatomy of the most of the callosal fibres, which interconnect with corresponding areas of both hemispheres (Crosby E.C. et al. 1962). The correlations between diffusion indices in the genu with the occipital lesion load, and those in the splenium with the frontal lesion load, could alternatively result from a minor contingent of callosal fibres terminating in areas of the controlateral hemisphere not homologous with their origin (Crosby E.C. et al. 1962). The strongest relationship between the cerebral lesion loads and diffusion indices in the body of the CC might be explained by a substantial number of fibres originating in the frontal and occipital lobes traversing the body of the CC (Barbas and Pandya 1984;Seltzer and Pandya 1983).

These findings, together with the correlations between MD in the whole CC and the total lesion volume, could however reflect other pathogenetic mechanisms than fibre degeneration. NAWM damage is known to involve more complex processes than simply axonal degeneration, including inflammation and astrogliosis (Allen and McKeown 1979;Kornek and Lassmann 2003). The relationship between these pathological abnormalities, i.e. inflammation, demyelination, axonal damage and gliosis, is intricate. Acute axonal damage is secondary to axon transection in the setting of inflammatory demyelination (Bitsch et al. 2000;Kuhlmann et al. 2002), while progressive axonal degeneration may be related to lack of trophic support from oligodendroglia and myelin (Kornek et al. 2000). Mice lacking proteolipid protein (PLP) (a myelin related protein) developed axonal loss and consequent progressive clinical disability, confirming that chronically demyelinated axons may undergo degeneration due to lack of trophic support from myelin and myelin forming cells (Griffiths et al. 1998). Moreover, it has been proposed that abnormal expression of sodium channel subtypes, occurring in response to demyelination, may render axons vulnerable to degeneration, conforming with the theory that MS may involve an acquired channelopathy (Waxman 2001). A spectroscopy investigation found a strong correlation between the concentration of NAA (a marker of axonal loss) within the spectroscopic volume and the total lesion load in the whole brain (Narayana et al. 1998), suggesting that an increased lesion burden anywhere in the brain is associated with the extent of axonal injury.

Recent evidence has suggested that besides axonal damage, the glial response may be clinically relevant in MS (at least in the progressive phase) (Petzold et al. 2002), and seems to precede secondary axonal degeneration (Griffiths et al. 1998). A spectroscopy study reported a significant correlation between T2 lesion load and the myo-inositol concentration in the NAWM, suggesting that focal inflammatory activity is related to a widespread glial proliferation in the NAWM (Chard et al. 2002a).

Moreover, MD and FA findings may simply reflect the relationship between the overall extent of pathology in lesions and NAWM, rather than implying a specific mechanism of NAWM abnormalities. Indeed, a strong correlation between overall mean lesion MD and mean NAWM MD (without specific anatomically-based correlations) has been reported (Werring et al. 2001). A recent study (Parry et al. 2002) investigating the relationship between T1 values (as marker of pathology) in the NAWM and lesions, found that the mean T1 value in the T1 hypointense lesions correlated strongly with the mean T1 value in the NAWM, suggesting that changes in the NAWM occur in parallel with pathology in lesions. Taking into account these findings, the correlations between the callosal regions and the lesion loads may simply indicate that the pathological mechanisms are widespread and interrelated throughout the brain.

3.2.4.2. Technical issues

Since the lesion load was calculated on non-diffusion weighted b0 images, which are characterised by a lower resolution than conventional T2-WI, the visualisation of small lesions or lesions located in the brain regions affected by geometric distortion could have been impaired (Wolansky et al. 2000). This could potentially reduce the total lesion load in each cerebral lobe, or cause the preferential detection of lesions with the most pathological damage. Furthermore, a small number of lesions located within the callosal regions were not well visualised and were thus excluded from the analysis. However, the lesions in the CC were detected on the axial images, since the sagittal slices were not acquired in this study, and it could have contributed to a definition of a small number of lesions.

3.3. Conclusion

DTI is sensitive to microstructural damage in the NAWM and in the NAGM. In particular, FA appears sensitive to the NAWM damage that is associated with disability and progression in MS. Correlations of DTI indices (particularly anisotropy) with lesion extent in connected brain regions support the hypothesis that Wallerian degeneration of axons transected by remote, but connected focal lesions, is an important pathogenetic mechanism of NAWM damage in MS.

One possible technical limitation of the two studies presented in this chapter is that the analysis was based on region of interest approach, which is highly dependent on the observer and on the region chosen. In the next chapter, we extend the investigation from a region of interest of a few voxels to the whole white matter tract, using the novel technique of diffusion based tractography. Tract mapping using tractography has been reported to improve correlations with disability by matching selected tracts with specific clinical scoring system (Wilson et al. 2003).

Chapter 4

Tracing white-matter pathways in the human brain with diffusion based tractography

In the previous chapter we investigated brain damage in MS using a region of interest approach, which consists of obtaining information about the diffusion indices in a few voxels located in specific areas of the brain. To gain a better understanding of white matter pathology, it would be more useful, instead, to obtain information about the entire length of the white matter pathways. This is possible *in vivo* using the novel technique of diffusion based tractography, which is described in chapter 2.

This chapter deals with the developments and applications of tractography, which are described in three studies. The first study describes a method for assessing the reproducibility of fast marching tractography (FMT) in tracing and quantifying the white matter pathways. The second study reports a preliminary methodology that allowed us to combine white matter tractography results from different individuals in order to create group maps of the major white matter tracts. The third study describes the first application of this methodology in a small group of patients one year after unilateral optic neuritis, in order to assess pathological changes in the optic radiations.

4.1. From diffusion tractography to quantitative white matter tract measures: a reproducibility study

4.1.1. Introduction

DTI has been used to study brain pathological changes occurring in MS (Horsfield et al. 1998;Tievsky et al. 1999;Werring et al. 1999), tumours (Bastin et al. 1999;Behrens et al. 2003a;Inglis et al. 1999;Wieshmann et al. 1999b), amyotrophic lateral sclerosis (Ellis et al. 1999), cerebral ischaemia (Chabriat et al. 1999;Jones et al. 1999b;Sorensen et al. 1999) and developmental malformations of the cortex (Eriksson et al. 2001). Since DTI is able to

detect, at the macroscopic scale of a voxel, the extent of directional bias of diffusion occurring at the microscopic level, it can distinguish between regions where fibres are highly aligned in the voxel from those where fibres are less coherent. However, although DTI provides directional information at the voxel level, it provides no explicit information about the connection between neighbouring voxels. A number of different tractography methods, which use the information provided by the diffusion tensor concerning the orientation of fibres within a voxel, have recently been developed in order to determine the pathways of cerebral connections *in vivo* (see chapter 2) (Basser et al. 2000;Behrens et al. 2003b;Conturo et al. 1999;Gossl et al. 2002;Jones et al. 1999c;Mori et al. 1999;Mori et al. 2000;Poupon et al. 2000;Stieltjes et al. 2001;Xue et al. 1999).(Tzourio-Mazoyer et al. 2002) The possibility of a non-invasive assessment of anatomical connectivity[1] has important clinical implications and may increase our understanding of neurological diseases and psychiatric conditions, in which connections between brain regions are known to be disrupted (Mori et al. 2002;Steel et al. 2001).

Fast marching tractography (FMT) (Parker et al. 2002c;Parker et al. 2002a) is a recently developed method that is able to detect connection pathways in the human brain. It has been validated, in part, by the results of tracking obtained in macaque brains (Parker et al. 2002a) and by comparison with standard atlases (Parker et al. 2002c). This tractography technique has the advantages that branching tracts can be traced, allowing reconstruction of the whole pathway, and providing quantification of white matter tracts via the generation of connectivity maps.

One of the ultimate goals for all tractography techniques is to define quantitative and reproducible parameters for measuring anatomical connectivity. As a first step toward this,

[1] We use the term 'connectivity' in this section as indicating bulk inter-regional anatomical connectivity that may be derived from Fast Marching Tractography. Whilst this does not permit an analysis of point-to-point connectivity it does shed light upon macroscopic routes of white matter fibre bundles. We do not use the terms in a functional context, either at the interaxonal or at the interregional level.

our study aimed to develop an *in vivo* method to assess the reliability of tractography by using two different quantitative measurements along the tracts generated by FMT: FA (Pierpaoli and Basser 1996) and "normalised" volume of the estimated tracts. Further, a new DTI sequence, which allows acquisition of images with small voxel size (1.8x1.8x2.5 mm) was performed. This initial investigation is focused on three major pathways: the anterior callosal fibres, the optic radiations and the pyramidal tracts. The selection of these pathways provide a number of advantages: 1) They show different fibre organisation, which allows the testing of FMT reproducibility under different conditions; 2) They have well-known anatomy, thus making the assessment of identified connections possible; 3) They are large, which makes the identification of connectivity more convenient than other fibre tracts of finer or more intricate structure; 4) They are clinically-relevant pathways in many neurological conditions, such as MS and stroke.

4.1.2. Methods

4.1.2.1. Subjects

Eleven healthy subjects were studied (8 female and 3 male). The mean age was 37.5 ± 9.7 years.

4.1.2.2. MRI protocol

All scans were performed on a 1.5-T Signa Echospeed MRI system (GE Medical Systems, Milwaukee, WI). All subjects had a conventional SE set of images acquired prior to DTI,

providing PD and T2-WI [TR 2000, TE 30/120ms, FOV 240 mm, matrix 256 × 256; 28 contiguous axial slices; 5 mm slice thickness].

The diffusion protocol consisted of a single-shot DW-EPI sequence. The diffusion acquisition parameters were: TE 95 ms; acquisition matrix 96 × 96 reconstructed as 128 × 128; FOV 240 mm; 3 $b \approx 0$ smm^{-2} images; 60 diffusion weighted images, with diffusion gradients applied along 60 optimised diffusion directions , diffusion times of δ = 32ms and Δ = 40ms, and max gradient amplitude of 22 10^{-3} T m^{-1}, giving a maximum b-factor b = 1000 smm^{-2} (Jones et al. 1999a); 42 contiguous axial slices; 2.5 mm slice thickness; diffusion data acquisition time = 20-30 minutes, dependent upon heart rate. Cardiac gating was used to reduce motion artefacts due to pulsation of blood and CSF. Correction of eddy-current distortions in DW-EPI was performed using a two-dimensional image registration technique (Symms et al. 1997), which also minimised the effect of any slight head motion during acquisition. The data were then processed to determine the diffusion tensor on a pixel-by-pixel basis (Basser et al. 1994). FA, eigenvector and eigenvalue maps were calculated (Basser and Pierpaoli 1996;Pierpaoli and Basser 1996). The information contained in these maps was then used by FMT to obtain Voxel Scale Connectivity (VSC) maps, which give an estimate of the connectivity between brain regions.

4.1.2.3. Data analysis

The FMT algorithm (Parker et al. 2002c;Parker et al. 2002a) was used to trace anterior callosal fibres, optic radiations and pyramidal tracts.

4.1.2.3.1. *Starting voxel definition criteria*

Single voxels were used as starting points for the FMT method on the FA maps, using the following anatomical guidelines:

1. Anterior callosal fibres:

- We first selected the lowest axial slice where both the genu and the splenium of CC were fully visible.
- We then selected a voxel on the midline in the anterior part of the genu, with its associated principal eigenvector, when projected onto the axial plane, orientated left-right. In particular, on the axial slice, a voxel in the first or second row from the anterior edge that did not show apparent partial volume effects, was chosen (Figure 4.1).

2. Optic radiation:

- We selected the axial slice where the transition from the posterior limb of the internal capsule to the cerebral peduncle was visible.
- A voxel close to the lateral geniculate nucleus and within the optic radiation at the apex of the arc around the lateral ventricle, with the main eigenvector in an anterior-medial to posterior-lateral orientation in axial projection was then chosen (Figure 4.1).

3. Pyramidal tract:

- We selected the first axial slice below the most inferior slice where both optic tracts are fully visible.
- A voxel in the middle third of the cerebral peduncle with the projection of the principal eigenvector onto the coronal plane oriented inferior-medial to superior-lateral was chosen. In particular, on the axial slice the most external voxel in this region was selected (Figure 4.1).

All starting voxels used had an FA value > 0.5, meaning that there was a high degree of directional coherence, and therefore implying that they were located within white matter tissue. In the selection of the starting points, particular care was taken regarding possible partial volume contamination. Placement was also checked with visual reference to the corresponding slices of the PD and T2-WI.

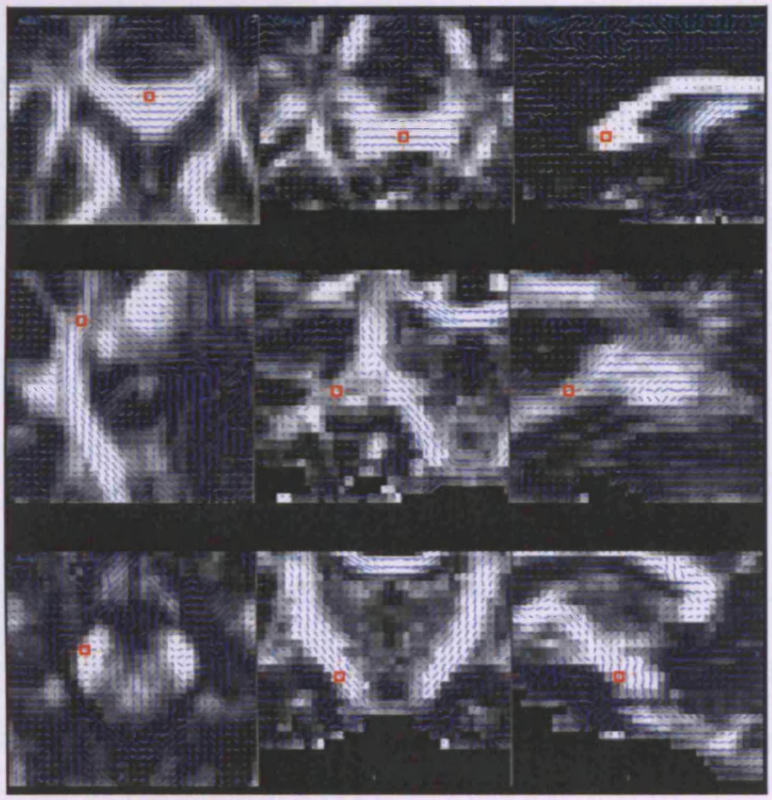

Figure 4.1. Principal eigenvector maps overlaid onto FA maps in one subject. The starting points are shown in the anterior genu of the corpus callosum (top row), in the optic radiations (middle row), and in the pyramidal tracts (bottom row) on axial, coronal and sagittal slices.

4.1.2.3.2. *Calculation of Voxel Scale Connectivity maps*

We subsequently applied the FMT method to estimate the connectivity between each starting point and other brain regions (Parker et al. 2002c;Parker et al. 2002a), and obtain Voxel Scale Connectivity (VSC) maps, that rank possible routes of connection through the dataset by assessing how well they match the directional information provided by the principal eigenvector of diffusion at each voxel (see chapter 2 for details).

To speed up the FMT analysis, a restricted brain volume was used which was defined depending on the expected white matter pathway locations. For the analysis of the pyramidal tract, the hemisphere of interest was included, and the inferior extent of the volume of interest was restricted to two slices below the slice containing the starting point. For the optic radiation, the analysis was again restricted to the hemisphere of interest and limited to the region posterior to the third ventricle. For tracing the callosal fibres, both hemispheres anterior to the central sulci were selected. All studies were performed with a threshold of FA>0.1, to ensure that the paths detected would not erroneously enter areas of cerebrospinal fluid while retaining all the other tissues of potential clinical interest, although this choice may have the possible inconvenience of extending the tracts into grey matter regions.

4.1.2.3.3. *Tract regions of interest: quantitative measurements*

For each FMT experiment, a histogram of the VSC map was obtained, and a threshold which defined voxels with the highest VSC to the start point was identified (Figure 4.2). It is important to note that this thresholding technique was objective and determined *a priori*. Every histogram possessed a significant peak that contained the greatest number of voxels with the highest connectivity values. The threshold for each histogram was defined by selecting the connectivity value that isolated this peak. The connectivity threshold varied between subjects, but was specific to each VSC map (see figure caption).

The connectivity threshold was applied to the VSC maps to define ROIs identifying the areas of highest connectivity. These ROIs were then overlaid on the FA maps and they were interpreted as regions defining the white matter pathways connected to the start point. From these ROIs two parameters were calculated: 1) the mean FA; 2) the total tract volume. The MD was not computed for two reasons: i) to reduce the number of correlations tested and

therefore, type I error; ii) in the previous studies FA was found to be more sensitive to the white-matter damage than MD.

Since the size of the brain differs between subjects, the "normalised" volume (NV) of the tract was calculated by dividing the total tract volume by total intracranial volume (TIV), calculated as follows: the T2-WI were automatically segmented using SPM99 [Wellcome Department of Cognitive Neurology, Institute of Neurology, London, UK] (Ashburner and Friston 1997) into grey matter (GM), white matter (WM) and CSF and other tissue (not further subclassified), and mask images corresponding to each class were generated; the spinal cord cut-off location was defined as the most rostral slice not containing cerebellum and was determined manually; in-house software was then used to calculate tissue volume from the segmented images rostral to the spinal cord cut-off level; the TIV was determined by adding the GM, WM, and CSF volumes (Chard et al. 2002b).

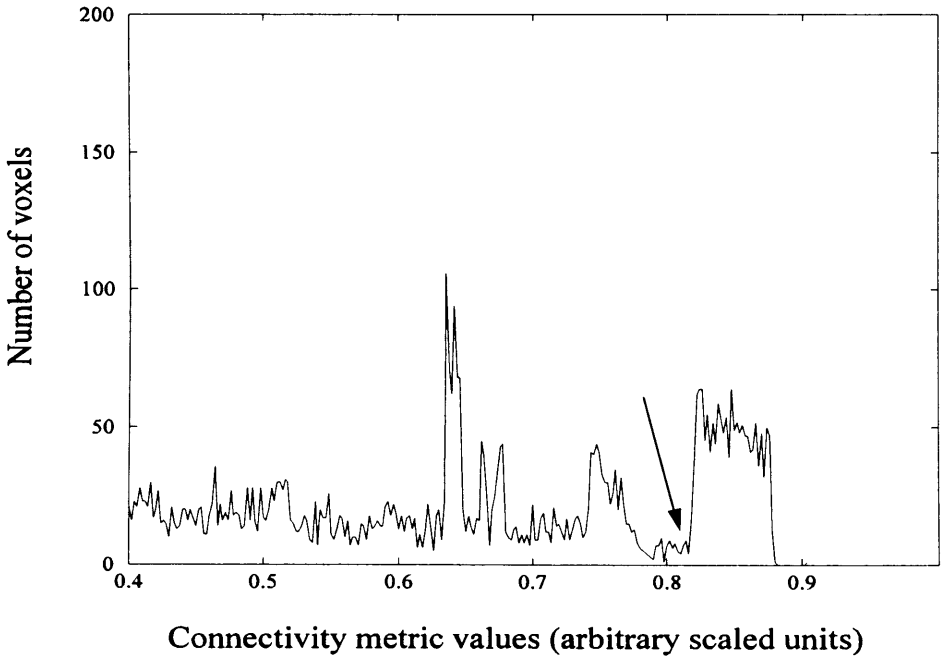

Figure 4.2. Histogram of the VSC map of the right pyramidal tract that has been obtained in one subject by choosing the starting point for the pyramidal tract displayed in Fig. 4.1. On the y axis the total number of voxels is represented, while on the x axis the value of the voxel-scale connectivity metric is given in arbitrary units (axis scaled to look at the highest connectivity values only). A threshold of 0.82, as defined by the last major group of peaks of the histogram (arrow), has been selected in this case to define voxels with the highest connectivity to the starting point.

4.1.2.3.4. *Post-processing time*

The time for each step of the analysis was: 1) the selection of the starting point and the application of FMT algorithm required about 15 minutes (on a Sun Microsystems SunBlade 100); 2) plotting the histogram of the VSC map and choosing the threshold required about 5 minutes; 3) the application of the threshold to the map of the connectivity metric to define voxels with the highest connectivity required about 10 minutes; 4) calculating the tract FA and total volume required 3 minutes; 5) calculating the TIV and subsequently the NV required about 30 minutes. The acquisition time, the image transfer and reconstruction times, the time for the diffusion tensor calculation, and the time for subsequent statistical analysis must also be added.

4.1.2.3.5. *Statistical analysis*

To compare the FA and NV between the left and right optic radiation and pyramidal tract the Wilcoxon test was used.

The Coefficient of Variation (CV) for tract FA and NV was calculated using the following formula (Bland and Altman 1996a;Bland and Altman 1996b):

$CV = \sqrt{}$ mean of the variance of a given measurement / mean measurement values.

<u>Sensitivity of FMT to adjacent starting points within subjects</u>

In order to assess the effect on the FMT results of deliberately selecting a starting voxel adjacent to the starting point chosen in the baseline experiment, a second trial was performed by the first observer (O.C.) in all subjects. For the optic radiations and pyramidal tracts, one

adjacent starting point was selected for each side of the brain, while for the analysis of the callosal fibres one adjacent voxel from the midline was chosen for each subject (Table 4.1). The adjacent voxel was selected using the following criteria: it had to share one face with the baseline starting voxel, it had to be on the same axial slice, it had to satisfy the starting voxel definition criteria (as accurately as possible but obviously excluding the voxel used at baseline). The VSC maps obtained by using these two adjacent voxels were used to calculate tract FA and NV, which were then considered for the calculation of the CV.

Intra-observer CV

A new FMT experiment was run after 3 weeks on the data from 6 subjects (no rescan) by the same observer (O.C.), who was blind to all the details of the baseline FMT analysis, including the coordinates of the starting points (for reproducibility of the starting points selection in these two experiments see Table 4.2). FMT experiments were performed once for each side of the brain for the optic radiations and pyramidal tracts and once for the callosal fibres. The mean FA and the NV obtained by this new evaluation were used together with those provided by the baseline experiments to calculate the tract variability in the same subject when FMT experiments are repeated by the same observer.

Table 4.1. The image coordinates (x = right (R)-left (L), y = anterior-posterior, z = superior-inferior) of two adjacent starting points selected in each of the 11 subjects are listed for each white matter tract under investigation. The coordinate that has changed between the two trials is displayed in bold. Note that the second starting point was selected always on the same slice, and moved either along the x or y coordinates.

Subjects	Callosal fibres	Optic radiations	Pyramidal tracts
1			
1st point	63,**44**,21	R: 48,**68**,26 L: 82,**68**,26	R: 48,**68**,29 L: **71**,70,29
2nd point	63,**45**,21	R: 48,**69**,26 L: 82,**69**,26	R: 48,**69**,29 L: **72**,70,29
2			
1st point	**61**,42,22	R: 45,**70**,26 L: 83,**70**,26	R: **55**,68,29 L: 69,**68**,29
2nd point	**62**,42,22	R: 45,**71**,26 L: 83,**71**,26	R: **56**,68,29 L: 69,**69**,29
3			
1st point	**63**,35,18	R: 46,**66**,24 L:83,**68**,24	R: 58,**66**,27 L: 71,**65**,27
2nd point	**64**,35,18	R: 46,**65**,24 L:83,**67**,24	R: 58,**65**,27 L: 71,**66**,27
4			
1st point	**64**,41,23	R: **44**,68,28 L: 85,**69**,28	R: 56,**67**,30 L: **71**,67,30
2nd point	**65**,41,23	R: **43**,68,28 L: 85,**68**,28	R: 56,**66**,30 L: **72**,67,30
5			
1st point	**64**,45,22	R: **45**,76,27 L: 84,**75**,27	R: 57,**68**,30 L: 71,**68**,30
2nd point	**63**,45,22	R: **44**,76,27 L: 84,**74**,27	R: 57,**69**,30 L: 71,**69**,30
6			
1st point	**64**,44,22	R: 44,**70**,25 L: 82, **71**,25	R: **57**,67,29 L: **71**,67,29
2nd point	**65**,44,22	R: 44,**71**,25 L: 82,**70**,25	R: **56**,67,29 L: **70**,67,29
7			
1st point	**61**,46,18	R: 44,**73**,25 L: 81,**72**,25	R: 56,**70**,27 L: **70**,70,27
2nd point	**62**,46,18	R: 44,**72**,25 L: 81,**73**,25	R: 56,**71**,27 L: **69**,70,27
8			
1st point	67,**43**,17	R: 49,**70**,24 L: 83,**69**,24	R: **57**,66,26 L: **76**,66,26
2nd point	67,**44**,17	R: 49,**69**,24 L: 84,**70**,24	R: **58**,66,26 L: **75**,66,26
9			
1st point	**65**,44,21	R: 47,**70**,23 L: 82,**71**,23	R: 47,**70**,23 L:82,**70**,23
2nd point	**66**,44,21	R: 47,**71**,23 L: 82,**70**,23	R: 47,**71**,23 L:82,**71**,23
10			
1st point	**62**,39,21	R: 45,**64**,24 L: 84,**64**,24	R: 54,**59**,29 L: **71**,60,29
2nd point	**61**,39,21	R: 45,**65**,24 L: 84,**65**,24	R: 54,**60**,29 L: **72**,60,29
11			
1st point	**62**,44,18	R: 46,**75**,21 L:85,**75**,21	R: 57,**67**,25 L: 71,**67**,25
2nd point	**63**,44,18	R: 46,**76**,21 L:85,**76**,21	R: 56,**66**,25 L: 71,**66**,25

Table 4.2. The starting points selected in two different occasions by the same observer in 6 subjects are summarised by showing the difference between the voxels coordinates (Δx, Δy, Δz, where x = right (R)-left (L), y = anterior-posterior, z = superior-inferior) of the second experiment and those of the first one. The last row shows the mean of the absolute differences for each white matter tract under investigation.

Subjects	Callosal fibres	Optic radiations	Pyramidal tracts
1	-1, 1, 0	R: 0, 1, 0; L: 0, 0, 0	R: 1, 1, 0; L: 1, 0, 0
2	0, 0, 0	R: 0, 1, 0; L: -1, -2, 0	R: 0, 0, 0; L: 0, 2, 0
3	1, 0, 0	R: 0, -1, 0; L: 0,-3, 0	R: 1, 0, 0; L: -1, 0, 0
4	0, 0, 0	R: -1, 1, 0; L: 1, 0, 0	R: -1, -1, 0; L: 0, 0, 0
5	-2, 0, 0	R: 0, 0, 0; L: 0, 1, 0	R: -1, 1, 0; L: 1, 1, 0
6	1, -1, 0	R: 0, 1, 0; L: 0, 1, 0	R: -1, 1, 0; L: 1, 0, 0
Mean	0.83, 0.33, 0	R: 0.16, 0.83, 0 L: 0.33, 1.16, 0	R: 0.83, 0.66, 0 L: 0.66, 0.5, 0

Inter-observer CV

A new FMT experiment was performed in the same 6 subjects by a second observer (A.T.T.) (to see the selection of the starting points performed by the second observer see Table 4.3). The mean tract FA and the NV, obtained separately by two different observers using FMT in the same subject, were considered for the calculation of the inter-observer CV.

Test-retest CV

Four subjects had a second scan after 3 to 6 months and the whole process of data acquisition, tensor estimation, starting point selection, FMT processing, and ROI analysis was performed again. The mean FA and the NV obtained by this retest were used for the calculation of the test-retest CV.

Table 4.3. The starting points selected by two different observers in 6 subjects are summarised by showing the difference between the voxels coordinates (Δx, Δy, Δz, where x = right (R)-left (L), y = anterior-posterior, z = superior-inferior) chosen by the second observer and those chosen by the first one. The last row shows the mean of the absolute differences for each white matter tract under investigation.

Subjects	Callosal fibres	Optic radiations	Pyramidal tracts
1	1, 1, 0	R: -1, 4, 0; L: 1, 4, 0	R: -1, 2, 0; L: 0, -1, 0
2	1, 1, 0	R: -1, 4, 0 L: -1, -3, 0	R: 1, -1, 0 L: 0, 1, 0
3	1, 0, 0	R: 0, -3, 1; L: 3, 5, 1	R: 1, 0, 0; L: -1, 0, 0
4	0, 0, 0	R: -1, 1, 0 L: 0, -1, 0	R: 1, -1, 0; L: 0, 0, 0
5	0, 0, 0	R: 0, 0, 0 L: 0, -2, 0	R: 0, 1, 0; L: 1, 2, 0
6	1, -1, -1	R: -1, 2, 0; L: 1, 3, 0	R: 0, 0, 0; L: 0, 1, 0
Mean	0.66, 0.5, 0.16	R: 0.66, 2.33, 0.16 L: 1, 3, 0.16	R: 0.66, 0.83,0 L: 0.33, 0.83, 0

4.1.3. Results

4.1.3.1. Tracing white matter pathways

The VSC maps derived from FMT are consistent with known anatomy of the tracts studied (Crosby E.C. et al. 1962). In particular, most of the callosal fibres that pass through the genu of the CC interconnect corresponding areas of each frontal lobe (Figure 4.3,A). The optic radiations show posterior connections to the visual areas and medial connections to the lateral geniculate nuclei (Figure 4.3,B). The pyramidal tracts travel from the middle portion of the cerebral peduncles (where the starting points were placed) to the motor cortices, passing through the posterior limb of the internal capsule and the corona radiata (Figure 4.4). False positive connections have been detected in the course of the analysis, such as anterior projections from the optic radiations (Figure 4.3,B). There was no significant difference in

mean FA, total uncorrected tract volume and NV obtained from the baseline FMT experiment between the left and right optic radiation and pyramidal tract (Table 4.4.).

Table 4.4. Mean fractional anisotropy (FA), total uncorrected volume (V) and normalised volume (NV) of the white-matter pathways obtained from the baseline FMT experiment in 11 normal subjects.

	FA (mean; ±SD)	**Total Uncorrected V (cm^3)** (mean; ±SD)	**NV** (mean; ±SD)
Callosal fibres	0.30 (0.02)	3.4 (0.9)	2.4 (0.05)
Optic radiations	0.33 (0.03)	5.03 (1.49)	3.6 (1.07)
Pyramidal tracts	0.34 (0.02)	9.89 (1.89)	7.06 (1.68)

(A)

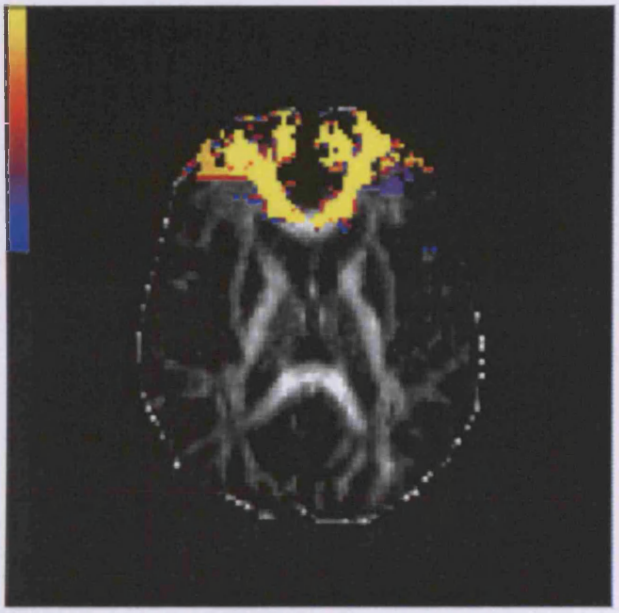

(B)

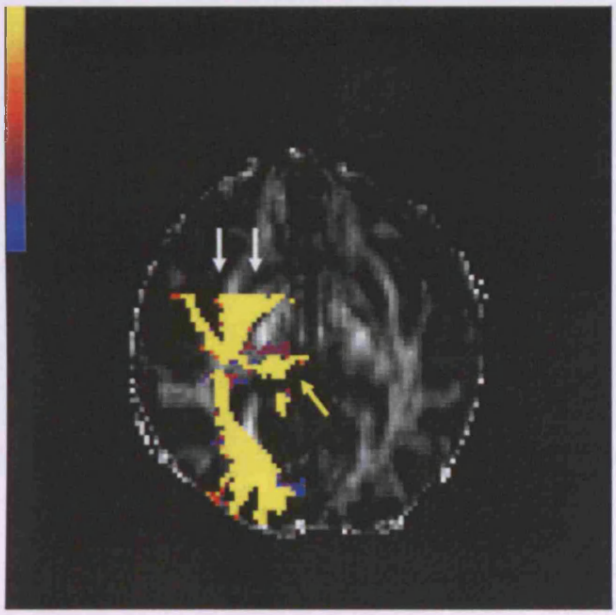

Figure 4.3. VSC maps of the anterior callosal fibres (A) and of the right optic radiation (B) of a normal subject overlaid on FA maps. Colour scale reflects the degree of connectivity (arbitrary units). The callosal fibres pass through the genu of corpus callosum and interconnect corresponding areas of each frontal lobe. The optic tract show posterior connections to the visual areas and medial connections to the lateral geniculate nuclei (yellow arrow). White arrows show the false positive connections.

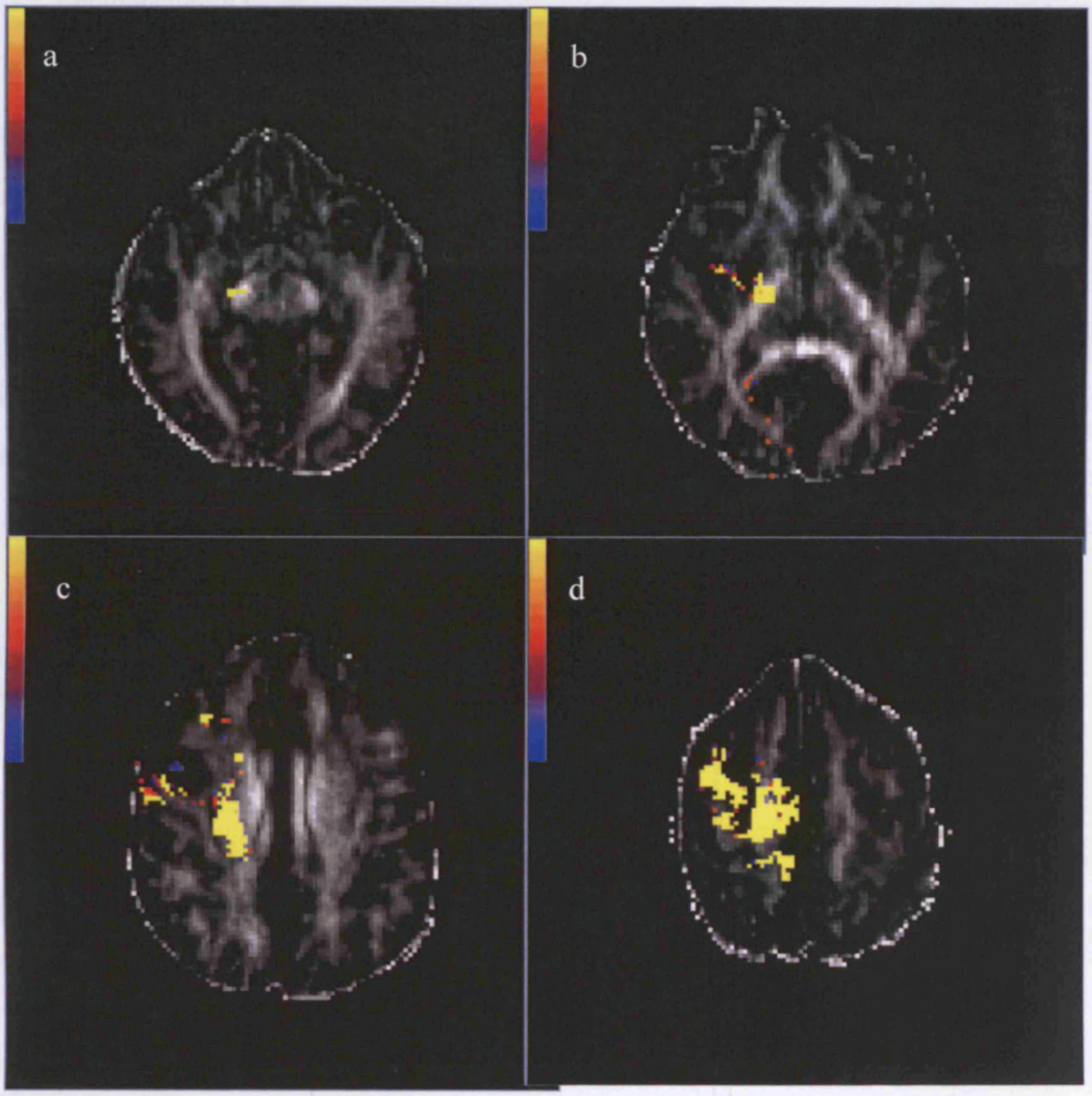

Figure 4.4. VSC map of the right pyramidal tract of a normal subject overlaid on a FA map. Colour scale reflects the degree of connectivity (arbitrary units). The pyramidal tracts travel from the middle portion of the cerebral peduncles (a) to the motor cortices (d), passing through the posterior limb of the internal capsule (b) and the corona radiata (c).

4.1.3.2. Reproducibility study

Coefficients of variation (CVs) for FA and NV in the white-matter pathways are shown in Table 4.5 (in case of bilateral tracts, they are given as mean of the CV of the right and left side). The CVs for FA (ranging from 1.7% to 7.1%) are generally lower than the CVs for NV (ranging from 2.2% to 18.6%). For both FA and NV, the inter-observer CVs were generally higher than the intra-observer CVs, and the test-retest CVs were the highest. The lowest CVs were found in the callosal fibres (range: 1.7% - 7.8%), followed by those in the optic radiations (range: 1.2% - 18.6%) and in the pyramidal tracts (range: 2.6% - 15.5%).

Table 4.5. Coefficients of variation (CVs) for fractional anisotropy (FA) and normalised volume (NV) of white matter pathways.

	Callosal fibres CV %		**Optic radiations CV %**		**Pyramidal tracts CV %**		**N. of subj.**
	FA	**NV**	**FA**	**NV**	**FA**	**NV**	
Adjacent starting points	**1.7**	**2.2**	**2.5**	*6.3*	**3.5**	13	11
Intra-observer	**2.9**	*7.2*	**1.2**	*6.6*	**2.6**	11.6	6
Inter-observer	**3.7**	*6*	**2.6**	13.9	**3.8**	15.3	6
Test-Retest	*6.2*	*7.8*	*7.1*	18.6	*5*	15.5	4

CVs lower than 5% are displayed in bold, those between 5% and 8% are displayed in italic, and those higher than 8% are shown in black. The CVs of the optic radiation and pyramidal tract are given as mean of the CV of the right and left side.

4.1.4. Discussion

We have investigated the reproducibility of quantitative white matter tract measures derived using FMT. We focused on the anterior callosal fibres, the optic radiations and the pyramidal tracts. Since these tracts are different in length, location, trajectory and fibre organisation, they provide the opportunity to test FMT reproducibility under different conditions.

Moreover, these pathways are of considerable clinical interest, and characterisation of the variability that may be expected in their examination will form the basis for future comparative studies between normal subjects and patients groups. First, we shall discuss the ability of FMT to reconstruct VSC maps, from which the white matter pathways can be inferred or segmented. This will be followed by an evaluation of the reproducibility of mean FA and tract volume measurements.

4.1.4.1. Segmentation of white matter pathways

The localisation and course of the white matter pathways identified on the VSC maps as the voxels with the highest connectivity to the start point are consistent with known anatomy. Although FMT is able, in many cases, to elucidate branching fibres, some problems arise when multiple tracts or orientations are present within a voxel. DTI provides information concerning the average orientation of fibres at the voxel level, and if this volume-averaged information is used to reconstruct a pathway, false positive projections may, on occasion, be observed. For example, the anterior projections from the optic radiations detected at the level of the Meyer loop (Figure 4.3,B) may reflect the inferior occipitofrontal fibres, which are known to accompany the optic radiations for a short distance (Burgel et al. 1999;Crosby E.C. et al. 1962). A solution to this problem could be provided by alternative approaches to the single tensor, as discussed in chapter 2.

4.1.4.2. Reproducibility of tract FA and volume

We have demonstrated the reproducibility of two quantitative measures, i.e. mean tract FA and NV, using DTI tractography information to bypass subjective determination of regions of

interest. Other studies have also focused on these tract parameters, mainly in the brainstem (Stieltjes et al. 2001;Virta et al. 1999), showing the importance of assessing the reproducibility of such measures. However, direct comparisons between studies are not possible because of the different aims, anatomical regions studied, and methodologies used. The anisotropy of the tracts gives information about the degree of fibre tract directional coherence within an imaging voxel. The relatively low value of FA in the white matter pathways suggests that some grey-matter regions, which contain the points of origin and termination of the fibres, were also included in the connected regions. Consequently, it might be thought that unrelated white matter tracts that share the same grey matter areas could be included into the reconstructed pathways. However, the risk of this happening is low, because the FMT algorithm only follows highly directionally coherent eigenvectors from the starting point. Moreover, the low value of tract mean FA might be due to the presence of crossing fibres from other tracts, and of angulating fibres within a voxel. We also examined the total tract volume, which was obtained using a threshold defined on the histogram of the connectivity maps. The total tract volumes of the optic radiations and pyramidal tracts obtained are strikingly consistent with data derived from post-mortem human brains (Burgel et al. 1999;Rademacher et al. 2001), suggesting that the FMT method enables for the first time *in vivo* quantification of tract volume without morphology-based segmentation, or post-mortem analysis.

A comparison between the CVs obtained for FA and NV shows that FA is more reproducible. Different starting points within the same tract produce different, but closely related, sub-samples of the tract itself. The ROIs for the quantitative measurement of FA and NV are determined by applying a tract-dependent threshold to the VSC map. These ROIs have different volumes, generating therefore different tract volumes, but show similar mean FA.

This indicates that the degree of fibre coherence is likely to be approximately constant on sub-sampling of the same tract.

The values of mean FA of the three tracts under investigation have a narrow range, and therefore it could be argued that mean FA is not the best measure to spatially distinguish between tracts. However, it has the potential to detect pathological conditions that are known to cause FA changes. The values of NV, on the other hand, which have higher within-subject CVs and higher within-subject standard deviations than FA, have relatively small between-subject standard deviations, an important factor in power and sample size calculation (Fisher and van Belle 2003). For example, in the specific case of the left pyramidal tract, the between-subject standard deviation on the first measurement was 1.4 cm^3. Consequently, group differences should be detectable in pathological conditions where a change in NV of 10% is expected with about 55 subjects in each group (for 80% power and alpha of 0.05). Moreover, NV could be used as a discriminating factor in selecting white matter diseases that can be investigated using FMT. For example, in FMT studies of MS or stroke, which show marked degeneration of white matter fibres, both mean FA and NV could be used to detect pathological changes.

The differences in fibre pathway volumes obtained when choosing two adjacent starting points within the same subject may in part reflect the anatomical mapping differences of fibres that pass through different regions of the brain. This hypothesis is supported by the evidence that the highest CV for adjacent starting points is seen in the pyramidal tracts, which show complex fibre organisation and a wide mapping volume. The pyramidal fibres are closely aligned and tightly packed in the cerebral peduncles, where the starting points are placed, but spread in multiple branches in the corona radiata and to the motor cortex, thus inducing the estimated tract volume to be sensitive to the starting point location. Conversely,

the lowest CV for NV for adjacent starting points is reported in the anterior callosal fibres, which interconnect the less extensive medial pre-frontal regions (Barbas and Pandya 1984).

The lists of the starting point coordinates used for the FMT experiments by the same observer and by two different observers, show that the placement of the seed point is fairly consistent with a mean distance between trials of less than a voxel. It can be observed, though, that it is more reproducible in the same observer than between observers. This is reflected in the fact that, when the FMT analysis is performed by a second observer, the CVs for FA and NV are slightly higher than the intra-observer CVs. Therefore, the development of new guidelines to define better the starting points may further improve both the intra-observer and inter-observer CVs. Also, future development of the DTI acquisition technique and higher field scanners, as noted earlier, could improve resolution, possibly allowing a narrower definition of the starting point of the tracts.

The lowest reproducibility for our quantitative measurements was found in the (intra-observer) test-retest analysis, suggesting that factors related to the data acquisition and reconstruction may play a role in inducing extra variability. In the present study the diffusion tensor calculation and FMT algorithm were performed in each subject's native space. The development of registration algorithms able to deal correctly with the diffusion tensor (Pautler et al. 1998), may allow transformation of the data into a normalised space before applying tractography algorithms, possibly improving the test-retest CV.

In conclusion, we have investigated *in vivo* anisotropy and volumetric quantification of FMT-derived white matter tracts within the brain and have shown that tract FA has better reproducibility than NV. The highest reproducibility was found in the frontal callosal fibres, followed by the optic radiations and pyramidal tracts, suggesting that the fibre organisation and the length of the pathway are important factors in determining the level of reproducibility.

It is important to assess the reliability of any tractography technique before moving on to investigate white matter pathology. In this study we have described a method by which the reproducibility of FMT can be assessed. Ideally all tractography techniques should be validated in a similar way before being clinically applied. In particular, information about the reproducibility of the quantitative measurements derived from tractography and the variability between the reconstructed tracts should always be obtained before interpreting clinical data.

4.2. Diffusion tractography based group connectivity maps of major white matter tracts

4.2.1. Introduction

The present study describes the evaluation of anatomical connection variability between normal subjects, using FMT. This step is essential in order to move on to the investigation of neurological and psychiatric diseases, known to disrupt white matter pathways (Foong et al. 2000;Mori et al. 2002;Pierpaoli et al. 2001;Steel et al. 2001). The ability to create group maps of white matter tracts, and therefore, to compensate for normal inter-subject variability, may ultimately allow the construction of "brain atlases" that represent *in vivo* white matter tracts (Johansen-Berg et al. 2004). Such atlases would be invaluable in investigating how white matter is affected by pathological conditions of the CNS (Steel et al. 2001).

As an initial step towards this goal, we have generated group connectivity maps of white matter pathways in a group of 21 healthy subjects using FMT. The three white matter pathways that were considered in the first study were examined: the left and right pyramidal tracts, the left and right optic radiations, and the anterior callosal fibres. We created three

different group mapping techniques for each pathway and investigated the contribution of each technique in understanding the connectivity behaviour between subjects. The first technique simply averaged the individual connectivity maps generated by FMT; the second produced maps that demonstrated inter-subject tract variability and degree of overlap; the third employed SPM (Ashburner and Friston 2000) to construct a statistical image that represented the group effect. With the last technique we were also able to investigate any asymmetry between left and right sides for the optic radiations and pyramidal tracts.

4.2.2. Methods

4.2.2.1. Subjects

Twenty-one healthy volunteers were studied (11 females and 10 males). The mean age was 33 ± 9.7 years. Informed consent was obtained from all subjects before entering into the study.

4.2.2.2. MRI protocol

The MRI protocol is as described in the first study.

4.2.2.3. FMT method

FMT was used to trace the three white matter pathways (Parker et al. 2002c;Parker et al. 2002a). A histogram of each VSC map generated from FMT was created, and a threshold defining a group of voxels with the highest connectivity to the seed voxel was identified, as

described in the first study. The means (with standard deviations) for histogram thresholds of each white matter tract were as follows: anterior callosal fibres 455 (SD 12), left optic radiation 456 (SD 39), right optic radiation 464 (SD 20), left pyramidal tract 434 (SD 48), right pyramidal tract 422 (SD 65). This threshold was then applied to the VSC map to define ROIs identifying the areas of highest connectivity, and subsequent "thresholded" connectivity maps were obtained. These were simply binary images that indicated where the tracts were likely to be located with greatest certainty.

Thus, for each of the five white matter pathways that were examined (left and right pyramidal tracts, left and right optic radiations, anterior callosal fibres), two types of VSC maps were generated for each subject: unthresholded maps that preserved the estimated degree of connectivity at each voxel within the restricted brain volume, and thresholded maps that provided spatial information purely about tract location and extent.

4.2.2.4. Spatial Normalisation

The thresholded and unthresholded connectivity maps were normalised into a standardised space (as defined by the Montreal Neurological Institute (MNI)) using SPM99 (Wellcome Department of Cognitive Neurology, London, UK). This was performed by initially normalizing each b0 image to the default EPI template, which shares similar T2-weighted contrast. The normalisation parameters were estimated with the following settings: 12 parameter affine transformation followed by non-linear warping with 7x8x7 basis function sets, 12 non-linear iterations, medium regularisation and default brain mask. The default EPI template (asymmetrical) was used in all cases except for the left-right comparisons (see later) when the original unthresholded connectivity maps were normalised again using symmetrical templates. The b0 normalisation parameters were then applied to all the VSC maps (which

were in the same stereotactic space as the original b=0 images). The resampled voxel size was 2x2x2mm for normalisation. Nearest neighbour interpolation of the connectivity maps was used to maintain the connectivity values derived using FMT. The resulting normalised thresholded and unthresholded connectivity maps were entered into the next stage of analysis.

4.2.2.5. Group mapping of white matter pathways

We calculated group maps for each of the five pathways under investigation. Three different group mapping techniques were employed using SPM99. Each has merits and limitations that will be discussed later:

1. Average group maps

The normalised unthresholded connectivity maps were averaged at each point in standard space across the whole group of subjects for each of the five white matter tracts. The mean images were overlaid onto a structural template.

2. Variability group maps

The normalised, thresholded connectivity maps were averaged at each point in standard space and the resulting images were overlaid onto a structural template. As the individual maps were binary and defined where the tracts were likely to be, mathematical averaging had the effect of indicating the degree of spatial variability and overlap of the tracts between subjects.

3. SPM analysis of unthresholded connectivity maps

The normalised, unthresholded connectivity maps were initially smoothed. Smoothing results in the voxel values approximating a parametric distribution and, through the central limit

theorem, allows the use of standard parametric statistics to make inferences about differences and similarities between connectivity distributions (Ashburner and Friston 2000). The unthresholded images were chosen in order to preserve as much spatial connectivity information about the particular white matter tract under investigation as possible. The size of Gaussian filter was chosen according to white matter tract: 10 mm was used for the anterior callosal fibres, 7 mm for the optic radiations and 5 mm for the pyramidal tracts. These values were chosen because the spatial variability, between subjects, in tract position was greatest for the anterior callosal fibres and least for the pyramidal tracts, as discussed in the results. The individual smoothed images were then entered into a design matrix for a one sample t-test. Significance was assigned to the resulting t fields using the theory of Gaussian random fields (Worsley et al. 1996). The resulting statistical maps were corrected for multiple comparisons across the volume under analysis and indicated the group effect, i.e. the degree of statistical compatibility within the group.

4.2.2.6. Tract volumes and asymmetry

Tract volume assessment - The ROIs derived from the histogram thresholds that defined the individual thresholded connectivity maps (before normalisation) were used to calculate the total tract volumes for each subject. The Wilcoxon test was used to compare the tract volumes, between left and right sides, for the pyramidal tract and optic radiation.

SPM analysis - An SPM analysis was also conducted to assess regional interhemispheric asymmetry for the pyramidal tract and optic radiation. To do this, the individual unthresholded connectivity maps were first normalised using a symmetrical EPI template and then smoothed as before. The resulting smoothed, normalised right sided tracts were then

flipped across the midline and the "mirror images" were subsequently compared, using SPM, to the left sided tracts with paired t-tests.

4.2.2.7. Assessment of seed voxel placement in normalised space

The consistency of seed voxel location within the standard stereotactic reference frame (MNI space) was assessed for each tract across the 21 subjects. Each seed voxel coordinate (defined in native space) was normalised with the same spatial transformation parameters as the connectivity maps (see spatial normalisation above).

4.2.3. Results

4.2.3.1. Average Group Maps

Average group maps of connectivity across all subjects for the white matter pathways under investigation were created and then overlaid onto a T1-weighted template image (Figure 4.5). On visual inspection, they qualitatively conformed to the known anatomy of the tracts. The colour intensity of these maps reflects the average connectivity value of each voxel to the seed point across all subjects.

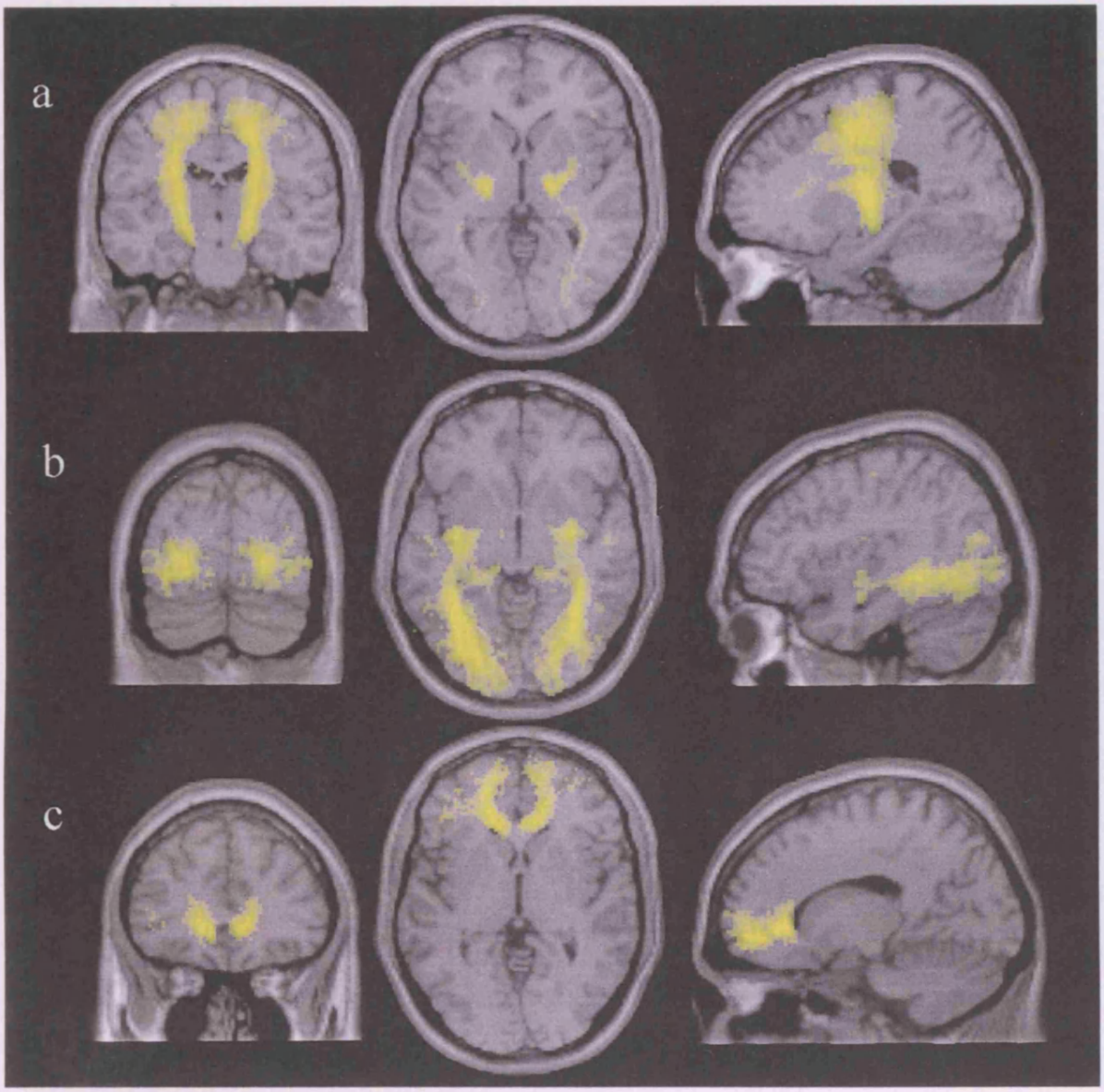

Figure 4.5. Average group maps are shown for the (a) pyramidal tracts (MNI coordinates x=-20 mm, y=-16 mm, z=0.4 mm), (b) optic radiations (MNI coordinates x=38 mm, y=-75.6 mm, z=2.7 mm) and (c) anterior callosal fibres (MNI coordinates x=-14.5 mm, y=33.3 mm, z=0 mm). The locations of the tracts conform to the known anatomy. The colour intensity indicates the average connectivity metric value across the whole group of subjects. The maps have been thresholded (at a value of 100) to exclude very low average values and highlight the tracts of interest. Note that in (b) some erroneous tracts are traced (centre image) anteriorly from the loop of Meyer; this may result from other white matter tracts in close proximity with Meyer's loop, for example inferior longitudinal fasciculus and uncinate fascicle. In (a) some finely traced tracts of low connectivity along the optic radiations are seen in the centre image.

4.2.3.2. Variability group maps

Variability group maps were constructed using the thresholded connectivity maps and were overlaid onto a structural template (Figure 4.6). They represented the degree of spatial variability between subjects, and were visually consistent with data derived from post-mortem human brains (Burgel et al. 1999;Rademacher et al. 2001). The "hot" colour scale indicates the proportional degree of overlap of the tracts between subjects; for example, the number 1 represents 100% subject overlap (i.e. the voxel in question is within the identified tract in all subjects), 0.5 represents 50% overlap, and 0.05 represents data from only 1 out of the 21 subjects. The inter-subject spatial variability was greatest for the anterior callosal fibres (range: 0.05 - 0.49) and smallest for the pyramidal tracts (maximum overlap was 1 for the left and 0.95 for the right). The optic radiations demonstrated intermediate variability (maximum overlap 0.72 for the right and 0.62 for the left). The greatest overlap, for each tract, was found centrally as indicated by the brighter colours. Greater inter-subject variability was consistently found around the terminal projections of the tracts adjacent to cerebral cortex, indicated by darker colours.

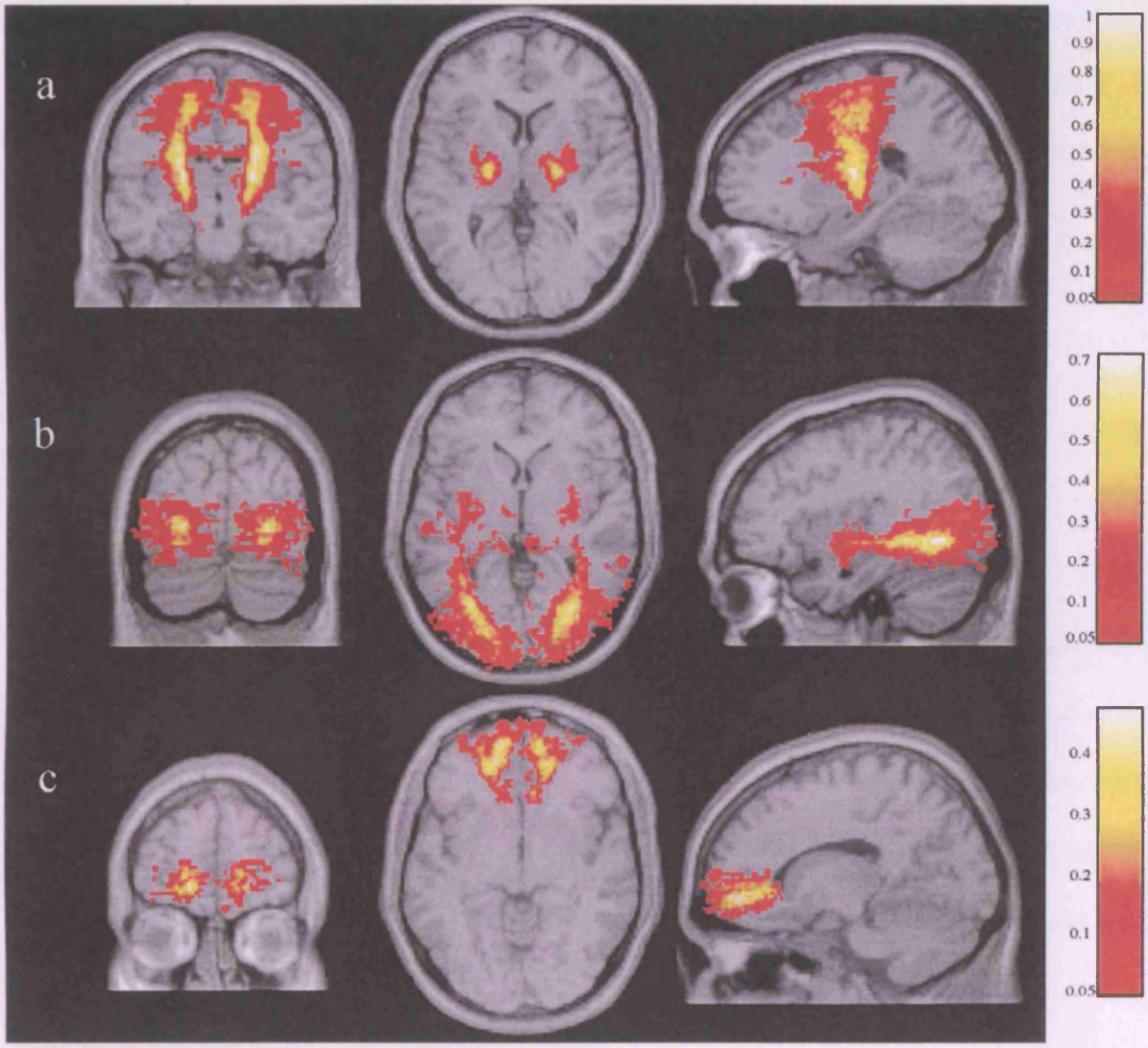

Figure 4.6. Variability maps for the (a) pyramidal tracts (MNI coordinates x=-20.8 mm, y=-12.9 mm, z=4.3 mm), (b) optic radiations (MNI coordinates x=37.2 mm, y=-77.9 mm, z=1.2 mm) and (c) anterior callosal fibres (MNI coordinates x=-14.5 mm, y=52.1 mm, z=-5.1 mm). A "hot" colour scale indicates the degree of overlap amongst subjects; 0.05 indicates that data is present in only 1 out of 21 subjects and 1 indicates 100% overlap. The peripheral distribution of each of the tracts demonstrates the greatest interindividual variability. Note that in (a) a few tracts extend across the corpus callosum (left image), which would conform to collaterals of cortico-spinal fibres. In (b) note few anteriorly projecting erroneous tracts from Meyer's loop (centre image).

4.2.3.3. SPM analysis of unthresholded maps

Statistical parametric maps were derived from one sample t-tests for each of the five tracts in order to determine if the unthresholded maps were significantly different from zero.

Statistical inference was performed with correction for multiple comparisons ($P<0.001$). Representative SPMs for the pyramidal tracts, optic radiations and anterior callosal fibres were overlaid onto standard template (Figure 4.7).

4.2.3.4. Tract volumes and asymmetry

Tract volume assessment - The anterior callosal fibres showed the smallest tract volume, while the pyramidal tracts showed the highest. There were no significant differences in tract volume between the left and right pyramidal tracts and optic radiations (Table 4.6). The tract volumes obtained for the pyramidal tracts and optic radiations were comparable to those that have been derived from myeloarchitectonic studies on post-mortem brains (Burgel et al. 1999;Rademacher et al. 2001). It should be noted that the tract volumes in our study were calculated before normalisation, i.e. they were not corrected for head size. The post-mortem tract volumes that were compared with our tract volumes were also uncorrected for head size.

SPM analysis - No significant group effect differences were detectable between left and right sides using SPM99 for the pyramidal tracts and optic radiations. This is consistent with the comparison that we performed, between left and right sides, of tract volumes.

Table 4.6. Total volumes of the major white matter pathways in 21 normal subjects.

White matter pathways	**FMT-derived total volume (cm^3)** (Mean±SD)	**Post-mortem total volume (cm^3)** (Mean±SD)
Callosal fibres	3.33 (±0.72)	n.a.
Left optic radiation	5.51 (±1.75)	6.81 (1.71)
Right optic radiation	5.16 (±1.44)	6.69 (1.69)
Left pyramidal tract	10.28 (±2.18)	9.32 (2.58)
Right pyramidal tract	11.49 (±3.57)	7.94 (2.34)

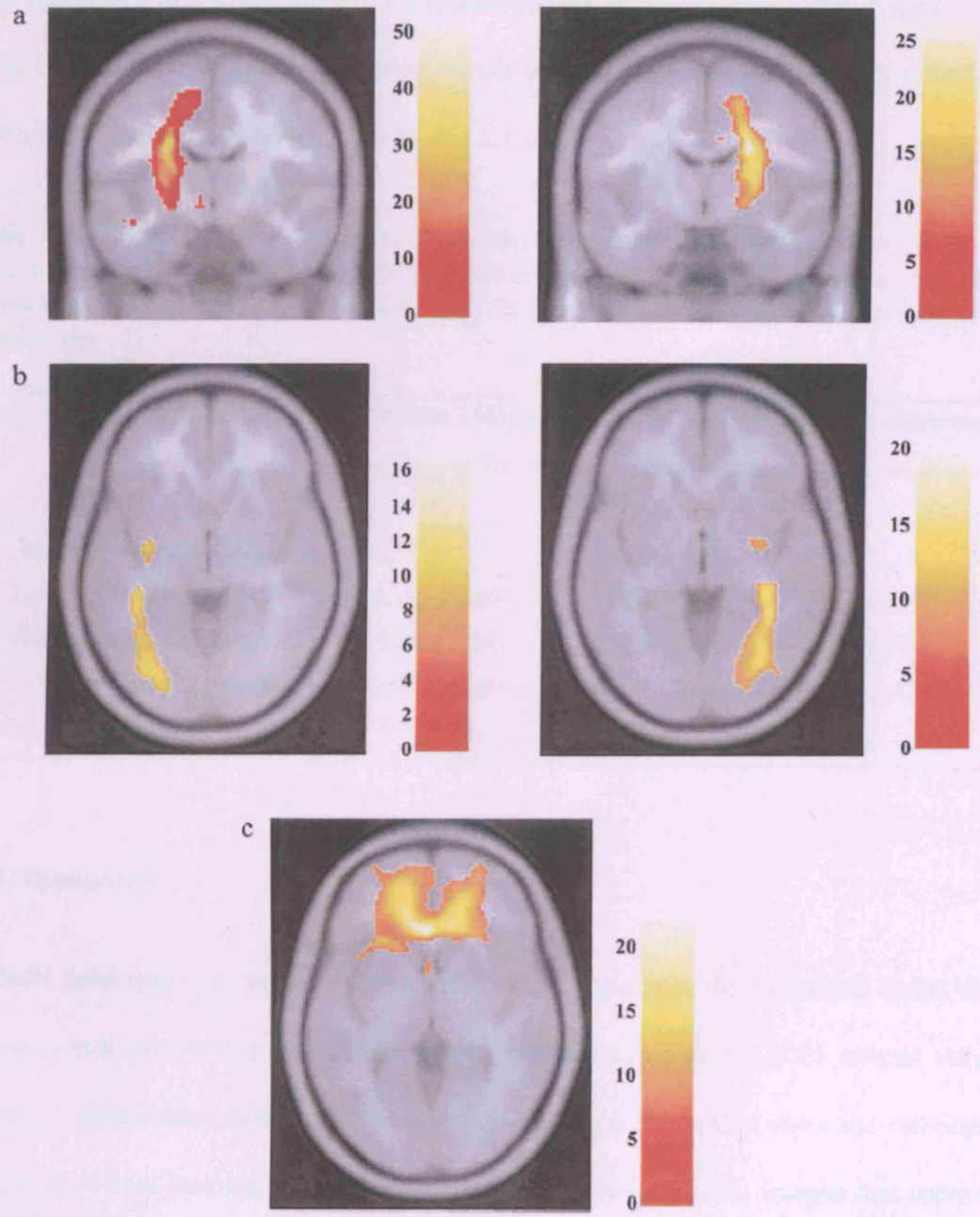

Figure 4.7. An example of the techniques to construct group effects using SPM is shown for the (a) left and right right pyramidal tracts (y=-9 mm in MNI coordinates), (b) left and right optic radiation (z=-3 mm in MNI coordinates), and (c) anterior callosal fibres (z=0.6 mm in MNI coordinates) (all maps corrected $p<0.001$). No asymmetry was detectable between left and right sides using SPM analysis. The colour scales indicate the t-scores.

4.2.3.5. Assessment of seed voxel placement in normalised space

The means and standard deviations of the x, y and z co-ordinates for the normalised seed voxels of each white matter tract are displayed in Table 4.7. The greatest variability in seed

point placement occurred with the y direction for the optic radiations (SD 7 mm for the left and 6.18 mm for the right). The lowest variability in seed point location was found in the x direction for the anterior callosal fibres (SD 1.1 mm).

Table 4.7. The mean x, y and z voxel-coordinates (in mm) across the 21 subjects in MNI space for each of the white matter tracts that were investigated. Standard deviations (SDs) are in brackets. The normalised voxel size was 2x2x2 mm. The template origin is the anterior commissure.

	Mean (SD) stereotactic seed voxel co-ordinates.		
	X	Y	Z
Anterior Corpus Callosum	-2 (1.1)	28.6 (3.24)	1.2 (3.12)
Left Optic Radiation	-38.8 (2.68)	-28.4 (7)	-5.6 (3.18)
Right Optic Radiation	34.4 (2.24)	-24.6 (6.18)	-6.0 (2.96)
Left Cerebral Peduncle	-14.4 (1.78)	-17.2 (2.14)	-16 (2.42)
Right Cerebral Peduncle	12 (2.04)	-17.4 (2.12)	-15.8 (2.16)

4.2.4. Discussion

We have used mapping methods with FMT to investigate how the pyramidal tracts, the optic radiations and the anterior callosal fibres are represented in a group of 21 normal volunteers. We have constructed group maps in a standard reference frame that show the interindividual variability of tract location and shape, and have generated statistical images that represent the group effect for each tract. Several other studies have recently addressed the issue of making group specific inferences with diffusion tractography. For example, recent work reported a method to create probabilistic maps of callosal fibres in a group of 10 subjects by combining methodologies for fibre tracking and spatial normalisation (Xu et al. 2002), although the tractography algorithm and the normalisation procedures were substantially different from those applied in our study. An alternative approach to tracking the fibres prior to creating

group maps is to average the tensor data sets before tracking fasciculi, in order to generate a generic map of brain connectivity (Jones et al. 2002).

We have also applied SPM to investigate asymmetry between left and right sides for the pyramidal tracts and optic radiations. Similar methods of assessing asymmetry of cerebral grey and white matter using voxel-wise statistical analysis have been previously reported (Good et al. 2001;Watkins et al. 2001). We shall first discuss the results for each of the three white matter tracts and then move on to issues regarding DTI, tractography and FMT. Finally, we will appraise each of the group mapping techniques that were employed and discuss the validation of tractography and its future potential.

4.2.4.1. Pyramidal tracts

The average group map of the pyramidal tracts (Figure 4.5), on inspection, qualitatively compares well with known pyramidal tract anatomy (Brodal 1981;Ross 1980). The variability maps (Figure 4.6) show a central core, along the tracts, of common overlap among 95% of subjects for the right side and 100% for the left. This indicates that relative tract location between individuals is generally constant. Outside this core there is considerable variability in tract overlap. We believe this reflects variation in tract volume between individuals, which is also reflected in the calculated tract volumes and their standard deviations (Table 4.6). The pyramidal tract volumes are approximately in the same range as volumes reported by Rademacher et al. (Rademacher et al. 2001), who performed a cytoarchitectonic and myeloarchitectonic study of the human motor system in 11 post-mortem brains. Our volumes are slightly higher on both sides (Table 4.6) than the volumes reported in their study. In our variability maps (defined by averaging the thresholded maps) (Figure 4.6), the pyramidal tracts mainly extend towards the motor cortex, but also show contributions from the premotor

cortex. This may account for the slightly larger volumes reported in our study. Pyramidal tract fibres are known to take their origin mainly from the motor and caudal premotor cortex (Jane et al. 1967) and the appearance of our variability maps probably reflects this.

The differences could also be explained by sample selection differences between the two studies. The relatively low sample sizes for the post-mortem study and our study may contribute to slightly different estimates of population parameters for the pyramidal tracts and so good agreement between the two studies should not necessarily be expected. In support of this, we find no differences between left and right pyramidal tract volumes, whereas the other authors report greater left sided tract volumes. Future studies with larger sample sizes should allow better estimates of normal population variability. Finally, methodological differences in tract volume calculations could also contribute to the observed differences between the two studies.

4.2.4.2. Optic radiations

The appearance of the optic radiations on the average (Figure 4.5) and variability group maps (Figure 4.6) again conform closely to their known anatomy. On the variability maps the maximum overlap was 62% (15 out 21 subjects) on the left and 72% (17 out of 21 subjects) on the right. This probably reflects relative differences in FMT-derived tract position between individuals and may be attributed to inter-individual anatomical differences in tract morphology. Also, the fact that the calculated optic radiation volumes are smaller than the pyramidal tract volumes (Table 4.6) may also make overlap between individual tracts less likely. The calculated tract volumes are only slightly lower than the volumes reported by Burgel's myeloarchitectonic study of 11 post-mortem human brains (Burgel et al. 1999). These differences could be explained by the fact that they identified optic radiation fibres that

originated from the lateral geniculate body, whereas we positioned our seed point within Meyer's loop, which would tend to produce lower FMT-derived tract volumes. As in our study, they found significant interindividual variability. They also found significant asymmetry of tract volumes (left being greater than right), which we did not reproduce *in vivo* either by statistical comparison between left and right optic radiation volumes or by SPM analysis. This is probably due to random differences in the population samples that were studied and methodological differences between DTI based tractography and myeloarchitectonic based histological studies.

4.3.4.3. Anterior callosal tracts

The anterior callosal fibres demonstrate the smallest overlap in tract position (Figure 4.6) with a maximum of 49% sharing the same voxel space. This may be because the tract volumes are the smallest of all three pathways examined in this study (mean 3.33 cm^3), which probably makes significant overlap unlikely. Also, it is known that the cortico-cortical connections through the CC are topographically organised (de Lacoste et al. 1985); those connections through the genu (anterior region) of the CC span out to serve a large area of the frontal cortex. The high variability in the position of FMT-derived callosal fibres may thus reflect natural anatomical differences, between individuals, in the topographical organisation of callosal projections. Moreover, the frontal regions can be highly affected by EPI geometric distortions (Farzaneh et al. 1990). These distortions may vary between individuals and limit the ability of FMT to trace tracts in these regions, and affect the registration methods used.

4.2.4.4. Benefits of tractography in mapping white matter pathways

Tractography is a promising technique capable of tracing white matter tracts *in vivo*. Validation for this technique is difficult and has normally relied upon the qualitative comparisons between tractography derived white matter pathways and known anatomy from histological post-mortem studies (Jones 1999). The recent emergence of manganese-enhanced MRI tracing techniques in animal models (Pautler et al. 1998) may provide an *in vivo* gold standard for quantitatively validating DTI in mapping white matter tracts (Lin et al. 2003). At present however, qualitative comparison with existing neuroanatomical knowledge remains an important tool in validating human tractography studies.

An advantage of FMT is that the algorithm permits the determined pathways of connection to divide, thus allowing for branching pathways (Parker et al. 2002b). This is useful for tracing the pyramidal tracts and optic radiations. A consequence of this, however, is that erroneous false positive branches that do not conform to known neuroanatomy may be traced (Figures 4.5 and 4.6). These tend to have lower VSC values and can be explained by the way the tract is traced locally through the particular orientations of a group of eigenvectors, which may be affected by crossing or "kissing" fibres. It is also clear from the examination of the variability maps in Figure 4.6 that the false positive pathways have inherently higher positional variability than the true paths.

A second advantage of FMT is the ability to quantify the degree of connection at every voxel in the brain for any given seed point. The resulting VSC maps can be compared across individuals to assess inter-subject group effects and variability.

4.2.4.5. Limitations of tractography

Several tractography techniques, including FMT, rely upon the placement of seed voxels or regions of interest, from which the resulting white matter pathways are mapped. Spatial

normalisation occurs after the tractography algorithm is run in native space. Differences between subjects in the resulting normalised tracts may arise from real anatomical differences in tract anatomy, errors during spatial transformation or differences in the relative locations of the seed voxels. In our study, seed voxel placement was fairly consistent in normalised space (Table 4.7) with standard deviations in each direction of about 2 to 3 mm. The seed voxel y coordinates for the optic radiations demonstrated greater variability (SDs 6.18 and 7 mm), possibly resulting from differences in axial tilt between datasets. It is uncertain to what degree this variability influenced the observed differences for the optic radiation group maps and volumes. In an attempt to overcome seed point placement variability, registration algorithms that allow the transformation of the diffusion tensor into normalised space before applying tractography, are being developed (Alexander et al. 2001). The normalised individual tensor datasets can then be mapped into a standardised reference frame and a predefined coordinate system used to place the seed point. However, as before, spatial transformation will not be error free. In addition, the resulting "normalised" datasets will possess some natural inter-individual variation of white matter tracts. A seed voxel placed at the same coordinate may therefore be located at relatively slightly different points, along the same white matter tract, in different subjects. Nevertheless, it would be useful to assess this method in future group mapping studies.

A quantitative evaluation of the errors that may occur with spatial normalisation techniques will be helpful in the future to assess the robustness of DTI and tractography normalisation procedures. In particular it would be interesting to compare the errors produced by spatial transformations of the tensor (before applying tractography) with spatial transformations of tractography derived maps (after tensor normalisation). SPM intersubject registration has been recently evaluated only for structural MRI anatomical data, and the mean error for

registering cortical sulci was about 8 mm, which compares favourably with other methods (Hellier et al. 2002).

4.2.4.6. Average group maps

The average group maps used the unthresholded maps from each subject (Figure 4.5). This allows quantitative information for a group effect to be calculated at each voxel and potentially has the ability to detect novel branching pathways. However, they do not provide information about inter-subject variability and also can be sensitive to the effects of outliers. For example, voxels with very high VSC values may skew the resulting means of the corresponding voxels in the average map.

4.2.4.7. Variability group maps

The variability maps are very informative at assessing inter-subject overlap (Figure 4.6). In addition, their appearance and their individual volumetric quantification compares favourably with white matter tract volumes reported in histological studies (Burgel et al. 1999;Rademacher et al. 2001). However, as they purely provide spatial information about tract location and morphology, they do not allow VSC quantification.

4.2.4.8. SPM analysis of unthresholded maps

SPM can be used to assess the group effect of the individual unthresholded maps (Figure 4.7). It can also be used to demonstrate variability between subjects (by displaying the residual variability map after model estimation). Caution should be taken, however, when

making inferences from one sample t-tests, because the assumption that residual errors are distributed normally about zero may not be valid. In this study, the figures depicting the results from one sample t-tests are displayed for visual aid. A more useful application would be in its ability to compare, at each voxel, VSC values between different groups (with the assumption that the residual errors behave similarly between them) and may be an important application in investigating white matter pathology, as will be shown in the next study.

4.2.4.9. Validation of DTI and tractography

A central assumption of DTI based tractography is that the measured diffusion characteristics of tissue water and their relationships between adjacent voxels are faithful representations of the underlying axonal microstructure. The validity of this assumption is unknown because there is no gold standard to authenticate the anatomical inferences of DTI tractography. Indirect comparisons with post-mortem studies may provide some partial validation. A potentially better technique would be to compare DTI and histological findings on the same post-mortem brain tissue. This has been performed for myocardium (Holmes et al. 2000), but inferences are limited by the fact that histological preparation may alter tissue microstructure and water diffusion properties (Wheeler-Kingshott et al. 2003). An alternative technique may be developed by directly comparing manganese-based with DTI-derived tractography, as mentioned in chapter 2 (Lin et al. 2003;Pautler et al. 1998). This is a promising strategy although it is really restricted to animal models, relies upon assumptions of the characteristics of manganese tracing, and is suitable only for certain types of white matter fascicles.

In our study, it is highly likely that major neuronal tract bundles are being followed; the question is with what degree of accuracy. Our results show the identification of regions that are likely to be well connected to the defined start point, and other regions that are likely to

be erroneous. However, even in the presence of errors this provides a specificity of *in vivo* tissue identification that is impossible without diffusion MRI fibre tracking methods. Thus a study of the inter-subject variability, when applying this unique tool, is of great potential use in the assessment of conditions that may affect structural connections within the brain.

4.2.4.10. Future applications

We have applied three group mapping techniques, which are complementary to one another and explored different aspects of the behaviour of estimated white matter pathways across individuals. The ability to combine white matter tractography maps across individuals is an essential step towards understanding how white matter pathways are organised and how they vary *in vivo* within populations. By constructing white matter "atlases" it should be possible to investigate diseases of white matter or conditions in which neural trajectories have altered (Johansen-Berg et al. 2004). The next study makes initial steps towards this goal by investigating the structural changes occurring in the optic radiations of patients one year after isolated unilateral optic neuritis using FMT and tractography based group mapping.

4.3. Optic radiation changes after optic neuritis detected by tractography based group mapping

4.3.1. Introduction

As a first step towards the investigation of white matter pathology, group maps in a large group of healthy volunteers have been created using FTM and SPM99. These probabilistic

group maps have the potential to identify differences in white matter connectivity between normal and disease groups.

Optic neuritis provides a useful model for studying the effects of inflammatory demyelination on the central nervous system through the ability of MRI to visualise the optic nerves and the optic radiations. Post-mortem data obtained from patients with MS has suggested that the pathological processes that affect the optic nerve may include a combination of inflammation, demyelination, astrocytosis and axonal destruction (de Preux and Mair 1974). Axonal transection occurring in the acute optic neuritis lesions (Ferguson et al. 1997;Trapp et al. 1998) may lead to Wallerian degeneration and subsequent optic nerve atrophy (Hickman et al. 2002). Trans-synaptic changes may also occur in the lateral geniculate nucleus (LGN) (Madigan et al. 1996), from which the efferent fibres projecting to the visual cortex and constituting the optic radiations originate. A recent study showed that axonal loss in the optic nerves of patients with multiple sclerosis correlated strongly with the selective atrophy of the smaller neurons of the parvocellular layer in the LGN (Evangelou et al. 2001).

This study was carried out to test the hypothesis that the quantitative tract measures (i.e. volume and anisotropy) and the VSC values of the FMT-derived optic radiations change in patients following an episode of optic neuritis. We used tractography based group mapping techniques to perform statistical comparisons between 7 patients and 10 controls.

4.3.2. Methods

4.3.2.1. Subjects

Seven patients (mean age 37.3, SD 9.4, all women), one year after the first episode of isolated unilateral optic neuritis (Compston et al. 1978) and 10 age-matched controls (mean age 33.7,

SD 9.7, all women) were studied. Patients underwent a complete clinical examination, which included tests of visual acuity, such as logMAR (log of the minimum angle of resolution) and Snellen test (Holladay 1997). Most of the patients made a good clinical recovery (note that a visual acuity of 0.0 or better (equivalent to Snellen 6/6) was considered normal) (Table 4.8). Four patients had lesions in the right optic radiation and three of them had lesions in the left tract.

4.3.2.2. MRI protocol

The MRI protocol is as described in the first study.

4.3.2.3. Quantification of tract measures

The mean FA and the total volume of the left and right optic radiations were calculated as described in the previous studies.

4.3.2.4. Group mapping

The details about the group mapping techniques are given in the previous study. In patients and controls two types of maps were constructed: 1) variability group maps, and 2) SPM-derived group maps.

4.3.2.5. Comparisons between groups

1) Quantitative tract measures

The Mann-Whitney U test was used to compare the FA values and the total tract volumes in the left and right optic radiations between patients and controls, and p values less than 0.05 were considered significant.

2) Variability group maps

In order to investigate the differences in the tract overlap between patients and controls, the variability group map that represented the patient group was subtracted from the control variability group map. The resulting "difference" map illustrated the degree of spatial overlap between the two groups.

Since the location of the reconstructed optic radiations depends on starting point placement, the consistency of seed voxel location within the standardised reference frame (MNI space) was assessed for each optic radiation across subjects. Each seed voxel coordinate (defined in native space) was normalised with the same spatial transformation parameters as the VSC maps. In each group, the mean and the standard deviations of the x, y, and z coordinates for the normalised starting voxels were calculated.

3) SPM-derived group maps

Differences in the group maps obtained by the SPM analysis of the unthresholded VSC maps between patients and controls were investigated using a two sample t-test. After model estimation, a one-tailed t contrast was used to test if VSC is reduced in the patient group. Uncorrected SPM(T) maps were generated at $p<0.001$. Statistical inferences were performed from the SPM(T) maps by correcting for multiple comparisons within a mask volume, which was generated *a priori* for the left and right optic radiation using MRIcro (Rorden and Brett 2000). The main cerebral sulci and the labelling of the Talairach and Tournoux atlas

(Talairach and Tournoux, 1988) were used to draw these masks on the high-resolution T1-WI.

In order to investigate whether the areas of significant change in VSC corresponded to any lesions present in the optic radiations, the coordinates of the centre of the lesions were assessed on the normalised b0 images in patients, using the T2-WI as guidance, and compared with the coordinates of the peak of the differences detected using the group maps. Moreover, comparisons between the optic radiation VSC of those patients who had lesions within the optic radiation with those who did not were performed using a two-sample t-test, and p values were corrected for multiple comparisons within the tract mask volume.

Systematic differences in the accuracy of spatial normalization may contribute to differences found in the statistical comparisons between the patient and control group VSC maps. For example, spatial normalisation in the patient group may be influenced by the presence of lesions around the trigones, whereas the control group would have no such influences. A two-sample t-test was therefore applied to test for differences in the normalised b0 images between the two groups.

Table 4.8. Clinical characteristics of seven patients with optic neuritis.

	Age	**Affected eye**	**logMAR**	**Snellen test**
1	36	R	-0.1	6/5
2	30	R	-0.2	6/4
3	25	R	-0.1	6/5
4	34	R	-0.1	6/5
5	39	L	-0.1	6/5
6	54	L	0.062	6/24
7	43	L	-0.08	6/5
Mean (SD)	37.3 (9.4)		-0.01 (0.28)	

R=right, L=left.

4.3.3. Results

4.3.3.1. Comparisons between groups

1) Tract measures

There were no significant differences in the mean FA of the left and right optic radiation between patients and controls (Table 4.9). Patients had lower volumes of both left and right optic radiations compared with controls, but these differences were not significant (Table 4.9).

2) Variability group maps

The "difference" map, which represented the degree of tract overlap between patients and controls, was overlaid onto a structural template (Figure 4.8, A). The "hot" colour scale indicates the proportional degree of overlap between the two groups. For example, the number 0.8 indicates that the voxel in question is within the optic radiation in 80% more controls than patients, -0.4 represents 40% more patients than controls, 0 represents no difference between the two groups (i.e. the voxel is within the optic radiation in the same proportion of patients and controls). In the patient group both optic radiations appear to be localised more laterally in the posterior part of the tracts and more inferiorly than in the control group.

There were no significant differences in starting point placement between the two groups (Table 4.10) which could have affected the location of the reconstructed optic radiations.

3) SPM-derived group maps

Optic neuritis patients demonstrated significantly reduced VSC in both optic radiations when compared with controls. In the left optic radiation the peak difference was adjacent to the

trigone (p=0.04), whilst in the right optic radiation the peak was in the distal part of the tract (p=0.01) (Figure 4.8, B). In the right optic radiation there was a second area posterior and adjacent to the trigone, with reduced VSC in patients (p=0.04) (Figure 4.8, B). The coordinates of these peaks of lower VSC in patients did not correspond to the coordinates of the centre of the lesions visible on the normalised b0 images. Moreover, patients who showed lesions in the optic radiations did not have different VSC compared with those without lesions. Finally, the comparison of the normalised b0 images between patients and controls did not show any differences.

Table 4.9. Differences in fractional anisotropy and tract volume of the left and right optic radiations between patients and controls.

	Patients		**Controls**	
	Left OR	**Right OR**	**Left OR**	**Right OR**
Mean FA (SD)	0.30 (0.04)	0.29 (0.02)	0.32 (0.04)	0.31 (0.03)
Mean tract volume (cm^3) (SD)	4.7 (1.5)	4.2 (1.2)	5.6 (1.6)	5.6 (1.4)

FA= fractional anisotropy; OR= optic radiations.

Table 4.10. Assessment of starting point placement in normalised space (MNI) for each optic radiation in each group of subjects. The mean x (left-right), y (posterior-anterior), and z (inferior-superior), coordinates (in voxel units) and the standard deviations were displayed. The normalised voxel size was 2x2x2 mm.

		Starting voxel coordinates [Mean and (SD)]		
		X	**Y**	**Z**
Left optic radiation	**Patients**	20.6 (1.1)	42.7 (3)	22.7 (1.9)
	Controls	20 (0.9)	43.1 (3.2)	23.1 (1.2)
Right optic radiation	**Patients**	56.3 (1)	43.6 (2.3)	24.1 (1.8)
	Controls	57.2 (1)	45.5 (2.2)	22.7 (1.8)

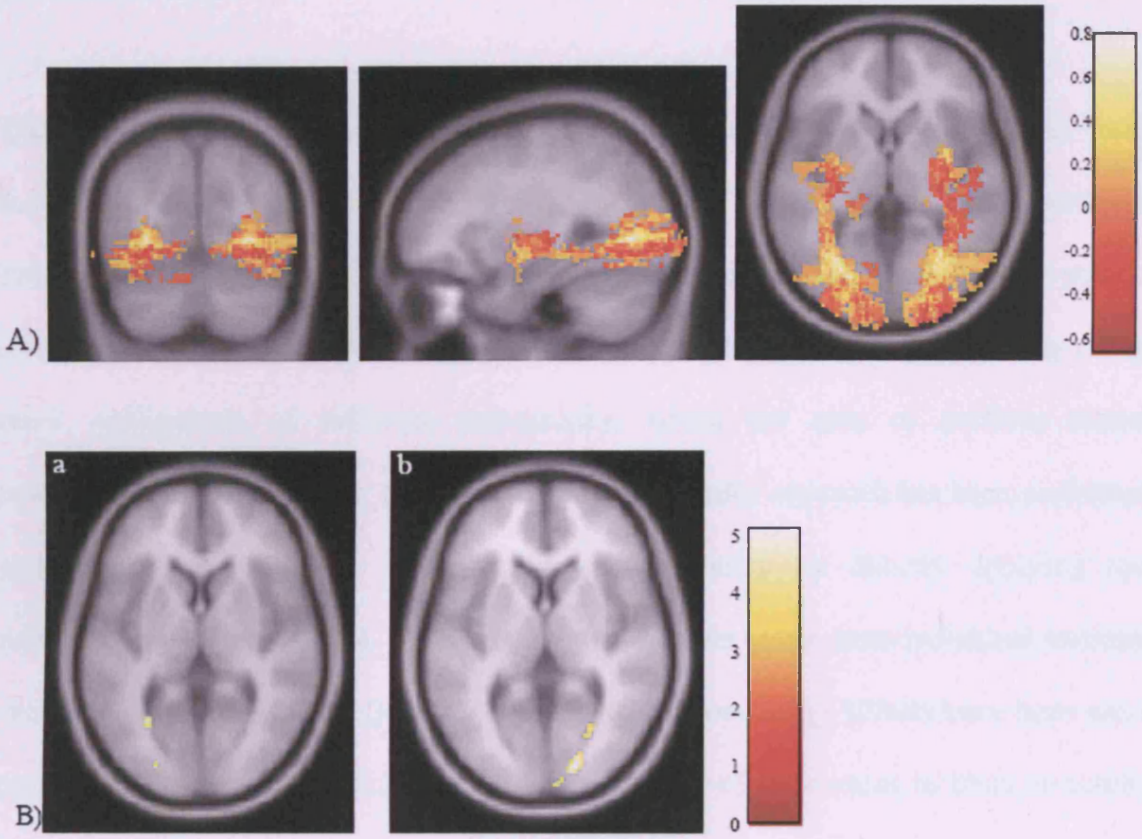

Figure 4.8. (A) Difference in tract overlap between patients and controls overlaid onto a structural template (MNI coordinates x=-30.2 mm, y=-70.1 mm, z=0.4 mm). In the "hot" colour scale, yellow represents a bias towards the control group and red towards the patient group. **(B)** Differences in SPM-derived group maps between patients and controls overlaid onto a structural template. (a) Left optic radiation: patients show reduced VSC than controls with the peak of the difference posterior and adjacent to the trigone (corrected p=0.04; MNI coordinates x=-28 mm, y=-62 mm, z=4 mm). A second area localised more distally shows a trend for reduced VSC in patients (corrected p=0.06; MNI coordinates x=-24 mm, y=-88 mm, z=6 mm). (b) Right optic radiation: patients show reduced VSC than controls with the peak localised in the distal part of the tract (corrected p=0.01; MNI coordinates x=18 mm, y=-88 mm, z=4 mm). A second area posterior and adjacent to the trigone also shows reduced VSC in patients (corrected p=0.04; MNI coordinates x=28 mm, y=-66 z=2 mm). A third area at the termination of the tract shows only a trend (corrected p=0.07; MNI coordinates x=10 mm, y=-96 mm, z=6 mm). The colour scales indicate the t-scores.

4.3.4. Discussion

This study has investigated the hypothesis that differences in anisotropy, volume, location and VSC of the optic radiations reconstructed using FMT (Ciccarelli et al. 2003;Parker et al. 2002c;Parker et al. 2002a) can be found between controls and patients after their first episode of isolated optic neuritis. The group mapping techniques used in this study comprise novel applications of diffusion tractography, which are able to perform statistical comparisons between groups, as discussed earlier. A similar approach has been performed to generate probability group maps of the callosal fibres by directly applying spatial normalisation to the tracked fibres in order to remove gross inter-individual anatomical variability (Xu et al. 2002). Qualitative group comparisons using SPM99 have been recently proposed (Guye et al. 2003). However, investigations of differences in brain connectivity between subject groups have not been previously performed.

Our findings suggest that the optic radiations of patients are localised more inferiorly and more laterally in the posterior part of the tracts (Figure 4.8, A), and have reduced VSC values (Figure 4.8, B), compared with controls. These results were not related to the starting point placement or to a difference in the normalisation process between patients and controls, and therefore could reflect genuine differences between the two groups. These changes in the connectivity and location of the optic radiations could be explained by the mechanism of trans-synaptic degeneration secondary to the optic nerve damage (Evangelou et al. 2001). The presence of lesions around the trigones in four patients, which is well described in optic neuritis (Hornabrook et al. 1992), also needs to be considered. Although there were no differences in VSC values between patients who had lesions in the optic radiations compared with those without lesions, they could have contributed to the observed changes. The lesions could have induced FMT to trace the optic radiations around the lesions rather than across

them (i.e. more laterally and inferiorly in patients), and have reduced the VSC due to the degeneration of locally transected axons (Ferguson et al. 1997;Trapp et al. 1998). Therefore, our findings have to be considered as preliminary and a larger sample of patients needs to be studied to determine whether these changes are independent of local demyelinating lesions.

No differences were found between patients and controls in the estimated anisotropy and tract volumes, although in the patient group a reduction of both types of measures, as a result of axonal degeneration, might have been expected. This may relate to technical limitations, such as the low spatial resolution of DTI (which provides information concerning the average orientation of fibres within the same voxel), or to the low value of FA in controls. This FA value might be due to the presence within the identified optic radiation volume of grey matter regions, which contain the points of origin and termination of the fibres, or to the presence of crossing or curving fibres within voxels. The fact that there were no significant differences in the estimated tract volume might relate to degeneration of the smaller neurons, which appear to be preferentially susceptible to the trans-synaptic damage of the LGN (Evangelou et al. 2001), from which the optic radiation takes origin. However, smaller axons might also be preferentially damaged by the presence of local lesions (DeLuca et al. 2004;Ganter et al. 1999). Moreover, the sample size of the patient group was small and may well have limited the detection of subtle group differences in both measures.

A possible criticism to our study is that in patients a low FA value within the FMT-derived tracts could have led to a low tract volume, making it diffucult to separate low FA from low volume. However, there was no correlation between FA and volume for both optic radiations in the patient group (data not shown), suggesting that it is unlikely that changes in FA would have had a significant effect on the tract volume.

4.4. Conclusion

In this chapter we have demonstrated that diffusion tractography can be used to investigate structural changes in patients with white matter diseases. In the first study of this chapter, we have shown that FMT can be used to quantify the anisotropy and volume of white matter tracts within the brain, and that pathways of complex structure are likely to be less reproducible than tracts of short length and simple fibre organisation. In the second study, we created group maps of the major white matter tracts in a group of normal controls, and found that the greater inter-subject spatial variability is present at the edge of the tracts, while the core of the tracts seems to be well preserved across individuals. In the third study, we employed these group mapping techniques to investigate axonal degeneration in the optic radiations of patients with optic neuritis, and suggested that tractography based group mapping can detect subtle pathological abnormalities beyond macroscopic lesions.

A further exciting prospect for DTI tractography is to elucidate neuronal connections between regions of cortical grey matter (Catani et al. 2003). This will help to answer how structural substrates influence, and are influenced by, functionally segregated neuronal circuits and how functionally integrated networks of high complexity interact. As will be discussed in the last chapter of this thesis, tractography maps may be combined with group maps of functional activation. This should contribute to a greater understanding of how brain function and structure are integrated in the normal healthy population and in pathology.

Chapter 5

Investigation of brain functional reorganisation in PP MS

This chapter describes the results of two studies conducted in normal controls and patients with primary progressive (PP) MS using motor fMRI. The first study reports in detail the fMRI response to active and passive movements of the ankle in a group of healthy subjects. A custom made wooden manipulandum, which allows measurements of movement amplitude, was used to perform the motor task for both the dominant and non-dominant foot. FMRI activation in the cortical and subcortical structures with both active and passive movements, suggesting integrative sensorimotor processing, was detected. The second study investigates PP patients with spinal cord syndrome, who performed the same fMRI experiment. The pattern and extent of their fMRI activations differed from that of healthy subjects. By investigating the correlations between fMRI activity and clinical measures, we concluded that brain functional reorganisation in our cohort of PP patients represented both adaptive and non-adaptive responses to the CNS damage.

5.1 Identifying brain regions for integrative sensorimotor processing with foot movement in healthy subjects

5.1.1. Introduction

Volitional movement is associated with activation of a widespread cortical and subcortical network (Kandel et al. 2000). Imaging studies, investigating the fMRI response to volitional movements in humans, have revealed activation in the bilateral premotor areas and supplementary motor cortex, and primary somatosensory and motor cortex contralateral to the moving limb (Lotze et al. 2000;Luft et al. 2002;Mayer et al. 2001;Rao et al. 1995;Scholz et al. 2000;Ward and Frackowiak 2003). Subcortical activation of the ipsilateral cerebellum and contralateral putamen has also been described (Allison et al. 2000;Gerardin

et al. 2003;Grodd et al. 2001;Luft et al. 2002;Maillard et al. 2000;Scholz et al. 2000;Ward and Frackowiak 2003). Much of this neural activity may be due to the processing of movement-related afferent input.

In an attempt to define the contribution of afferent feedback to the observed movement-generated neural activity, comparisons have been made between active and passive movements. Positron Emission Tomography (PET) (Mima et al. 1999;Weiller et al. 1996;Yetkin et al. 1995) and fMRI studies (Reddy et al. 2001;Yetkin et al. 1995) have consistently demonstrated that both active and passive movements activate the contralateral primary somatosensory and motor areas for hand movements. It has also been shown that premotor areas (premotor and supplementary motor areas) and subcortical structures (contralateral putamen and ipsilateral cerebellum) are similarly activated during both types of movement (Jueptner et al. 1997;Reddy et al. 2001;Thickbroom et al. 2003;Weiller et al. 1996). This finding supports the hypothesis that the basal ganglia and the cerebellum play a role in sensorimotor processing. Involvement of the basal ganglia in sensorimotor integration is of particular interest for understanding the genesis of movement disorders, such as Parkinson disease and dystonia (Abbruzzese and Berardelli 2003). However, other authors have failed to find activation in cortical regions (e.g. premotor cortex and SMA) (Mima et al. 1999) and subcortical areas (e.g. cerebellum and basal ganglia) (Mima et al. 1999;Sahyoun et al. 2004) with passive movements, suggesting that the contribution of the sensory (proprioceptive) input to the activation of these structures, if any, is small.

To investigate this issue further, we compared the fMRI response to identical active and passive movements of the ankle. While previous studies have focused mainly on upper limb joints, we assessed the ankle, as it is commonly and rhythmically activated during locomotion in a similar way to that seen in the present study. In addition, unlike previous studies, we applied the technique of conjunction analysis (Price and Friston 1997) to determine

statistically those regions that were commonly activated by active and passive movements and, thus, may be involved in sensorimotor processing. As a critical control experiment for interpretation of these results, we also assessed whether there was an effect on muscular activity, recorded during training sessions, and ankle joint angle, maintained during the fMRI experiments, on the fMRI response.

5.1.2. Methods

5.1.2.1. Subjects

Eighteen healthy subjects without any neurological or orthopedic impairment were studied (mean age 36.22, SD 11.7, 12 men and 6 women). As will be discussed later, two subjects were excluded from the analysis, leaving a total of 16 subjects (mean age 37.3, SD 11.9, 10 men and 6 women). All subjects were right-foot dominant and gave informed, written consent for the study which had been approved by the local research ethics committee.

5.1.2.2. Motor paradigm

The motor task involved dorsi-plantar flexion of the foot. Subjects were studied supine with their knees flexed and their thighs supported, to ensure that spine was relaxed and minimum amount of movement was transferred to the head during the motor task. Both feet were strapped into a custom made wooden manipulandum (see Figure 5.1) with the rotation axes aligned to the ankle joints, and each side was assessed separately. The paradigm consisted of a pseudo-randomly interleaved block design of 20 second periods of active and passive movement. Each active and each passive period was followed by 20 seconds of rest. For each

session, a total of 11 blocks of active and 11 blocks of passive movement were performed. The active task was auditory-cued by a metronome at a rate of 1.25Hz. The same rate was followed by the operator (O.C.), who elicited the passive movement. The operator visually monitored the execution of the active task to ensure accurate performance throughout both sessions. During the rest and passive periods, subjects were instructed to relax as much as possible without mentally rehearsing the movement. To avoid activation in the visual cortex, subjects were told to keep their eyes closed throughout.

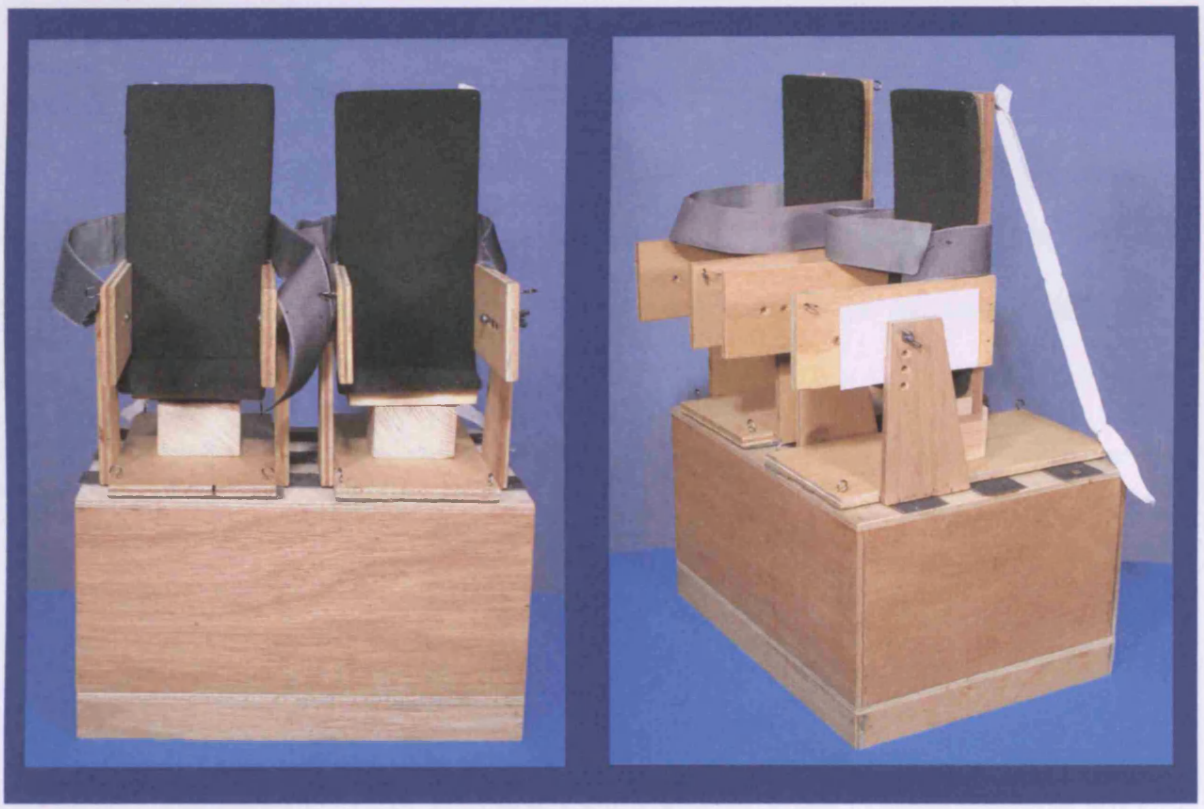

Figure 5.1. Bipedal wooden apparatus used for performing active and passive movements. The subject lay down with the knees supported by cushions and placed both feet in the pedals. Measurements of the ankle joint angle were also obtained.

5.1.2.3. Assessment of muscular activity

All subjects underwent a training session prior to the fMRI that involved simultaneous recording of surface electromyography (EMG) from tibialis anterior and soleus. Firstly, subjects firstly performed a maximal voluntary contraction of tibialis anterior and soleus for 5 seconds. They then performed unilateral active and passive ankle movements for two periods of 20 seconds each. Movements were paced by a metronome at 1.25Hz.

The EMG was sampled at 2 KHz, filtered (30-1000 Hz) and amplified x 2000 (D360 Digitimer Ltd Welwyn Garden City, UK). Data was AD converted (1410-plus CED Cambridge, UK) and recorded using the SPIKE programme (Version 4 CED Cambridge, UK).

The EMG analysis was performed for active and passive movements. Firstly, the maximum EMG signal was obtained by averaging the signal from 1 second period of maximum contraction. Following this, the average EMG signal, recorded over 10 dorsi-plantar flexion cycles was calculated, and then expressed as a percentage of the maximum EMG signal (EMG-percentage).

To investigate the differences in EMG-percentage during active and passive sessions between the left and the right foot, a Wilcoxon signed ranks test was used.

5.1.2.4. Ankle joint angle measurements

The position of each foot at the start of the task was neutral. The angular range of the ankle dorsi- and plantar-flexion during active movement was marked during the training session for each foot, after subjects were asked to move the foot in the most comfortable way. The same angle was maintained by the operator during passive movement. Although each subject was told to maintain the same angle during the fMRI experiments, the ankle joint angle was re-

measured during the first active movement, and this new angle was maintained by the operator throughout the subsequent passive periods.

To investigate the differences in ankle joint angle measured during the fMRI experiments between the left and the right foot, a Wilcoxon signed ranks test was used.

5.1.2.5. MRI protocol

All imaging was performed on a 1.5 T Signa Echospeed MRI system (GE Medical System, Milwaukee, Wis., USA). All subjects had axial brain dual echo fast spin echo (FSE) imaging acquired prior to fMRI experiment, providing proton density and T2-weighted images [TR 2000ms, TE 30/120ms, field of view (FOV) 24 x 24 cm, matrix 256 x 256, 28 contiguous axial slices, 5 mm slice thickness]. The functional protocol consisted of 27 interleaved ascending slices covering the whole brain using a single shot gradient echo EPI [slice thickness 4.6 mm, slice gap 0.4 mm, in-plane resolution 3×3 mm, TR 4 seconds, TE 60 msec, matrix 128×64, 220 scans acquired over 14 min 40 sec].

5.1.2.6. fMRI analysis

The analysis was performed using Statistical Parametric Mapping (SPM99; Wellcome Department of Imaging Neuroscience, London, UK) (Friston et al. 1995;Worsley and Friston 1995). The images were realigned to the first image of each experiment in order to correct for inter-scan movement. Realignment parameters were checked in all subjects, and it was noted that in two cases they were higher than 2 mm in at least one direction; these two subjects were excluded from the study. The images were normalised into a standardised space for the remaining 16 subjects (as defined by the Montreal Neurological Institute (MNI)) and

smoothed using a full width half maximum Gaussian filter of 8 mm. By the central limit theorem, smoothing renders the errors more normal in their distribution, thereby validating the use of standard parametric statistics. Smoothing also helps to compensate for intersubject neuroanatomical variability. For each subject a fixed-effects approach was adopted where the individual smoothed images were then entered into a design matrix in which the realignment parameters were included as covariates of no interest. The contrasts of parameter estimates for active, passive, active greater than passive, and passive greater than active, were generated for each subject. One sample t-tests were then performed for each of these four groups of contrasts using a random-effects approach (Friston et al. 1999;Worsley et al. 1996). Statistical SPM(T) images were thresholded at $p < 0.05$ corrected at voxel level for multiple comparisons across the whole brain to determine the significant main effects. As a "step down" analysis, in order to investigate whether there were clusters of significant activation that did not contain any significant voxels at the chosen threshold (Friston et al. 1996a), a p value < 0.05 corrected at cluster level for multiple comparisons across the whole brain was also used (Poline et al. 1997). Activation maps were spatially identified using MRIcro (Rorden and Brett 2000).

5.1.2.7. Effect of muscular activity and ankle joint angle on the fMRI response

Previous analysis determined that gender did not correlate with either fMRI response or age (data not shown), whilst there was a trend between age and fMRI activity during active and passive movement. Therefore age was considered in the subsequent analyses.

We were interested in assessing the main effects of muscular activity and ankle joint angle on the fMRI response. Three separate linear regression analyses using SPM99 were performed. In the first analysis, EMG-percentage of the tibialis anterior and soleus during the active

periods was included as a regressor, and age as a covariate of no interest. Both negative and positive correlations between the fMRI response to active movement and EMG-percentage were investigated. In the second regression analysis, the ankle joint angle maintained during the fMRI experiments was used as a regressor, and age as a covariate of no interest. Both negative and positive correlations between the fMRI responses to active movements and ankle joint angle maintained during the fMRI experiments were tested. The third regression analysis was the same as the second except that the passive movement related contrasts were substituted for the active ones. Statistical inferences were performed by using a p value < 0.05 corrected at voxel level for multiple comparisons across the whole brain.

5.1.2.8. Conjunction of active and passive movement

To identify the areas of common activation during the active and passive movements, a conjunction analysis (Price and Friston 1997) was used using SPM2 (Wellcome Department of Imaging Neuroscience, London, UK) (Friston et al. 2002). Conjunction analysis assesses the conjoint expression of two effects and tests the null hypothesis that there is no effect of the two tasks on the fMRI response. In order to perform a conjunction analysis, it was necessary to obtain in each fMRI experiment two baselines, i.e. rest periods, one for active movement and one for passive movement. Therefore, the rest periods were divided into two groups: the rest scans acquired after the active periods were considered as baseline for active movement (rest[active]), while the rest scans after the passive periods were used as baseline for passive movement (rest[passive]). For each subject, at the first level, a new design matrix was generated, and the following four contrasts were created: active, rest[active], passive, and rest[passive]. These contrasts were entered into the second level analysis using a multi-subjects conditions and covariates model. Two new contrasts, i.e. active greater than

rest[active], and passive greater than rest[passive] were generated and a conjunction analysis between these two contrasts was performed.

Since more than one contrast per subject was entered into the model, there was a potential risk of violating assumptions about non-sphericity (independently and equally distributed error terms (Friston 1995)). Therefore, a non-sphericity correction was implemented (Friston et al. 2002). The SPM(T) maps generated by the conjunction analysis were thresholded at p value < 0.05 corrected at voxel level for multiple comparisons across the whole brain.

5.1.3. Results

5.1.3.1. Effect of muscular activity and ankle joint angle on the fMRI response

The EMG-percentages calculated for the tibialis anterior and soleus during both active and passive periods are summarised in Table 5.1. All subjects were able to relax completely during passive movements and no stretch-evoked activity was observed. The apparently higher EMG-percentage of the soleus muscle during passive movement was due to movement related noise in two subjects. There were no significant differences in the EMG-percentages during active and passive sessions between the dominant and non-dominant foot. Also, there was no correlation between either tibialis anterior or soleus EMG-percentage during active movement and the fMRI response to active movement.

The mean right and left ankle joint angles, measured during foot movement, were 29.25° (SD 12.20) and 33.31° (SD 14.9), respectively, during the training session, and 28.94° (SD 12.86) and 33.44° (SD 13.8), respectively, during the fMRI experiment. The differences in these joint angles between the two sides were not significant. Further, no correlation was found

between the ankle joint angles maintained during the fMRI experiments and the fMRI responses to either active or passive movement.

Table 5.1. EMG-percentage recorded during the training session.

	Right foot		Left foot	
	Tibialis ant	**Soleus**	**Tibialis ant**	**Soleus**
Mean EMG-percentage of active movements (SD)	12.3 (7.5)	17 (11.7)	15.1 (10.9)	14.2 (10.8)
Mean EMG-percentage of passive movements (SD)	0.8 (0.9)	2.6 (3.1)	0.6 (0.6)	2.5 (2.6)

5.1.3.2. Brain activation

The cortical and subcortical regions significantly activated during active and passive movement of the right and left foot are listed in Table 5.2. Figure 5.2 shows the corresponding SPM(T) maps.

1) Cortical activation during active movement

Both right and left foot active movements were associated with activation of the contralateral primary somatosensory cortex (SI) and primary motor cortex (MI) in the paracentral lobule. Activation was also found, more posteriorly, in the contralateral post-central gyrus, and in the ipsilateral superior temporal gyrus. Additionally, active movement of the right foot activated the ipsilateral supplementary motor cortex (SMA), as well as the bilateral insula and rolandic operculum. In contrast, active movement of the left foot activated the contralateral SMA, contralateral rolandic operculum and supramarginal gyrus, and ipsilateral superior temporal

pole. Thus, the right SMA was significantly activated by both right and left active movements.

2) Subcortical activation during active movement

Active movements of both feet activated the ipsilateral cerebellum in lobules III, IV and V and the rostral vermis. Also, active movement of the right foot activated the contralateral thalamus and cerebellum, whilst active movement of the left foot activated the contralateral posterior and superior putamen.

3) Cortical activation during passive movement

Both right and left foot passive movements were associated with activation of the contralateral SI-MI and the contralateral post-central gyrus. Bilateral activation of the rolandic operculum, with extension to the supramarginal gyrus or to the superior temporal gyrus in either foot, was also found. Passive movement of the left foot additionally activated the contralateral SMA and the bilateral superior temporal pole.

4) Subcortical activation during passive movement

Passive movements of both feet were associated with activation of the ipsilateral cerebellum and contralateral posterior putamen.

5.1.3.3. Differences in brain activation between active and passive movement

A list of all regions which showed a greater activation during active than passive movement is given in Table 5.3. Figure 5.3 shows two of these regions.

Active movements of either feet generated greater activation than passive movement in the ipsilateral SI-MI, ipsilateral cerebellum and ipsilateral superior temporal gyrus. Additionally, active movement of the right foot was associated with greater activation in the ipsilateral SMA and inferior parietal gyrus, as well as in the superior vermis and contralateral superior temporal gyrus, whilst active movement of the left foot generated a greater fMRI response in the contralateral posterior and superior putamen.

Passive movement of both feet did not generate greater activation in any region when compared with active movement.

5.1.3.4. Common activation between active and passive movement

The conjunction analysis of the active and passive contrasts, revealed that several regions were commonly activated during both active and passive movements of each foot (Table 5.4). Figure 5.4 shows the corresponding SPM(T) maps.

Significant activation was found in the contralateral SI-MI (paracentral lobule), contralateral SMA, bilateral rolandic operculum and insula, ipsilateral cerebellum, and contralateral posterior putamen. Additionally, conjunction of the left foot showed a common activation in the ipsilateral superior temporal gyrus and contralateral superior temporal pole.

Table 5.2. Brain regions activated by movement of the right and left foot.

Right foot				Left foot			
Active movement	**x y z**	**Zscore**	**P value at voxel level**	**Active movement**	**x y z**	**Zscore**	**P value at voxel level**
Right cerebellum	18 -34 -30	5.52	0.003	Left cerebellum	-18 -38 -28	6.48	0.0001
Left SI-MI	-6 -10 68	5.48	0.004	Right SI-MI, SMA, post-central g.	8 -38 64	6.19	0.0001
Vermis	2 -48 -8	5.46	0.005	Left sup. temporal g.	-46 -30 12	5.56	0.003
Right SMA	8 2 56	5.44	0.005	Vermis	-2 -52 -6	5.49	0.004
Left thalamus	-16 -16 10	5.26	0.014				
Left post-central g.	-10 -40 64	5.08	0.038				
			P value at cluster level (cluster size)				**P value at cluster level (cluster size)**
Right sup. temp. g. /rolandic op.	48 -26 18	4.89	0.0001 (506)	Right putamen	26 -6 12	4.77	0.0001 (771)
Right insula	46 6 -4	4.68	0.004 (176)	Right rolandic op. /supramarginal g.	46 -26 16	4.29	0.0001 (543)
Left cerebellum	-34 -58 -32	4.44	0.01 (150)	Left sup. temp. pole	-50 4 -2	4.30	0.046 (129)
Left insula /rolandic op.	-48 4 2	4.27	0.012 (143)				
Passive movement			**P value at voxel level**	**Passive movement**			**P value at voxel level**
Left post-central g.	-8 -36 62	5.80	0.001	Right SMA	8 -18 70	5.95	0.0001
Left SI-MI	-4 -20 64	5.25	0.015	Right SI-MI, and post-central g.	8 -34 68	5.80	0.001
				Left cerebellum	-16 -38 -32	5.24	0.016
			P value at cluster level (cluster size)				**P value at cluster level (cluster size)**
Right cerebellum	22 -36 -28	4.87	0.0001 (415)	Right rolandic op. /supramarginal g.	50 -26 18	4.85	0.0001 (842)
Left putamen	-30 -6 6	4.53	0.006 (183)	Right sup. temp. pole	52 6 -2	4.45	0.001 (208)
Left sup. temp. g. /rolandic op.	-46 -28 20	4.33	0.01 (169)	Left rolandic op. /supramarginal g.	-50 -20 20	4.20	0.004 (170)
Right sup. temp. g. /rolandic op.	48 -26 18	4.25	0.004 (200)	Right putamen	32 -8 2	4.04	0.002 (196)
				Left sup. temp. pole	-44 6 2	3.79	0.036 (109)

Regions are listed accordingly to their Z-scores. Coordinates are given in mm in MNI space. P values are corrected at voxel level for multiple comparisons; as a "step down" analysis, p values corrected at cluster level for multiple comparisons across the whole brain are also shown. SI-MI = primary sensorymotor, SMA = supplementary, g. = gyrus, sup. = superior, post. = posterior, temp.=temporal, g.=gyrus, op.operculum.

a)

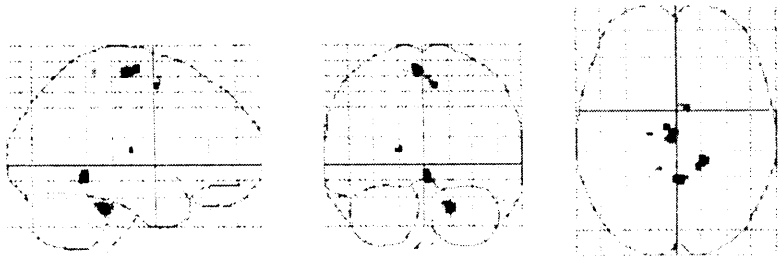

b)

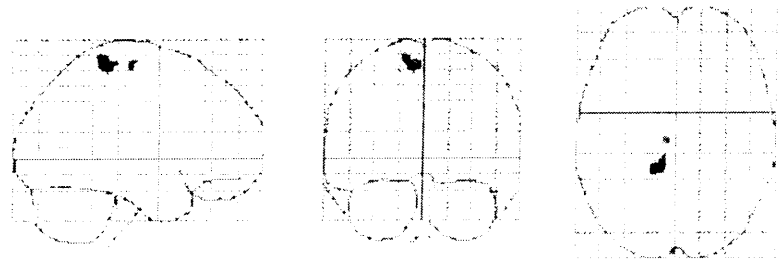

c)

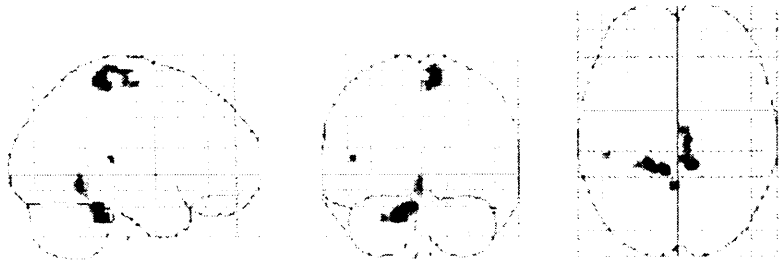

d)

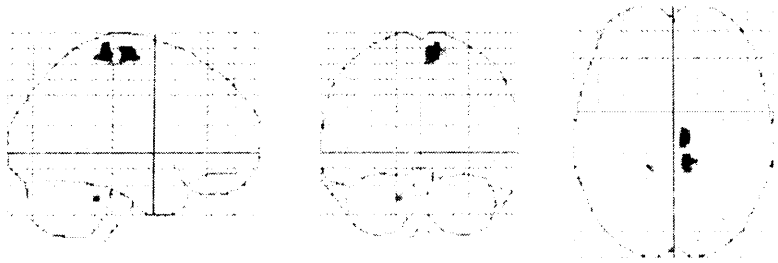

Figure 5.2. Brain activation during movements of the right (a and b) and left (c and d) foot.
(a) Active movement of the right foot activates the right cerebellum, left SI-MI, rostral vermis, right SMA, left thalamus and left post-central gyrus.
(b) Passive movement of the right foot activates the left SI-MI and post-central gyrus.
(c) Active movement of the left foot activates the left cerebellum, right SI-MI and SMA, right superior temporal gyrus and rostral vermis.
(d) Passive movement of the left foot activates the right SMA and SI-MI, and the left cerebellum.
The SPM(T) maps were thresholded at $p < 0.05$ corrected at voxel level for multiple comparisons across the whole brain and overlaid onto glass brain.

Table 5.3. Brain regions activated to a greater extent by active movement than passive movement.

Right foot				Left foot			
Regions	**x y z**	**Zscore**	**P value at voxel level**	**Regions**	**x y z**	**Zscore**	**P value at voxel level**
Right SI-MI, SMA	8 -26 60	5.81	0.001	Left cerebellum	-10 -40 -20	5.76	0.001
Right sup. temporal g.	64 -22 4	5.32	0.01	Left SI-MI	-6 -28 60	5.07	0.04
			P value at cluster level (cluster size)				**P value at cluster level (cluster size)**
Right cerebellum/ vermis	10 -46 -14	4.98	0.0001 (1025)	Left sup. temporal g.	-48 -30 8	4.25	0.01 (173)
Right inf. parietal g.	46 -42 44	4.16	0.033 (112)	Right putamen	26 -6 14	3.83	0.069 (110)
Left sup. temporal g	-56 -26 6	4.03	0.003 (180)				

Regions are listed accordingly to their Z-scores. Coordinates are given in mm in MNI space. P values are corrected at voxel level for multiple comparisons; as a "step down" analysis, p values corrected at cluster level for multiple comparisons across the whole brain are also shown. SI-MI = primary sensorymotor, SMA = supplementary, g. = gyrus, sup. = superior, inf. = inferior.

a)

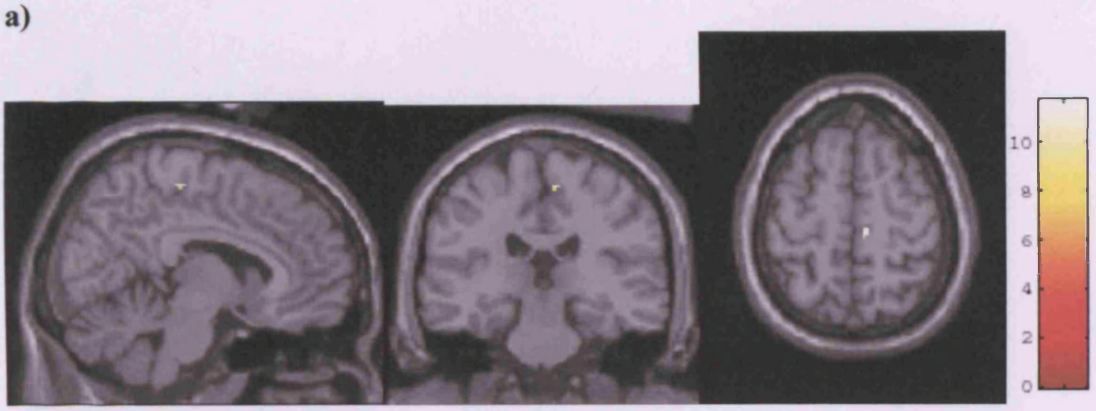

b)

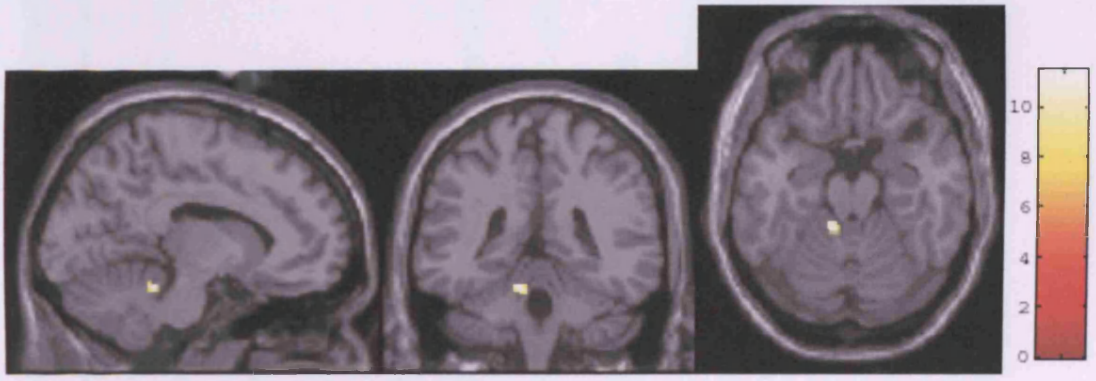

Figure 5.3. Examples of brain regions which are activated to a greater extent by active movement than passive movement.
(a) Right SI-MI showed a greater activation during active movement of the right foot than passive (MNI coordinates 8 -26 60).
(b) Left cerebellum showed a greater activation during active movement of the left foot than passive (MNI coordinates -10 -40 -20).
The SPM(T) maps were thresholded at $p < 0.05$ corrected at voxel level for multiple comparisons across the whole brain and overlaid onto single-subject T1 template.

Table 5.4. Brain regions commonly activated during active and passive movements detected by the conjunction analysis.

Right foot				Left foot			
Regions	**x y z**	**Zscore**	**P value**	**Regions**	**x y z**	**Zscore**	**P value**
Left SI-MI	-10 -40 64	7.83	0.0001	Right SI-MI	10 -38 66	Inf	0.0001
Left SMA	-4 -20 62	7.00	0.0001	Right SMA	8 -20 72	Inf	0.0001
Right rolandic operculum	42 -28 22	6.57	0.0001	Left cerebellum	-16 -38 -30	Inf	0.0001
Right cerebellum	18 -34 -26	6.24	0.0001	Right rolandic operculum	42 -28 18	Inf	0.0001
Left rolandic operculum	-48 -26 20	5.75	0.001	Left insula/rolandic operc.	-50 6 -2	6.36	0.0001
Left putamen	-30 -2 8	5.45	0.005	Left sup. temporal g.	-48 -26 16	6.07	0.0001
Left insula	-48 2 2	5.27	0.012	Right sup. temporal pole	56 6 0	6.02	0.0001
Right insula	52 6 0	5.21	0.016	Right putamen	32 -8 4	5.78	0.001
				Right insula	44 6 4	5.02	0.038

Regions are listed accordingly to their Z-scores. Coordinates are given in mm in MNI space. All the p values listed are corrected at voxel level for multiple comparisons across the whole brain. SI-MI = primary sensorymotor, SMA = supplementary, g. = gyrus, sup. = superior.

a)

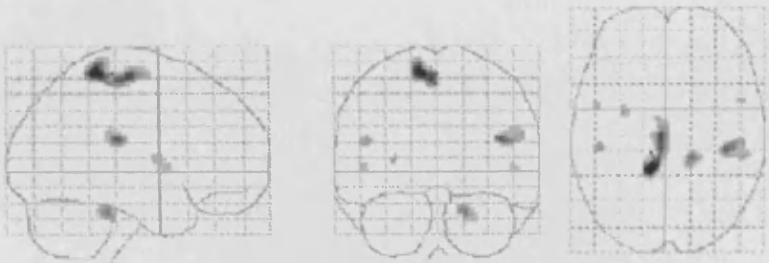

b)

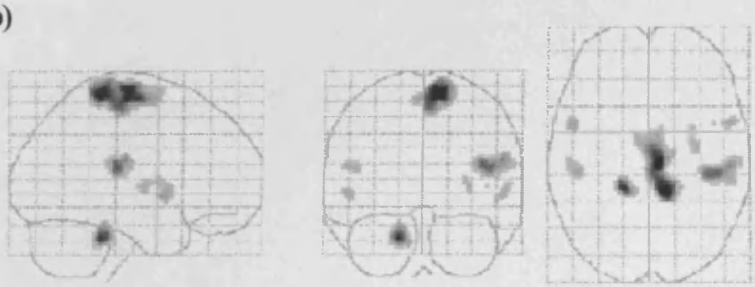

Figure 5.4 (a and b)

Figure 5.4. Brain regions which were statistically commonly activated during active and passive movements.
(a and c*) The conjunction analysis of the active and passive contrasts of the right foot shows significant activation in the left SI-MI and SMA, in the right cerebellum, in the left putamen, in the bilateral rolandic operculum and in the bilateral insula.
(b and d)** The conjunction analysis of the active and passive contrasts of the left foot shows significant activation in the right SI-MI and SMA, in the left cerebellum, in the bilateral rolandic operculum and insula, in the left superior temporal gyrus and in the right superior temporal pole.
The SPM(T) maps were thresholded at $p < 0.05$ corrected at voxel level for multiple comparisons across the whole brain and overlaid onto glass brain (a and b) and onto single-subjects T1 template in axial sections 2 mm apart (c* and d**).

* Figure 5.4 (c) ** Figure 5.4 (d) are displayed on the following two pages, respectively.

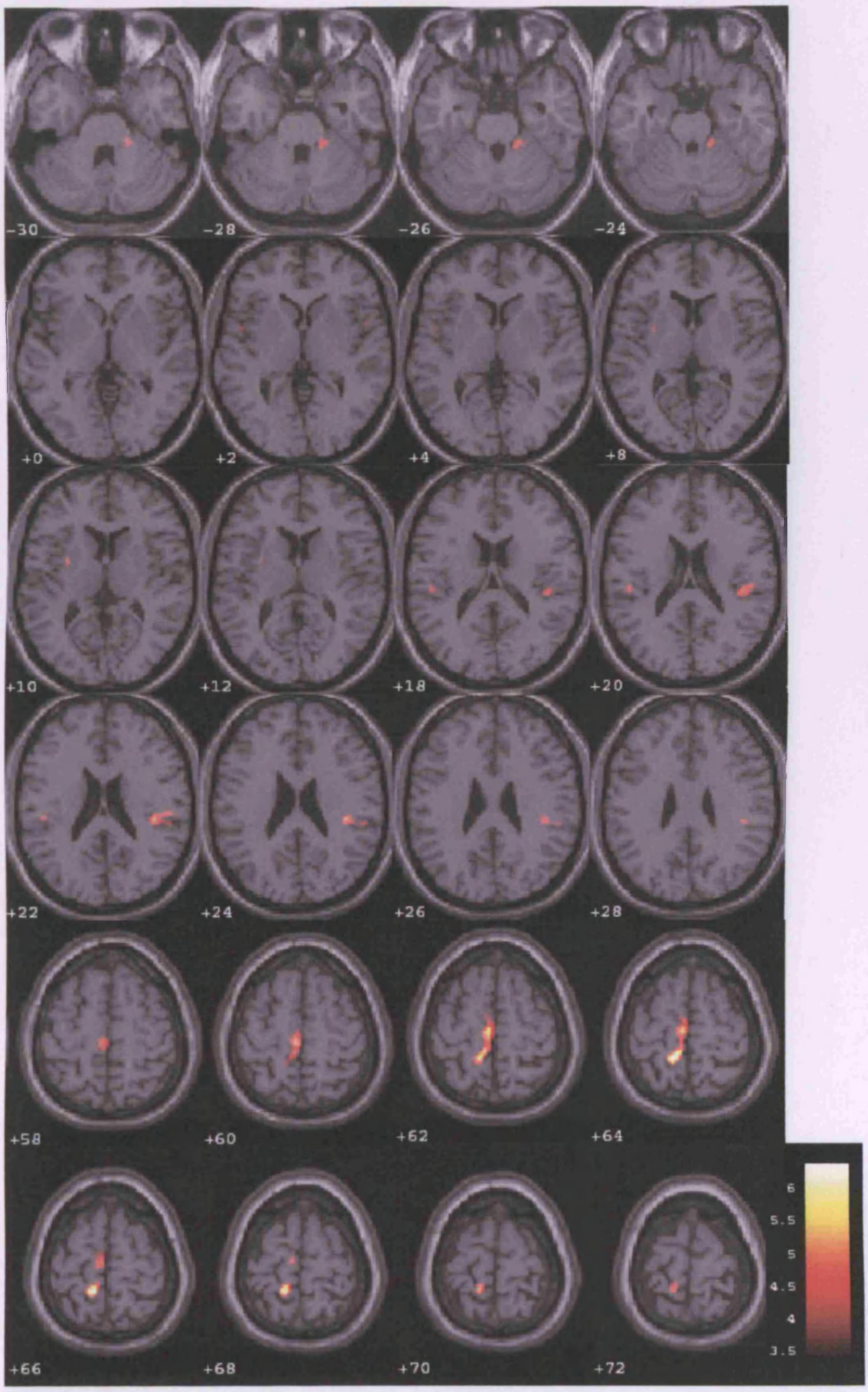
-30
-28
-26
-24
+0
+2
+4
+8
+10
+12
+18
+20
+22
+24
+26
+28
+58
+60
+62
+64
+66
+68
+70
+72
6
5.5
5
4.5
4
3.5

Figure 5.4 (c).

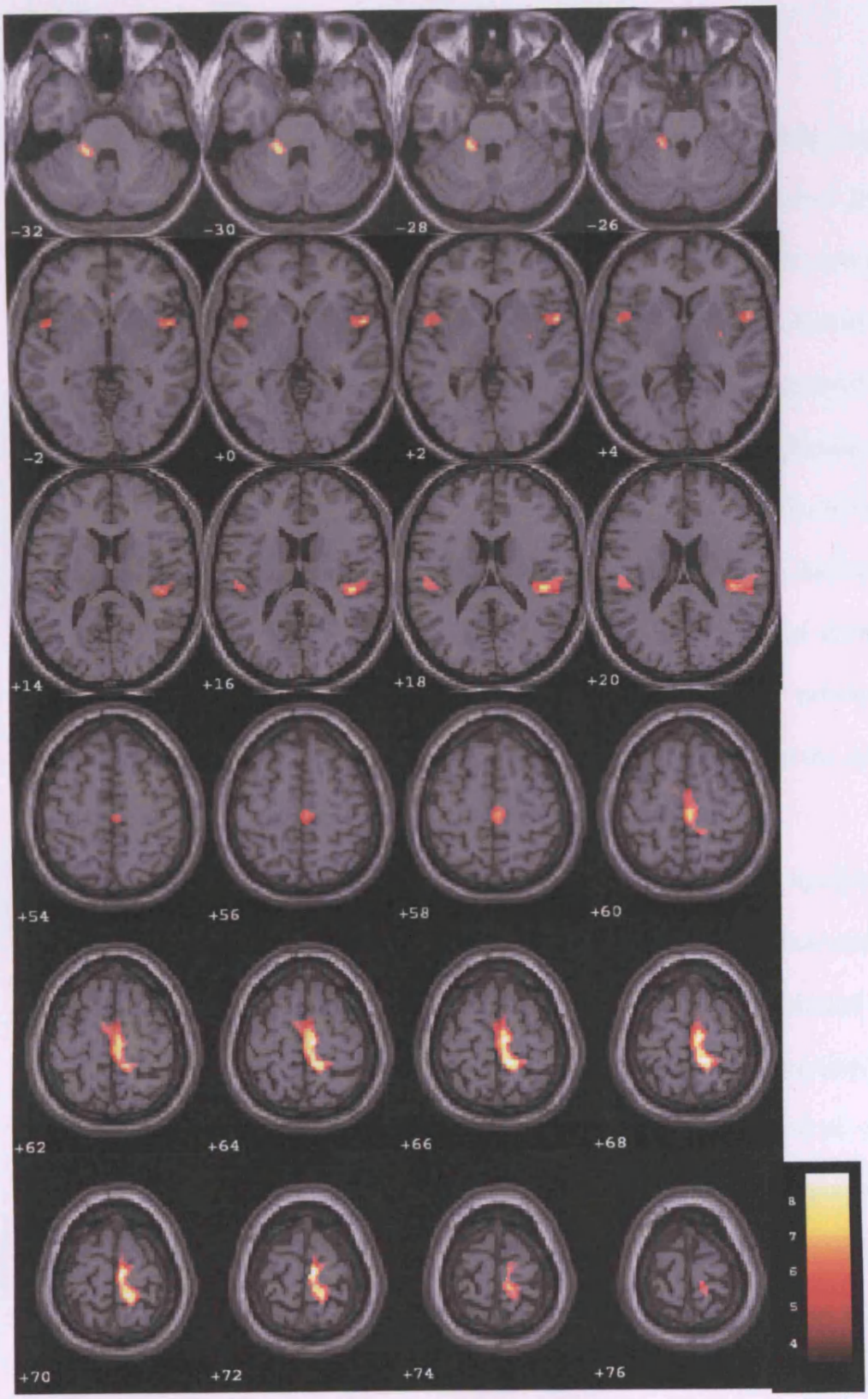

Figure 5.4 (d).

5.1.4. Discussion

The present study identified regions that were commonly activated during passive and active ankle movements using fMRI. Such a study required that the movements performed were identical and that subjects were completely relaxed during the passive movement. Previous PET studies (Mima et al. 1999) have used computer controlled torque motors to standardise the movement amplitude and speed between conditions. Here, we also ensured careful control of the amplitude and timing of movements by using a wooden manipulandum. Our subjects had a training session, with recording of surface EMG prior to the study, to ensure that they relaxed fully during the passive movements. In addition, we confirmed that small differences of voluntary muscle recruitment for movement between subjects were not strong determinants of the magnitude of the fMRI activation. This finding extends previous fMRI data (Thickbroom et al. 1999), which also failed to show a strong effect of the level of force on the fMRI activation with dynamic finger flexion.

We have described an extensive network that is common to or "shared" by active and passive movements. Looking at the results obtained in both feet using conjunction analysis, a general fMRI pattern can be identified, which includes activation in the contralateral primary motor and somatosensory cortex, which has been consistently demonstrated previously (Alary et al. 1998;Carel et al. 2000;Mima et al. 1999;Sahyoun et al. 2004;Weiller et al. 1996). We also found a significant activation in the premotor cortex (the bilateral rolandic operculum), contralateral SMA, bilateral insula, ipsilateral cerebellum and contralateral putamen. Such common activation during active and passive movements might reflect the activation of regions that are directly involved in sensorimotor processing. Therefore, the fMRI response in the premotor and subcortical structures might reflect the contribution of these regions in processing sensory information. This is supported by the finding that proprioceptive

discrimination may be impaired after cerebellar (Grill et al. 1994;Shimansky et al. 1997) and basal ganglia lesions (Demirci et al. 1997). Abnormalities in these regions of sensorimotor integration may have a role in the aetiology of movement disorders, such as Parkinson's disease (Abbruzzese and Berardelli 2003;Middleton and Strick 2000) and dystonia (Hallett 1995). This type of evidence could also help to explain clinical characteristics of these diseases, such as the complexity of the patterns of muscle activation and stimulus sensitivity in dystonia.

The identification of activation in the premotor cortical and subcortical structures during passive movement confirms earlier findings in studies employing finger (Reddy et al. 2001;Thickbroom et al. 2003) or elbow movement (Weiller et al. 1996), whilst it is in contrast with the findings of others authors (Mima et al. 1999;Sahyoun et al. 2004). Sahyoun et al. did not identify significant subcortical activation with passive movement of the right foot, although they reported activation in the premotor areas (Sahyoun et al. 2004). Mima et al reported that only the contralateral primary and sensory somatosensory areas were activated by the passive movement of the right middle finger (Mima et al. 1999). There are several possible reasons for these discrepancies. The most likely explanation may simply be the different sensitivity of the imaging experiments. Differences could also arise from differences in joints examined or in types of afferent stimulation. In particular, Mima et al (Mima et al. 1999) avoided cutaneous afferent stimulation, whilst our task involved a continuous cutaneous stimulation of the plantar aspect of the foot. Thus, differences in the pattern and context of afferent stimulation may result in different activation patterns. For example, the cerebellum is notable for showing context-specific responses to afferent input (Prochazka 1989). Neurons within the inferior olive, which projects to the cerebellum, may show differential responses to afferent stimulation depending on whether it is actively or passively generated, and depending on whether or not the stimulus is normally associated with a

particular movement (Gellman et al. 1985;Hartmann and Bower 2001;Houk and Wise 1995). Therefore, the relationship between the nature of afferent stimulation and patterns of subcortical brain activation deserves further study.

We have demonstrated that active movements induced a greater fMRI response than passive movement in the ipsilateral primary motor and somatosensory cortex and in the ipsilateral SMA. This suggests greater relative involvement of the ipsilateral motor and premotor cortices in the control of simple foot movement than for similar hand movements (Reddy et al. 2001;Weiller et al. 1996). Luft et al. (Luft et al. 2002) found that knee movement showed a lower lateralisation of the primary motor and somatosensory cortex than other upper limb tasks, suggesting that the ipsilateral cortex has a significant specific role in the motor processing of lower limb movement. We also found that the ipsilateral cerebellum and the contralateral posterior putamen showed a significantly greater activation during active movement than passive. These findings are in general agreement with the study of Sahyoun et al (Sahyoun et al. 2004), that reported a greater activation during active movements in similar regions, extending to the contralateral cortical and ipsilateral subcortical regions.

In conclusion, our investigation of passive movements emphasises the wide distribution of afferent input into brain regions involved in motor control of the foot. Abnormalities of sensory processing or sensorimotor integration might be associated with a broad range of pathologies of movement control. FMRI studies, aimed at identifying the common functional activation during active and passive movements might assist in this characterisation. More generally, since passive movements do not depend on conscious motor planning or the ability to execute a movement, such studies may prove valuable in the investigation of neurological patients, such as those with multiple sclerosis, as shown in the next study.

5.2. Role of functional brain changes in PP MS

5.2.1. Introduction

Recent fMRI studies have shown that in patients with MS the pattern of brain activation during motor tasks differs from that of normal controls, in both location and extent of activation (Filippi and Rocca 2003;Pantano et al. 2002a;Rocca et al. 2003a). The key question is whether these functional changes are adaptive and contribute to maintain clinical function, or are non-adaptive. The importance of addressing this question is that, if the cortical fMRI changes are adaptive and limit the impact of brain injury, they might present targets for future therapies.

Previous fMRI studies aimed to answer this question, and reported increased functional activation with increasing brain and spinal cord pathology measured by conventional and non-conventional MRI (Filippi et al. 2002b;Lee et al. 2000;Pantano et al. 2002b;Reddy et al. 2000a;Rocca et al. 2002a;Rocca et al. 2003a). Since patients were performing the motor task using unaffected limbs, the authors suggested that cortical reorganisation following MS tissue damage has an adaptive role. However, these studies mainly employed active movement of the hand, which is more extensively represented in the motor cortex than is the foot (Penfield W. and Rasmusseun T. 1950). The fMRI response to foot movement in patients with MS has not been widely investigated, although movement at the ankle joint is critical for walking and directly relates to mobility.

Primary progressive (PP) MS (Thompson et al. 2000) offers the possibility of investigating the mechanisms of progression of disability in MS without the confounding factors of clinical attacks and high MRI activity (Thompson et al. 1991;Wolinsky 2003). The majority of patients with PP MS present with a progressive spinal cord syndrome and, therefore, reduced

mobility is one of the main areas of disability. Hence, investigation of brain fMRI response to foot movement might provide insights into the mechanisms underlying the disability.

A common issue with fMRI studies of pathology is that the motor task may not be matched for performance between patients and controls, which could contribute to differences in fMRI activation between the groups. A possible solution is to employ passive movement, which theoretically activates the motor output via the sensory afferents only, as discussed in the previous study. A recent fMRI study in patients with relapsing-remitting MS used passive movement of the third finger and reported activation changes that were felt to reflect true functional reorganisation of the motor pathways (Reddy et al. 2002).

Therefore, the aim of this study was to investigate functional reorganisation in patients with PP MS using the motor paradigm and the custom made wooden manipulandum employed in the previous study. The paradigm included both active and passive movement of the dominant and non-dominant foot, and all subjects underwent a training session, during which measurements of muscular activity were obtained by using superficial electromyography (EMG). Movement amplitude during the fMRI acquisition was also recorded and taken into account in the analysis. To investigate further the role of functional changes in patients, the relationships between the fMRI responses to active and passive movements and clinical and brain and spinal cord MRI measures were assessed. We expected a greater fMRI response in patients with lower disability, along with lower brain and spinal cord damage, supporting the hypothesis of adaptive functional changes.

5.2.2. Methods

5.2.2.3. Subjects

We recruited 14 patients with PP MS (Thompson et al. 2000) (mean age 46.6 SD 11.3, 9 men and 5 women), who attended the National Hospital for Neurology and Neurosurgery in London. All patients underwent conventional neurological assessment and were scored on the EDSS (Kurtzke 1983), 25foot Timed Walk Test (TWT), Paced Auditory Serial Addition Test (3 seconds) (PASAT), Nine Hole Peg Test (9HPT) (Cutter et al. 1999), and Ashworth scale for spasticity (Bohannon and Smith 1987). Patients with PP MS affected by spinal cord syndrome, with lower limb spasticity = 3 at the Ashworth scale, and normal or mild proprioceptive deficit, were recruited. One patient could not complete the fMRI experiment and was then excluded from the analysis, leaving a total of 13 patients (mean age 46 SD 11.5, 9 men and 4 women).

The characteristics of the healthy controls included in this study are described above (paragraph 5.1.2.1).

All patients and controls were right-foot dominant. All subjects gave informed, written consent before the study, which was approved by the local research ethics committee.

The difference in age between patients and controls was not significant ($p=0.06$, two sample t test). Moreover, there was no significant effect of age on the fMRI response in both patients and controls at p value < 0.05 corrected for multiple comparisons (data not shown). Therefore, age was not considered in the subsequent statistical modelling.

5.2.2.4. Motor paradigm

The motor paradigm is described above (paragraph 5.1.2.2).

5.2.2.5. Assessment of muscular activity

The assessment of muscular activity was performed as reported above (paragraph 5.1.2.3).

In the patient group, to investigate the differences in EMG-percentage of active and passive movements between the dominant and non-dominant foot, a Wilcoxon signed ranks test was used. The same analysis was performed in the control group, as reported above (paragraph 5.1.2.3). Differences in EMG-percentage between patients and controls were assessed using a Mann-Whitney U test.

5.2.2.6. Ankle joint angle measurements

Measurements of the movement amplitude are described above (paragraph 5.1.2.4).

In the patient group, a Wilcoxon signed ranks test was used to investigate the differences in ankle joint angle during the fMRI between the dominant and non-dominant foot. The same analysis was performed in the control group, as reported above (paragraph 5.1.2.4). To assess differences in movement amplitude between patients and controls, a Mann-Whitney U test was used. Furthermore, the ankle joint angle was taken into account (as a covariate) in the following analysis as a possible factor contributing to the differences in the fMRI response between the two groups.

5.2.2.7. fMRI protocol and analysis

The functional protocol is described in paragraph 5.1.2.5. The analysis of the fMRI data in patients was performed using SPM99 and included the following steps (which are identical to those used in the analysis of controls described above (paragraph 5.1.2.6)): realignment, normalisation, and smoothing. A fixed effects approach was adopted for each patient's foot and the contrasts of parameter estimates for active and passive were generated. For each foot,

two types of analyses were repeated for active and passive movement. Firstly, to investigate the behavior of the fMRI response in patients, one-sample t test was performed for each contrast using a random-effects approach (Friston et al. 1999) (Worsley et al. 1996). This is the same approach that was used to investigate the fMRI response in controls (see paragraph 5.1.2.6). Statistical SPM(T) images were thresholded at $p < 0.05$ corrected at voxel level for multiple comparisons across the whole brain to determine the significant main effects. Secondly, to investigate differences in the fMRI response between patients and controls, a conditions and covariates model was employed, entering the subject specific contrasts; patient and control groups were considered as conditions and ankle joint angle as covariate. Active and passive movements were assessed with separate models. For each model, two contrasts were estimated, e.g. patients greater than controls and controls greater than patients. Statistical SPM(T) images were thresholded at $p < 0.05$ corrected at voxel level for multiple comparisons within ROIs which were chosen *a priori*. These ROIs were created as spheres or boxes and centred on brain structures which are known to be part of the motor network and/or were reported in previous publications (Filippi et al. 2002b;Filippi and Rocca 2003;Rocca et al. 2002b;Sahyoun et al. 2004), using MRIcro (Rorden and Brett 2000) as a reference. A list of the ROIs used for this analysis is provided in Table 5.5.

Table 5.5. Regions of interest defined *a priori* for the SPM99 analysis.

Regions	**Shape and radius (r) or dimensions (d) in mm**	**x, y, z of the centre**
Right paracentral lobule (SI-MI, area 3,1,2,4)	Sphere, r=15	10 -32 68
Left paracentral lobule	Sphere r=15	-10 32 68
Right cerebellum	Sphere, r=15	25 -48 -37
Left cerebellum	Sphere, r=15	-25 -48 -37
Right supplementary motor area (SMA)	Sphere, r=15	8 -6 64
Left supplementary motor area	Sphere, r=15	-8 -6 64
Right premotor cortex	Sphere, r=15	20 -8 64
Left premotor cortex	Sphere, r=15	-20 -8 64
Superior vermis	Box, d=15×25×20	0 -55 -16
Inferior vermis	Box, d= 15×18×20	0 -61 -40
Right thalamus	Sphere, r= 12	13 -17 7
Left thalamus	Sphere, r= 12	-13 -17 7
Right putamen (post. part)	Sphere, r= 12	30 0 9
Left putamen	Sphere, r= 12	-30 0 9
Right caudate	Sphere, r= 12	14 13 13
Left caudate	Sphere, r= 12	-14 13 13
Right precuneus	Sphere, r=15	8 -54 64
Left precuneus	Sphere, r=15	-8 54 64
Right postcentral gyrus (SII, area 5 and 7)	Sphere, r= 12	20 -36 72
Left postcentral gyrus	Sphere, r= 12	-20 -36 72
Right superior frontal gyrus (ant. part, area 10)	Sphere, r= 12	28 60 13
Left superior frontal gyrus	Sphere, r= 12	-28 60 13
Right middle frontal gyrus	Sphere, r= 12	37 34 40
Left middle frontal gyrus	Sphere, r= 12	-37 34 40
Right middle cingulate cortex(area 24)	Sphere, r= 12	7 -12 44
Left middle cingulate cortex	Sphere, r= 12	-7 -12 44
Right inferior parietal gyrus (area 40)	Sphere, r= 12	48 -24 20
Left inferior parietal gyrus	Sphere, r= 12	-48 -24 20
Right rolandic operculum	Sphere, r= 12	55 9 4
Left rolandic operculum	Sphere, r= 12	-55 9 4
Right sup. temporal gyrus	Sphere, r=10	54 15 -12
Left sup. temporal gyrus	Sphere, r=10	-54 15 -12
Right inferior frontal gyrus	Sphere, r= 12	46 31 12
Left inferior frontal gyrus	Sphere, r= 12	-46 31 12
Right insula	Sphere, r= 10	44 12 -2
Left insula	Sphere, r= 10	-44 12 -2

5.2.2.8. Structural MRI protocol and analysis

Brain lesion load All subjects had axial brain dual echo FSE imaging acquired prior to fMRI experiment, providing PD and T2-WI (see paragraph 5.2.1.5 for acquisition parameters). These images were displayed on a Sun workstation (Sun Mycrosystems, Mountain View, CA using the DispImage software package). Lesion loads were calculated by a single observer (O.C.) blinded to the clinical details on the PD images (with reference to the T2 images) using a semiautomated local contour thresholding technique (Plummer 1992).

Brain atrophy. Patients underwent also a 3D inversion-prepared fast spoiled gradient recall (FSPGR) sequence of the brain [TR 13.3ms, TE 4.2ms, FOV 300×225, matrix 256×160 reconstructed as 256×256 for a final in plane resolution of 1.17 mm, 124 contiguous axial slices, 1.5 mm slice thickness]. Images were segmented into white matter (WM), grey matter (GM) and cerebrospinal fluid (CSF) using SPM99 accordingly to a protocol previously described (Chard et al. 2002b). The SPM99 outputs were checked to ensure that the segmentation was successful. Images were displayed on a Sun workstation and lesions were outlined using a semiautomated local thresholding technique (Plummer 1992). The lesion contours were then subtracted from WM, GM and CSF masks, producing four mutually exclusive masks (i.e. WM, GM, CSF, and lesions) with their associated volumes in ml. Volumes were estimated with a caudal cut-off point which was defined as the most cranial slice of the cord not-containing cerebellum. Brain parenchymal fraction (BPF) was calculated as WM + GM + lesion mask volumes divided by the total intracranial volume, which was defined as WM + GM + CSF + lesion mask volumes. Grey matter fraction (GMF) was calculated as GM mask volume divided by the total intracranial volume. Although the impact of lesions' masks on brain tissue fraction is known to be small (lesion fraction in our cohort

was of 0.6% of total intracranial volume), considering all lesions within WM further reduces this miscalculation (all lesions outlined on the FSPGR were indeed in the WM).

Spinal cord atrophy. Patients also had a volume-acquired, inversion-prepared, fast spoiled-gradient (FSPG) echo sequence of the spinal cord [TR 15.6ms, TE 4.2ms, TI 450ms, flip angle 20°, FOV 250×250, matrix 256×256, 60 slices, 1 mm slice thickness]. Five contiguous 3mm axial slices (perpendicular to the spinal cord) were reformatted from the caudal landmark of C2-3 inter-vertebral disc, and a coil radiofrequency uniformity correction was applied (Tofts et al. 1994). Cord area was measured using a semiatomated method previously described (Losseff et al. 1996b).

Spinal cord lesions. Finally, patients also underwent an FSE sequence of the whole spinal cord [TR 2500ms, TE 45/90ms, echo train length 16, FOV 48×48, matrix 512×512, 9 contiguous sagittal slices, 3 mm slice thickness]. On the printed images, the number of spinal cord lesions was identified by expert radiologists.

Correlations between all the above mentioned structural MRI measures and EDSS were investigated using Spearman's correlation coefficient.

5.2.2.9. Correlations between fMRI and clinical and structural MRI measures

In order to investigate whether clinical measures (e.g., EDSS, TWT, PASAT, 9HPT, Ashworth score), brain structural MRI measures (e.g., T2 lesion load, BPF, GMF), and spinal cord MRI measures (e.g., atrophy and lesion number) have an effect on the fMRI response of patients, a linear regression analysis using SPM99 was performed separately for each

measure. An arbitrary value of 20 for spinal cord lesions was given to the patients who showed diffuse T2 signal change in the spine. Both negative and positive correlations between the fMRI response to active and passive movement and the clinical or MRI measure were investigated separately. To reduce the risk of obtaining false positive results, due to the high number of correlations tested, statistical inferences were performed by using a p value < 0.01 corrected at voxel level for multiple comparisons within the ROIs (Table 5.5). No further correction for the number of ROIs considered was applied, for the following reasons: (i) Neither the BOLD response within ROIs, nor the clinical and MRI measures, can be considered as independent tests, (ii) This is an exploratory study, and further work is needed to confirm our findings. For significant voxels, the value of R-squared and the plot of parameter estimates against the variable of interest were obtained using SPSS 11.5 for Windows.

5.2.3. Results

5.2.3.1. Clinical and structural MRI findings in patients

In Table 5.6, clinical and MRI characteristics of patients are reported. Only three patients had mild sensory deficits in the lower limbs. Two patients had diffuse T2 signal change which affected the whole spine.

There was a significant correlation between EDSS and T2 lesion load ($r=0.57$, $p=0.04$). No other correlations were found between EDSS and other structural MRI measures.

Table 5.6. Clinical and radiological characteristics of patients with PPMS.

Disease duration	mean 8.69 years (SD 7.49)
EDSS	median 4.0 (range 3-6.5)
25-foot timed walk test	mean 7.42 sec (SD 3.44)
PASAT	mean 50.77 (SD 8.86)
9hpt-dh	mean 24.99 sec (SD 5.03)
9hpt-ndh	mean 26.55 sec (SD 6.33)
Ashworth left leg	median 1 (range 0-3)
Ashworth right leg	median 2 (range 0-3)
T2 lesion load	mean 10.7 ml (SD 11.18)
Spinal cord area	mean 64.08 mm^2 (SD 9.68)
Spinal cord lesions	mean 4.4 (SD 3.5)*
Brain parenchymal fraction	mean 0.80 (SD 0.03)
Grey matter fraction	mean 0.53 (SD 0.3)

EDSS= Expanded disability status scale, PASAT= Paced Auditory Serial Addition Test, 9hpt-dh= Nine Hole Peg Test-dominant hand, 9hpt-ndh= Nine Hole Peg Test-non-dominant hand. *Two patients had diffuse T2 signal change in the spine and were not included in the calculation of this mean.

5.2.3.2. Muscular activity and ankle joint angle measurements

All subjects were able to relax completely during passive movements. In the patient group, there were no significant differences in: (i) EMG activity, measured during the training sessions, for either active or passive movement, and (ii) movement amplitude, measured during both the training and fMRI sessions, between the dominant and non-dominant foot (Table 5.7 and 5.8). These findings were similar to those obtained in the control group (paragraph 5.1.3.1). Although the EMG-percentages and the ankle joint angles of controls have been already shown (Table 5.1), they are repeated in Table 5.7 and 5.8 for display purposes. Although patients and controls showed similar EMG activity in both muscles

during active and passive movements (Table 5.7), patients had a smaller left ankle joint angle than controls during both the EMG (p=0.045) and fMRI sessions (p=0.022) (Table 5.8).

Table 5.7. EMG activity recorded during the training session before the fMRI.

	Controls				**Patients**			
	Right foot		**Left foot**		**Right foot**		**Left foot**	
	Tib.	**Soleus**	**Tib.**	**Soleus**	**Tib.**	**Soleus**	**Tib.**	**Soleus**
mEMG-% (SD) of active movement	12.3 (7.5)	17 (11.7)	15.1 (10.9)	14.2 (10.8)	17.6 (10.1)	25.6 (21.7)	16.6 (10.5)	22.6 (17.1)
mEMG-% (SD) of passive movement	0.8 (0.9)	2.6 (3.1)	0.6 (0.6)	2.5 (2.6)	1.1 (0.9)	4.02 (3.1)	0.99 (0.8)	4.25 (3.7)

M= mean Tib.= tibialis anterior

Table 5.8. Ankle joint angles maintained during the EMG and fMRI sessions in patients and controls.

	Controls		**Patients**	
	Right foot	**Left foot**	**Right foot**	**Left foot**
Mean ankle joint angle during EMG (SD)	29.25 (12.2)	33.31 (14.9)	25.77 (6.65)	22.92 (11.7)*
Mean ankle joint angle during fMRI (SD)	28.94 (12.9)	33.44 (13.8)	25.62 (11.5)	22.15 (11.5)**

*Significantly different from controls, p=0.045, Mann-Whitney U test, **Significantly different from controls, p=0.022, Mann-Whitney U test.

5.2.3.3. fMRI response to active and passive movements

Patients and controls activated several regions during active and passive movements of either the dominant or non-dominant foot (Table 5.9). All the brain regions activated in controls with both movements are summarised and displayed above (paragraph 5.1.3.2, Table 5.2, Figure 5.2). In Table 5.9 only those which showed activation at $p < 0.05$ corrected at voxel level for multiple comparisons across the whole brain are listed. Figure 5.5 shows the SPM(T) maps of the patient group.

Considering the results of active movements of either foot in both groups, there was a significant activation in the contralateral SI-MI, as well as in the contralateral SMA and SII, in the ipsilateral cerebellum and vermis, and in the basal ganglia. Passive movements activated similar regions, including the contralateral SI-MI, as well as the SMA and SII, and the ipsilateral cerebellum.

Table 5.9. Brain regions activated by active and passive movements of the right (dominant) and left (non-dominant) foot in patients and controls.

	Right foot							Left foot						
	Controls				Patients				Controls				Patients		
Active	x	y	z	Z *P*	x	y	z	Z *P*	**Active**	x	y	z	Z P	x	y	z	Z P
Right cerebellum	18	-34	-30	5.52 0.003	14	-36	-30	4.98 0.05	Left cerebellum	-18	-38	-28	6.48 0.0001				
Left SI-MI	-6	-10	68	5.48 0.004	-6	-28	70	5.52 0.003	Right SI-MI, SMA, SII	8	-38	64	6.19 0.0001	2	-32	68	5.46 0.004
									Left SMA					-4	-6	62	5.40 0.006
Vermis	2	-48	-8	5.46 0.005					Left sup. temporal g.	-46	-30	12	5.56 0.003				
Right SMA	8	2	56	5.44 0.005					Vermis	-2	-52	-6	5.49 0.004				
Left thalamus	-16	-16	10	5.26 0.014					Right corpus striatum					16	-6	14	5.34 0.015
Left SII	-10	-40	64	5.08 0.038													
Passive									**Passive**								
Left SII	-8	-36	62	5.80 0.001					Right SMA	8	-18	70	5.95 0.0001				
Left SI-MI	-4	-20	64	5.25 0.015	-2	-34	60	5.35 0.009	Right SI-MI, SII	8	-34	68	5.80 0.001	6	-40	62	5.39 0.007
									Left cerebellum	-16	-38	-32	5.24 0.016				
									Right rolandic op.					46	-32	22	5.68 0.001

Regions are listed for each foot accordingly to their Z-scores in controls. Coordinates are given in mm in MNI space. *P* values are corrected at $p<0.05$ at voxel level for multiple comparisons across the whole brain. SI-MI = primary sensorymotor, SMA = supplementary, g. = gyrus, sup. = superior, post. = posterior.

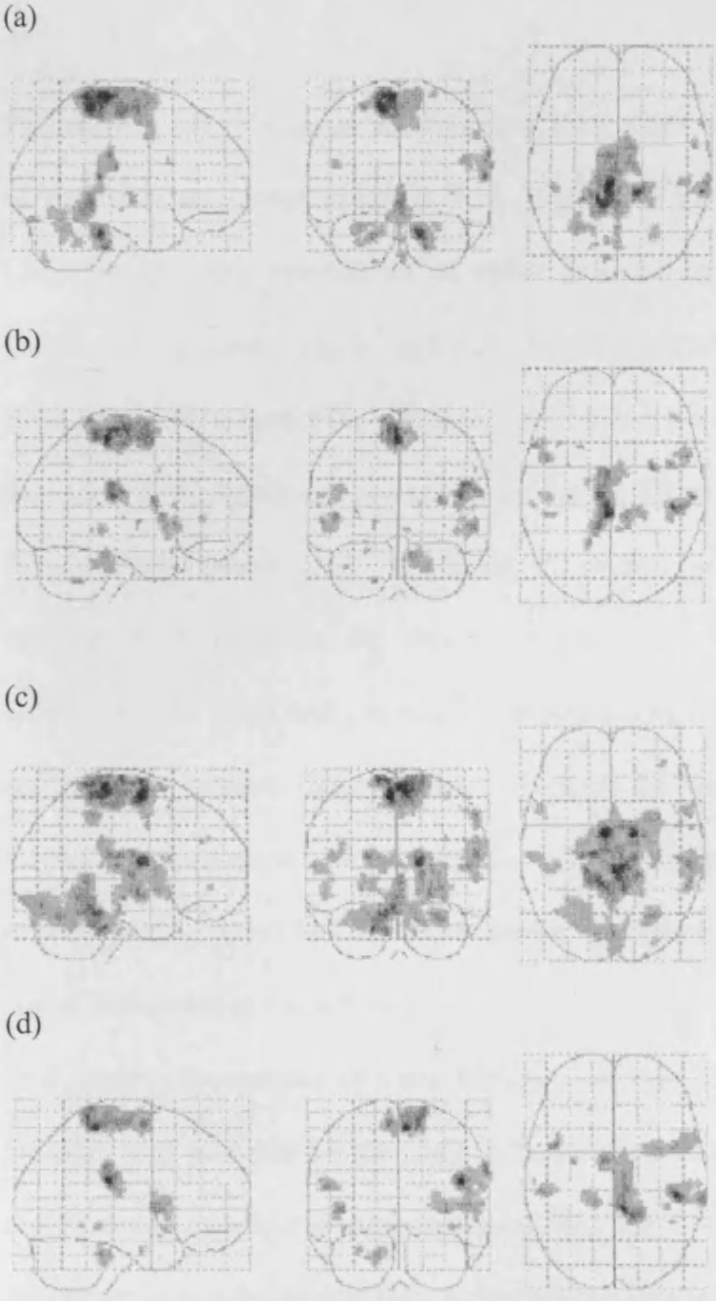

Figure 5.5. FMRI response in patients with active (a) and passive movements (b) of the right foot and active (c) and passive movements (d) of the left foot. Results are displayed onto a glass brain. All voxels are significant at $p < 0.0001$ (uncorrected for multiple comparisons) for display purposes. Brain regions that showed significant activation after correction for multiple comparisons across the whole brain are reported in Table 5.9.

5.2.3.4. fMRI differences between PP MS patients and controls

The regions where patients activate more than controls during active and passive movements of both feet are given in Table 5.10. Figure 5.6 shows the corresponding SPM(T) maps. Considering active movements of either foot, patients activated more than controls in a pattern of regions, which included the contralateral cerebellum and the contralateral precuneus. When borderline significant differences were considered ($0.05<p<0.1$), this pattern extended to the ipsilateral precuneus, ipsilateral SII and ipsilateral SMA. Moreover, patients demonstrated greater fMRI responses in several other regions, depending on the foot considered. In particular, the superior frontal gyrus, ipsilateral cingulate cortex, ipsilateral superior frontal gyrus and contralateral superior temporal gyrus showed a significantly greater activation in patients during active movement of the right foot. In contrast, the bilateral thalamus, contralateral caudate, superior vermis, contralateral rolandic operculum, ipsilateral inferior parietal gyrus and SI-MI showed a significantly greater activation in patients during active movement of the left foot.

With passive movements of either foot, patients activated more than controls in the ipsilateral striatum (e.g. putamen for the right side and caudate for the left side). Other regions, such as the contralateral superior temporal gyrus and the contralateral rolandic operculum showed greater activation in patients only during passive movement of the right foot.

During passive movement of the right foot, controls activated more than patients in the inferior vermis (p value=0.04, Z score 3.32) (Figure 5.7), but they did not demonstrate greater fMRI response to the active and passive movements of the left foot when compared to patients.

Table 5.10. Regions that showed greater activation in patients than in controls.

Right foot				Left foot			
Active		**Passive**		**Active**		**Passive**	
	***P* (Zscore)**		***P* (Zscore)**		***P* (Zscore)**	**Regions**	***P* (Zscore)**
Right SII	0.003 (4.14)	Left sup.temporal g.	0.008 (3.76)	Right thalamus	0.002 (4.29)	Left caudate	0.012 (3.80)
Right sup.frontal g.	0.016 (3.61)	Right putamen	0.012 (3.80)	Right caudate	0.007 (3.90)		
Left cerebellum	0.02 (3.73)	Left rolandic op.	0.047 (3.32)	Super. vermis	0.01 (3.79)		
	0.027 (3.63)						
Right cingulate c.	0.022 (3.49)			Left precuneus	0.011 (3.98)		
Left sup.temporal g.	0.03 (3.20)			Left thalamus	0.02 (3.57)		
Left precuneus	0.032 (3.58)			Right rolandic op.	0.021 (3.54)		
Right SMA	0.068 (3.31)			Right cerebellum	0.042 (3.53)		
Right precuneus	0.09 (3.19)			Right precuneus	0.043 (3.53)		
				Left inf.parietal g.	0.046 (3.28)		
				Left SI-MI	0.047 (3.49)		
				Left SII.	0.066 (3.14)		
				Left SMA	0.088 (3.25)		

Regions are listed accordingly to their Z-scores. Coordinates are given in mm in MNI space. P values are corrected at voxel level for multiple comparisons within the ROIs. SI-MI = primary sensorymotor, SMA = supplementary, g. = gyrus, c. = cortex, sup. = superior, inf. = inferior, op. = operculum.

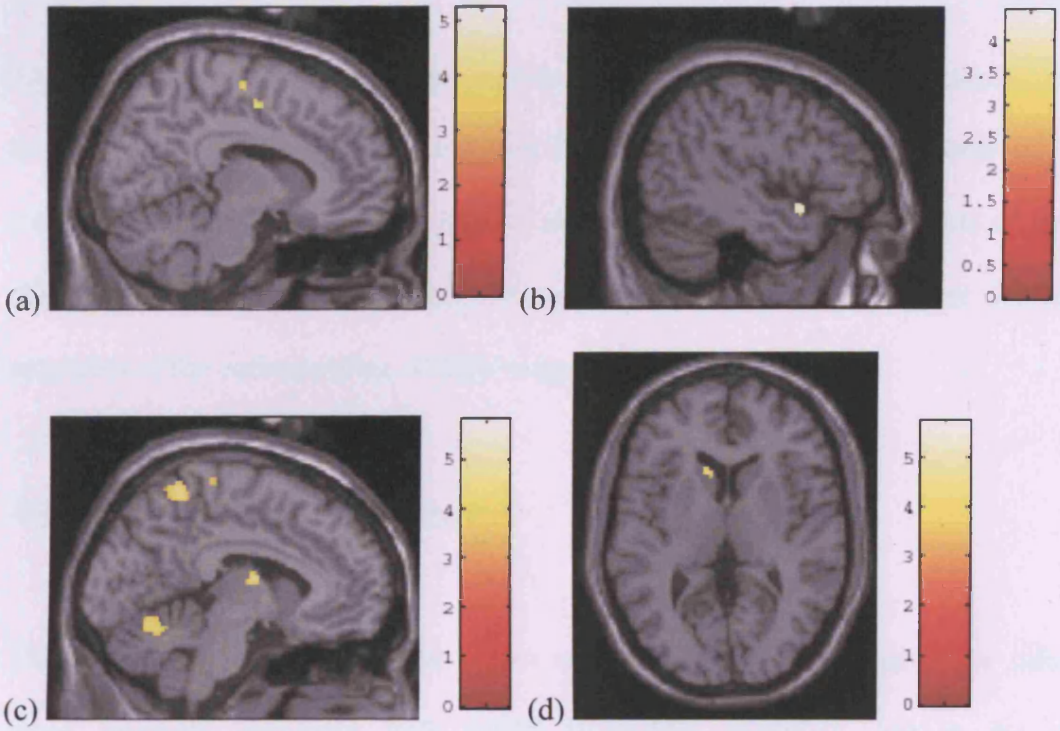

Figure 5.6. Examples of differences in fMRI response between patients and controls. Patients activated more than controls (a) in the right SMA and right cingulate cortex during active movement of the right foot (MNI coordinates x=10, y=-6, z=50), (b) in the left superior temporal gyrus during passive movement of the right foot (x=-44, y=8, z=-10) (c) in the left precuneus, left SI-MI, superior vermis and left thalamus during active movement of the left foot (x=-6, y=-31, z=70), (d) in the left caudate during passive movement of the left foot (x=-10, y=20, z=6). Results are overlaid onto T1-W template and corrected for multiple comparisons. The colour scale indicates the T score.

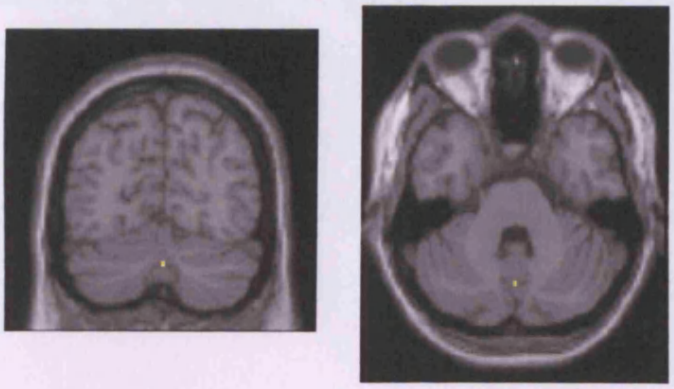

Figure 5.7. Controls activated more than patients in the inferior vermis (MNI coordinates x=2, y=-70, z=-32) during passive movement of the right foot. Results are overlaid onto coronal and axial T1-WI and corrected for multiple comparisons. The colour scale indicates the T score.

5.2.3.5. Correlations between fMRI and clinical and structural MRI measures

The fMRI response to active and passive movements showed several correlations, positive and negative, with clinical and structural MRI measures depending not only on the measure considered, but also on the side, type of movement and brain region. Plots of the significant correlations for selected brain regions are shown in Figure 5.8. Figure 5.9 shows some examples of the corresponding SPM(T) maps.

1) Correlations with clinical measures

The fMRI response to active movement of the right foot in the ipsilateral inferior frontal gyrus inversely correlated with EDSS (Rsq=0.80, p=0.001), and in the contralateral cerebellum with TWT (Rsq=0.84, p=0.004). There was an inverse correlation between the fMRI response to passive movement of the left foot in the contralateral postcentral gyrus and 9HPT of the left hand (Rsq=0.82, p=0.004). In contrast, the fMRI response to passive movement of the right foot in the ipsilateral superior frontal gyrus positively correlated with PASAT (Rsq=0.80, p=0.008). The fMRI response to passive movement of the left foot in the contralateral SMA positively correlated with left lower limb spasticity (Rsq=0.83, p=0.008), while the correlation between the two was inverse in the ipsilateral caudate (Rsq=0.81, p=0.004). No significant correlation was found between the fMRI response to passive movement in any brain region and right lower limb spasticity.

2) Correlations with MRI measures

The fMRI response to passive movement of the right foot in the ipsilateral inferior frontal gyrus inversely correlated with T2 lesion load (Rsq=0.82 p=0.0006), in line with the significant correlation between EDSS and fMRI activity with right active movement in the same region. Brain T2 lesion load also positively correlated with the fMRI response to active movement of the left foot in the ipsilateral superior (Rsq=0.82, p=0.002) and middle (Rsq=0.82, p=0.004) temporal gyrus and in the ipsilateral superior frontal gyrus (Rsq=0.79, p=0.007). Finally, the fMRI response to passive movement of the left and right foot in the contralateral postcentral gyrus inversely correlated with the cervical spinal cord area (Rsq=0.78, p=0.01, and Rsq=0.82, p=0.006, respectively).

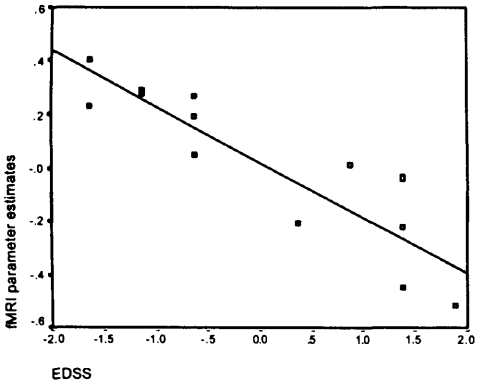

(a)

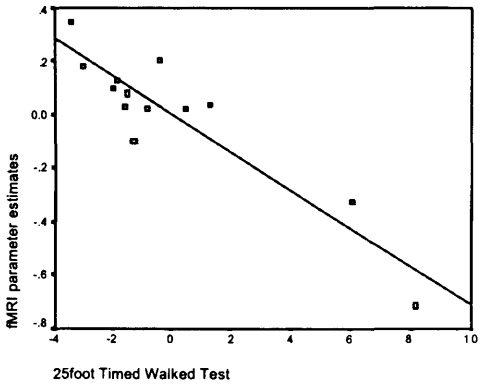

(b)

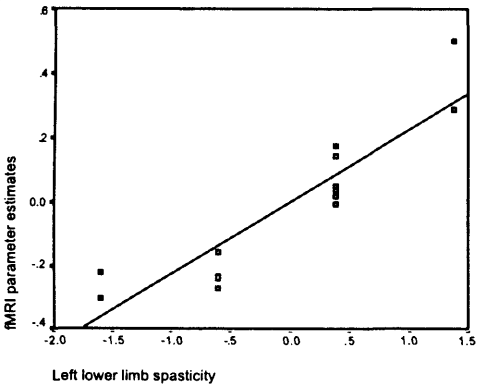

(c)

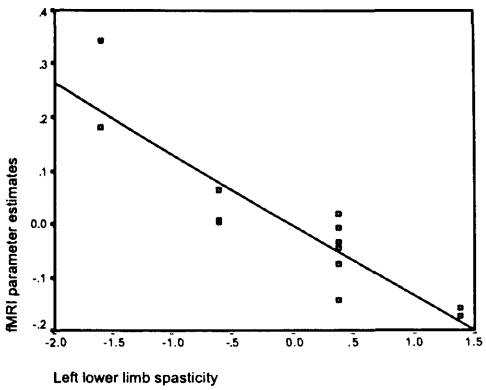

(d)

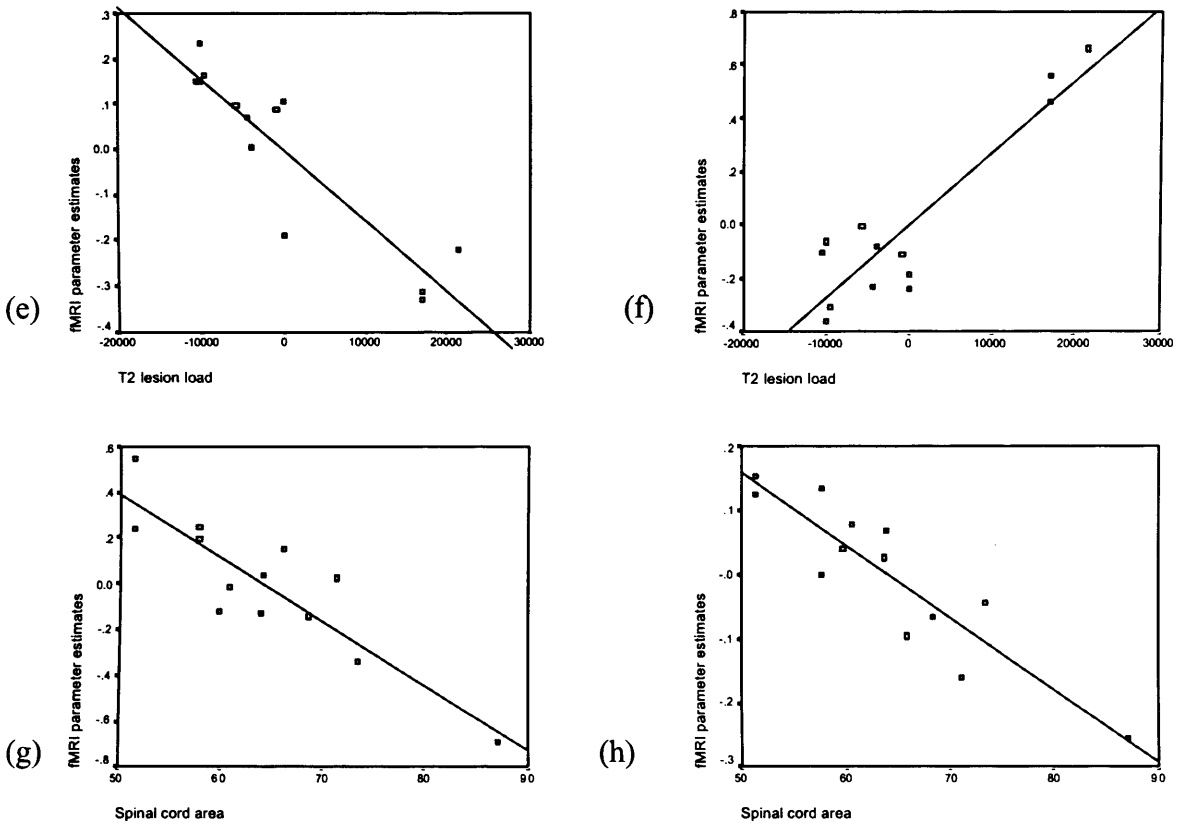

Figure 5.8. Plots of the correlations between size of effect and clinical and structural MRI measures, for selected brain regions. (a) Plot of the parameters estimates in the right inferior frontal gyrus (MNI coordinates x=42, y=30, z=12) during active movement of the right foot against EDSS (Rsq=0.08, p=0.001). (b) Plot of the parameters estimates in the left cerebellum (x=-34, y=-42, z=-46) during active movement of the right foot against 25foot Timed Walked Test (TWT) (Rsq=0.84, p=0.004). (c) Plot of the parameters estimates in the right SMA (x=6, y=2, z=72) during passive movement of the left foot against left lower limb spasticity (Rsq=0.83, p=0.008). (d) Plot of the parameters estimates in the left caudate (x=-6, y=6, z=8) during passive movement of the left foot against left lower limb spasticity (Rsq=0.81, p=0.004). (e) Plot of the parameter estimates in the right inferior frontal gyrus (x=42, y=30, z=22) during passive movement of the right foot against T2 lesion load (Rsq=0.82, p=0.006). (f) Plot of the parameter estimates in the left superior temporal gyrus (x=-46, y=16, z=-10) during active movement of the left foot against T2 lesion load (Rsq=0.82, p=0.002). (g) Plot of the parameter estimates in the right postcentral gyrus (x=18, y=-34, z=74) during passive movement of the left foot against the spinal cord area (Rsq=0.78, p=0.01). (h) Plot of the parameter estimates in the left postcentral gyrus (x=-22, y=-42, z=62) during passive movement of the right foot against spinal cord area (Rsq=0.82, p=0.006). In all plots, x and y are mean corrected.

The corresponding images are displayed in Figure 5.9.

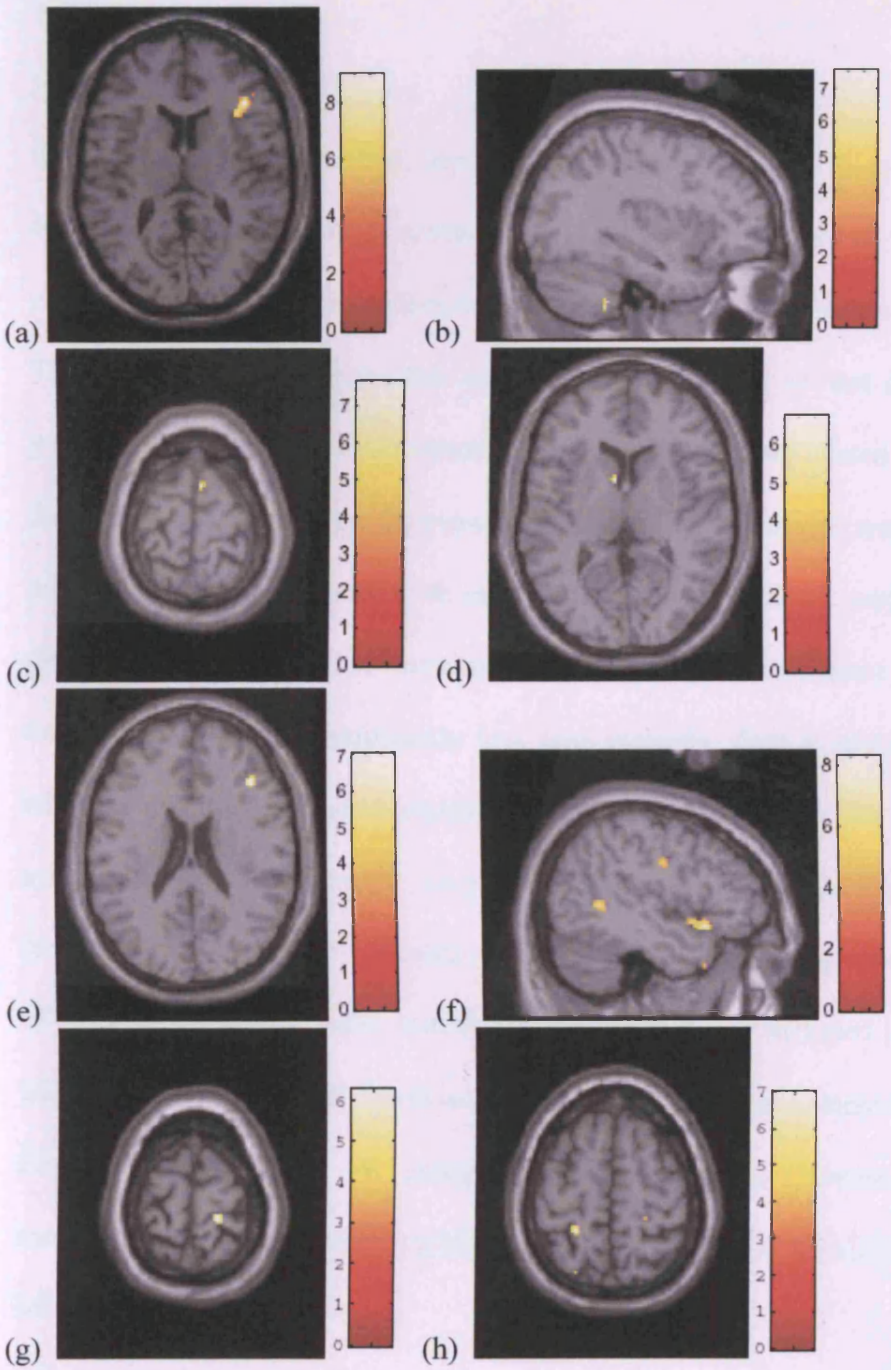

Figure 5.9. Results of the correlations between size of effect and clinical and structural MRI measures, for selected brain regions. (a) Right inferior frontal gyrus (MNI coordinates x=42, y=30, z=12), which correlates with EDSS. (b) Left cerebellum (x=-34, y=-42, z=-46), which correlates with TWT. (c) Right SMA (x=6, y=2, z=72), which correlates with left lower limb spasticity. (d) Left caudate (x=-6, y=6, z=8), which correlates with left lower limb spasticity. (e) Right inferior frontal gyrus (x=42, y=30, z=22), which correlates with T2 lesion load. (f) Left superior temporal gyrus (x=-46, y=16, z=-10), which correlates with T2 lesion load. (g) Right postcentral gyrus (x=18, y=-34, z=74), which correlates with spinal cord area. (h) Left postcentral gyrus (x=-22, y=-42, z=62), which correlates with spinal cord area. Regions of activation are overlaid onto T1-weighted template and corrected for multiple comparisons. The colour scale indicates the T score.

5.2.4. Discussion

The present study identified functional brain reorganisation in patients with PP MS. We focused our investigation on ankle dorsi-plantar flexion, because of its fundamental role in the physiology of locomotion (Miyai et al. 2001), and employed active and passive movements. The advantage of using passive movements is that they do not depend on the ability to perform a task or on volitional planning or execution, but are related to sensory afferents only. In order to ensure that the amplitude of the passive movement was identical to that of the active movement, a custom made manipulandum was used. All subjects were free to choose the amplitude of their movement in order to limit the occurrence of fatigue, and patients moved the left ankle significantly less than controls. This is not surprising, and could be related to the mild functional impairment of these patients, who had a progressive spinal cord syndrome and mild spasticity. All patients were able to perform the motor task correctly, as confirmed by the muscular activity recorded during the training session. Therefore, the angle of the ankle joint associated with the foot movement was included in the statistical model to take into account the differences in the amplitude of the movement between the two groups. First, we shall discuss the group effect on the fMRI response to active and passive movements, then the relationship between strength of BOLD signal and clinical and structural MRI measures.

5.2.4.1. Effect of group on the fMRI response to active movement

Patients activated significantly more than controls in the contralateral cerebellum, which is normally activated during foot extension (Grodd et al. 2001) and has facilitatory connections with the motor cortex (Okabe et al. 2003) and precuneus, which is recruited during motor

imagery in order to perform the task in the absence of visual input (Ogiso et al. 2000). When borderline significant differences were also considered, patients activated more than controls in the ipsilateral postcentral gyrus (SII) and SMA. The former has recently shown increased activation in PP MS, who performed a motor task with the clinically affected foot (Rocca et al. 2002b). Previous studies have reported that the contralateral SMA, rather than the ipsilateral SMA, activates more in patients with MS than in controls, though only with movements of the clinically unaffected limb (Filippi et al. 2002b;Lee et al. 2000;Reddy et al. 2000a). Moreover, we found that other regions, located within and outside the primary and secondary motor and somatosensory cortices, activated more in patients, depending on the foot considered. For example, in line with previous publications in MS (Filippi et al. 2002b;Lee et al. 2000;Reddy et al. 2000a;Reddy et al. 2000b;Reddy et al. 2002;Rocca et al. 2002b), we found increased BOLD responses to active movement of the left foot in the contralateral rolandic operculum and in the ipsilateral SI-MI, and to active movement of the right foot in the contralateral superior temporal gyrus and the ipsilateral cingulate cortex.

5.2.4.2. Effect of group on the fMRI response to passive movement

The most striking result of this study is the increased activation in the ipsilateral striatum (e.g. putamen for the right side and caudate for the left side) during passive movement in the patient group. Previously, activation in the basal ganglia has been demonstrated mainly during active movement in the side contralateral to the limb (Gerardin et al. 2003;Weiller et al. 1996). However, these subcortical structures may have a role in processing sensory information, as is seen in patients with movement disorders (Abbruzzese and Berardelli 2003). Additionally, during passive movement of the dominant foot, patients activated more than controls in the contralateral superior temporal gyrus and operculum. The former has

consistently shown increased activation in patients with PP MS with active movement of the right affected foot (Rocca et al. 2002b) or unaffected hand (Filippi et al. 2002b). In animals, this region has been shown to be part of the auditory associative network, and to have widespread corticostriatal projections (Yeterian and Pandya 1998). The latter constitutes a premotor region, and has been found to participate in the volitional hand motor network (Ward and Frackowiak 2003).

Finally, during passive movement of the right foot, controls activated more than patients in the inferior vermis, which has been consistently included in the homunculoid representations of the caudal cerebellum in healthy subjects (Grodd et al. 2001).

5.2.4.3. Role of the functional changes in patients

We found that the fMRI activation in the ipsilateral inferior frontal gyrus with active movement of the right foot was greater in patients who had lower EDSS and lower brain T2 lesion load. A similar relationship was found between the extent of activation in the contralateral cerebellum with active movement of the right foot and the time to walk 25 feet. These negative relationships, which were expected, suggest that the increased fMRI activity in the inferior frontal gyrus and contralateral cerebellum might have a role in maintaining function. The inferior frontal gyrus is associated with the planning and control of motor tasks, and has reciprocal connections with other premotor and cortical areas (Rizzolatti and Luppino 2001). A recent study, investigating the functional connectivity of the motor cortex, found increased regional cerebral blood flow in the contralateral cerebellum with low frequency transcranial magnetic stimulation of the primary motor cortex, suggesting the presence of facilitatory connections between the motor cortex and the contralateral cerebellum (Okabe et al. 2003).

We also identified that the fMRI activation in the ipsilateral superior and middle temporal gyrus with active movement of the left foot was greater in patients with higher brain T2 lesion load, which, in turn, correlates with higher disability. Such activity may reflect an increase in attention to the auditory input, given by the pacing metronome, in order to perform the motor task with the non-dominant foot. Movement-related activation of the temporal lobes, as well as activation in other regions involved in multi-modal integration, has been reported previously in PP MS (Filippi et al. 2002b;Rocca et al. 2002b). Thus, the increased activation in these regions might reflect the additional processing which is necessary to maintain task performance with increasing disability. A similar explanation might be proposed for the relationship between the fMRI response to active movement of the left foot in the ipsilateral superior frontal gyrus, or frontopolar regions, and brain T2 lesion load. Indeed, the superior frontal gyrus has been shown in healthy controls to activate during periods of preparation or anticipation to foot movement (Sahyoun et al. 2004).

Additionally, the fMRI response to passive movement of both feet in the contralateral postcentral gyrus was greater in patients with more spinal cord atrophy. This finding supports a recent fMRI study, which has reported a correlation between the fMRI activity in the contralateral postcentral gyrus and brain T2 lesion load in PP patients, who were functionally impaired (Rocca et al. 2002b). Thus, the increased functional activity in the contralateral postcentral gyrus with increasing spinal cord pathology might simply represent the effect of spinal pathological damage in the afferent and efferent fibres, which pass through the spinal cord, and induce a non-adaptive or "stress-related" response in the contralateral sensorymotor regions.

Leg spasticity, which theoretically might interfere with the execution of passive movements, had a different effect on the strength of BOLD response depending on regions: higher left leg spasticity was associated with greater activation in the contralateral SMA and with a smaller

activation in the ipsilateral caudate. The explanation of these findings and the lack of concordance between left and right foot, is unclear. The effect that limb spasticity might have on the brain fMRI response to passive limb movement requires dedicated studies, which have to take into account the damage in the spinal cord. The differences in the functional activation between the dominant and non-dominant foot in both healthy controls and patients also warrant further investigations.

5.3. Conclusion

Previous fMRI studies have shown that functional reorganisation in patients with MS might help to maintain clinical function and reduce the impact of brain and spinal cord damage on disability progression. In this chapter we have employed active and passive movements of the foot to investigate the role of functional reorganisation in patients with PP MS, and suggested that some functional changes might well be "adaptive", but others may be "non-adaptive" or represent a stress-related response to CNS injury. Longitudinal fMRI studies, which employ passive movements, are needed to confirm our findings and investigate the complex dynamics of functional brain reorganisation. The key question is whether the adaptive or non-adaptive role of some brain regions may change over time, accordingly to disease type, disability progression and increasing brain and spinal cord damage. Also, future studies are needed to assess the differences in the fMRI response to active and passive movements between the dominant and non-dominant foot, and establish if the motor network activated by the non-dominant foot changes over the course of the disease. Finally, we wish to highlight the possibility that lower limb spasticity affectes the fMRI response to passive movements, and therefore it is a factor that needs to be considered in future fMRI studies that employ passive movements.

Chapter 6

Conclusion:

Combining diffusion tensor imaging and functional MRI

This chapter describes two studies which demonstrate the feasibility and potential of combining the results obtained by DTI with those obtained by fMRI in the same subject. They represent preliminary steps towards the integration of information about tissue microstructure, provided by DTI, with the pattern of the fMRI response, and provide a unique insight into the pathological mechanisms of neurological diseases. The first study reports a methodology which allows the "qualitative" combination of FMT-derived pyramidal tract with the fMRI activation with foot movement. The second study describes a "quantitative" investigation of the relationship of the DTI measures in the optic radiation, such as FA, with the extent of fMRI activation with visual stimuli. In the first study a patient with RR MS, who developed a lesion in the pyramidal tract, was studied. Seven patients with ON were investigated in the second study.

6.1. Combining diffusion tractography of the pyramidal tract and motor fMRI: a qualitative study

6.1.1. Introduction

Information about white matter connections between cortical grey matter regions might help to interpret regional functional imaging data more effectively. Recent developments in MRI have provided information about both white matter pathways and cortical function *in vivo* in the same subject. The potential for diffusion based tractography to track the major white matter tracts in the brain, including the pyramidal tract, has been demonstrated in chapter 4. In chapter 5, BOLD MRI has been used to measure regional cerebral activity (Logothetis et al. 2001) induced by a motor task. It has been suggested that changes in both DTI and tractography measures reflect pathologic changes affecting the microscopic structures of the

white matter fibres (Pierpaoli et al. 2001;Werring et al. 2000c;Wieshmann et al. 1999a;Wilson et al. 2003). Similarly, changes in the fMRI response to motor and sensory stimuli reflect the effect of the pathology in processing the stimuli (Ward et al. 2003;Werring et al. 2000b). However, there is evidence that functional changes might also represent an adaptive brain response and/or enhance recovery from acute symptoms (Carey et al. 2002;Filippi and Rocca 2003;Johansen-Berg et al. 2002;Toosy et al. 2002).

The use of diffusion based tractography and fMRI in investigating the structure and function of the motor system is well established. Combining these two techniques might give an insight into the relationship between the degree of integrity of the pyramidal tract (as measured by changes in anisotropy or connectivity) and the extent of functional reorganisation (as measured by changes in the location and extent of fMRI activity).

In the present study, we applied these two techniques to a patient with RR MS following recovery from a motor relapse, and combined the pyramidal tract, derived by tractography, with the fMRI response to active and passive movement of the foot in a "qualitative" way.

6.1.2. Methods

6.1.2.1. Subjects

A 50-year old woman with a diagnosis of RR MS was studied. The onset of her disease was in 1993, when she presented with sensory symptoms affecting the right upper limb. Since then, she suffered from recurrent episodes of sensory disturbance affecting one or more limbs. In May 2000, she developed a sudden onset of moderate weakness in the left arm and leg and left side of her face, which was associated with numbness. She made a very good recovery, and she was left with slight distal weakness. Two years after her left sided hemiparesis, she

was recruited for this study. On examination there was a slight pyramidal weakness in the left arm and leg, and a mild light-touch and pinprick impairment in the left fingers and right arm and leg, respectively. Her EDSS was 2.5. Conventional brain MRI showed several supratentorial lesions in the periventricular regions and one infratentorial lesion, in the right cerebral peduncle (Figure 6.1). Spinal cord MRI showed a lesion at C5. She performed the motor fMRI experiment described in chapter 5 (see paragraph 5.2.2.4) and the whole-brain DTI described in chapter 4 (see paragraph 4.1.2.2)

Sixteen healthy controls (mean age 37.3, SD 11.9, 10 men and 6 women), which were recruited for the fMRI studies described in chapter 5, were used as a matched group to investigate the differences in the fMRI activity with foot movement.

Ten different healthy women (mean age 33.70, SD 9.71), belonging to the group of normal controls recruited for the tractography studies described in chapter 4, were used as a matched group to investigate the differences in the pyramidal tract DTI-measures.

6.1.2.2. MRI protocol and analysis

For the details about the conventional dual echo MRI see chapter 4.

Functional MRI: The motor paradigm, the fMRI protocol and data analysis were performed as described in chapter 5. Two-sample t-tests were conducted in SPM99 to determine whether the RR patient differed from controls in the fMRI response to movement of the left and right foot. In particular, the two-sample t-test compared at each voxel the patient activation to the control activation, and if the patient activation was an outlier, it was considered significantly different. The variance estimate was assumed to be the same for both groups. Active and passive movements were assessed with separate models. For each model, two contrasts, e.g.

patient greater than controls and controls greater than patient, were estimated. Statistical SPM(T) images were thresholded at $p < 0.05$ corrected at voxel level for multiple comparisons across the whole brain.

DTI and tractography: The DTI protocol and the FMT tracking of the pyramidal tract were performed as described in chapter 4. In the patient, the seed voxel for the right pyramidal tract (which was affected by lesion) was chosen in the middle third of the cerebral peduncle on the slice above the slice where the lesion was visible (Figure 6.2). The anatomical guidelines explained in paragraph 4.1.2.3.1 were followed in order to track the left pyramidal tract in the patient, and the right and left tracts in controls. Each VSC map was thresholded to generate a binary mask, from which the mean FA and volume of the pyramidal tract was calculated in each subject (see paragraph 4.1.2.3.3 for details on the thresholding technique). An independent sample t-test was used to investigate differences in tract FA and volume between the patient and controls.

Using the unthresholded VSC map of each control, the SPM-derived group maps were derived as described in paragraph 4.2.2.5. Differences in these group maps between the patient and controls were investigated using a two sample t-test. Statistical inferences were performed from the SPM(T) maps by correcting for multiple comparisons within a mask volume, which was generated *a priori* for the left and right pyramidal tract using MRIcro (Rorden and Brett 2000). The main cerebral sulci and the labelling of the Talairach and Tournoux atlas (Talairach and Tournoux, 1988) were used to draw these masks on the high-resolution T1-W images.

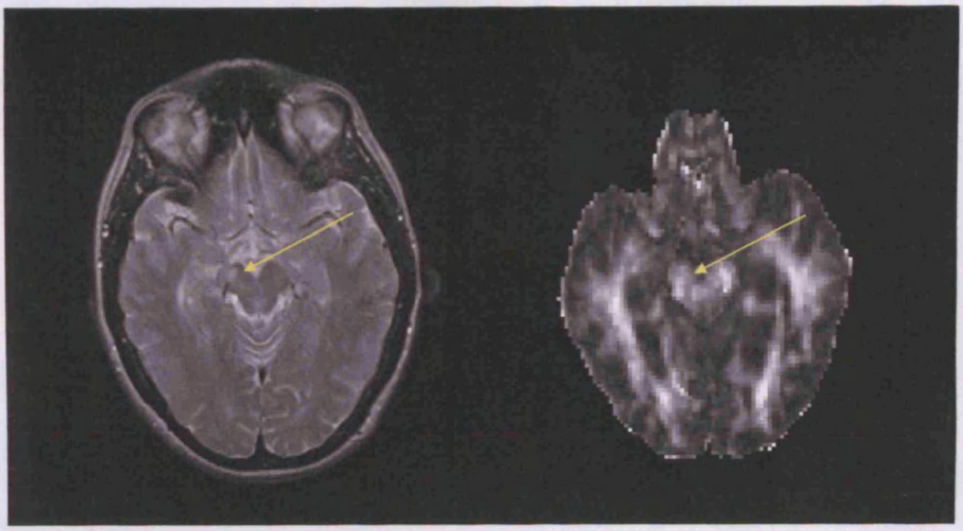

Figure 6.1. Lesion visible in the right cerebral peduncle on T2 WI and FA map.

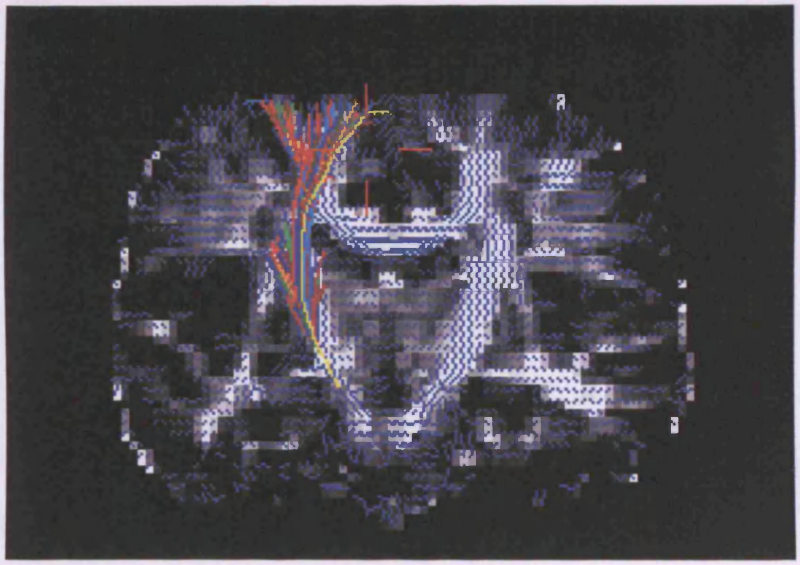

Figure 6.2. The right pyramidal tract, which was traced in the patient using FMT, is overlaid onto FA and principal eigenvector maps. The starting voxel for this tract was above the demyelinating lesion in the middle third of the cerebral peduncle.

6.1.2.3. Displaying the fMRI response and pyramidal tract

In the patient, the unthresholded VSC map of the right pyramidal tract was overlaid with the SPM(T) map that represented the fMRI activation, obtained with the fixed-effect analysis of the active movement of the left foot, onto an MNI structural template. It was not possible to

obtain the same "qualitative" combination of structure with function in controls because few of them underwent both DTI and fMRI protocols.

6.1.3. Results

6.1.3.1. Differences in the fMRI response

The patient was able to relax completely during the passive movement and showed similar values of EMG-percentage (Right foot: Tibialis ant. = 10.2, Soleus = 21.7 with active movement, and Tibialis ant. = 0.4, Soleus = 4.4 with passive movement; Left foot: Tibialis ant. = 8.7, Soleus= 10.8 with active movement and 0.9 and 4.8 with passive movement) and ankle joint angle (Right foot: 14°, Left foot: 15°) compared with controls (see Table 5.1 and paragraph 5.1.3.1 in chapter 5 for control data).

The brain regions that showed greater activation in either the patient or controls are given in Tables 6.1 and 6.2, and some examples are displayed in Figure 6.3. Considering active movement of both feet, the patient activated more than controls in the inferior vermis and in the contralateral thalamus, whilst controls activated more than the patient in the contralateral middle frontal gyrus.

As regards passive movement of both feet, the patient showed a greater activation in the inferior vermis, in the ipsilateral superior frontal gyrus, in the posterior part of the ipsilateral middle frontal gyrus, and in the superior part of the contralateral insula. In contrast, controls showed greater activation in the following regions: the vermis (lobule 7), the contralateral superior frontal gyrus, the ipsilateral anterior cingulate cortex, the anterior part of ipsilateral middle frontal gyrus, the ipsilateral postcentral gyrus, the inferior part of the contralateral

insula, the ipsilateral inferior parietal gyrus, and the anterior and inferior part of the ipsilateral middle frontal gyrus.

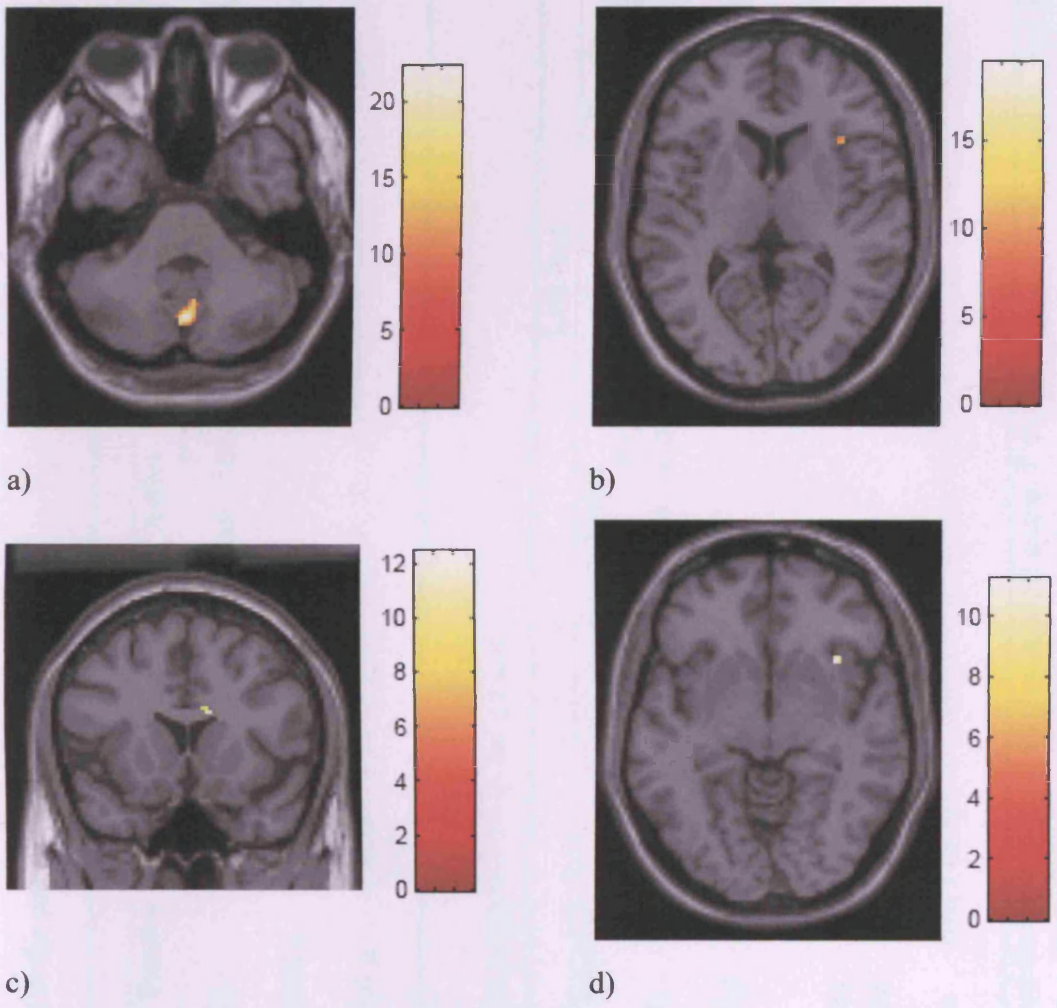

Figure 6.3. Examples of differences in fMRI response between the patient and controls. The patient activates more than controls in the vermis (a) with passive movement of the right foot (MNI coordinates: x= 2, y= -70, z= -38), and in the right superior insula (b) with passive movement of the left foot (x= 38, y= 20, z= 8). Controls activate more than the patient in the right anterior cingulate cortex (c) during the passive movement of the right foot (x= 14, y= 16, z= 22), and in the right inferior insula (d) during passive movement of the left foot (x= 36, y= 18, y= -6). Activations are overlaid onto single-subject T1-weighted template. This might have caused a small displacement in the activations, such as in the cingulate cortex (c). Results are corrected for multiple comparisons across the whole brain. The colour scale indicates the T score.

Table 6.1. Regions that showed greater activation in the patient than in controls.

Right foot				Left foot			
Active		**Passive**		**Active**		**Passive**	
	***P* (Zscore)**		***P* (Zscore)**		***P* (Zscore)**	**Regions**	***P* (Zscore)**
Inferior vermis (lob.8)	0.016 (5.24)	Inferior vermis (lob.8, 9)	0.0001 (7.18)	Right thalamus	0.0001 (6.38)	Vermis (lob.6,7)	0.0001 (6.90)
		Right sup. frontal g.	0.0001 (6.72)			Right sup. insula	0.002 (5.58)
		Right m. frontal g. (post. part)	0.006 (5.42)				

Table 6.2. Regions that showed greater activation in controls than in the patient.

Right foot				Left foot			
Active		**Passive**		**Active**		**Passive**	
	***P* (Zscore)**		***P* (Zscore)**		***P* (Zscore)**	**Regions**	***P* (Zscore)**
n.s.		Vermis (lob.7)	0.0001 (5.95)	Right m. frontal g.	0.017 (5.22)	Right inf. insula	0.001 (5.72)
		Left sup. frontal g.	0.001 (5.81)			Left inf. parietal g.	0.008 (5.37)
		Right ant. cingulate cortex	0.001 (5.70)			Right m. frontal g. (ant-inf. part)	0.012 (5.29)
		Right m. frontal g. (ant. part)	0.007 (5.39)				
		Right postcent. g.	0.011 (5.3)				

Regions are listed accordingly to their Z-scores. Coordinates are given in mm in MNI space. P values are corrected at voxel level for multiple comparisons across the whole brain. Lob=lobule, g. = gyrus, sup. = superior, m. = middle, ant. = anterior, postcent. = postcentral.

6.1.3.2. Differences in tract FA and volume

There were no significant differences in the left and right pyramidal tract FA between the patient and controls (Table 6.3). Although tract volumes were lower in the patient compared with controls, these differences were not significant (Table 6.3). There were no significant differences in the voxel-scale connectivity of the left and right pyramidal tract between the patient and controls.

Table 6.3. Fractional anisotropy (FA) and volume (Vol.) of the left and right pyramidal tract in the patient and controls.

Right pyramidal tract				**Left pyramidal tract**			
Mean FA (SD)		**Mean Vol. (SD)**		**Mean FA (SD)**		**Mean Vol. (SD)**	
Pt	**Co**	**Pt**	**Co**	**Pt**	**Co**	**Pt**	**Co**
0.328	0.330 (0.02)	6.02	10.5 (3.3)	0.275	0.328 (0.03)	8.78	10.89 (2.3)

Tract volumes are given in mm^3. Pt. = RR MS patient, Co.= Controls.

6.1.3.3. Displaying the fMRI response and pyramidal tract

Figure 6.4 shows the unthresholded VSC map of the right pyramidal tract overlaid together with the SPM(T) map, that represented the fMRI activity with active movement of the left foot, onto an MNI structural template.

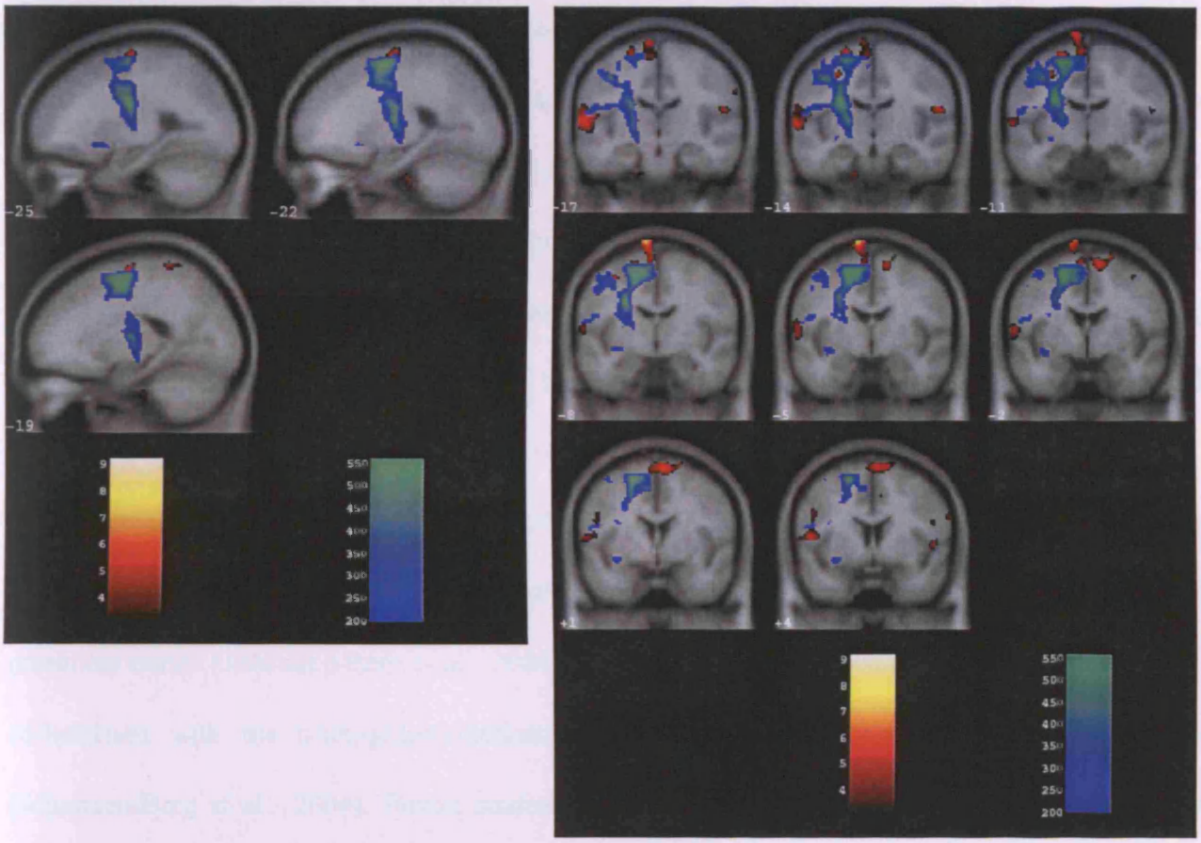

Figure 6.4. The fMRI activation detected in the patient with active movement of the left foot and the right pyramidal tract, estimated using FMT, are overlaid onto a structural template. The fMRI activity was derived from the fixed-effect for the patient. The hot (red) colour scale shows the T scores. The winter (blue) colour scale shows the VSC map thresholded at 200 for display purposes.

6.1.4. Discussion

This study has shown that is possible to overlay fMRI activation maps, together with the FMT-derived motor tract, onto a structural template. This provides, in a single map, complementary information about pyramidal tract shape and location in relation to the cortical regions of functional activation, and represents the first step towards assessing the impact of pathology on tract anisotropy and cortical function. Recent work has qualitatively matched structure with

function in eight controls and one patient with a left precentral tumour (Guye et al. 2003). The authors traced the pyramidal tract in each subject from a seed point in the white matter adjacent to the location of the maximum fMRI activation, and performed group comparisons between the left and right side in controls and between the tumour patient and controls. Results showed that the connectivity of the primary motor cortex was more extensive in the dominant (right) side and differed in the tumour patient. These findings suggested that fMRI-correlated tractography represents a promising tool to investigate the basis of a functional network in the normal and pathological brain.

In a recent functional-anatomical validation work, we have found that activation centres during movement co-localised with the tractography-defined thalamic regions connecting to motor and premotor cortex (Johansen-Berg et al. 2004). Similarly, activation centres during executive tasks co-localised with the tractography-defined thalamic regions connecting to prefrontal cortex (Johansen-Berg et al. 2004). Future studies might use connectivity-defined thalamic regions to assign probabilities of connection to each cortical region for any activation co-ordinate within the thalamus when circuitry is unknown.

First, we shall discuss the differences in the fMRI response to active and passive movements between the patient and controls, then the findings that relate to the differences in FA and volume of the pyramidal tract between groups.

Our patient showed similar values of muscular activity during the training session, and amplitude of movement, recorded during the fMRI experiment, compared with controls. The most striking results from the comparisons of the fMRI activity between the patient and controls was that different parts of the same regions showed greater activation in either the patient or in the controls, depending on which foot and type of movement were considered. For example, with

passive movement of the right foot, the inferior vermis activated more in the patient than in controls in the lobule 8 and 9, whilst the vermal lobule 7 showed greater activation in controls. The inferior vermis has been consistently included in the homunculoid representations of the caudal cerebellum in healthy subjects (Grodd et al. 2001), but the role of its activation in pathology is unknown. Additionally, with passive movement of the left foot, the superior part of the right insula activated more in the patient, while the inferior part of the same region showed greater fMRI activity in controls. The insula has been identified as a centre of multi-modal integration and has connections with the main sensory areas, the premotor cortex, the multi-modal association cortex, the limbic and cingulate areas (Mesulam and Mufson 1982). It has been reported to show greater activation in patients with MS compared with controls, suggesting that it might be recruited to maintain functional capacity in response to tissue damage (Filippi et al. 2002b;Rocca et al. 2002b). The topographic distribution of the connections from the insula suggests that the postero-dorsal insula is specialised in the auditory-somesthetic-skeleton-motor function, whereas the antero-ventral part in the olfactory-gustatory-autonomic function and is connected to the limbic structure. Therefore, different parts of the insula might be activated to a different extent in patients or controls (Mesulam and Mufson 1982). Also, the posterior part of the right middle frontal gyrus activated more in the patient than in controls during passive movement of the right foot, whilst its anterior and inferior part showed greater activation in controls with the same type of movement. This region has been generally found to activate more in patients with MS than in controls (Filippi et al. 2002b;Rocca et al. 2002b;Rocca et al. 2003a). Whether different parts of this region, which participates in the associative sensory and motor network, are differently activated in patients with MS could be a key question in future studies investigating a larger patient group.

Other regions showed greater activation in the patient than in controls during the active movement of the left foot, such as the contralateral thalamus. This is in agreement with previous papers, which detected an increased activation in the thalamus in SP MS patients during the flexion-extension of the right foot (Rocca et al. 2003a) or in MS patients with non-specific T2 weighted abnormalities on conventional MRI during the performance of a simple movement of the right hand (Rocca et al. 2003c). Moreover, RR patients without fatigue showed more significant activation in the contralateral thalamus compared with RR patients with fatigue (Filippi et al. 2002a). The thalamus, one of the basal ganglia nuclei, is part of circuits which are involved in motor planning and execution, associative and limbic functions (Alexander 1994). Thus, our finding suggests that the activity of this region might increase in the disease in order to maintain motor function, or as a result of dysfunction of cortico-subcortical circuits.

On the contrary, the ipsilateral anterior cingulate cortex, which plays a role in emotional self-control and in the ability to focus on problems (Allman et al. 2001), and the ipsilateral postcentral gyrus, were found to activate more in controls than in the patient during the passive movement of the right foot. These findings are in contrast with previous studies, that detected a greater activation in the ipsilateral cingulate cortex and postcentral gyrus in PP patients when they performed voluntary movements of the clinically affected foot (Rocca et al. 2002b), and in the bilateral cingulate motor area in RR patients during the voluntary flexion-extension of the last four fingers of the right hand (Filippi et al. 2002a). The anterior cingulate cortex has numerous projections into the motor system, and plays a crucial role in initiation, motivation and goal-directed behaviour (Devinsky et al. 1995). It is divided into "affect" and "cognition" components, and the caudal area 24, which corresponds to the region of increased activation found in this study, is included in the "cognition" division, that is engaged in skeleton-motor

activity (Devinsky et al. 1995). Therefore, it is possible that its reduced activation in the RR patient during passive movements of the dominant foot reflects impaired stimuli processing.

We have also traced the pyramidal tract using diffusion based tractography. We expected that the anisotropy of the pyramidal tract traced above the demyelinating lesion in the patient would have been lower than in controls, reflecting mechanisms of axonal degeneration of the white matter fibres which pass through the lesion. However, the value of pyramidal tract FA was found to be similar between the patient and controls. One possible explanation is that the tract degeneration might have been too small to be detected by this technique, and this was supported by the fact that the patient recovered well from her motor symptoms. A recent study detected reduced anisotropy along the pyramidal tract, that was tracked using a different diffusion based tractography algorithm, in 25 RR patients compared with controls (Wilson et al. 2003). Moreover, a newly developed measure of anisotropy of the estimated tract was found to correlate with EDSS and, more strongly, with Kurtzke's pyramidal functional score, suggesting that tractography might improve the correlation between MRI measure and disability (Wilson et al. 2003).

Although the volume of both pyramidal tracts appeared to be lower in the patient than in controls, the differences were not significant. This could be due to the degeneration of smaller axons, which are preferentially damaged by focal lesions, that might have a little effect in reducing the total tract volume (DeLuca et al. 2004;Ganter et al. 1999). Finally, if we consider the results of the first study described in chapter 4, which showed that the pyramidal tract is the least reproducible pathway in the brain, the comparison between one patient and a small group of controls may have limited the detection of subtle differences in both FA and tract volume. Studies including a larger sample of patients, who are followed-up after the development of a

lesion in the pyramidal tract, might clarify the impact of acute lesions on axonal degeneration of the tracts which are connected to them, and assess their contribution to irreversible disability.

6.2. Combining diffusion tractography of the optic radiation and visual fMRI: a quantitative study

6.2.1. Introduction

In chapter 4, we reported that tractography-based group mapping can detect subtle pathological abnormalities in the optic radiations of patients previously affected by optic neuritis. Previous visual fMRI studies have demonstrated a functional reorganisation of the cerebral response to visual stimuli after optic neuritis, that may represent an adaptive brain response to abnormal input (Toosy et al. 2002;Werring et al. 2000b). This reorganisation is dynamic and consists of activation of regions located outside the visual cortex, which were proposed as areas of multimodal sensory integration. The key question is whether the structural changes occurring in the visual pathway contribute, together with the functional reorganisation, to clinical recovery. As a first step towards the investigation of the effect of structural and functional factors on clinical recovery, we employed fMRI and DTI with tractography to investigate the relationship between the fMRI response to visual stimuli and anisotropy and connectivity of the optic radiation (as measures of fibre coherence and integrity) in patients previously affected by optic neuritis.

6.2.2. Methods

6.2.2.1. Subjects

The seven patients, who were recruited one year after isolated optic neuritis for the third study described in chapter 4, were also investigated in this study (see paragraph 4.3.2.1. for details). Three patients had history of left optic neuritis and four of right. Seven controls (mean age 27.6, SD 4.3, all women) were recruited.

6.2.2.2. MRI protocol and analysis

Functional MRI: Each subject underwent two monocular fMRI experiments (one for each eye) that lasted 10 mins. and covered the whole brain with 27 near-axial slices. For each fMRI experiment, 150 T2* W images sensitive to BOLD contrast were acquired [TE 40 ms, TR 4000 ms, FOV 38cm x 19cm; matrix size 128 × 64; voxel size 3x3x3.6 mm3, inter-slice gap 0.4 mm]. Lightproof goggles with flashing LED displays in each eyepiece were used to provide photic stimulation. During each experiment subjects passively viewed a visual display which alternated periodically between 20 sec. epochs of photic stimulation and darkness.

SPM99 was used. Each fMRI time series was realigned, normalised to a standard stereotactic space (MNI) and smoothed (8mm isotropic Gaussian kernel). The general linear model was implemented to determine the main effect of the photic stimulation paradigm, with realignment parameters entered as covariates of no interest. For each time series a fixed effects analysis was performed to derive the contrast image that represented the fMRI response to photic stimulation. The control contrast images were regrouped to match the affected and unaffected sides in the

patient group (i.e. 3 left- and 4 right- sided stimulation control derived contrasts were chosen to match the affected eyes in the patient group).

Two-sample t-tests were conducted in SPM99 for both the affected and unaffected eyes versus side matched controls to determine whether controls and patients differed in the fMRI response within the visual cortex. In particular, two contrasts were estimated, e.g. patients greater than controls and controls greater than patients. Statistical SPM(T) images were thresholded at $p < 0.05$ corrected at voxel level for multiple comparisons within a predefined spherical volume (10mm radius) centred in the visual cortex. Age did not affect the fMRI response of the stimulation of either eye in patients or controls and, therefore, it was not considered in the following analysis.

DTI and tractography: The DTI protocol was as in chapter 4. PICo (Probabilistic Index of Connectivity) algorithm was used in each subject to obtain a map, that provides, at each voxel, the probability of connection to the seed voxel (Parker et al. 2003). The seed voxel was placed in the optic radiation at the apex of the arc around the lateral ventricle. The PICo analysis consisted of 10.000 Monte Carlo probabilistic streamline-based tracking iterations for each chosen seed voxel. The number of iterations was chosen *a priori* and was based on results from PICo experiments performed on a single subject, unrelated to this study (Toosy et al. 2004). Details about PICo can be found in chapter 2 (paragraph 2.2.7.2). The maps had previously been CSF segmented using dedicated local software (Hadjiprocopis et al. 2003), but a FA threshold of 0.01 was used in order to limit the residual CSF contamination. A restricted brain volume was used in the analysis in order to speed up the PICo analysis and to focus upon the tracts under investigation. The voxel values of the PICo output maps for the optic radiations ranged from 0 to 1 with an intensity resolution step of 0.001. Each PICo map was thresholded at 0.02 to generate a

binary mask, from which the mean FA and volume of the optic radiation was calculated (Toosy et al. 2004). The mean FA and volume of the estimated left and right tracts were averaged. An independent sample t-test was used to investigate differences in tract FA and volume between patients and controls.

6.2.2.3. Combining structure with function using SPM

Two SPM based general linear models were fitted. The first regressed the fMRI derived contrast images for the affected eye with the mean tract FA for patients with optic neuritis and controls, who were entered as fixed factors. By specifying the appropriate contrasts, a comparison between the function-structure gradients of the posterior visual pathways between patients and controls was made. The second model examined the function-structure relationships of the unaffected eyes of patients with optic neuritis and the side matched controls. Statistical inferences were performed on the resulting SPM(t) maps by correcting for multiple comparisons within the same ROI used for the fMRI analysis (i.e. a spherical volume centered in the visual cortex). The data from the most significant suprathresholded voxels were extracted and plotted for affected and unaffected eyes.

6.2.3. Results

6.2.3.1. Comparisons between groups

1) Tract measures

Patients with optic neuritis showed lower mean FA in the optic radiation than controls (0.41, SE 0.09 versus 0.44, SE 0.09; p=0.035). To investigate whether the reduced FA reflected the presence of lesions within the optic radiations, a repeated measures ANOVA analysis (for the patient group with side as the repeated measure) was performed. We found no significant effect for the presence of lesions on the FA of the left (p=0.120) or right (p=0.189) optic radiations.

Patients also showed lower mean volume in the optic radiation than controls (1.40, SE 0.13 vs 1.90, SE 0.10; p=0.01).

2) Functional fMRI

There were no differences between patients and controls in the overall fMRI response within the visual cortex.

6.2.3.2. Function-structure gradients for the affected eye

A higher fMRI response of the affected eye within the visual cortex was weakly associated with greater tract FA in both patients (p=0.078) and controls (p=0.059) after correcting for multiple comparisons. There was no difference in the function-structure gradients between patients and controls (Figure 6.5).

6.2.3.3. Function-structure gradients for the unaffected eye

There was a significant positive correlation between mean tract FA and the fMRI response of the unaffected eye for both patients (p=0.002) and controls (p=0.02) after correction for multiple

comparisons. There was a trend (p=0.073) for a difference in the function-structure relationship between patients and controls (Figure 6.5). For illustration, the SPM(T) maps are shown for the analysis of the unaffected eye in Figure 6.6.

(a)

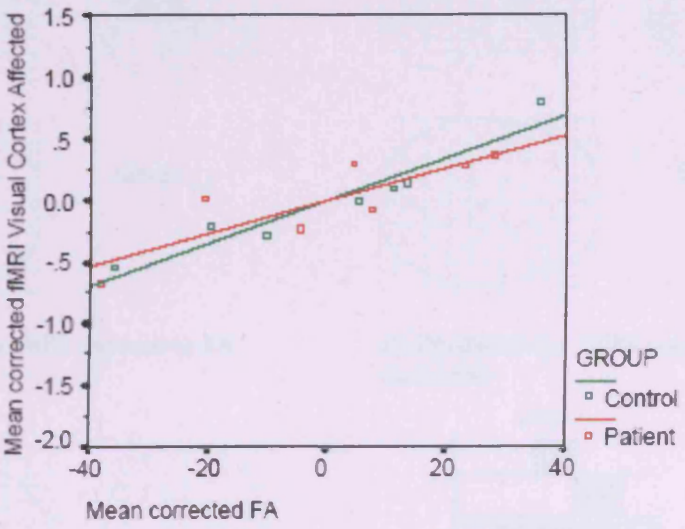

(b)

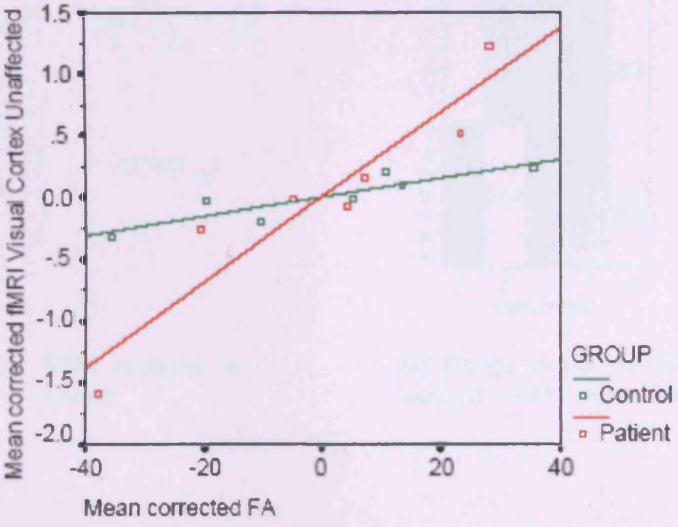

Figure 6.5. The fMRI response of the affected eye (a) and unaffected eye (b) (raw adjusted fMRI parameter estimates) at MNI coordinate [0,-78,-10] within the visual cortex is plotted against optic radiation FA for patients and side matched controls. For the affected eye (a), there is weak evidence for a function-structure gradient in patients (P=0.078) and in controls (P=0.059) but no difference between the two groups. For the unaffected eye (b), there are significant function-structure gradients for both patients (p=0.002) and controls (p=0.02) and weak evidence for a difference between the two groups (p=0.073). For the unaffected eye (b), the relationship between function and structure in the optic radiations of patients appears to be steeper than the relationship for controls.

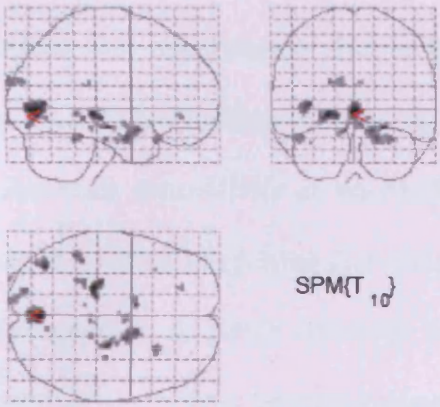

A) Unaffected eye fMRI response vs FA for patients

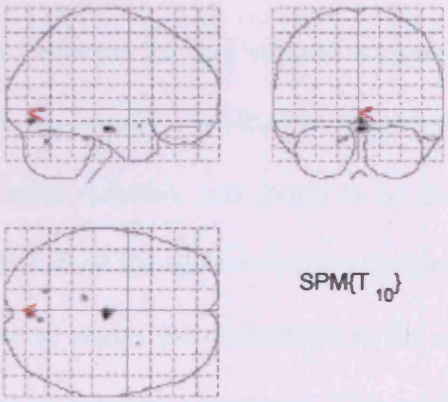

B) Unaffected eye fMRI response vs FA for controls

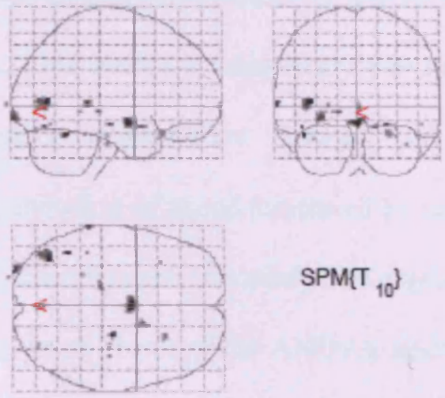

C) Unaffected eye fMRI response vs tract FA – patients > controls

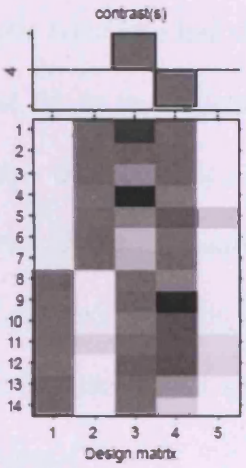

D) Design matrix for SPM regression analysis – fMRI response vs FA.

Figure 6.6. SPM(T) maps were derived for the analysis of the unaffected eye thresholded at $p<0.001$ (uncorrected). Maps are shown for (A) patients, (B) controls and (C) patients>controls. Small volume correction was applied within the visual cortex. The regions outside the visual cortex were not part of the *a priori* hypothesis. The design matrix in (D) was used for the regression analysis; the contrast demonstrates patients > controls.

6.2.4. Discussion

Patients with optic neuritis showed lower optic radiation FA and volume compared with normal controls. These findings confirm results of the third study described in chapter 4, in which the voxel-scale connectivity of the FMT-derived optic radiation was found to be lower in patients than in controls, suggesting that axonal degeneration of the optic radiations follows optic neuritis (Evangelou et al, 2001). However, in our previous study, the differences in the optic radiations quantitative measures between patients and controls were not significant. This could be due to the different tractography algorithm used and to the different control group involved.

We found that the presence of lesions within the optic radiations had no significant effect on tract FA. This makes it more likely that the lower tract FA in the patient group results from trans-synaptic degenerative changes (i.e. through the lateral geniculate nucleus) rather than degeneration of axons transected by lesions. However, the latter possibility cannot be completely excluded because this study was cross-sectional at one year after the acute episode, and the non-significant result of the ANOVA analysis may have arisen from a type II error, due to the low number of subjects studied (i.e. low degrees of freedom).

We have also demonstrated a relationship between function and structure in controls and in patients with optic neuritis. This relationship is most striking when the unaffected eye of the patient group is stimulated. Although the reasons for this are unclear, one explanation is that a trans-synaptic degeneration occurs after optic neuritis reducing the FA of both optic radiations (both are involved because the affected eye pathways decussate). As a consequence, the structural integrity of remaining optic radiation fibres, which originate from the unaffected eye, will now

contribute to the estimated tract FA, resulting in a stronger function-structure relationship when the fMRI response of the unaffected eye is measured.

The function-structure gradients of the affected eye were very similar between patients and controls. However, in Figure 6.5 the gradient of the patient line is slightly less steep than that of the control line, supporting the above hypothesis. The similarity between structure-function gradients could be explained by an adaptive reorganisation of the fMRI response strength within the visual cortex for the patient group. This reorganisation presumably occurs in the presence of degenerating optic radiations in order to maintain visual function.

6.3. Conclusion

In this chapter, we have demonstrated the potential usefulness of combining structural and functional information in helping to understand pathologic mechanisms in patients with MS and optic neuritis, who recover from acute symptoms. Studies with a higher number of subjects and longitudinal observations are required to confirm and expand our results. They may investigate the activitation of different cortical regions at different stages of the recovery process, in order to elucidate the relationship of the degree of recovery with the fMRI activity. Future work will also address how structural changes in the white matter tracts relate to brain functional reorganisation, and how the interaction of these structural and functional factors contribute to clinical recovery.

Conclusions: future directions

Mechanisms of damage

The lack of pathological specificity of MRI has been discussed in chapter 2. DTI offers the prospect of improved differentiation of the pathological processes in MS. The key questions are: 1) Can DTI detect NAWM and NAGM damage that contributes to disability? 2) Are the structural changes in NAWM related to those in lesions? The work presented in chapter 3 helps answer these two questions. We found that DTI is sensitive to the pathological changes in NAWM that contribute to disability and progression in MS. We suggested that the relationship found between anisotropy in the NAWM and the lesion load reflects the relation between axonal damage, due to axonal transection within focal lesions, and the extent of inflammation within lesions. However, the exact mechanisms resulting in axonal transection within lesions are unknown. Future studies will aim to understand the mechanisms of damage in the clinically eloquent lesions that occur in MS patients, and assess the impact of these lesions on the axons which traverse them. An assessment of the effect of damage in lesions and related tracts on clinical disability will be of significant clinical importance.

In chapter 4we demonstrated that it is possible to trace the whole white matter tracts in vivo using diffusion tractography, and that the use of tractography in human pathology allows us to detect abnormalities that are not visible on conventional sequences or DTI maps. However, technical limitations of tractography still exist (such as a reduced ability to distinguish between crossing fibres), but methodological improvements, which will expand the clinical applications of tractography, are likely to emerge in the near future. These developments will allow us to use diffusion tractography, not only as a tool to segment white matter tracts and compute FA values,

but also to obtain quantitative measures of anatomical connectivity between cortical regions. Future work will quantify the left-right asymmetry of connectivity either between cortical regions, such as the superior temporal gyrus (Wernicke) and the pars opercularis of the frontal inferior gyrus (Broca), or of the major white matter pathways, as a function of handedness or age. It will be of great interest to identify whether differences in the left-right brain asymmetry change after CNS injury. Future tractography work will aim to define in the visual system and in the motor cortex anatomical "subunits" that are functionally relevant and cannot be distinguished with conventional or functional MRI.

Mechanisms of recovery

The fMRI findings in our cohort of patients with PP MS, described in chapter 5, has made an important contribution towards our understanding of the role of functional activity in determining recovery or irreversible disability in patients with deyelinating diseases. Previous work has focused on functional changes in patients with MS, who performed the motor task with the unaffected limb. We tried to investigate changes in the fMRI response in patients by controlling movement rhythm and amplitude, and suggested that some changes are adaptive and contribute to maintain clinical function, while others are non-adaptive and represent a stress-related response. Future work will aim to establish whether these changes develop over time, and, in case the adaptive response of some brain regions is confirmed to be beneficial, it may be of value in developing or monitoring new rehabilitation strategies to improve patients' outcome. Also, the way in which demyelination, including the occurrence of lesions in the grey matter, may affect the BOLD response requires further investigation. Further, it will also be of interest to combine

functional imaging studies with neurophysiological measures of motor pathway, such as transcranial magnetic stimulation (TMS), in order to understand the mechanisms of cortical excitability and connectivity, and investigate functional adaptive response to brain injury.

Exploring the relationship between structure and function

The study in patients with optic neuritis demonstrated that combining structural and functional information may shed light on mechanisms of recovery and persistent deficit. Studying a larger number of patients during a follow-up period will allow a comparison between patients who recovered their visual or motor function with those who did not, and might help to answer the question whether the observed functional changes contribute to patients' outcome. Future studies will assess the evolution of structural changes at the injury site, together with the cortical activation pattern, and their relationship to clinical outcome. A current hypothesis is that the extent of visual or motor disability following an injury can be accounted by changes in: 1) structural integrity of the white matter pathways; 2) fMRI response to visual or motor stimuli, (i.e. cortical reorganisation), including a new activation in regions outside the primary cortices and/or increased fMRI response in regions which are part of the network. Future studies will test the hypothesis that in patients with good clinical recovery, but a high degree of structural damage in the visual or motor pathway, there is evidence of increased brain functional activity, which may represent an adaptive brain response.

References

Abbruzzese G, Berardelli A. Sensorimotor integration in movement disorders. *Mov Disord* 2003; **18:** 231-240.

Aboitiz F, Scheibel AB, Fisher RS, Zaidel E. Fiber composition of the human corpus callosum. *Brain Res* 1992; **598:** 143-153.

Alary F, Doyon B, Loubinoux I *et al.* Event-related potentials elicited by passive movements in humans: characterization, source analysis, and comparison to fMRI. *Neuroimage* 1998; **8:** 377-390.

Alexander DC, Barker GJ, Arridge SR. Detection and modeling of non-Gaussian apparent diffusion coefficient profiles in human brain data. *Magn Reson Med* 2002; **48:** 331-340.

Alexander DC, Pierpaoli C, Basser PJ, Gee JC. Spatial transformations of diffusion tensor magnetic resonance images. *IEEE Trans Med Imaging* 2001; **20:** 1131-1139.

Alexander GE. Basal ganglia-thalamocortical circuits: their role in control of movements. *J Clin Neurophysiol* 1994; **11:** 420-431.

Alexander GE, Crutcher MD, DeLong MR. Basal ganglia-thalamocortical circuits: parallel substrates for motor, oculomotor, "prefrontal" and "limbic" functions. *Prog Brain Res* 1990; **85:** 119-146.

Allen IV, McKeown SR. A histological, histochemical and biochemical study of the macroscopically normal white matter in multiple sclerosis. *J Neurol Sci* 1979; **41:** 81-91.

Allison JD, Meador KJ, Loring DW, Figueroa RE, Wright JC. Functional MRI cerebral activation and deactivation during finger movement. *Neurology* 2000; **54:** 135-142.

Allman JM, Hakeem A, Erwin JM, Nimchinsky E, Hof P. The anterior cingulate cortex. The evolution of an interface between emotion and cognition. *Ann N Y Acad Sci* 2001; **935:** 107-117.

Arden GB, Gucukoglu AG. Grating test of contrast sensitivity in patients with retrobulbar neuritis. *Arch Ophthalmol* 1978; **96:** 1626-1629.

Ashburner J, Friston K. Multimodal image coregistration and partitioning--a unified framework. *Neuroimage* 1997; **6:** 209-217.

Ashburner J, Friston KJ. Voxel-based morphometry--the methods. *Neuroimage* 2000; **11:** 805-821.

Assaf Y, Ben Bashat D, Chapman J *et al.* High b-value q-space analyzed diffusion-weighted MRI: application to multiple sclerosis. *Magn Reson Med* 2002; **47:** 115-126.

Bakshi R, Benedict RH, Bermel RA *et al.* T2 hypointensity in the deep gray matter of patients with multiple sclerosis: a quantitative magnetic resonance imaging study. *Arch Neurol* 2002; **59:** 62-68.

Bakshi R, Miletich RS, Kinkel PR, Emmet ML, Kinkel WR. High-resolution fluorodeoxyglucose positron emission tomography shows both global and regional cerebral hypometabolism in multiple sclerosis. *J Neuroimaging* 1998; **8:** 228-234.

Bammer R, Augustin M, Strasser-Fuchs S*et al.* Magnetic resonance diffusion tensor imaging for characterizing diffuse and focal white matter abnormalities in multiple sclerosis. *Magn Reson Med* 2000; **44:** 583-591.

Bandettini PA, Cox RW. Event-related fMRI contrast when using constant interstimulus interval: theory and experiment. *Magn Reson Med* 2000; **43:** 540-548.

Bandettini PA, Kwong KK, Davis TL *et al.* Characterization of cerebral blood oxygenation and flow changes during prolonged brain activation. *Hum Brain Mapp* 1997; **5:** 93-109.

Barbas H, Pandya DN. Topography of commissural fibers of the prefrontal cortex in the rhesus monkey. *Exp Brain Res* 1984; **55:** 187-191.

Barkhof F, Filippi M, Miller DH *et al.* Comparison of MRI criteria at first presentation to predict conversion to clinically definite multiple sclerosis. *Brain* 1997; **120 (Pt 11):** 2059-2069.

Barkhof F, va n Walderveen M. Characterization of tissue damage in multiple sclerosis by nuclear magnetic resonance. *Philos Trans R Soc Lond B Biol Sci* 1999; **354:** 1675-1686.

Barnes D, Munro PM, Youl BD, Prineas JW, McDonald WI. The longstanding MS lesion. A quantitative MRI and electron microscopic study. *Brain* 1991; **114 (Pt 3):** 1271-1280.

Bashir K, Whitaker JN. Clinical and laboratory features of primary progressive and secondary progressive MS. *Neurology* 1999; **53:** 765-771.

Basser PJ, Mattiello J, LeBihan D. Estimation of the effective self-diffusion tensor from the NMR spin echo. *J Magn Reson B* 1994; **103:** 247-254.

Basser PJ, Pajevic S. Statistical artifacts in diffusion tensor MRI (DT-MRI) caused by background noise. *Magn Reson Med* 2000; **44:** 41-50.

Basser PJ, Pajevic S, Pierpaoli C, Duda J, Aldroubi A. In vivo fiber tractography using DT-MRI data. *Magn Reson Med* 2000; **44:** 625-632.

Basser PJ, Pierpaoli C. Microstructural and physiological features of tissues elucidated by quantitative-diffusion-tensor MRI. *J Magn Reson B* 1996; **111:** 209-219.

Bastin ME, Delgado M, Whittle IR, Cannon J, Wardlaw JM. The use of diffusion tensor imaging in quantifying the effect of dexamethasone on brain tumours. *Neuroreport* 1999; **10:** 1385-1391.

Beaulieu C. The basis of anisotropic water diffusion in the nervous system - a technical review. *NMR Biomed* 2002; **15:** 435-455.

Beck RW. Optic Neuritis. In: Miller NR, Newman NJ, editors. Walsh and Hoyt's Clinical Neuro-ophthalmology. Baltimore: Williams and Wilkins, 1998: 599-647.

Beck RW, Cleary PA. Optic neuritis treatment trial. One-year follow-up results. *Arch Ophthalmol* 1993; **111:** 773-775.

Beck RW, Cleary PA, Backlund JC. The course of visual recovery after optic neuritis. Experience of the Optic Neuritis Treatment Trial. *Ophthalmology* 1994; **101:** 1771-1778.

Beck RW, Gal RL, Bhatti MT *et al.* Visual function more than 10 years after optic neuritis: experience of the optic neuritis treatment trial. *Am J Ophthalmol* 2004; **137:** 77-83.

Beck RW, Trobe JD, Moke PS *et al.* High- and low-risk profiles for the development of multiple sclerosis within 10 years after optic neuritis: experience of the optic neuritis treatment trial. *Arch Ophthalmol* 2003; **121:** 944-949.

Behrens TE, Johansen-Berg H, Woolrich MW *et al.* Non-invasive mapping of connections between human thalamus and cortex using diffusion imaging. *Nat Neurosci* 2003a; **6:** 750-757.

Behrens TE, Woolrich MW, Jenkinson M*et al.* Characterization and propagation of uncertainty in diffusion-weighted MR imaging. *Magn Reson Med* 2003b; **50:** 1077-1088.

Bergers E, Bot JC, van der Valk *et al.* Diffuse signal abnormalities in the spinal cord in multiple sclerosis: direct postmortem in situ magnetic resonance imaging correlated with in vitro high-resolution magnetic resonance imaging and histopathology. *Ann Neurol* 2002; **51:** 652-656.

Bitsch A, Schuchardt J, Bunkowski S, Kuhlmann T, Bruck W. Acute axonal injury in multiple sclerosis. Correlation with demyelination and inflammation. *Brain* 2000; **123 (Pt 6):** 1174-1183.

Bjartmar C, Kinkel RP, Kidd G, Rudick RA, Trapp BD. Axonal loss in normal-appearing white matter in a patient with acute MS. *Neurology* 2001; **57:** 1248-1252.

Bland JM, Altman DG. Measurement error. *Br Med J* 1996a; **313:** 744.

Bland JM, Altman DG. Measurement error proportional to the mean. *Br Med J* 1996b; **313:** 106.

Blinkenberg M, Rune K, Jensen CV *et al.* Cortical cerebral metabolism correlates with MRI lesion load and cognitive dysfunction in MS. *Neurology* 2000; **54:** 558-564.

Bloch F. Nuclear induction. *Phys Rev* 1946; **70:** 460.

Bo L, Vedeler CA, Nyland H, Trapp BD, Mork SJ. Intracortical multiple sclerosis lesions are not associated with increased lymphocyte infiltration. *Mult Scler* 2003; **9:** 323-331.

Bohannon RW, Smith MB. Interrater reliability of a modified Ashworth scale of muscle spasticity. *Phys Ther* 1987; **67:** 206-207.

Boulby P. T2: the transverse relaxation time. In: Paul Tofts, editor. Quantitative MRI of the brain. London: John Wiley & Sons, Ltd., 2003: 141-99.

Bozzali M, Cercignani M, Sormani MP, Comi G, Filippi M. Quantification of brain gray matter damage in different MS phenotypes by use of diffusion tensor MR imaging. *Am J Neuroradiol* 2002; **23:** 985-988.

Braver TS, Cohen JD, Nystrom LE, Jonides J, Smith EE, Noll DC. A parametric study of prefrontal cortex involvement in human working memory. *Neuroimage* 1997; **5:** 49-62.

Brex PA, Ciccarelli O, O'Riordan JI, Sailer M, Thompson AJ, Miller DH. A longitudinal study of abnormalities on MRI and disability from multiple sclerosis. *N Engl J Med* 2002; **346:** 158-164.

Brex PA, Gomez-Anson B, Parker GJ *et al.* Proton MR spectroscopy in clinically isolated syndromes suggestive of multiple sclerosis. *J Neurol Sci* 1999; **166:** 16-22.

Brodal A. Descending Supraspinal Pathways. In: Brodal A, editor. Neurological Anatomy in relation to Clinical Medicine. Oxford: Oxford University Press, 1981: 180-293.

Brownell B, Hughes JT. The distribution of plaques in the cerebrum in multiple sclerosis. *J Neurol Neurosurg Psychiatry* 1962; **25:** 315-320.

Buckner RL. Event-related fMRI and the hemodynamic response. *Hum Brain Mapp* 1998; **6:** 373-377.

Burgel U, Schormann T, Schleicher A, Zilles K. Mapping of histologically identified long fiber tracts in human cerebral hemispheres to the MRI volume of a reference brain: position and spatial variability of the optic radiation. *Neuroimage* 1999; **10:** 489-499.

Buxton RB, Wong EC, Frank LR. Dynamics of blood flow and oxygenation changes during brain activation: the balloon model. *Magn Reson Med* 1998; **39:** 855-864.

Carel C, Loubinoux I, Boulanouar K *et al.* Neural substrate for the effects of passive training on sensorimotor cortical representation: a study with functional magnetic resonance imaging in healthy subjects. *J Cereb Blood Flow Metab* 2000; **20:** 478-484.

Carey JR, Kimberley TJ, Lewis SM *et al.* Analysis of fMRI and finger tracking training in subjects with chronic stroke. *Brain* 2002; **125:** 773-788.

Carr HY, Purcell EM. Effects of diffusion on free precession in nuclear magnetic resonance experiments. *Phys Rev* 1954; **94:** 630.

Catani M, Jones DK, Donato R, ffytche DH. Occipito-temporal connections in the human brain. *Brain* 2003; **126:** 2093-2107.

Cercignani M, Bozzali M, Iannucci G, Comi G, Filippi M. Magnetisation transfer ratio and mean diffusivity of normal appearing white and grey matter from patients with multiple sclerosis. *J Neurol Neurosurg Psychiatry* 2001a; **70:** 311-317.

Cercignani M, Horsfield MA. The physical basis of diffusion-weighted MRI. *J Neurol Sci* 2001; **186 Suppl 1:** S11-S14.

Cercignani M, Iannucci G, Rocca MA, Comi G, Horsfield MA, Filippi M. Pathologic damage in MS assessed by diffusion-weighted and magnetization transfer MRI. *Neurology* 2000; **54:** 1139-1144.

Cercignani M, Inglese M, Pagani E, Comi G, Filippi M. Mean diffusivity and fractional anisotropy histograms of patients with multiple sclerosis. *Am J Neuroradiol* 2001b; **22:** 952-958.

Chabriat H, Pappata S, Poupon C *et al.* Clinical severity in CADASIL related to ultrastructural damage in white matter: in vivo study with diffusion tensor MRI. *Stroke* 1999; **30:** 2637-2643.

Charcot JM. Histologie de la sclerose en plaques. *Gazette Hopital* 1868; **41:** 554-558.

Chard DT, Griffin CM, McLean MA *et al.* Brain metabolite changes in cortical grey and normal-appearing white matter in clinically early relapsing-remitting multiple sclerosis. *Brain* 2002a; **125:** 2342-2352.

Chard DT, Parker GJ, Griffin CM, Thompson AJ, Miller DH. The reproducibility and sensitivity of brain tissue volume measurements derived from an SPM-based segmentation methodology. *J Magn Reson Imaging* 2002b; **15:** 259-267.

Ciccarelli O, Giugni E, Paolillo A *et al.* Magnetic resonance outcome of new enhancing lesions in patients with relapsing-remitting multiple sclerosis. *Eur J Neurol* 1999; **6:** 455-459.

Ciccarelli O, Parker GJ, Toosy AT *et al.* From diffusion tractography to quantitative white matter tract measures: a reproducibility study. *Neuroimage* 2003; **18:** 348-359.

Cifelli A, Arridge M, Jezzard P, Esiri MM, Palace J, Matthews PM. Thalamic neurodegeneration in multiple sclerosis. *Ann Neurol* 2002; **52:** 650-653.

Clark CA, Le Bihan D. Water diffusion compartmentation and anisotropy at high b values in the human brain. *Magn Reson Med* 2000; **44:** 852-859.

Compston DA, Batchelor JR, Earl CJ, McDonald WI. Factors influencing the risk of multiple sclerosis developing in patients with optic neuritis. *Brain* 1978; **101:** 495-511.

Confavreux C, Aimard G, Devic M. Course and prognosis of multiple sclerosis assessed by the computerized data processing of 349 patients. *Brain* 1980; **103:** 281-300.

Confavreux C, Vukusic S, Adeleine P. Early clinical predictors and progression of irreversible disability in multiple sclerosis: an amnesic process. *Brain* 2003; **126:** 770-782.

Confavreux C, Vukusic S, Moreau T, Adeleine P. Relapses and progression of disability in multiple sclerosis. *N Engl J Med* 2000; **343:** 1430-1438.

Conturo TE, Lori NF, Cull TS *et al.* Tracking neuronal fiber pathways in the living human brain. *Proc Natl Acad Sci U S A* 1999; **96:** 10422-10427.

Cottrell DA, Kremenchutzky M, Rice GP *et al.* The natural history of multiple sclerosis: a geographically based study. 5. The clinical features and natural history of primary progressive multiple sclerosis. *Brain* 1999; **122 (Pt 4):** 625-639.

Cox TA, Thompson HS, Corbett JJ. Relative afferent pupillary defects in optic neuritis. *Am J Ophthalmol* 1981; **92:** 685-690.

Crosby E.C., Humphrey T., Laver E.W. Correlative anatomy of the nervous system. New York: 1962.

Cutter GR, Baier ML, Rudick RA *et al.* Development of a multiple sclerosis functional composite as a clinical trial outcome measure. *Brain* 1999; **122:** 871-882.

Dalton CM, Brex PA, Miszkiel KA *et al.* Application of the new McDonald criteria to patients with clinically isolated syndromes suggestive of multiple sclerosis. *Ann Neurol* 2002; **52:** 47-53.

Davies MB, Williams R, Haq N, Pelosi L, Hawkins CP. MRI of optic nerve and postchiasmal visual pathways and visual evoked potentials in secondary progressive multiple sclerosis. *Neuroradiology* 1998; **40:** 765-770.

de Lacoste MC, Kirkpatrick JB, Ross ED. Topography of the human corpus callosum. *J Neuropathol Exp Neurol* 1985; **44:** 578-591.

de Preux J, Mair WG. Ultrastructure of the optic nerve in Schilder's disease, Devic's disease and disseminated sclerosis. *Acta Neuropathol (Berl)* 1974; **30:** 225-242.

De Stefano N, Matthews PM, Filippi M *et al.* Evidence of early cortical atrophy in MS: relevance to white matter changes and disability. *Neurology* 2003; **60:** 1157-1162.

De Stefano N, Matthews PM, Fu L *et al.* Axonal damage correlates with disability in patients with relapsing- remitting multiple sclerosis. Results of a longitudinal magnetic resonance spectroscopy study. *Brain* 1998; **121 (Pt 8):** 1469-1477.

De Stefano N, Narayanan S, Francis GS *et al.* Evidence of axonal damage in the early stages of multiple sclerosis and its relevance to disability. *Arch Neurol* 2001; **58:** 65-70.

De Stefano N, Narayanan S, Matthews PM, Francis GS, Antel JP, Arnold DL. In vivo evidence for axonal dysfunction remote from focal cerebral demyelination of the type seen in multiple sclerosis. *Brain* 1999; **122 (Pt 10):** 1933-1939.

De Stefano N, Narayanan S, Mortilla M*et al.* Imaging axonal damage in multiple sclerosis by means of MR spectroscopy. *Neurol Sci* 2000; **21:** S883-S887.

Dean G, McLoughlin H, Brady R, Adelstein AM, Tallett-Williams J. Multiple sclerosis among immigrants in Greater London. *Br Med J* 1976; **1:** 861-864.

Dehmeshki J, Chard DT, Leary SM *et al.* The normal appearing grey matter in primary progressive multiple sclerosis: a magnetisation transfer imaging study. *J Neurol* 2003; **250:** 67-74.

DeLuca GC, Ebers GC, Esiri MM. Axonal loss in multiple sclerosis: a pathological survey of the corticospinal and sensory tracts. *Brain* 2004; **127 (Pt 5):** 1009-1018.

Demirci M, Grill S, McShane L, Hallett M. A mismatch between kinesthetic and visual perception in Parkinson's disease. *Ann Neurol* 1997; **41:** 781-788.

Devinsky O, Morrell MJ, Vogt BA. Contributions of anterior cingulate cortex to behaviour. *Brain* 1995; **118 (Pt 1):** 279-306.

Duncan GH, Bushnell MC, Bates R, Dubner R. Task-related responses of monkey medullary dorsal horn neurons. *J Neurophysiol* 1987; **57:** 289-310.

Ebers GC, Bulman DE, Sadovnick AD *et al.* A population-based study of multiple sclerosis in twins. *N Engl J Med* 1986; **315:** 1638-42.

Ellis CM, Simmons A, Jones DK *et al.* Diffusion tensor MRI assesses corticospinal tract damage in ALS. *Neurology* 1999; **53:** 1051-1058.

Engel SA, Glover GH, Wandell BA. Retinotopic organization in human visual cortex and the spatial precision of functional MRI. *Cereb Cortex* 1997; **7:** 181-192.

Eriksson SH, Rugg-Gunn FJ, Symms MR, Barker GJ, Duncan JS. Diffusion tensor imaging in patients with epilepsy and malformations of cortical development. *Brain* 2001; **124:** 617-626.

Ernst T, Hennig J. Observation of a fast response in functional MR. *Magn Reson Med* 1994; **32:** 146-149.

Evangelou N, Esiri MM, Smith S, Palace J, Matthews PM. Quantitative pathological evidence for axonal loss in normal appearing white matter in multiple sclerosis. *Ann Neurol* 2000a; **47:** 391-395.

Evangelou N, Konz D, Esiri MM, Smith S, Palace J, Matthews PM. Regional axonal loss in the corpus callosum correlates with cerebral white matter lesion volume and distribution in multiple sclerosis. *Brain* 2000b; **123 (Pt9):** 1845-1849.

Evangelou N, Konz D, Esiri MM, Smith S, Palace J, Matthews PM. Size-selective neuronal changes in the anterior optic pathways suggest a differential susceptibility to injury in multiple sclerosis. *Brain* 2001; **124:** 1813-1820.

Fabene PF, Marzola P, Sbarbati A, Bentivoglio M. Magnetic resonance imaging of changes elicited by status epilepticus in the rat brain: diffusion-weighted and T2-weighted images, regional blood volume maps, and direct correlation with tissue and cell damage. *Neuroimage* 2003; **18:** 375-389.

Fabiano AJ, Sharma J, Weinstock-Guttman B *et al.* Thalamic involvement in multiple sclerosis: a diffusion-weighted magnetic resonance imaging study. *J Neuroimaging* 2003; **13:** 307-314.

Farzaneh F, Riederer SJ, Pelc NJ. Analysis of T2 limitations and off-resonance effects on spatial resolution and artifacts in echo-planar imaging. *Magn Reson Med* 1990; **14:** 123-139.

Fazekas F, Barkhof F, Filippi M*et al.* The contribution of magnetic resonance imaging to the diagnosis of multiple sclerosis. *Neurology* 1999; **53:** 448-456.

Ferguson B, Matyszak MK, Esiri MM, Perry VH. Axonal damage in acute multiple sclerosis lesions. *Brain* 1997; **120 (Pt 3):** 393-399.

Filippi M, Bozzali M, Comi G. Magnetization transfer and diffusion tensor MR imaging of basal ganglia from patients with multiple sclerosis. *J Neurol Sci* 2001a; **183:** 69-72.

Filippi M, Bozzali M, Horsfield MA *et al.* A conventional and magnetization transfer MRI study of the cervical cord in patients with MS. *Neurology* 2000a; **54:** 207-213.

Filippi M, Bozzali M, Rovaris M *et al.* Evidence for widespread axonal damage at the earliest clinical stage of multiple sclerosis. *Brain* 2003; **126:** 433-437.

Filippi M, Campi A, Dousset V *et al.* A magnetization transfer imaging study of normal-appearing white matter in multiple sclerosis. *Neurology* 1995; **45:** 478-482.

Filippi M, Cercignani M, Inglese M, Horsfield MA, Comi G. Diffusion tensor magnetic resonance imaging in multiple sclerosis. *Neurology* 2001b; **56:** 304-311.

Filippi M, Iannucci G, Cercignani M, Assunta RM, Pratesi A, Comi G. A quantitative study of water diffusion in multiple sclerosis lesions and normal-appearing white matter using echo-planar imaging. *Arch Neurol* 2000b; **57:** 1017-1021.

Filippi M, Iannucci G, Tortorella C *et al.* Comparison of MS clinical phenotypes using conventional and magnetization transfer MRI. *Neurology* 1999; **52:** 588-594.

Filippi M, Rocca MA. Disturbed function and plasticity in multiple sclerosis as gleaned from functional magnetic resonance imaging. *Curr Opin Neurol* 2003; **16:** 275-282.

Filippi M, Rocca MA, Colombo B *et al.* Functional magnetic resonance imaging correlates of fatigue in multiple sclerosis. *Neuroimage* 2002a; **15:** 559-567.

Filippi M, Rocca MA, Falini A *et al.* Correlations between structural CNS damage and functional MRI changes in primary progressive MS. *Neuroimage* 2002b; **15:** 537-546.

Filippi M, Rovaris M, Capra R *et al.* A multi-centre longitudinal study comparing the sensitivity of monthly MRI after standard and triple dose gadolinium-DTPA for monitoring disease activity in multiple sclerosis. Implications for phase II clinical trials. *Brain* 1998; **121 (Pt 10):** 2011-2020.

Fisher LD, van Belle G. Sample size for observational studies. In: Wiley-Interscience, editor. Biostatistics. A Methodology for the Health Sciences. New York: 2003.

Foong J, Maier M, Clark CA, Barker GJ, Miller DH, Ron MA. Neuropathological abnormalities of the corpus callosum in schizophrenia: a diffusion tensor imaging study. *J Neurol Neurosurg Psychiatry* 2000; **68:** 242-244.

Fox PT, Raichle ME. Focal physiological uncoupling of cerebral blood flow and oxidative metabolism during somatosensory stimulation in human subjects. *Proc Natl Acad Sci U S A* 1986; **83:** 1140-1144.

Frank LR. Characterization of anisotropy in high angular resolution diffusion-weighted MRI. *Magn Reson Med* 2002; **47:** 1083-1099.

Friston KJ. Commentary and opinion: II. Statistical parametric mapping: ontology and current issues. *J Cereb Blood Flow Metab* 1995; **15:** 361-370.

Friston KJ, Frith CD, Liddle PF, Dolan RJ, Lammertsma AA, Frackowiak RS. The relationship between global and local changes in PET scans. *J Cereb Blood Flow Metab* 1990; **10:** 458-466.

Friston KJ, Frith CD, Liddle PF, Frackowiak RS. Comparing functional (PET) images: the assessment of significant change. *J Cereb Blood Flow Metab* 1991; **11:** 690-699.

Friston KJ, Glaser DE, Henson RN, Kiebel S, Phillips C, Ashburner J. Classical and Bayesian inference in neuroimaging: applications. *Neuroimage* 2002; **16:** 484-512.

Friston KJ, Holmes A, Poline JB, Price CJ, Frith CD. Detecting activations in PET and fMRI: levels of inference and power. *Neuroimage* 1996a; **4:** 223-235.

Friston KJ, Holmes AP, Worsley KJ. How many subjects constitute a study? *Neuroimage* 1999; **10:** 1-5.

Friston KJ, Holmes AP, Worsley KJ, Poline JB, Frith CD, Frackowiak RSJ. Statistical parametric maps in functional imaging: A general linear approach. *Hum Brain Mapp* 1995; **2:** 189-210.

Friston KJ, Williams S, Howard R, Frackowiak RS, Turner R. Movement-related effects in fMRI time-series. *Magn Reson Med* 1996b; **35:** 346-355.

Fu L, Matthews PM, De Stefano N *et al.* Imaging axonal damage of normal-appearing white matter in multiple sclerosis. *Brain* 1998; **121 (Pt 1):** 103-113.

Gale CR, Martyn CN. Migrant studies in multiple sclerosis. *Prog Neurobiol* 1995; **47:** 425-448.

Ganter P, Prince C, Esiri MM. Spinal cord axonal loss in multiple sclerosis: a post-mortem study. *Neuropathol Appl Neurobiol* 1999; **25:** 459-467.

Gass A, Barker GJ, MacManus D *et al.* High resolution magnetic resonance imaging of the anterior visual pathway in patients with optic neuropathies using fast spin echo and phased array local coils. *J Neurol Neurosurg Psychiatry* 1995; **58:** 562-569.

Gass A, Filippi M, Rodegher ME, Schwartz A, Comi G, Hennerici MG. Characteristics of chronic MS lesions in the cerebrum, brainstem, spinal cord, and optic nerve on T1-weighted MRI. *Neurology* 1998; **50:** 548-550.

Gean-Marton AD, Vezina LG, Marton KI *et al.* Abnormal corpus callosum: a sensitive and specific indicator of multiple sclerosis. *Radiology* 1991; **180:** 215-221.

Gellman R, Gibson AR, Houk JC. Inferior olivary neurons in the awake cat: detection of contact and passive body displacement. *J Neurophysiol* 1985; **54:** 40-60.

Gerardin E, Lehericy S, Pochon JB *et al.* Foot, hand, face and eye representation in the human striatum. *Cereb Cortex* 2003; **13:** 162-169.

Gjedde A. Brain energy metabolisms and the physiological basis of the haemodynamic response. In: Jezzard P, Matthews P.M., Smith SM, editors. Functional MRI: an introduction to methods. Oxford: Oxford University Press, 2001: 37-65.

Good CD, Johnsrude I, Ashburner J, Henson RN, Friston KJ, Frackowiak RS. Cerebral asymmetry and the effects of sex and handedness on brain structure: a voxel-based morphometric analysis of 465 normal adult human brains. *Neuroimage* 2001; **14:** 685-700.

Goodkin DE, Rooney WD, Sloan R *et al.* A serial study of new MS lesions and the white matter from which they arise. *Neurology* 1998; **51:** 1689-1697.

Gossl C, Fahrmeir L, Putz B, Auer LM, Auer DP. Fiber tracking from DTI using linear state space models: detectability of the pyramidal tract. *Neuroimage* 2002; **16:** 378-388.

Griffiths I, Klugmann M, Anderson T *et al.* Axonal swellings and degeneration in mice lacking the major proteolipid of myelin. *Science* 1998; **280:** 1610-1613.

Grill SE, Hallett M, Marcus C, McShane L. Disturbances of kinaesthesia in patients with cerebellar disorders. *Brain* 1994; **117 (Pt 6):** 1433-1447.

Grimaud J, Millar J, Thorpe JW, Moseley IF, McDonald WI, Miller DH. Signal intensity on MRI of basal ganglia in multiple sclerosis. *J Neurol Neurosurg Psychiatry* 1995; **59:** 306-308.

Grodd W, Hulsmann E, Lotze M, Wildgruber D, Erb M. Sensorimotor mapping of the human cerebellum: fMRI evidence of somatotopic organization. *Hum Brain Mapp* 2001; **13:** 55-73.

Grossman RI, Gonzalez-Scarano F, Atlas SW, Galetta S, Silberberg DH. Multiple sclerosis: gadolinium enhancement in MR imaging. *Radiology* 1986; **161:** 721-725.

Guy J, Fitzsimmons J, Ellis EA, Beck B, Mancuso A. Intraorbital optic nerve and experimental optic neuritis. Correlation of fat suppression magnetic resonance imaging and electron microscopy. *Ophthalmology* 1992; **99:** 720-725.

Guye M, Parker GJ, Symms M *et al.* Combined functional MRI and tractography to demonstrate the connectivity of the human primary motor cortex in vivo. *Neuroimage* 2003; **19:** 1349-1360.

Haase A, Frahm J, Matthaei D, Hanicke W, Merboldt KD. Flash imaging: rapid NMR imaging using low flip angle pulses. *J Magn Reson* 1986; **67:** 258.

Hadjiprocopis, A., Rashid, W., and Tofts, P. S. Segmentation of T2-weighted MRI using an ensemble of neural network and clustering experts. *Proc Intl Soc Mag Reson Med* 2003. Abstract.

Hahn EL. Spin echoes. *Phys Rev* 1950; **80:** 580.

Hallett M. Is dystonia a sensory disorder? *Ann Neurol* 1995; **38:** 139-140.

Hartmann MJ, Bower JM. Tactile responses in the granule cell layer of cerebellar folium crus IIa of freely behaving rats. *J Neurosci* 2001; **21:** 3549-3563.

Hayreh SS, Massanari RM, Yamada T, Hayreh SM. Experimental allergic encephalomyelitis. I. Optic nerve and central nervous system manifestations. *Invest Ophthalmol Vis Sci* 1981; **21:** 256-269.

Hellier, P., Ashburner, J., Corouge, I., Barillot, C., and Friston, K. J. Intersubject registration of functional and anatomical data using SPM. *Proceedings of the 5th International Conference for Medical Image Computing and Computer-Assisted Intervention* 2002. Abstract.

Henkelman RM, Neil JJ, Xiang QS. A quantitative interpretation of IVIM measurements of vascular perfusion in the rat brain. *Magn Reson Med* 1994; **31:** 637-644.

Henry RG, Oh J, Nelson SJ, Pelletier D. Directional diffusion in relapsing-remitting multiple sclerosis: a possible in vivo signature of Wallerian degeneration. *J Magn Reson Imaging* 2003; **18:** 420-426.

Hickman SJ, Brex PA, Brierley CM *et al.* Detection of optic nerve atrophy following a single episode of unilateral optic neuritis by MRI using a fat-saturated short-echo fast FLAIR sequence. *Neuroradiology* 2001; **43:** 123-128.

Hickman SJ, Brierley CM, Brex PA *et al.* Continuing optic nerve atrophy following optic neuritis: a serial MRI study. *Mult Scler* 2002; **8:** 339-342.

Hoge RD, Atkinson J, Gill B, Crelier GR, Marrett S, Pike GB. Linear coupling between cerebral blood flow and oxygen consumption in activated human cortex. *Proc Natl Acad Sci U S A* 1999; **96:** 9403-9408.

Holladay JT. Proper method for calculating average visual acuity. *J Refract Surg* 1997; **13:** 388-391.

Holmes AA, Scollan DF, Winslow RL. Direct histological validation of diffusion tensor MRI in formaldehyde- fixed myocardium. *Magn Reson Med* 2000; **44:** 157-161.

Hornabrook RS, Miller DH, Newton MR *et al.* Frequent involvement of the optic radiation in patients with acute isolated optic neuritis. *Neurology* 1992; **42:** 77-79.

Horsfield MA, Lai M, Webb SL *et al.* Apparent diffusion coefficients in benign and secondary progressive multiple sclerosis by nuclear magnetic resonance. *Magn Reson Med* 1996; **36:** 393-400.

Horsfield MA, Larsson HB, Jones DK, Gass A. Diffusion magnetic resonance imaging in multiple sclerosis. *J Neurol Neurosurg Psychiatry* 1998; **64 Suppl 1:** S80-S84.

Houk JC, Wise SP. Distributed modular architectures linking basal ganglia, cerebellum, and cerebral cortex: their role in planning and controlling action. *Cereb Cortex* 1995; **5:** 95-110.

Ikuta F, Zimmerman HM. Distribution of plaques in seventy autopsy cases of multiple sclerosis in the United States. *Neurology* 1976; **26:** 26-28.

Ingle, G. T., Sastre-Garriga J., Miller, D. H., and Thompson, A. J. Does inflammation have a role in early PPMS: a longitudinal MRI study. *Multiple Sclerosis* 2003. Abstract.

Inglis BA, Neubauer D, Yang L, Plant D, Mareci TH, Muir D. Diffusion tensor MR imaging and comparative histology of glioma engrafted in the rat spinal cord. *Am J Neuroradiol* 1999; **20:** 713-716.

Jane JA, Yashon D, DeMyer W, Bucy PC. The contribution of the precentral gyrus to the pyramidal tract of man. *J Neurosurg* 1967; **26:** 244-248.

Jezzard P, Ramsey NF. Functional MRI. In: Tofts P, editor. Quantitative MRI of the brain. London: John Wiley and Sons, Ltd., 2003: 414-53.

Johansen-Berg H, Behrens TE, Sillery E *et al.* Functional-anatomical validation and individual variation of diffusion tractography-based segmentation of the human thalamus. *Cereb Cortex* 2005; **15:** 31-39.

Johansen-Berg H, Rushworth MF, Bogdanovic MD, Kischka U, Wimalaratna S, Matthews PM. The role of ipsilateral premotor cortex in hand movement after stroke. *Proc Natl Acad Sci U S A* 2002; **99:** 14518-14523.

Jones DK, Griffin LD, Alexander DC *et al.* Spatial normalization and averaging of diffusion tensor MRI data sets. *Neuroimage* 2002; **17:** 592-617.

Jones DK, Horsfield MA, Simmons A. Optimal strategies for measuring diffusion in anisotropic systems by magnetic resonance imaging. *Magn Reson Med* 1999a; **42:** 515-525.

Jones DK, Lythgoe D, Horsfield MA, Simmons A, Williams SC, Markus HS. Characterization of white matter damage in ischemic leukoaraiosis with diffusion tensor MRI. *Stroke* 1999b; **30:** 393-397.

Jones DK, Simmons A, Williams SC, Horsfield MA. Non-invasive assessment of axonal fiber connectivity in the human brain via diffusion tensor MRI. *Magn Reson Med* 1999c; **42:** 37-41.

Jones EG. Making brain connections: neuroanatomy and the work of TPS Powell, 1923-1996. *Annu Rev Neurosci* 1999; **22:** 49-103.

Jueptner M, Ottinger S, Fellows SJ *et al.* The relevance of sensory input for the cerebellar control of movements. *Neuroimage* 1997; **5:** 41-48.

Kandel ER, Schwarts JH, Jessell TM. Voluntary movement. In: Mc graw Hill, editor. Principle of Neural Science. New York: 2000: 756-79.

Kantarci O, Siva A, Eraksoy M *et al.* Survival and predictors of disability in Turkish MS patients. Turkish Multiple Sclerosis Study Group (TUMSSG). *Neurology* 1998; **51:** 765-772.

Keltner JL, Johnson CA, Spurr JO, Beck RW. Baseline visual field profile of optic neuritis. The experience of the optic neuritis treatment trial. Optic Neuritis Study Group. *Arch Ophthalmol* 1993; **111:** 231-234.

Keltner JL, Johnson CA, Spurr JO, Beck RW. Visual field profile of optic neuritis. One-year follow-up in the Optic Neuritis Treatment Trial. *Arch Ophthalmol* 1994; **112:** 946-953.

Kermode AG, Thompson AJ, Tofts P *et al.* Breakdown of the blood-brain barrier precedes symptoms and other MRI signs of new lesions in multiple sclerosis. Pathogenetic and clinical implications. *Brain* 1990; **113 (Pt 5):** 1477-1489.

Kidd D, Barkhof F, McConnell R, Algra PR, Allen IV, Revesz T. Cortical lesions in multiple sclerosis. *Brain* 1999; **122 (Pt 1):** 17-26.

Kidd D, Thorpe JW, Thompson AJ *et al.* Spinal cord MRI using multi-array coils and fast spin echo. II. Findings in multiple sclerosis. *Neurology* 1993; **43:** 2632-2637.

King MD, Houseman J, Roussel SA, van Bruggen N, Williams SR, Gadian DG. q-Space imaging of the brain. *Magn Reson Med* 1994; **32:** 707-713.

Koch MA, Norris DG, Hund-Georgiadis M. An investigation of functional and anatomical connectivity using magnetic resonance imaging. *Neuroimage* 2002; **16:** 241-250.

Kornek B, Lassmann H. Neuropathology of multiple sclerosis-new concepts. *Brain Res Bull* 2003; **61:** 321-326.

Kornek B, Storch MK, Weissert R *et al.* Multiple sclerosis and chronic autoimmune encephalomyelitis: a comparative quantitative study of axonal injury in active, inactive, and remyelinated lesions. *Am J Pathol* 2000; **157:** 267-276.

Kuhlmann T, Lingfeld G, Bitsch A, Schuchardt J, Bruck W. Acute axonal damage in multiple sclerosis is most extensive in early disease stages and decreases over time. *Brain* 2002; **125:** 2202-2212.

Kuperman V. Magnetic Resonance Imaging: Physical Principles and Applications. San Diego, USA: Academic Press, 2000.

Kupersmith MJ, Nelson JI, Seiple WH, Carr RE, Weiss PA. The 20/20 eye in multiple sclerosis. *Neurology* 1983; **33:** 1015-1020.

Kurtzke JF. Rating neurologic impairment in multiple sclerosis: an expanded disability status scale (EDSS). *Neurology* 1983; **33:** 1444-1452.

Kurtzke JF. Epidemiologic evidence for multiple sclerosis as an infection [published erratum appears in Clin Microbiol Rev 1994 Jan;7(1):141]. *Clin Microbiol Rev* 1993; **6:** 382-427.

Kurtzke JF, Beebe GW, Nagler B, Kurland LT, Auth TL. Studies on the natural history of multiple sclerosis--8. Early prognostic features of the later course of the illness. *J Chronic Dis* 1977; **30:** 819-830.

Kwong KK, Belliveau JW, Chesler DA *et al.* Dynamic magnetic resonance imaging of human brain activity during primary sensory stimulation. *Proc Natl Acad Sci U S A* 1992; **89:** 5675-9.

Lassmann H. Neuropathology in multiple sclerosis: new concepts. *Mult Scler* 1998; **4:** 93-98.

Lassmann H. Brain damage when multiple sclerosis is diagnosed clinically. *Lancet* 2003; **361:** 1317-1318.

Lassmann H, Bruck W, Lucchinetti C. Heterogeneity of multiple sclerosis pathogenesis: implications for diagnosis and therapy. *Trends Mol Med* 2001; **7:** 115-121.

Lassmann H, Suchanek G, Ozawa K. Histopathology and the blood-cerebrospinal fluid barrier in multiple sclerosis. *Ann Neurol* 1994; **36 Suppl:** S42-S46.

Lazar M, Alexander AL. An error analysis of white matter tractography methods: synthetic diffusion tensor field simulations. *Neuroimage* 2003; **20:** 1140-1153.

Lazar M, Weinstein DM, Tsuruda JS *et al.* White matter tractography using diffusion tensor deflection. *Hum Brain Mapp* 2003; **18:** 306-321.

Le Bihan D, Breton E, Lallemand D, Grenier P, Cabanis E, Laval-Jeantet M. MR imaging of intravoxel incoherent motions: application to diffusion and perfusion in neurologic disorders. *Radiology* 1986; **161:** 401-407.

Lee M, Reddy H, Johansen-Berg H *et al.* The motor cortex shows adaptive functional changes to brain injury from multiple sclerosis. *Ann Neurol* 2000; **47:** 606-613.

Lin CP, Wedeen VJ, Chen JH, Yao C, Tseng WY. Validation of diffusion spectrum magnetic resonance imaging with manganese-enhanced rat optic tracts and ex vivo phantoms. *Neuroimage* 2003; **19:** 482-495.

Ljunggren S. A simple graphical representation of Fourier-based imaging methods. *J Magn Reson* 1983; **54:** 338.

Logothetis NK, Pauls J, Augath M, Trinath T, Oeltermann A. Neurophysiological investigation of the basis of the fMRI signal. *Nature* 2001; **412:** 150-157.

Lori NF, Akbudak E, Shimony JS *et al.* Diffusion tensor fiber tracking of human brain connectivity: aquisition methods, reliability analysis and biological results. *NMR Biomed* 2002; **15:** 494-515.

Losseff NA, Wang L, Lai HM *et al.* Progressive cerebral atrophy in multiple sclerosis. A serial MRI study. *Brain* 1996a; **119 (Pt 6):** 2009-2019.

Losseff NA, Webb SL, O'Riordan JI *et al.* Spinal cord atrophy and disability in multiple sclerosis. A new reproducible and sensitive MRI method with potential to monitor disease progression. *Brain* 1996b; **119:** 701-708.

Lotze M, Erb M, Flor H, Huelsmann E, Godde B, Grodd W. fMRI evaluation of somatotopic representation in human primary motor cortex. *Neuroimage* 2000; **11:** 473-481.

Lublin FD, Reingold SC. Defining the clinical course of multiple sclerosis: results of an international survey. National Multiple Sclerosis Society (USA) Advisory Committee on Clinical Trials of New Agents in Multiple Sclerosis. *Neurology* 1996; **46:** 907-911.

Lucchinetti C, Bruck W, Parisi J, Scheithauer B, Rodriguez M, Lassmann H. A quantitative analysis of oligodendrocytes in multiple sclerosis lesions. A study of 113 cases. *Brain* 1999; **122 (Pt 12):** 2279-2295.

Lucchinetti C, Bruck W, Parisi J, Scheithauer B, Rodriguez M, Lassmann H. Heterogeneity of multiple sclerosis lesions: implications for the pathogenesis of demyelination. *Ann Neurol* 2000; **47:** 707-717.

Lucchinetti CF, Bruck W, Rodriguez M, Lassmann H. Distinct patterns of multiple sclerosis pathology indicates heterogeneity on pathogenesis. *Brain Pathol* 1996; **6:** 259-74.

Lueck CJ, Zeki S, Friston KJ *et al.* The colour centre in the cerebral cortex of man. *Nature* 1989; **340:** 386-389.

Luft AR, Smith GV, Forrester L*et al.* Comparing brain activation associated with isolated upper and lower limb movement across corresponding joints. *Hum Brain Mapp* 2002; **17:** 131-140.

Lycklama G, Thompson A, Filippi M*et al.* Spinal-cord MRI in multiple sclerosis. *Lancet Neurol* 2003; **2:** 555-562.

Madigan MC, Rao NS, Tenhula WN, Sadun AA. Preliminary morphometric study of tumor necrosis factor-alpha (TNF alpha)-induced rabbit optic neuropathy. *Neurol Res* 1996; **18:** 233-236.

Magistretti PJ, Pellerin L. The contribution of astrocytes to the 18F-2-deoxyglucose signal in PET activation studies. *Mol Psychiatry* 1996; **1:** 445-452.

Maillard L, Ishii K, Bushara K, Waldvogel D, Schulman AE, Hallett M. Mapping the basal ganglia: fMRI evidence for somatotopic representation of face, hand, and foot. *Neurology* 2000; **55:** 377-383.

Malonek D, Dirnagl U, Lindauer U, Yamada K, Kanno I, Grinvald A. Vascular imprints of neuronal activity: relationships between the dynamics of cortical blood flow, oxygenation, and volume changes following sensory stimulation. *Proc Natl Acad Sci U S A* 1997; **94:** 14826-14831.

Mansfield P, Pykett IL. Biological and medical imaging by NMR. *J Magn Reson* 1978; **29:** 355.

Mayer AR, Zimbelman JL, Watanabe Y, Rao SM. Somatotopic organization of the medial wall of the cerebral hemispheres: a 3 Tesla fMRI study. *Neuroreport* 2001; **12:** 3811-3814.

McDonald I. Diagnostic methods and investigation in multiple sclerosis. In: Compston A EGLHMIMBWH, editor. Mc Alpine's Multiple Sclerosis. London: Churcill Livingstone, 1998: 251-79.

McDonald WI. Pathophysiology in multiple sclerosis. *Brain* 1974; **97:** 179-196.

McDonald WI. Conduction in the optic nerve. *Trans Ophthalmol Soc U K* 1976; **96:** 352-354.

McDonald WI, Compston A, Edan G *et al.* Recommended diagnostic criteria for multiple sclerosis: guidelines from the International Panel on the diagnosis of multiple sclerosis. *Ann Neurol* 2001; **50:** 121-127.

McDonnell GV, Hawkins SA. Application of the Poser criteria in primary progressive multiple sclerosis. *Ann Neurol* 1997; **42:** 982-983.

Menage MJ, Papakostopoulos D, Dean Hart JC, Papakostopoulos S, Gogolitsyn Y. The Farnsworth-Munsell 100 hue test in the first episode of demyelinating optic neuritis. *Br J Ophthalmol* 1993; **77:** 68-74.

Menon RS, Goodyear BG. Submillimeter functional localization in human striate cortex using BOLD contrast at 4 Tesla: implications for the vascular point-spread function. *Magn Reson Med* 1999; **41:** 230-235.

Mesulam MM, Mufson EJ. Insula of the old world monkey. III: Efferent cortical output and comments on function. *J Comp Neurol* 1982; **212:** 38-52.

Middleton FA, Strick PL. Basal ganglia output and cognition: evidence from anatomical, behavioral, and clinical studies. *Brain Cogn* 2000; **42:** 183-200.

Miller DH, Barkhof F, Nauta JJ. Gadolinium enhancement increases the sensitivity of MRI in detecting disease activity in multiple sclerosis. *Brain* 1993; **116 (Pt 5):** 1077-1094.

Miller DH, Grossman RI, Reingold SC, McFarland HF. The role of magnetic resonance techniques in understanding and managing multiple sclerosis. *Brain* 1998; **121 (Pt 1):** 3-24.

Miller DH, Ormerod IE, McDonald WI *et al.* The early risk of multiple sclerosis after optic neuritis. *J Neurol Neurosurg Psychiatry* 1988a; **51:** 1569-1571.

Miller DH, Rudge P, Johnson G *et al.* Serial gadolinium enhanced magnetic resonance imaging in multiple sclerosis. *Brain* 1988b; **111 (Pt 4):** 927-939.

Mima T, Sadato N, Yazawa S *et al.* Brain structures related to active and passive finger movements in man. *Brain* 1999; **122 (Pt 10):** 1989-1997.

Miyai I, Tanabe HC, Sase I *et al.* Cortical mapping of gait in humans: a near-infrared spectroscopic topography study. *Neuroimage* 2001; **14:** 1186-1192.

Moreau T, Coles A, Wing M *et al.* Transient increase in symptoms associated with cytokine release in patients with multiple sclerosis. *Brain* 1996; **119 (Pt 1):** 225-237.

Mori S, Crain BJ, Chacko VP, van Zijl PC. Three-dimensional tracking of axonal projections in the brain by magnetic resonance imaging. *Ann Neurol* 1999; **45:** 265-269.

Mori S, Kaufmann WE, Davatzikos C *et al.* Imaging cortical association tracts in the human brain using diffusion-tensor-based axonal tracking. *Magn Reson Med* 2002; **47:** 215-223.

Mori S, Kaufmann WE, Pearlson GD *et al.* In vivo visualization of human neural pathways by magnetic resonance imaging. *Ann Neurol* 2000; **47:** 412-414.

Mori S, van Zijl PC. Fiber tracking: principles and strategies - a technical review. *NMR Biomed* 2002; **15:** 468-480.

Narayana PA, Doyle TJ, Lai D, Wolinsky JS. Serial proton magnetic resonance spectroscopic imaging, contrast-enhanced magnetic resonance imaging, and quantitative lesion volumetry in multiple sclerosis. *Ann Neurol* 1998; **43:** 56-71.

Nijeholt G, Barkhof F. Differences between subgroups of MS: MRI findings and correlation with histopathology. *J Neurol Sci* 2003; **206:** 173-174.

Nijeholt GJ, Bergers E, Kamphorst W*et al.* Post-mortem high-resolution MRI of the spinal cord in multiple sclerosis: a correlative study with conventional MRI, histopathology and clinical phenotype. *Brain* 2001; **124:** 154-166.

Nijeholt GJ, van Walderveen MA, Castelijns JA *et al.* Brain and spinal cord abnormalities in multiple sclerosis. Correlation between MRI parameters, clinical subtypes and symptoms. *Brain* 1998; **121 (Pt 4):** 687-697.

Noseworthy J, Paty D, Wonnacott T, Feasby T, Ebers G. Multiple sclerosis after age 50. *Neurology* 1983; **33:** 1537-1544.

Ogawa S, Lee TM, Kay AR, Tank DW. Brain magnetic resonance imaging with contrast dependent on blood oxygenation. *Proc Natl Acad Sci U S A* 1990; **87:** 9868-9872.

Ogiso T, Kobayashi K, Sugishita M. The precuneus in motor imagery: a magnetoencephalographic study. *Neuroreport* 2000; **11:** 1345-1349.

Okabe S, Hanajima R, Ohnishi T *et al.* Functional connectivity revealed by single-photon emission computed tomography (SPECT) during repetitive transcranial magnetic stimulation (rTMS) of the motor cortex. *Clin Neurophysiol* 2003; **114:** 450-457.

Optic Neuritis Study Group. The clinical profile of optic neuritis. Experience of the Optic Neuritis Treatment Trial. *Arch Ophthalmol* 1991; **109:** 1673-1678.

Ormerod IE, Miller DH, McDonald WI *et al.* The role of NMR imaging in the assessment of multiple sclerosis and isolated neurological lesions. A quantitative study. *Brain* 1987; **110 (Pt 6):** 1579-1616.

Ozawa K, Suchanek G, Breitschopf H *et al.* Patterns of oligodendroglia pathology in multiple sclerosis. *Brain* 1994; **117 (Pt 6):** 1311-1322.

Pantano P, Iannetti GD, Caramia F*et al.* Cortical motor reorganization after a single clinical attack of multiple sclerosis. *Brain* 2002a; **125:** 1607-1615.

Pantano P, Mainero C, Iannetti GD *et al.* Contribution of corticospinal tract damage to cortical motor reorganization after a single clinical attack of multiple sclerosis. *Neuroimage* 2002b; **17:** 1837-1843.

Parker GJ, Haroon HA, Wheeler-Kingshott CA. A framework for a streamline-based probabilistic index of connectivity (PICo) using a structural interpretation of MRI diffusion measurements. *J Magn Reson Imaging* 2003; **18:** 242-254.

Parker GJ, Klaas SE, Barker GJ *et al.* Initial demonstration of in vivo tracing of axonal projections in the Macaque brain and comparison with the human brain using diffusion tensor imaging and fast marching tractography. *Neuroimage* 2002a.

Parker GJ, Luzzi S, Alexander D, Wheeler-Kingshott CA, Ciccarelli O, Lambon Ralph MA. Lateralization of ventral and dorsal auditory-language pathways in the human brain. *Neuroimage* 2004; **(In Press).**

Parker GJ, Stephan KE, Barker GJ *et al.* Initial demonstration of in vivo tracing of axonal projections in the macaque brain and comparison with the human brain using diffusion tensor imaging and fast marching tractography. *Neuroimage* 2002b; **15:** 797-809.

Parker GJ, Wheeler-Kingshott CA, Barker GJ. Estimating distributed anatomical connectivity using fast marching methods and diffusion tensor imaging. *IEEE Trans Med Imaging* 2002c; **21:** 505-512.

Parry A, Clare S, Jenkinson M, Smith S, Palace J, Matthews PM. White matter and lesion T1 relaxation times increase in parallel and correlate with disability in multiple sclerosis. *J Neurol* 2002; **249:** 1279-1286.

Paulesu E, Perani D, Fazio F*et al.* Functional basis of memory impairment in multiple sclerosis: a[18F]FDG PET study. *Neuroimage* 1996; **4:** 87-96.

Pauling L, Coryell C. The magnetic properties and structure of hemoglobin, oxyhemoglobin, and carbon monoxyhemoglobin. *Proceedings of the National Academy of Sciences (USA)* 1936; **22:** 210-216.

Pautler RG, Silva AC, Koretsky AP. In vivo neuronal tract tracing using manganese-enhanced magnetic resonance imaging. *Magn Reson Med* 1998; **40:** 740-748.

Peled S, Gudbjartsson H, Westin CF, Kikinis R, Jolesz FA. Magnetic resonance imaging shows orientation and asymmetry of white matter fiber tracts. *Brain Res* 1998; **780:** 27-33.

Penfield W., Rasmusseun T. The cerebral cortex of man. New York: Macmillan: 1950.

Perkin GD, Rose FC. Optic Neuritis and its differential diagnosis. Oxford: Oxford University Press, 1979.

Peterson JW, Bo L, Mork S, Chang A, Trapp BD. Transected neurites, apoptotic neurons, and reduced inflammation in cortical multiple sclerosis lesions. *Ann Neurol* 2001; **50:** 389-400.

Petzold A, Eikelenboom MJ, Gveric D *et al.* Markers for different glial cell responses in multiple sclerosis: clinical and pathological correlations. *Brain* 2002; **125:** 1462-1473.

Pierpaoli C, Barnett A, Pajevic S *et al.* Water diffusion changes in Wallerian degeneration and their dependence on white matter architecture. *Neuroimage* 2001; **13:** 1174-1185.

Pierpaoli C, Basser PJ. Toward a quantitative assessment of diffusion anisotropy. *Magn Reson Med* 1996; **36:** 893-906.

Pierpaoli C, Jezzard P, Basser PJ, Barnett A, Di Chiro G. Diffusion tensor MR imaging of the human brain. *Radiology* 1996; **201:** 637-648.

Plant GT, Kermode AG, Turano G *et al.* Symptomatic retrochiasmal lesions in multiple sclerosis: clinical features, visual evoked potentials, and magnetic resonance imaging. *Neurology* 1992; **42:** 68-76.

Plummer DL. Dispimage: a display and analysis tool for medical images. *Rev Neuroradiol* 1992; **5:** 489-495.

Poline JB, Worsley KJ, Evans AC, Friston KJ. Combining spatial extent and peak intensity to test for activations in functional imaging. *Neuroimage* 1997; **5:** 83-96.

Poser CM, Paty DW, Scheinberg L *et al.* New diagnostic criteria for multiple sclerosis: guidelines for research protocols. *Ann Neurol* 1983; **13:** 227-231.

Poupon C, Clark CA, Frouin V *et al.* Regularization of diffusion-based direction maps for the tracking of brain white matter fascicles. *Neuroimage* 2000; **12:** 184-195.

Price CJ, Friston KJ. Cognitive conjunction: a new approach to brain activation experiments. *Neuroimage* 1997; **5:** 261-270.

Prineas J. Pathology of the early lesion in multiple sclerosis. *Hum Pathol* 1975; **6:** 531-554.

Prochazka A. Sensorimotor gain control: a basic strategy of motor systems? *Prog Neurobiol* 1989; **33:** 281-307.

Rademacher J, Burgel U, Geyer S *et al.* Variability and asymmetry in the human precentral motor system. A cytoarchitectonic and myeloarchitectonic brain mapping study. *Brain* 2001; **124:** 2232-2258.

Ramsaransing G, Maurits N, Zwanikken C, de Keyser J. Early prediction of a benign course of multiple sclerosis on clinical grounds: a systematic review. *Mult Scler* 2001; **7:** 345-347.

Ranjeva JP, Pelletier J, Confort-Gouny S *et al.* MRI/MRS of corpus callosum in patients with clinically isolated syndrome suggestive of multiple sclerosis. *Mult Scler* 2003; **9:** 554-565.

Rao NA, Tso MO, Zimmerman EL. Experimental allergic optic neuritis in guinea pigs: preliminary report. *Invest Ophthalmol Vis Sci* 1977; **16:** 338-342.

Rao SM, Binder JR, Hammeke TA *et al.* Somatotopic mapping of the human primary motor cortex with functional magnetic resonance imaging. *Neurology* 1995; **45:** 919-924.

Rashid W., Hadjiprocopis A., Griffin C.M. *et al.* Diffusion tensor imaging of early relapsing remitting multiple sclerosis with histogram analysis using automated segmentation and brain volume correction. *Multiple Sclerosis* 2004; **10:** 9-15.

Rashid W, Parkes LM, Ingle GT *et al.* Abnormalities of cerebral perfusion in multiple sclerosis. *J Neurol Neurosurg Psychiatry* 2004; **75:** 1288-1293.

Reddy H, Floyer A, Donaghy M, Matthews PM. Altered cortical activation with finger movement after peripheral denervation: comparison of active and passive tasks. *Exp Brain Res* 2001; **138:** 484-491.

Reddy H, Narayanan S, Arnoutelis R *et al.* Evidence for adaptive functional changes in the cerebral cortex with axonal injury from multiple sclerosis. *Brain* 2000a; **123:** 2314-2320.

Reddy H, Narayanan S, Matthews PM *et al.* Relating axonal injury to functional recovery in MS. *Neurology* 2000b; **54:** 236-239.

Reddy H, Narayanan S, Woolrich M *et al.* Functional brain reorganization for hand movement in patients with multiple sclerosis: defining distinct effects of injury and disability. *Brain* 2002; **125:** 2646-2657.

Rees G, Friston K, Koch C. A direct quantitative relationship between the functional properties of human and macaque V5. *Nat Neurosci* 2000; **3:** 716-723.

Revesz T, Kidd D, Thompson AJ, Barnard RO, McDonald WI. A comparison of the pathology of primary and secondary progressive multiple sclerosis. *Brain* 1994; **117 (Pt 4):** 759-765.

Riise T. Is the incidence of MS increasing? In: Thompson A.J., Polman C, Hohlfeld R, editors. Multiple Sclerosis: clinical challenges and controversies. London: Martin Dunitz Ltd, 1997.

Rizzolatti G, Luppino G. The cortical motor system. *Neuron* 2001; **31:** 889-901.

Rocca MA, Cercignani M, Iannucci G, Comi G, Filippi M. Weekly diffusion-weighted imaging of normal-appearing white matter in MS. *Neurology* 2000; **55:** 882-884.

Rocca MA, Falini A, Colombo B, Scotti G, Comi G, Filippi M. Adaptive functional changes in the cerebral cortex of patients with nondisabling multiple sclerosis correlate with the extent of brain structural damage. *Ann Neurol* 2002a; **51:** 330-339.

Rocca MA, Gavazzi C, Mezzapesa DM *et al.* A functional magnetic resonance imaging study of patients with secondary progressive multiple sclerosis. *Neuroimage* 2003a; **19:** 1770-1777.

Rocca MA, Iannucci G, Rovaris M, Comi G, Filippi M. Occult tissue damage in patients with primary progressive multiple sclerosis is independent of T2-visible lesions--a diffusion tensor MR study. *J Neurol* 2003b; **250:** 456-460.

Rocca MA, Matthews PM, Caputo D *et al.* Evidence for widespread movement-associated functional MRI changes in patients with PPMS. *Neurology* 2002b; **58:** 866-872.

Rocca MA, Pagani E, Ghezzi A *et al.* Functional cortical changes in patients with multiple sclerosis and nonspecific findings on conventional magnetic resonance imaging scans of the brain. *Neuroimage* 2003c; **19:** 826-836.

Rodriguez M, Siva A, Cross SA, O'Brien PC, Kurland LT. Optic neuritis: a population-based study in Olmsted County, Minnesota. *Neurology* 1995; **45:** 244-250.

Roelcke U, Kappos L, Lechner-Scott J *et al.* Reduced glucose metabolism in the frontal cortex and basal ganglia of multiple sclerosis patients with fatigue: a 18F-fluorodeoxyglucose positron emission tomography study. *Neurology* 1997; **48:** 1566-1571.

Rorden C, Brett M. Stereotaxic display of brain lesions. *Behav Neurol* 2000; **12:** 191-200.

Ross ED. Localization of the pyramidal tract in the internal capsule by whole brain dissection. *Neurology* 1980; **30:** 59-64.

Rovaris M, Agosta F, Sormani MP *et al.* Conventional and magnetization transfer MRI predictors of clinical multiple sclerosis evolution: a medium-term follow-up study. *Brain* 2003; **126:** 2323-2332.

Rovaris M, Bozzali M, Iannucci G *et al.* Assessment of normal-appearing white and gray matter in patients with primary progressive multiple sclerosis: a diffusion-tensor magnetic resonance imaging study. *Arch Neurol* 2002b; **59:** 1406-1412.

Rovaris M, Bozzali M, Iannucci G *et al.* Assessment of normal-appearing white and gray matter in patients with primary progressive multiple sclerosis: a diffusion-tensor magnetic resonance imaging study. *Arch Neurol* 2002a; **59:** 1406-1412.

Rovaris M, Bozzali M, Santuccio G*et al.* In vivo assessment of the brain and cervical cord pathology of patients with primary progressive multiple sclerosis. *Brain* 2001; **124:** 2540-2549.

Rovaris M, Filippi M. The value of new magnetic resonance techniques in multiple sclerosis. *Curr Opin Neurol* 2000; **13:** 249-254.

Rovaris M, Iannucci G, Falautano M *et al.* Cognitive dysfunction in patients with mildly disabling relapsing-remitting multiple sclerosis: an exploratory study with diffusion tensor MR imaging. *J Neurol Sci* 2002c; **195:** 103-109.

Russo C, Smoker WR, Kubal W. Cortical and subcortical T2 shortening in multiple sclerosis. *Am J Neuroradiol* 1997; **18:** 124-126.

Rutten GJ, van Rijen PC, van Veelen CW, Ramsey NF. Language area localization with three-dimensional functional magnetic resonance imaging matches intrasulcal electrostimulation in Broca's area. *Ann Neurol* 1999; **46:** 405-408.

Sadatipour BT, Greer JM, Pender MP. Increased circulating antiganglioside antibodies in primary and secondary progressive multiple sclerosis. *Ann Neurol* 1998; **44:** 980-983.

Sahyoun C, Floyer-Lea A, Johansen-Berg H, Matthews P.M. Towards an understanding of gait control: brain activation during the anticipation, preparation and execution of foot movements. *Neuroimage* 2004; **21:** 568-575.

Sarchielli P, Presciutti O, Pelliccioli GP *et al.* Absolute quantification of brain metabolites by proton magnetic resonance spectroscopy in normal-appearing white matter of multiple sclerosis patients. *Brain* 1999; **122 (Pt 3):** 513-521.

Sawcer S, Robertson N, Compston A. Genetic epidemiology of MS. In: Thompson A.J., Polman C, Hohlfeld R, editors. Multiple Sclerosis: clinical challenges and controversies. London: Martin Dunitz Ltd, 1997.

Scholz VH, Flaherty AW, Kraft E *et al.* Laterality, somatotopy and reproducibility of the basal ganglia and motor cortex during motor tasks. *Brain Res* 2000; **879:** 204-215.

Seltzer B, Pandya DN. The distribution of posterior parietal fibers in the corpus callosum of the rhesus monkey. *Exp Brain Res* 1983; **49:** 147-150.

Shimansky Y, Saling M, Wunderlich DA, Bracha V, Stelmach GE, Bloedel JR. Impaired capacity of cerebellar patients to perceive and learn two-dimensional shapes based on kinesthetic cues. *Learn Mem* 1997; **4:** 36-48.

Simon JH, Kinkel RP, Jacobs L, Bub L, Simonian N. A Wallerian degeneration pattern in patients at risk for MS. *Neurology* 2000; **54:** 1155-1160.

Smith KJ, Lassmann H. The role of nitric oxide in multiple sclerosis. *Lancet Neurol* 2002; **1:** 232-241.

Sorensen AG, Wu O, Copen WA *et al.* Human acute cerebral ischemia: detection of changes in water diffusion anisotropy by using MR imaging. *Radiology* 1999; **212:** 785-792.

Steel RM, Bastin ME, McConnell S *et al.* Diffusion tensor imaging (DTI) and proton magnetic resonance spectroscopy (1H MRS) in schizophrenic subjects and normal controls. *Psychiatry Res* 2001; **106:** 161-170.

Stejskal EO, Tanner JE. Spin diffusion measurements: spin echoes in the presence of a time-dependent field gradient. *J Chem Phys* 1965; **42:** 288-292.

Stevenson VL, Miller DH, Rovaris M *et al.* Primary and transitional progressive MS: a clinical and MRI cross- sectional study. *Neurology* 1999; **52:** 839-845.

Stieltjes B, Kaufmann WE, van Zijl PC *et al.* Diffusion tensor imaging and axonal tracking in the human brainstem. *Neuroimage* 2001; **14:** 723-735.

Suhy J, Rooney WD, Goodkin DE *et al.* 1H MRSI comparison of white matter and lesions in primary progressive and relapsing-remitting MS. *Mult Scler* 2000; **6:** 148-155.

Symms, M. R., Barker, G. J., Franconi, F., and Clark, C. A. Correction of eddy-current distortions in diffusion-weighted echo-planar images with a two-dimensional registration technique. *Proc Int Soc Magn Reson Med* 1997. Abstract.

Tartaglino LM, Friedman DP, Flanders AE, Lublin FD, Knobler RL, Liem M. Multiple sclerosis in the spinal cord: MR appearance and correlation with clinical parameters. *Radiology* 1995; **195:** 725-732.

Thickbroom GW, Byrnes ML, Mastaglia FL. Dual representation of the hand in the cerebellum: activation with voluntary and passive finger movement. *Neuroimage* 2003; **18:** 670-674.

Thickbroom GW, Phillips BA, Morris I, Byrnes ML, Sacco P, Mastaglia FL. Differences in functional magnetic resonance imaging of sensorimotor cortex during static and dynamic finger flexion. *Exp Brain Res* 1999; **126:** 431-438.

Thompson AJ, Kermode AG, Wicks D *et al.* Major differences in the dynamics of primary and secondary progressive multiple sclerosis. *Ann Neurol* 1991; **29:** 53-62.

Thompson AJ, Montalban X, Barkhof F *et al.* Diagnostic criteria for primary progressive multiple sclerosis: a position paper. *Ann Neurol* 2000; **47:** 831-835.

Thompson AJ, Polman CH, Miller DH *et al.* Primary progressive multiple sclerosis. *Brain* 1997; **120 (Pt 6):** 1085-1096.

Thorpe JW, Kidd D, Moseley IF *et al.* Serial gadolinium-enhanced MRI of the brain and spinal cord in early relapsing-remitting multiple sclerosis. *Neurology* 1996a; **46:** 373-378.

Thorpe JW, Kidd D, Moseley IF *et al.* Spinal MRI in patients with suspected multiple sclerosis and negative brain MRI. *Brain* 1996b; **119 (Pt 3):** 709-714.

Thulborn KR, Waterton JC, Matthews PM, Radda GK. Oxygenation dependence of the transverse relaxation time of water protons in whole blood at high field. *Biochim Biophys Acta* 1982; **714:** 265-270.

Tievsky AL, Ptak T, Farkas J. Investigation of apparent diffusion coefficient and diffusion tensor anisotrophy in acute and chronic multiple sclerosis lesions. *Am J Neuroradiol* 1999; **20:** 1491-1499.

Tintore M, Rovira A, Martinez MJ *et al.* Isolated demyelinating syndromes: comparison of different MR imaging criteria to predict conversion to clinically definite multiple sclerosis. *Am J Neuroradiol* 2000; **21:** 702-706.

Tofts PS, Barker GJ, Simmons A *et al.* Correction of nonuniformity in images of the spine and optic nerve from fixed receive-only surface coils at 1.5 T. *J Comput Assist Tomogr* 1994; **18:** 997-1003.

Toosy A, Werring D, Bullmore E *et al.* Functional magnetic resonance imaging of the cortical response to photic stimulation in humans following optic neuritis recovery. *Neurosci Lett* 2002; **330:** 255.

Toosy AT, Ciccarelli O, Parker GJ, Wheeler-Kingshott CA, Miller DH, Thompson AJ. Characterizing function-structure relationships in the human visual system with functional MRI and diffusion tensor imaging. *Neuroimage* 2004; **21:** 1452-1463.

Tourbah A, Stievenart JL, Gout O *et al.* Localized proton magnetic resonance spectroscopy in relapsing remitting versus secondary progressive multiple sclerosis. *Neurology* 1999; **53:** 1091-1097.

Traboulsee A, Dehmeshki J, Peters KR *et al.* Disability in multiple sclerosis is related to normal appearing brain tissue MTR histogram abnormalities. *Mult Scler* 2003; **9:** 566-573.

Trapp BD, Peterson J, Ransohoff RM, Rudick R, Mork S, Bo L. Axonal transection in the lesions of multiple sclerosis. *N Engl J Med* 1998; **338:** 278-285.

Trapp BD, Ransohoff R, Rudick R. Axonal pathology in multiple sclerosis: relationship to neurologic disability. *Curr Opin Neurol* 1999; **12:** 295-302.

Traugott U, Reinherz EL, Raine CS. Multiple sclerosis: distribution of T cell subsets within active chronic lesions. *Science* 1983; **219:** 308-310.

Trojano M, Avolio C, Manzari C *et al.* Multivariate analysis of predictive factors of multiple sclerosis course with a validated method to assess clinical events. *J Neurol Neurosurg Psychiatry* 1995; **58:** 300-306.

Tseng WY, Lin CP, Chen JH, Wedeen VJ. Diffusion spectrum imaging of complex cortical cytoarchitecture in adult rats. *Proceedings of the International Society for Magnetic Resonance in Medicine* 2002 441.

Tuch, D. S., Wiegell, M. R., Reese, T. G., Belliveau J.W., and Wedeen, V. Measuring cortico-cortical connectivity matrices with diffusion spectrum imaging. *Proc Int Soc Magn Reson Med* 2001. Abstract.

Turner R, Le Bihan D, Moonen CT, DesPres D, Frank J. Echo-planar time course MRI of cat brain oxygenation changes. *Magn Reson Med* 1991; **22:** 159-166.

Tweig DB. The k-trajectory formulation of the NMR imaging process with applications in analysis and synthesis of imaging methods. *Med Phys* 1983; **10:** 610.

Tzourio-Mazoyer N, Landeau B, Papathanassiou D *et al.* Automated anatomical labeling of activations in SPM using a macroscopic anatomical parcellation of the MNI MRI single-subject brain. *Neuroimage* 2002; **15:** 273-289.

van Meulen P, Groen JP, Cuppen JJM. Very fast MR imaging by field echoes and small angle excitation. *Magn Reson Imaging* 1985; **3:** 297.

van Waesberghe JH, Kamphorst W, De Groot CJ *et al.* Axonal loss in multiple sclerosis lesions: magnetic resonance imaging insights into substrates of disability. *Ann Neurol* 1999; **46:** 747-754.

van Waesberghe JH, van Walderveen MA, Castelijns JA *et al.* Patterns of lesion development in multiple sclerosis: longitudinal observations with T1-weighted spin-echo and magnetization transfer MR. *Am J Neuroradiol* 1998; **19:** 675-683.

van Walderveen MA, Kamphorst W, Scheltens P *et al.* Histopathologic correlate of hypointense lesions on T1-weighted spin- echo MRI in multiple sclerosis. *Neurology* 1998; **50:** 1282-1288.

van Walderveen MA, Lycklama ANG, Ader HJ *et al.* Hypointense lesions on T1-weighted spin-echo magnetic resonance imaging: relation to clinical characteristics in subgroups of patients with multiple sclerosis. *Arch Neurol* 2001; **58:** 76-81.

Virta A, Barnett A, Pierpaoli C. Visualizing and characterizing white matter fiber structure and architecture in the human pyramidal tract using diffusion tensor MRI. *Magn Reson Imaging* 1999; **17:** 1121-1133.

Ward NS, Brown MM, Thompson AJ, Frackowiak RS. Neural correlates of outcome after stroke: a cross-sectional fMRI study. *Brain* 2003; **126:** 1430-1448.

Ward NS, Frackowiak RS. Age-related changes in the neural correlates of motor performance. *Brain* 2003; **126:** 873-888.

Watkins KE, Paus T, Lerch JP *et al.* Structural asymmetries in the human brain: a voxel-based statistical analysis of 142 MRI scans. *Cereb Cortex* 2001; **11:** 868-877.

Waxman SG. Acquired channelopathies in nerve injury and MS. *Neurology* 2001; **56:** 1621-1627.

Wedeen, V. J., Reese, T. G., Tuch, D. S., Weigel, M. R., Dou, J. G., Weiskoff, R. M., and Chessler, D. Mapping fiber orientation spectra in cerebral white matter with Fourier-tranform diffusion MRI. *Proc Int Soc Magn Reson Med* 2000. Abstract.

Weiller C, Juptner M, Fellows S *et al.* Brain representation of active and passive movements. *Neuroimage* 1996; **4:** 105-110.

Weinshenker BG, Bass B, Rice GP *et al.* The natural history of multiple sclerosis: a geographically based study. 2. Predictive value of the early clinical course. *Brain* 1989a; **112 (Pt 6):** 1419-1428.

Weinshenker BG, Bass B, Rice GP *et al.* The natural history of multiple sclerosis: a geographically based study. I. Clinical course and disability. *Brain* 1989b; **112 (Pt 1):** 133-146.

Weinshenker BG, Issa M, Baskerville J. Long-term and short-term outcome of multiple sclerosis: a 3-year follow-up study. *Arch Neurol* 1996; **53:** 353-358.

Werring DJ, Brassat D, Droogan AG *et al.* The pathogenesis of lesions and normal-appearing white matter changes in multiple sclerosis: a serial diffusion MRI study. *Brain* 2000a; **123 (Pt 8):** 1667-1676.

Werring DJ, Bullmore ET, Toosy AT *et al.* Recovery from optic neuritis is associated with a change in the distribution of cerebral response to visual stimulation: a functional magnetic resonance imaging study. *J Neurol Neurosurg Psychiatry* 2000b; **68:** 441-449.

Werring DJ, Clark CA, Barker GJ, Thompson AJ, Miller DH. Diffusion tensor imaging of lesions and normal-appearing white matter in multiple sclerosis. *Neurology* 1999; **52:** 1626-1632.

Werring DJ, Clark CA, Droogan AG, Barker GJ, Miller DH, Thompson AJ. Water diffusion is elevated in widespread regions of normal-appearing white matter in multiple sclerosis and correlates with diffusion in focal lesions. *Mult Scler* 2001; **7:** 83-89.

Werring DJ, Toosy AT, Clark CA *et al.* Diffusion tensor imaging can detect and quantify corticospinal tract degeneration after stroke. *J Neurol Neurosurg Psychiatry* 2000c; **69:** 269-72.

Westin CF, Maier SE, Mamata H, Nabavi A, Jolesz FA, Kikinis R. Processing and visualization for diffusion tensor MRI. *Med Image Anal* 2002; **6:** 93-108.

Wheeler-Kingshott CA, Barker GJ. D - the Diffusion of water. In: Tofts P, editor. Quantitative MRI of the brain. London: John Wiley & Sons, 2003: 201-55.

Wheeler-Kingshott, C. A., Schmierer K., Ciccarelli, O., Boulby, P., Parker, G. J., and Miller, D. H. Diffusion tensor imaging of post-mortem brain slices (freshed and fixed) on a clinical scanner. *Proc Int Soc Magn Reson Med* 2003. Abstract.

Wiegell MR, Tuch DS, Larsson HB, Wedeen VJ. Automatic segmentation of thalamic nuclei from diffusion tensor magnetic resonance imaging. *Neuroimage* 2003; **19:** 391-401.

Wieshmann UC, Clark CA, Symms MR, Franconi F, Barker GJ, Shorvon SD. Anisotropy of water diffusion in corona radiata and cerebral peduncle in patients with hemiparesis. *Neuroimage* 1999a; **10:** 225-230.

Wieshmann UC, Clark CA, Symms MR, Franconi F, Barker GJ, Shorvon SD. Reduced anisotropy of water diffusion in structural cerebral abnormalities demonstrated with diffusion tensor imaging. *Magn Reson Imaging* 1999b; **17:** 1269-1274.

Willer CJ, Ebers GC. Susceptibility to multiple sclerosis: interplay between genes and environment. *Curr Opin Neurol*2000; **13:** 241-247.

Wilson M, Tench CR, Morgan PS, Blumhardt LD. Pyramidal tract mapping by diffusion tensor magnetic resonance imaging in multiple sclerosis: improving correlations with disability. *J Neurol Neurosurg Psychiatry* 2003; **74:** 203-207.

Wolansky LJ, Holodny AI, Sheth MP, Axen R, Prasad V. Double-shot magnetic resonance imaging of cerebral lesions: fast spin-echo versus echo planar sequences. *J Neuroimaging* 2000; **10:** 131-137.

Wolinsky JS. The diagnosis of primary progressive multiple sclerosis. *J Neurol Sci* 2003; **206:** 145-152.

Woods RP, Cherry SR, Mazziotta JC. Rapid automated algorithm for aligning and reslicing PET images. *J Comput Assist Tomogr* 1992; **16:** 620-633.

Worsley KJ, Friston KJ. Analysis of fMRI time-series revisited--again. *Neuroimage* 1995; **2:** 173-181.

Worsley KJ, Marrett S, Neelin P, Vandal AC, Friston KJ, Evans AC. A unified statistical approach for determining significant signals in images of cerebral activation. *Hum Brain Mapp* 1996; **4:** 58-73.

Wylezinska M, Cifelli A, Jezzard P, Palace J, Alecci M, Matthews PM. Thalamic neurodegeneration in relapsing-remitting multiple sclerosis. *Neurology* 2003; **60:** 1949-1954.

Xu D, Mori S, Solaiyappan M, van Zijl PC, Davatzikos C. A framework for callosal fiber distribution analysis. *Neuroimage* 2002; **17:** 1131-1143.

Xue R, van Zijl PC, Crain BJ, Solaiyappan M, Mori S. In vivo three-dimensional reconstruction of rat brain axonal projections by diffusion tensor imaging. *Magn Reson Med* 1999; **42:** 1123-1127.

Yeterian EH, Pandya DN. Corticostriatal connections of the superior temporal region in rhesus monkeys. *J Comp Neurol* 1998; **399:** 384-402.

Yetkin FZ, Mueller WM, Hammeke TA, Morris GL, III, Haughton VM. Functional magnetic resonance imaging mapping of the sensorimotor cortex with tactile stimulation. *Neurosurgery* 1995; **36:** 921-925.

Young IR, Hall AS, Pallis CA, Legg NJ, Bydder GM, Steiner RE. Nuclear magnetic resonance imaging of the brain in multiple sclerosis. *Lancet* 1981; **2:** 1063-1066.

Zettl UK, Kuhlmann T, Bruck W. Bcl-2 expressing T lymphocytes in multiple sclerosis lesions. *Neuropathol Appl Neurobiol* 1998; **24:** 202-208.